
Behavior of concrete structures subjected to static and dynamic loading after fire exposure

Von der Fakultät Bau- und Umweltingenieurwissenschaften
der Universität Stuttgart zur Erlangung der Würde
eines Doktor-Ingenieurs (Dr.-Ing.)
genehmigte Abhandlung

Vorgelegt von
Luka Lacković
aus Zagreb, Kroatien

Hauptberichter: Prof. Dr.-Ing. habil. Joško Ožbolt
Mitberichter: Prof. Dr.-Ing. Viktor Mechtcherine
Mitberichter: Prof. Dr.-Ing. Harald Garrecht

Tag der mündlichen Prüfung: **14.07.2021**

Institut für Werkstoffe im Bauwesen der Universität Stuttgart

2021

DECLARATION OF ORIGINALITY

I declare that I have written this thesis independently and have not used any sources or auxiliary materials other than those indicated. All segments of the work that have been taken verbatim or in substance from publications or other statements are marked as such.

EIGENSTÄNDIGKEITSERKLÄRUNG

Ich erkläre, dass ich die vorliegende Arbeit selbstständig verfasst und keine anderen als die angegebenen Quellen und Hilfsmittel benutzt habe. Alle Stellen der Arbeit, die wörtlich oder sinngemäß aus Veröffentlichungen oder aus anderweitigen Äußerungen entnommen wurden, sind als solche gekennzeichnet.

Stuttgart, April 2021

Luka Lacković

ACKNOWLEDGEMENTS

I would like to express my deepest appreciation to my advisor, Prof. Dr.-Ing. Joško Ožbolt, who has guided me through the last couple of years at IWB with his invaluable advices, encouragement and positive energy. Without his unconditional support and constructive discussions this thesis wouldn't be possible. Thank you.

Furthermore I would like to thank Prof. Dr.-Ing. Victor Mechtcherine and Prof. Dr.-Ing. Harald Garrecht, for kindly accepting to be the co-reporters of my thesis. Additionally, I'm grateful to Prof. Harald Garrecht for the constant encouragement he has provided me with during my stay at IWB.

I would like to express my sincerest gratitude to Dr. Josipa Bošnjak and her team, for helping me prepare and carry out the experiments at the MPA Stuttgart.

For his continuous support and dedicated friendship, I would like to thank Mr. Simon Hampel. I will never forget the many laughs we had while sharing the office together.

Furthermore, my special thanks goes to Dr. Serena Gambarelli, who was always supportive in whatever idea I had and always lightened the day with a kind word. Special thanks goes to Mrs. Dana Ullmann and Mr. Hitesh Lakhani, who both supported me either in advisory capacity or whatever scientific or administrative query I had, as well.

I would like to thank Mrs. Monika Werner, who always found a way to provide me with the exact article or book I was looking for. The continuous support in circumventing the administrative obstacles, received from Mrs. Simone Stumpp and Mrs. Olga Weber, is greatly appreciated.

To the following colleagues and friends, I'm forever grateful for making my stay at IWB and in Stuttgart much more pleasant: Dr. Christian Baumert, Mr. Markus Berndt, Mr. Christian Blatt, Mrs. Christiane Ditzen, Mrs. Helen Hein, Mr. Piotr Lazik, Mr. Zaher Ramadan, Mr. Danijel Soldo, Mr. Ante Vučemilović - Šimunović and Dr. Kaipei Tian. Thank you all.

I would like to express special thanks to my fiancée, Doris, for her constant support during my time at IWB. She stood by me through thick and thin, always full of love and understanding. Along with her, I would like to thank my parents, Vesna and Željko, and my sister Željka, for always being there for me.

This thesis summarizes the results of the work on two projects: the behavior of fasteners under fire and preloading as well as the behavior of concrete under extreme loading - explosion and fire. Both projects were funded by the German Research Foundation DFG. Their support is greatly acknowledged.

Stuttgart, July 2021

ABSTRACT

The resistance of concrete structures exposed to extreme loading conditions such as explosion, impact, industrial accidents, tsunami, earthquake or their combination represents one of the major topics in research today. Such loading conditions are characterized with high loading rates often acting in conjunction with fire exposure. Especially vulnerable are the structures located in the seismically active areas with high level of urbanization and proximity to HAZMAT landfills, which additionally exacerbate fire conflagrations. The behavior of concrete changes significantly when exposed to elevated temperatures resulting in the decrease of its mechanical properties. Reinforced concrete (RC), when exposed to high temperature culminates in a simultaneous thermal behavior of its two constituents, steel and concrete, that should be considered in the analysis. It is also known that the resistance, crack pattern and failure mode in concrete are strongly influenced by the loading rate. The dynamic response of RC structures previously exposed to fire changes significantly when compared to initially undamaged RC structures.

The main objective of the present work is to further improve the existing rate sensitive thermo-mechanical model for concrete through the following: (i) the implementation of the experimentally obtained thermal dependence of concrete fracture energy in the thermo-mechanical model, (ii) the calculation of concrete thermally dependent mechanical properties by means of nonlocal (average) temperature and (iii) to perform parametric study on fastening elements and RC frames in order to investigate the interaction between the thermally induced damage and mechanical behavior of structures.

The experimental investigations in the present work indicated that the concrete fracture energy has a declining tendency with the temperature increase, measured on small and mid-sized concrete beams. This is implemented in the thermo-mechanical model and it is indicated that the decrease of fracture energy has a relatively mild influence on reaction values in terms of loading rate. However, its effect on the fracture patterns and reaction-time histories can be considered as more significant. The influence of the nonlocal temperature is validated against the experimental results carried out on RC frames which had been thermally pre-damaged and subsequently loaded with impact. Currently there are almost no models that can realistically predict the structural behavior at this level of complexity. Furthermore, a parametric study is carried out to show the influence of preloading of single-headed stud anchor and anchor group with two and four studs, on the residual concrete edge failure capacity after fire exposure. The

anchors are exposed to fire and loaded in shear, perpendicular to the free edge of the concrete member up to failure, in both hot and cold state (after cooling). The influence of different geometry configurations and initial conditions such as the edge distance, embedment depth, anchor diameter and duration of fire on the load-bearing behavior of anchors is investigated. It is demonstrated that the preloading has a strong negative influence on the residual load-bearing capacity of the concrete.

Finally, the numerical parametric study is performed to investigate the influence of fire duration and the loading rate on the resistance of RC frames. The response of the RC structures strongly depends on whether it was loaded in hot or residual (cold) state, i.e. after being naturally cooled down to ambient temperature. Furthermore, an extensive numerical investigation on the influence of post-earthquake fire on the residual capacity of RC frames with and without ductile detailing is conducted. The numerical investigation encompassed the validation of the thermo-mechanical model in terms of temperature distributions, thermal deflections and load-bearing capacity against the test data and subsequent parametric analysis with different levels of fire exposure ranging from 15 to 120 min.

KURZFASSUNG

Die Widerstandsfähigkeit von Betonkonstruktionen unter Einwirkung extremer Belastungsbedingungen wie z.B. Explosionen, Stoßwirkungen, Industrieunfällen, Tsunamis, Erdbeben oder deren Kombination stellt heute eines der Hauptthemenfelder in der Forschung dar. Derartige Lastfälle sind durch hohe Belastungsraten gekennzeichnet, die oft in Verbindung mit Brandeinwirkung auftreten. Besonders gefährdet sind Bauwerke, die sich in seismisch aktiven Gebieten mit hohem Urbanisierungsgrad und in der Nähe von Sondermülldeponien befinden, was Brandausbrüche zusätzlich begünstigt. Das Verhalten von Beton ändert sich erheblich, wenn dieser erhöhten Temperaturen ausgesetzt wird, was zu einer Abnahme der mechanischen Eigenschaften führt. Im Stahlbeton (RC) kommt es im Brandfall zu einem gleichzeitigen wärmeinduziertem Verhalten der beiden Komponenten Stahl und Beton, welches bei der Analyse berücksichtigt werden sollte. Zudem ist bekannt, dass der Widerstand das Rissbild und das Schadensbild im Beton stark von der Belastungsrate beeinflusst werden. Das dynamische Verhalten von Stahlbetonkonstruktionen, die zuvor einem Feuer ausgesetzt waren, ändert sich signifikant im Vergleich zu ursprünglich ungeschädigten Stahlbetonkonstruktionen.

Das Hauptziel der vorliegenden Arbeit ist es, das bestehende lastabhängige thermo-mechanische Modell für Beton durch die folgenden Aspekte zu erweitern: (i) die Implementierung der experimentell ermittelten thermischen Abhängigkeit der Betonbruchenergie in das thermomechanische Modell, (ii) die Berechnung der thermisch abhängigen mechanischen Eigenschaften des Betons mit Hilfe der nichtlokalen (durchschnittlichen) Temperatur und (iii) die Durchführung einer parametrischen Studie an Befestigungselementen und RC-Rahmen, um die Wechselwirkung zwischen der thermisch induzierten Schädigung und dem mechanischen Verhalten der Strukturen zu untersuchen.

Die experimentellen Untersuchungen in der vorliegenden Arbeit zeigen, dass die Betonbruchenergie bei Temperaturanstieg tendenziell abnimmt, was an kleinen und mittelgroßen Betonbalken gemessen wurde. Diese Erkenntnisse werden in das thermo-mechanische Modell implementiert und es wird gezeigt, dass die Abnahme der Bruchenergie einen relativ geringen Einfluss auf die Werte in Bezug auf die Belastungsrate hat. Die Auswirkung auf die Rissbilder und die Kraftreaktionsverläufe kann jedoch als bedeutender angesehen werden. Der Einfluss der nichtlokalen Temperatur wird anhand der experimentellen Ergebnisse validiert, die an thermisch vorgeschädigten und anschließend stoßbelasteten (dynamisch belasteten) RC-Rahmen durchgeführt wurden. Derzeit gibt es fast keine Modelle,

die das Strukturverhalten auf diesem Komplexitätsniveau realistisch vorhersagen können. Mit Hilfe der parametrischen Untersuchungen wird der Einfluss der Vorbelastung von Einzelbolzen und Bolzengruppen auf den Betonkantenbruch nach Brandbeanspruchung gezeigt. Die Kopfbolzen werden zuerst dem Feuer ausgesetzt und nach der Brandbelastung, sowohl im heißen als auch im kalten Zustand (nach Abkühlung), quer in die Richtung der freien Kante des Betonbauteils bis zum Bruch belastet. Der Einfluss der Geometrie (Randabstand, Verankerungstiefe, Bolzen-durchmesser) und Branddauer auf das Tragverhalten von Ankern wurde untersucht. Es wird gezeigt, dass die Vorbelastung einen starken negativen Einfluss auf den Betonkantenbruch nach der Brandbelastung aufweist.

Zudem wird eine numerische Parameterstudie durchgeführt, um den Einfluss der Branddauer und der Belastungsrate auf den Widerstand von RC-Rahmen zu untersuchen. Das Verhalten der RC-Strukturen hängt stark davon ab, ob diese im heißen oder im erkalteten Zustand, d. h. nach langsamer Abkühlung auf Umgebungstemperatur, belastet werden. Des Weiteren wird eine umfangreiche numerische Untersuchung zum Einfluss eines Brandes nach einem Erdbeben auf die Resttragfähigkeit von RC-Rahmen mit und ohne duktile Bewehrungsführung durchgeführt. Die numerische Untersuchung umfasst die Validierung des thermo-mechanischen Modells hinsichtlich der Temperaturverteilung, der thermischen Durchbiegung und der Tragfähigkeit in Abhängigkeit der Versuchsdaten und eine anschließende parametrische Analyse mit unterschiedlichen Brandbeanspruchungsgraden von 15 bis 120 min.

CONTENTS

1. INTRODUCTION	1
1.1 Background, motivation and problem statement	1
1.2 Research objectives.....	5
1.3 Scope of the work	6
2. LITERATURE REVIEW	7
2.1 Concrete at extreme loading conditions.....	7
2.1.1 Behavior of concrete at elevated temperatures	8
2.1.1.1 Fire load (scenarios).....	8
2.1.1.2 Mechanical properties of concrete	10
2.1.1.3 Thermal properties of concrete	16
2.1.2 Concrete spalling	19
2.1.3 Behavior of concrete subjected to high loading rates	21
2.2 Steel at extreme loading conditions	25
2.2.1 Behavior of steel at elevated temperatures	25
2.2.1.1 Mechanical properties	25
2.2.1.2 Steel thermal and physical properties	27
2.2.2 Behavior of steel subjected to high loading rates	29
2.3 Combined thermal and static/dynamic loading.....	33
2.3.1 Influence of fire on anchors loaded in shear perpendicular to the concrete edge..	33
2.3.1.1 Design provisions for fasteners loaded in shear exposed to fire.....	36
2.3.2 Dynamic behavior of concrete at high temperatures	38
2.4 Behavior of concrete structures subjected to seismic loading	41
2.4.1 Structures subjected to post-earthquake fire	41
2.5 Conclusions.....	43
3. EXPERIMENTAL INVESTIGATIONS.....	45
3.1 Measurement of fracture energy	45
3.1.1 Influence of temperature on fracture energy.....	45
3.1.2 Methods of determining fracture energy	47
3.1.3 Parameters affecting the work of fracture (load – displacement curve)	49
3.2 Experimental investigation: temperature dependent fracture energy	52
3.2.1 Test preparation	52
3.2.2 Thermal exposure	55

3.2.3	Small concrete specimens	57
3.2.4	Midsized concrete specimens	60
3.2.5	Fracture energy measurements	64
3.2.6	Tensile strength.....	65
3.3	Conclusions.....	66
4.	THERMO-MECHANICAL MODEL FOR CONCRETE AND THE 3D FE ANALYSIS	68
4.1	Introduction.....	68
4.2	Microplane mechanical model with relaxed kinematic constraint	69
4.2.1	Isothermal constitutive law for concrete – Microplane model	69
4.2.2	Cyclic loading in the microplane model	72
4.2.3	Microplane model for steel	73
4.2.4	Rate sensitivity.....	74
4.3	Thermo-mechanical coupling	75
4.3.1	Thermally dependent mechanical properties in the microplane model	76
4.3.2	Thermal strains	80
4.3.3	Nonlocal temperature model.....	82
4.3.3.1	Formulation.....	82
4.3.3.2	Weight function	83
4.4	3D FE analysis	85
4.4.1	Static analysis	86
4.4.2	Nonstationary (transient) thermal analysis	86
4.4.3	Transient dynamic analysis.....	88
4.5	Conclusions.....	89
5.	INFLUENCE OF EXPERIMENTALLY OBTAINED FRACTURE ENERGY ON DYNAMIC RESPONSE OF THE CT SPECIMEN.....	90
5.1	Introduction.....	90
5.2	Experimental studies of plain concrete CT specimen subjected to thermal and dynamic loading.....	91
5.3	FE analysis of CT specimens.....	94
5.3.1	FE discretization and material properties	94
5.3.2	Results of the numerical analysis.....	95
5.3.2.1	Dynamic behavior of thermally undamaged CT specimen.....	96
5.3.2.2	Dynamic behavior of thermally pre-damaged specimen (200°C)	97

5.3.2.3	Dynamic behavior of thermally pre-damaged specimen (400°C)	101
5.4	Conclusions.....	105
6.	INFLUENCE OF PRELOADING ON THE CONCRETE EDGE FAILURE OF STUD ANCHORS AFTER FIRE EXPOSURE	106
6.1	Introduction.....	106
6.2	Geometry and material properties.....	108
6.3	Numerical analysis.....	109
6.3.1	Geometry, material properties and FE model	109
6.3.2	Verification of the model	111
6.3.3	Parametric study	113
6.3.3.1	Single anchor	113
6.3.3.2	Group of anchors.....	117
6.4	Conclusions.....	119
7.	RC FRAME SUBJECTED TO THERMAL AND DYNAMIC LOADING	121
7.1	Introduction.....	121
7.2	Finite element analysis.....	122
7.3	Experimental study and verification of the numerical model.....	123
7.3.1	Geometry, FE discretization and material properties	124
7.3.2	Loading history (fire exposure and side impact)	127
7.3.3	Comparison of the experimental and numerical results.....	129
7.4	Parametric study	132
7.4.1	Static analysis	132
7.4.2	Dynamic analysis	135
7.4.3	Rate sensitivity study	138
7.5	Conclusions.....	141
8.	RC FRAME SUBJECTED TO THERMAL AND CYCLIC LOADING (POST-EARTHQUAKE FIRE).....	143
8.1	Introduction.....	143
8.2	Experimental studies on RC frame structures in post-earthquake fire scenario	143
8.2.1	Seismic load test	146
8.2.2	Fire test	148
8.2.3	Residual test.....	150
8.3	FE model, initial and boundary conditions	150
8.4	Validation of the thermo-mechanical model.....	155

8.4.1	Simulated seismic load (cyclic analysis)	155
8.4.2	Fire simulation (thermal analysis)	156
8.4.3	Residual analysis.....	162
8.5	Parametric study	166
8.5.1	Thermal exposure according to ISO 834 fire curve.....	166
8.5.2	Residual capacity (parametric study).....	172
8.6	Conclusions.....	175
9.	CONCLUSIONS AND OUTLOOK.....	176
	BIBLIOGRAPHY	179
	CURRICULUM VITAE	196

LIST OF INDICES

Microplane model

σ	stress	[N/mm ²]
ε	strain	[-]
ε_{ij}	total strain tensor for concrete	[-]
ε_{ij}^m	mechanical strain tensor	[-]
ε_{ij}^{ft}	free thermal strain tensor	[-]
ε_{ij}^{tm}	thermo-mechanical strain tensor (LITS)	[-]
ε_N	normal component of the microplane strain	[-]
ε_V	volumetric component of the microplane strain	[-]
ε_D	deviatoric component of the microplane strain	[-]
$\varepsilon_{D,eff}$	effective deviatoric component of the microplane strain	[-]
ε_S	shear component of the microplane strain	[-]
$\varepsilon_{S,eff}$	effective shear component of the microplane strain	[-]
ε_{11}	principal tensile strain	[-]
$\dot{\varepsilon}_{ij}$	macroscopic strain rate tensor	[s ⁻¹]
σ_N	normal component of the microplane stress	[N/mm ²]
σ_V	volumetric component of the microplane stress	[N/mm ²]
σ_D	deviatoric component of the microplane stress	[N/mm ²]
σ_S	shear component of the microplane stress	[N/mm ²]
σ_{11}	principal tensile stress	[N/mm ²]
S	sphere surface	[mm ²]
δ_{ij}	Kronecker delta (operator)	[-]
k_i, m_i	directions of shear microplane components	[-]
F_V	uniaxial stress-strain relations for volumetric component	[N/mm ²]
F_D	uniaxial stress-strain relations for deviatoric component	[N/mm ²]
F_S	uniaxial stress-strain relations for shear component	[N/mm ²]
ψ	discontinuity function	[-]
ε_{max}	maximum value of the effective microplane strain	[-]
ε_{min}	minimum value of the effective microplane strain	[-]
E_i	unloading-reloading tangent moduli	[N/mm ²]
E_0	initial elastic stiffness moduli	[N/mm ²]
C	secant stiffness moduli	[N/mm ²]
σ_{p+}	positive peak stress	[N/mm ²]
ε_{p+}	positive peak strain	[-]
σ_{p-}	negative peak stress	[N/mm ²]
ε_{p-}	negative peak strain	[-]

α	empirically chosen constant between 1 and 0	[-]
β	empirically chosen constant between 1 and 0	[-]
a	internal miroplane model parameter	[-]
b	internal miroplane model parameter	[-]
p	internal miroplane model parameter	[-]
q	internal miroplane model parameter	[-]
c_0, c_2	material rate constants	[-]
s_{cr}	crack spacing	[mm]
V_R	representative volume (nonlocal analysis)	[mm ³]
α_n	nonlocal weighting function	[-]

Thermo – mechanical coupling

t	time	[s]
Δt	time step	[s]
θ	relative temperature (model dependent)	[K]
T_0	absolute reference temperature	[K]
T	temperature (local)	[K]
\bar{T}	temperature (nonlocal)	[K]
$E_{c,20}$	Young's modulus of concrete at $T_0 = 20^\circ\text{C}$	[N/mm ²]
$\omega_{t,E}$	temperature-dependent damage parameter – Young's modulus (concrete)	[-]
$E_{s,20}$	Young's modulus of steel at $T_0 = 20^\circ\text{C}$	[N/mm ²]
$f_{y,s,20}$	yield strength of steel $T_0 = 20^\circ\text{C}$	[N/mm ²]
$f_{c,20}$	concrete uniaxial compressive strength at $T = 20^\circ\text{C}$	[N/mm ²]
ω_{t,f_c}	temperature-dependent damage parameter – compressive strength (concrete)	[-]
$f_{t,20}$	concrete uniaxial tensile strength at $T = 20^\circ\text{C}$	[N/mm ²]
ω_{t,f_t}	temperature-dependent damage parameter – tensile strength (concrete)	[-]
$G_{F,20}$	concrete fracture energy at $T=20^\circ\text{C}$	[N/mm]
ω_{t,G_F}^1	temperature-dependent damage parameter – fracture energy (concrete – model I)	[-]
ω_{t,G_F}^2	temperature-dependent damage parameter – tensile strength (concrete – model II)	[-]
A, B, C	model constants for the definition of LITS	[-]
l_{ch}	characteristic length	[mm]
s	coordinates of the contributing point (nonlocal formulation)	[mm]
x	coordinates of the averaging point (nonlocal formulation)	[mm]
d_{ag}	maximum aggregate size	[mm]

FE analysis

w	crack width	[mm]
h	mean element size	[mm]
V	volume of the FE element	[mm ³]
λ	thermal conductivity	[W/mK]
c_p	specific heat capacity	[J/kgK]
α_h	heat transfer coefficient	[W/m ² K]
ρ	density	[kg/m ³]
W	internal heat source	[J]
\mathbf{n}	normal on the surface	[-]
T_M	temperature of the medium	[K]
Γ	surface of the element	[mm ²]
Ω	volume of the element	[mm ³]
β	backward difference coefficient (direct time integration method)	[-]
M	mass matrix	[kg]
\ddot{u}	nodal accelerations	[m/s ²]
C	damping matrix	[Ns/m]
\dot{u}	nodal velocities	[m/s]
f	resulting nodal forces	[N]
f^{ext}	external nodal forces	[N]
f^{int}	internal nodal forces	[N]

Fracture energy measurements and numerical studies

G_F	macroscopic fracture energy (tension)	[N/mm]
A_1	area underneath the load displacement curve (Peterson method)	[mm ²]
M	total mass of the beam	[kg]
g	gravity constant (9.806)	[m/s ²]
δ_0	maximum deflection at the ultimate peak	[mm]
b	width of the beam	[mm]
d	depth of the beam	[mm]
a	depth of the crack	[mm]
$L(l)$	length of the beam	[mm]
S	distance between the supports in a TPB test	[mm]
d_c	distance between the notch tip and the upper beam surface (beam ligament)	[mm]
A_{lig}	the cross-section area of the beam ligament	[mm ²]
E_c	compressive Young's modulus	[N/mm ²]
W_t	area under the entire load-displacement curve (RILEM)	[mm ²]

W_m	area under the curve AMBA	[mm ²]
W_F	work of fracture (Guinea, Planas and Elices model)	[J]
U_A	displacement at the point A	[mm]
U_B	displacement at the point B	[mm]
P	load	[N]
P_U	peak load	[N]
ν	Poisson's ratio	[-]
f_t	tensile strength of concrete	[N/mm ²]
f_c	compressive strength of concrete	[N/mm ²]
σ_B	bending strength	[N/mm ²]
α_t	size effect coefficient	[-]
H	enthalpy of the system	[J]
ξ	conversion degree of the reactants	[-]
α_c	temperature expansion coefficient of the concrete	[1/K]
\bar{c}_p	apparent specific heat	[J/kgK]
$V_{u,c}^0$	shear resistance at ambient temperature	[N]
d_{nom}	the nominal diameter of fastener	[mm]
l_f	the effective load transfer length	[mm]
$f_{cc,200}$	cube compressive strength	[N/mm ²]
f_{cm}	mean concrete cylinder compressive strength	[N/mm ²]
$A_{c,V}$	projected area of the failure surface for the anchor group	[mm ²]
$A_{c,V}^0$	projected area of the fully developed failure surface for a single anchor	[mm ²]
$V_{u,c}$	shear failure of anchor groups	[N]
$V_{Rk,c,fi(90)}^0$	characteristic resistance of concrete edge failure at 90 min of fire exposure	[N]
$V_{Rk,c,fi(120)}^0$	characteristic resistance of concrete edge failure at 120 min of fire exposure	[N]
$P_{fi,Rd}$	design shear resistance as obtained from <i>EN 1994-1-2</i>	[N]
$k_{c,\vartheta}$	reduction factor for stress-strain relationship of concrete at high temperature.	[-]
V_b	design shear resistance as obtained from <i>ACI 318</i>	[N]
s	distance between the anchors	[mm]
h_{ef}	embedment depth	[mm]
d_a	anchor diameter	[mm]
c	edge distance (single anchor)	[mm]
c_1, c_2	edge distance (anchor group)	[mm]

1. INTRODUCTION

1.1 Background, motivation and problem statement

The behavior of concrete and steel components subjected to elevated temperatures differs substantially from their behavior at ambient temperature (Khoury, 1985a; Schneider, 1988; de Borst and Peeters, 1988; Takeuchi, 1993). It's one of the major topics of the research today where most of the current design codes provide simplified guidelines for the design of RC structures to withstand fire (EN 1992-1-2:2010. Part 1.2; IS 456:2000; ASTM E2748 - 12a; ACI 216.1-14 Fire code). However, if the loading rate, complexity of the structure, earthquake or preloading conditions are combined with fire exposure, the task of predicting structural behavior becomes more demanding.

The physical processes that take place in concrete at high temperatures represent the foundation for realistic modeling and have already been discussed and described in detail (Bažant & Thongutai, 1978; Bažant & Kaplan, 1996; Khoury et al., 1985a, 1985b; Khoury, 1996). The mechanical properties of concrete decrease significantly with the increase of temperature as well (Schneider 1988) whereby the recuperation of steel properties upon cooling differs from that of concrete. In recent years, the influence of loading velocity on the behavior of quasi-brittle materials has been intensively investigated (Dilger et al., 1978; Reinhardt, 1982; Banthia et al., 1987; Bentur et al., 1987; Curbach, 1987; Bischoff and Perry, 1991; Reinhardt and Weerheijm, 1991; Cusatis, 2011; Ožbolt et al., 2011, 2015; fib 2012). The loading rate influences the structural behavior by two effects: (i) the time-dependent growth of micro-cracks or the viscous behavior of the concrete between cracks and (ii) various influences of inertia such as formation and path of the macro-cracks, non-linear behavior of the material (hardening or softening) and inertia at the structural level. Although both effects are always present, depending on the material and the loading rate, the first or the second influence is predominant. In the case of concrete, as a quasi-brittle material, the first influence dominates for medium and high load velocities. The second influence dominates for very fast, explosive loads (Ožbolt et al., 2011), whereby the influence of high strain rates on the behavior of the material should not be neglected here either.

Principally, the resistance of the material increases with increasing loading rate, and above a certain loading rate the increase is progressive. The numerical investigations show that this progressive increase in resistance is due to the inertia and not to the strength of the material. However, this is very difficult to prove by experiments, as it is not possible to filter out the

influence of inertia completely in the experiments. This is because the experiments to determine the dynamic properties of the material are carried out on structures (e.g. concrete cylinders) and in such investigations, various inertial effects are always present, especially at very high strain rates.

The extremely rapid loads not only influence the mechanical behavior of the concrete, but also the type of failure (Ožbolt et al., 2016). Based on experimental and numerical investigations it has been confirmed (Ožbolt et al., 2006) that for various problems (e.g. uniaxial tension, bending or pulling of concrete shear connectors) the Mode I failure changes to the Mode II shear failure mode with increasing loading speed. The phenomenon can be explained by the influence of inertial forces (Ožbolt et al., 2006, 2011, 2015). The behavior of concrete at high strain rates and simultaneously at high temperature has been relatively little studied so far. In principle, there are two load scenarios: (1) thermally induced damage due to fire exposure and subsequent dynamic loading. These cases would be viable from the safety aspect, e.g. explosion or impact as a consequence of fire outbursts; (2) Post-fire scenario after dynamic or cyclic loading, e.g. a fire conflagration after an earthquake would represent a relevant scenario for engineering applications.

An unloaded test specimen under high temperature expands unhindered (free thermal expansion). The same test under mechanical load shows a completely different overall elongation behavior. The effect that leads to this difference is called "transient creep" or "load-induced thermal strain" (LITS) (RILEM, 1998). The transient creep is significantly larger than the creep of concrete loaded at normal temperature. Numerical investigations on the meso-scale of concrete have shown that the reason for such behavior is the interaction between the load-induced damage and the free thermal strains (Bošnjak, 2014). In numerical modelling of building components, both strain components have a significant influence on the behavior of the components under fire load.

The decrease of the mechanical properties of the concrete at high temperature as well as the non-elastic strains and relatively high pore pressure lead to damage and to a decrease of the load-bearing capacity of structures. Explosive or non-explosive spalling (erosion) represent a major type of damage of the concrete at its surface (Ožbolt et al., 2005b, 2008, 2014; Lakhani et al., 2014; Sharma et al., 2016). Damage in the concrete caused by thermal stress has a significant impact on the behavior of the concrete under dynamic load. With this in mind, there are virtually no test results available in the literature.

Up to now, the design rules for reinforced concrete (RC) structures exposed to fire loads have mostly been of a prescriptive nature (minimum cover and minimum dimensional requirements), which are insufficient and are not based on sound mechanical principles. Due to the lack of rational and prevention-based design methods, several incidents including the collapse of the structure due to fire exposure or simply inability for reparation after fire outburst have occurred in the past. Some of the well-known recent natural hazards that led to the structure collapses subjected previously to complex loading scenarios mentioned above are the San Fernando, USA (1971); Kobe, Japan (1995); Marmara, Turkey (1999); Fukushima, Japan (2011) and Chile (2014) earthquakes (Figure 1-1a and b). Most of these hazardous events caused uncontrollable fire conflagrations in residential and industrial buildings followed by another hazardous event (earthquake) or a series of explosions. The design guidelines for providing an adequate level of fire or seismic resistance are made separately and do not link these two events (Shah et al., 2017). If the structure collapses during the fire, there is a very high probability of personal injury, which is an unacceptable scenario for civil engineers and must be prevented. However, prescriptive design models cannot guarantee sufficient safety against the collapse of RC structures exposed to fire. The safety of an RC structure against fire load can only be guaranteed by reliable models that are able to take into account the complex phenomena mentioned above.

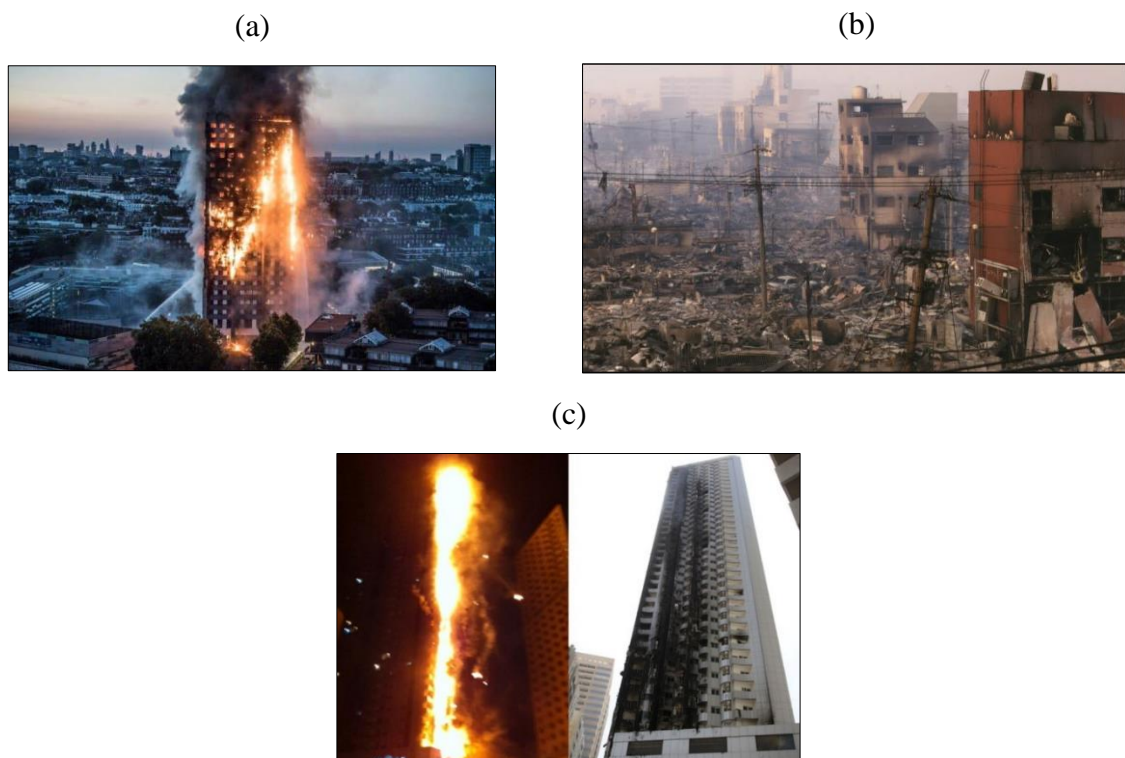


Figure 1-1. (a) London fire in 2017, (b) the aftermath of the Kobe earthquake in 1995 and (c) the Sharjah tower blaze in 2012 (Source: see bibliography).

In cases where the structure is fire resistant, damage that occurs is in the form of a concrete spalling, exposing reinforcement and culminating in degraded material properties. Few examples of structures that resisted fire without collapsing are shown in Figure 1.1c. Once the structure has been exposed to fire, it is necessary to assess whether the structure is capable of fulfilling its post-fire function or whether remedial action is required. The procedures are required to qualify the structure functionally and structurally and to estimate the type and extent of repairs required (quantitative) as well. Non-destructive investigations to estimate the extent of the decrease in material properties are necessary, but not sufficient to estimate the load-bearing capacity of the structure in a post-fire scenario.

The evaluation of seismically damaged RC frame structures pointed out the fact that the structures constructed before the mid-1970s were especially vulnerable to earthquakes due to the absence of a reliable seismic design such as the reinforcement ductile detailing in the beam-column joint and supported columns. Therefore, building code requirements for seismic design and detailing of RC have changed significantly since the mid-1970s, in response to observed earthquake damage and an increased understanding of the importance of ductile detailing of reinforcement (Shah et al., 2016). Since earthquakes are very often regarded as a low-occurrence but high-consequence event, it is difficult to account for all possible loading scenarios that could occur and to pinpoint the location of the impact.

The post-earthquake scenario (PEF) encompasses the event of fire exposure preceded by an earthquake. Structural members of an RC frame subjected to cyclic load representing an earthquake event and subsequently exposed to fire are still not investigated enough. Several experimental tests on full-scale concrete structures that have been done in the past decade will be used for the validation and calibration of thermo-mechanical model implemented into a 3D finite element (FE) program.

1.2 Research objectives

The main objectives of the presented work can be summarized with the following milestones:

1. Investigate the influence of preloading and fire duration of a single anchor and anchor groups with two and four studs, on the residual concrete edge capacity loaded in shear, perpendicular to the free edge of concrete member.
2. Investigate the influence of thermal and dynamic load or their combination on the response of RC structures from the numerical point of view.
3. Perform experimental investigation on small and mid-sized plain concrete beams to determine the influence of temperature on fracture energy up to 600°C.
4. Update the existing thermo-mechanical model with the experimentally obtained data and perform parametric numerical analysis on CT specimens subjected to high loading rates.
5. Find the causes for the horizontal displacement underestimation of thermally pre-damaged RC frames subjected high loading rates.
6. Implementation of the nonlocal temperature field in the existing rate-dependent thermo-mechanical microplane model in order to properly calculate the reduction of concrete mechanical properties in the case of combined thermal and dynamic load.
7. With the improved thermo-mechanical model, predict correctly the response of the RC structure subjected to successive thermal and dynamic loading.
8. Investigate the influence of structural inertia and loading rate on the dynamic response of the RC structure.
9. Validate the thermo-mechanical model against the experimental data of RC frames in the PEF scenario in terms of deformations during the initial seismic analysis, temperature distributions, thermal dilatations and load-carrying capacity after the residual cyclic analysis.
10. Investigate numerically the influence of the post-earthquake fire based on the ISO 834 fire curve on the residual capacity of RC frames with and without ductile detailing.

1.3 Scope of the work

Within the scope of the present work, the influence of thermally induced damage on the static and dynamic behavior of plain and reinforced concrete structures will be investigated. Particular attention will be paid on the fire duration times, rate of loading, the complexity of the reinforcement configuration, the deterioration of concrete mechanical properties at elevated temperature and the loading boundary conditions. The thermo-mechanical model will be validated against each of the study cases and subsequently a parametric analysis will be carried out.

Although the influence of temperature on the concrete load-bearing capacity with single and group of fasteners in both hot and cold state has already been investigated (Tian, 2018), the influence of preloading of single and anchor groups on the residual concrete capacity after fire exposure, in both hot and cold (residual) state still has to be properly appraised. In that manner, an extensive parametric study including different geometry configurations and initial conditions (fire exposure duration) is carried out to investigate the effect of preloading.

The second part of the numerical study will be focused on the response of RC frame under combined thermal and dynamic loading conditions. Particularly, the influence of the nonlocal temperature field on the reduction of concrete mechanical properties and the dynamic response of the RC structure is investigated. Furthermore, the contribution of the rate sensitive constitutive law for concrete on the dynamic structural resistance and failure mode is examined.

Fracture energy was assumed to be the reason for the mismatch between the experimental and numerical results in the preceding numerical study (Ruta, 2018). To get a better insight on the influence of temperature on fracture energy, an experimental study including small and mid-sized specimens has been carried out. The obtained temperature dependence was implemented in the existing thermo-mechanical model and subsequently, the FE study under the same boundary conditions as in the experiment was carried out again.

Furthermore, a large part of the numerical study was dedicated to the numerical investigation on the influence of PEF on the residual capacity of RC frames with and without ductile detailing. The numerical study initially focuses on the validation of the numerical model in terms of temperature distribution, thermal deflections of structural members and the residual capacity of the RC frames against the experimental results. Subsequently the influence of fire duration, considering the same loading sequence as in the experiment, on the load bearing capacity is numerically studied.

2. LITERATURE REVIEW

The following text encompasses four subject matters concerning the behavior of concrete and steel under various loading conditions with the emphasis on temperature and dynamic loading:

- (i) Concrete behavior under extreme loading conditions (elevated temperature and high loading rates),
- (ii) Steel behavior under extreme loading conditions,
- (iii) Preliminary work on the subject of thermal and dynamic loading,
- (iv) Behavior of concrete subjected to seismic loading and post-earthquake fire (PES).

In the previous chapter, a short summary was provided as to what these types of extreme loading conditions could culminate in.

2.1 Concrete at extreme loading conditions

The use of terminology for extreme loading conditions will be further in the text considered as the combination of boundary conditions consisted of fire exposure and/or dynamic loading. To evaluate correctly the results of the experimental work and numerical investigations, one must understand the complex processes occurring in concrete and reinforced concrete (RC) structures under extreme loading conditions. The behavior of concrete under fire exposure is a complex phenomenon, especially because concrete contains water that changes its aggregate state when heated whereby the free water behaves differently from physically or chemically bounded water. Moreover, aggregates can change their crystal structure (quartz) or lose mass (limestone). Often, due to boundary conditions, the thermal expansion is prevented resulting in constraining forces and strong temperature gradients that materialize in the event of fire resulting in thermally induced stresses. The creep and relaxation, which may be increased at high temperatures, play an important role as well. The deterioration of concrete mechanical properties subjected to elevated temperature can be attributed to (Arioz O., 2007):

- (i) Physico – chemical changes in the cement paste,
- (ii) Physico – chemical changes in the aggregate,
- (iii) Thermal incompatibility between the aggregates and the cement paste.

The chemo-physical processes occurring in concrete and its constituents at different temperature levels are illustrated in Figure 2-1a. An example of the concrete microstructure based on silico-calcareous aggregates at 600°C is shown in Figure 2-1b.

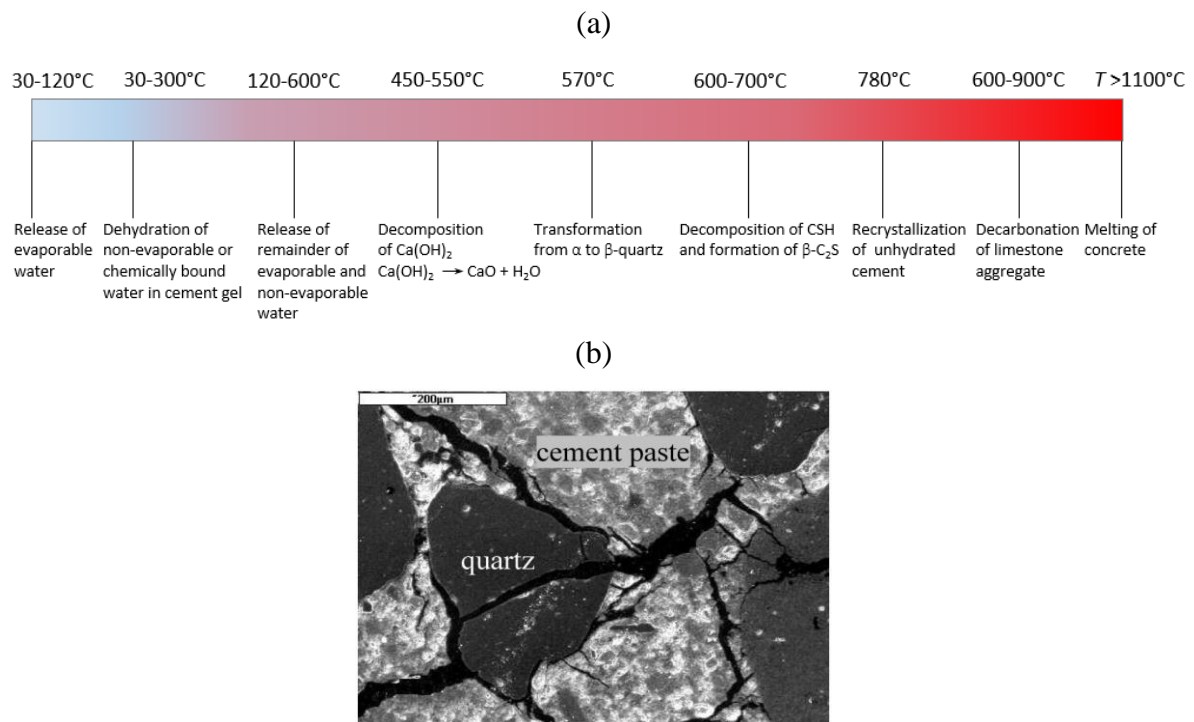


Figure 2-1. (a) Physical and chemical changes that occur in concrete at elevated temperatures and (b) the microstructure of concrete based on silico-calcareous aggregates heated to 600°C (Hager et al., 2013).

2.1.1 Behavior of concrete at elevated temperatures

2.1.1.1 Fire load (scenarios)

Structural members exposed to fire will react differently depending on the temperature gradient, utilized fuel, the oxygen supply or the presence of wind. To ensure a consistent comparison of the structural sensitivity to fire, the temperature-time ($T-t$) curves, known also as design fire curves are used. These curves are classified by their heating gradient, area of application (tunnel, train, car fires etc.) or the scenarios types. Table 2-1 provides an overview of the fire design curves for different fire scenarios, while the RWS and RABT curve are described below.

RWS (Rijkswaterstaat) curve

For the purpose of evaluation of tunnel protecting materials, the RWS curve was proposed for the worst-case scenario, i.e. a 50 m^3 fuel, oil or petrol fire in a tunnel. It is characterized with high thermal gradients, reaching 1200°C in the first 10 minutes and further increase to 1350°C .

RABT curves

The RABT curves represent a scenario with fire developed in train and car accidents. The rapid increase in temperature to 1200°C where it remains constant for about one hour is observed,

followed by a linear cooling branch to the room temperature.

Table 2-1. Fire design curves for different fire scenarios.

Design fire curve	Equation	Area of application
Standard ISO 834	$T = 20 + 345 \log_{10}(8t + 1)$	All fire design scenarios
Eurocode I	$T = 20 + 660(1 - 0.687e^{-0.32t}) - 0.313e^{-3.8t}$	External fire curve
Hydrocarbon curve (HC)	$T = 20 + 1080(1 - 0.325e^{-0.167t}) - 0.675e^{-2.5t}$	Ignition of oil, gas, chemicals etc.
modified HC curve	$T = 20 + 1280(1 - 0.325e^{-0.167t}) - 0.675e^{-2.5t}$	based on the HC curve but with increased safety requirements

In the present work, the standard ISO 834 design fire curve is utilized in the parametric numerical simulations. For comparison, the nominal design fire curves are plotted in Figure 2-2a.

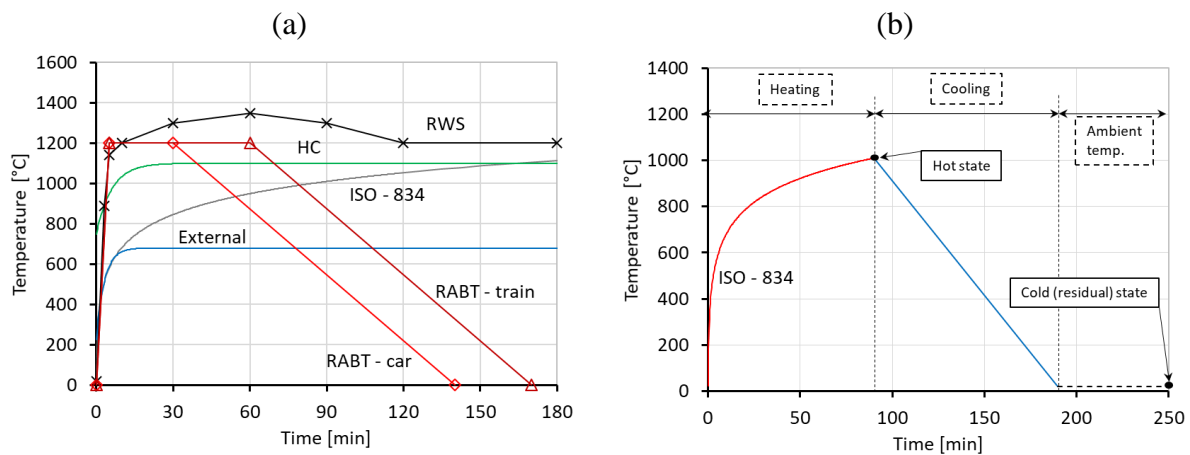


Figure 2-2. Design fire curves (a) and the clarification of the temperature states for the numerical analysis (b).

Since the majority of the numerical study is performed in either hot or cold state (residual state), a schematic description of these terms is given in Figure 2-2b. Loading in hot state is referring to application of the load or displacement when the specimen or structure is still at high temperature. The cold state refers to results obtained after the specimen has been cooled down to ambient conditions from its corresponding target temperature.

2.1.1.2 Mechanical properties of concrete

Thermal expansion of concrete

When subjected to elevated temperature, concrete undergoes a nonlinear expansion. As already mentioned, due to the difference in thermal properties of its constituents, the complete concrete microstructure is exposed to micro-strains, micro-cracking and overall deterioration process. Indeed, a large amount of concrete strength degradation can be linked to the disparity of volume expansion between the concrete and the cement paste.

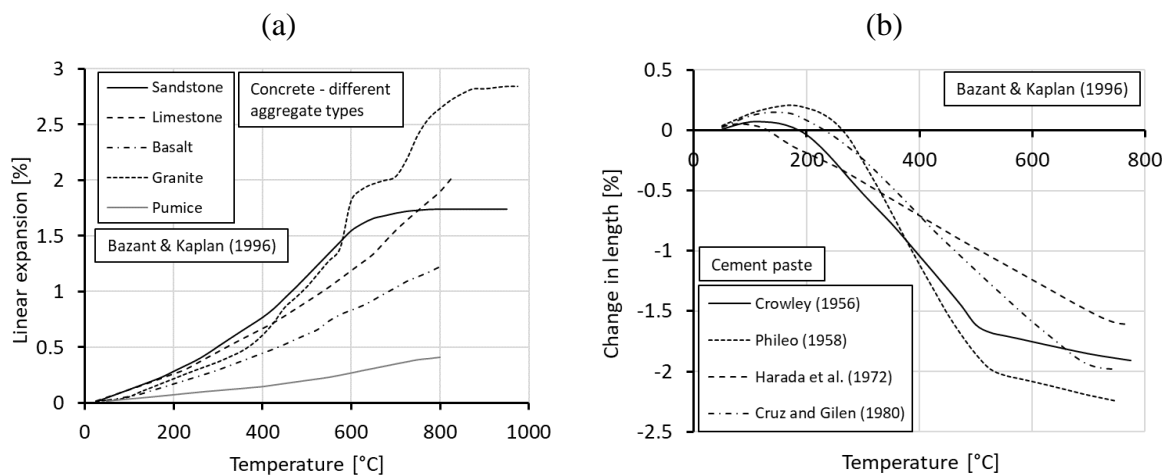


Figure 2-3. Linear thermal expansion of different aggregates (a) and a change in length of cement paste from different sources (b) as a function of temperature.

Aggregates and cement paste behave and expand differently when exposed to high temperature (Bazant and Kaplan, 1996; Khoury, 2006). Namely, aggregates such as sandstone, basalt, limestone, granite or pumice undergo a constant thermal expansion with the increase of temperature, although significant differences occur between different aggregate types. Hardened cement paste, on the contrary, expands with a maximum dilatation of 0.2% in the first stage of the heating phase, up to 150°C and then shortly before the temperature reaches 300°C, it starts to shrink and continues to contract to about 1.6 – 2.15% at 800°C. This expansion-contraction behavior of the cement paste above 100°C can be attributed to the loss of evaporable water and to different dehydration temperatures of various hydrates in the paste.

Free thermal strain

Since the aim of this study was to investigate the structure response after the first heating, no heating cycle regime was introduced as a boundary condition. Therefore, the following text will focus on the strains developed during the “first” heating cycle. The thermal strains that develop with the increase of temperature consist of “load-free” and “load-induced” components, which

have different properties. The thermal strain (TS) is the “load-free” component of total strain that develops in the non-drying concrete when it is exposed to elevated temperature without any applied load. For drying concrete, thermal strain and shrinkage are normally determined together and are considered as non-separable. With that notion, the term “thermal strain” further in the text is related to both shrinkage and thermal strains.

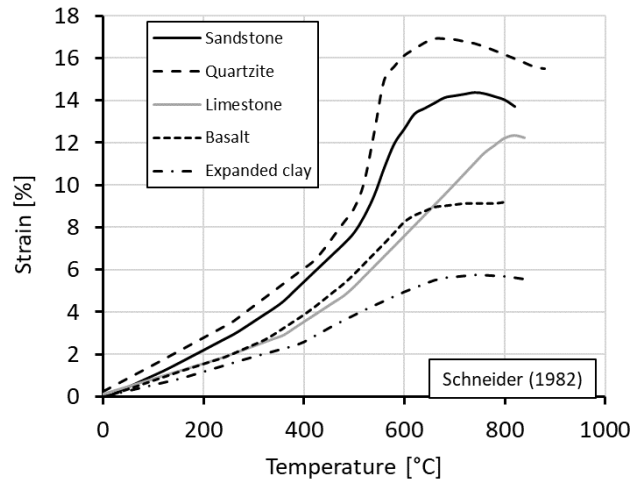


Figure 2-4. Thermal expansion of concrete with different aggregates.

Load induced thermal strain

Experimental evidence suggests that mechanically loaded concrete upon virgin heating experiences a quasi-instantaneous load-induced thermal strain (LITS). The understanding of the origin of LITS is crucial for a reliable assessment of structures affected by fire. Khoury et al. (1985b) noted the difference in strain, which develops in a concrete specimen, loaded in compression and exposed to elevated temperature compared to an unloaded concrete and referred it to as LITS.

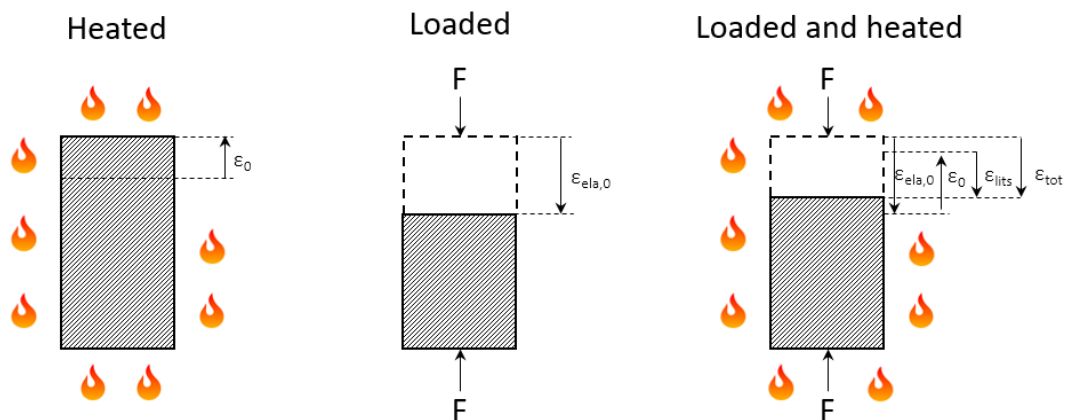


Figure 2-5. Schematic description of LITS – strain components developing in a concrete specimen for: heated state (a), Loaded state (b) and combined loaded and heated state (c) (adapted from Torrelli et al., 2016).

The LITS can be obtained by subtracting the free thermal strains in an unloaded control specimen subjected to the same thermal load as the loaded one and the elastic strain at ambient temperature from the total strain. (Figure 2-5). Anderberg and Thelandersson (1976) performed a series of measurements where the LITS component was detected (Figure 2-6b). The results were plotted for a cylindrical concrete specimen having 75 mm in diameter and 150 mm in height. It is evident that concrete at lower load levels (up to 22.5% of f_c) expands with the increase of temperature. However, at higher load levels (45% of f_c and more) concrete starts to undergo contraction.

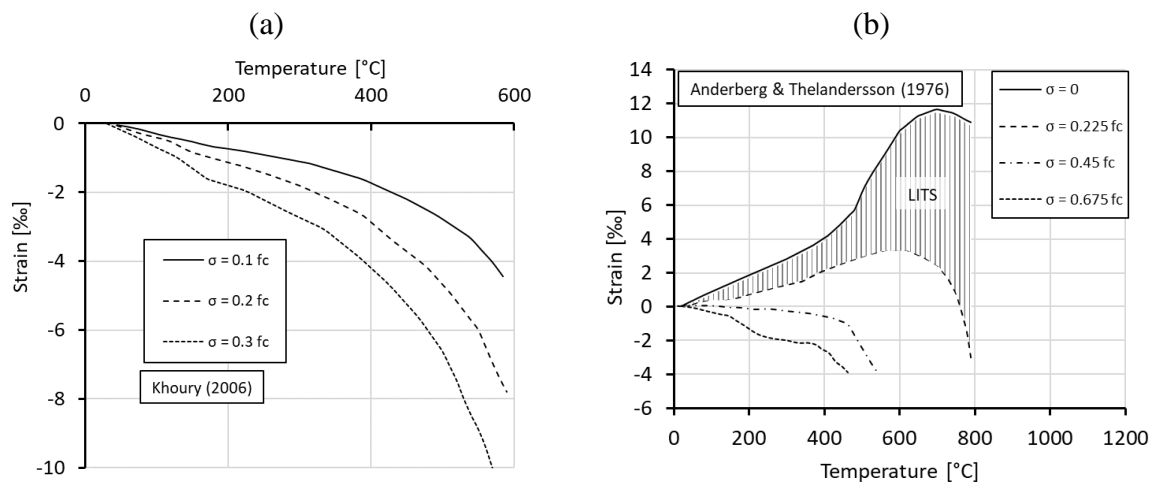


Figure 2-6. Master LITS curves (a) and total elongation of concrete during heating in unloaded and loaded condition (uniaxial compression) (b) of concrete as a function of temperature.

An important feature of LITS is that it occurs only during the first heating cycle and it is irreversible upon cooling. Figure 2-6a displays the “master” LITS curves observed by Khoury (2006), which are plotted as the difference between free thermal strain and strain from various load levels. LITS are independent of the initial moisture content for unsealed conditions and temperatures above 250°C. Furthermore, LITS are also independent of the aggregates nature for temperatures up to 400°C and on the heating rate when the rate is lower than 5°C/min (Torelli, 2016). The experimentally measured values of LITS exceeded the expected creep and elastic strain increments during the Heat-then-load tests (Schneider et al., 1988; Thelandersson, 1974 and 1982). This led to an introduction of an additional strain component that occurs during the first heating, referred to as TS (transient strain). It is important to note that it is very difficult to measure directly the isolated transient strain. For unsealed specimens, the TS is consisted of two components, the drying creep ε_{dcr} manifesting itself from the occurrence of accelerated drying process during heating and a moisture flux independent component - transient thermal creep ε_{ttc} (Hansen et al., 1966).

Concrete Young's modulus

The increase in temperature causes the formation of rapid short-time creep, which ultimately leads to the decrease of Young's modulus. Usually, the conventional value of E corresponds to the loading duration of 15 min. Since the Young's modulus represents a measure of the material stiffness, a reduction in stiffness leads to a reduction of the modulus. The breakage of bond contacts between the aggregates and the cement paste in the microstructure causes the reduction in stiffness at high temperatures. The type of the aggregate has a significant influence on the reduction of the Young's modulus with temperature. Lightweight concrete exhibits the lowest decrease in elasticity modulus, while siliceous the highest (Schneider, 1982; Cruz, 1966). Aoyagi et al. (1972) showed that the relative elastic modulus decrease is more pronounced in the high strength concrete than in the low strength concrete. Abrams et al. (1979) indicated that prolonged heating up to temperatures of 230°C causes a further reduction of the elasticity modulus. This reduction was turned out to be several times larger than that measured in short term tests.

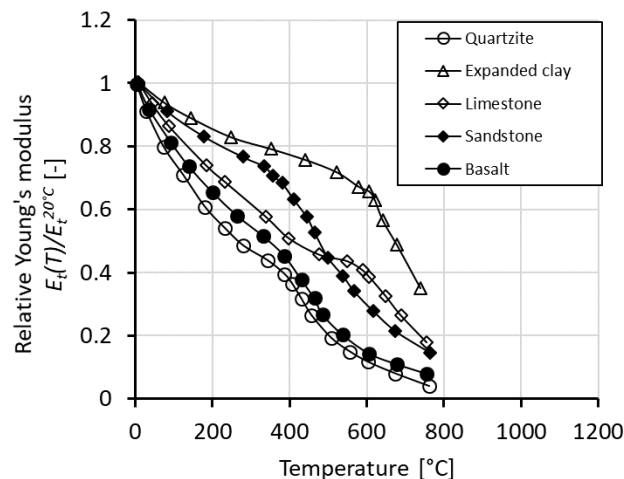


Figure 2-7. Relative elasticity modulus of concrete as a function of temperature (adapted from Schneider, 1982).

Concrete compressive strength

Compressive strength of concrete at ambient temperature depends upon water-cement ratio, aggregate-paste interface transition zone, curing conditions, aggregated type and size, admixture types and type of stress state (Mehta, 2006). At high temperature, compressive strength is highly influenced by room temperature strength, rate of heating and binders in batch mix (such as silica fume, fly ash, and slag) (Kodur, 2014). Abrams (1971) published the results of compressive strength tests on concrete cylindrical specimens made with different types of aggregate (calcareous, siliceous and lightweight expanded shale) heated to temperatures from 200 to 1600°F (93 to 870°C). Some of the results are shown in Figure 2-8. The compressive

strength, tested in hot state, gradually declines up to 650°C where the reduction amounts to 75% of its initial value.

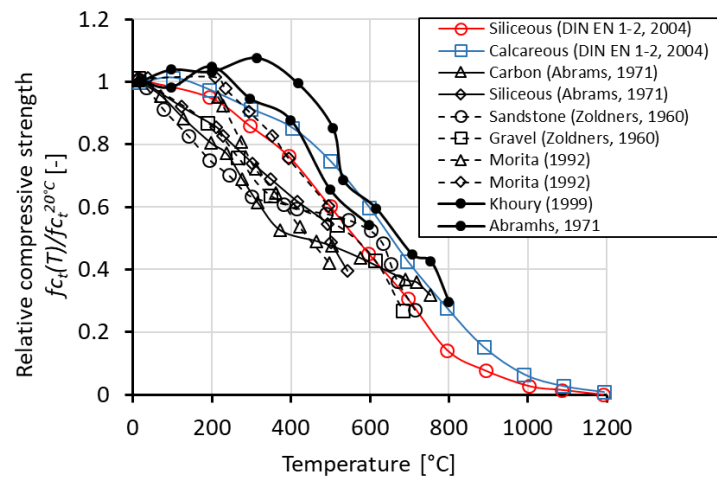


Figure 2-8. Relative compressive strength of concrete as a function of temperature.

Schneider (1982) compared the influence of temperature on compressive strength for three different aggregate types: Limestone, Expanded clay and Quartzite. A rather constant relative strength is observed up to 300°C for all three aggregate types. However, with the increase of temperature, the concrete with expanded clay exhibits the strongest reduction, while Limestone and Quartzite aggregates react approximately the same. Note that the tests were performed on unsealed specimens. Figure 2-9b displays different behavior of various concrete types depending on whether they have been tested in hot or cold state. It can be observed that the cold state negatively influences the relative decrease of compressive strength compared to its counterpart in the hot state. Concrete material suffers greater thermally induced damage when it has been cooled down to ambient temperature, hence the drop in strength.

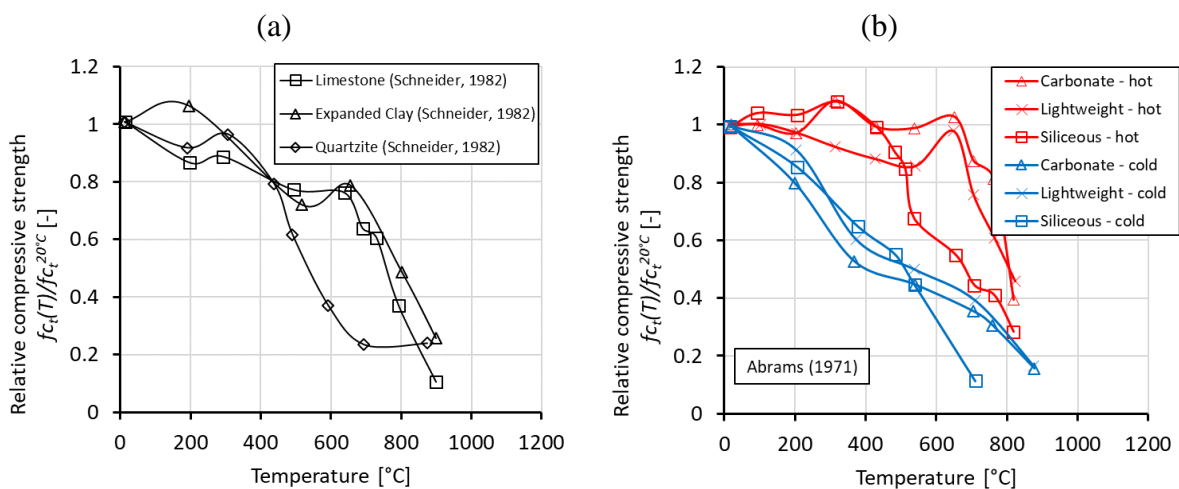


Figure 2-9. Relative compressive strength of concrete with different aggregates (a) and comparison between the hot and cold state (b) as a function of temperature.

Concrete tensile strength

Most of the tests to determine the tensile strength at elevated temperatures are carried out using the cylinder splitting test method. Concerning the mix proportions, the relative reductions of tensile strength are lower for concretes of lower original compressive strength, i.e. lean concretes with lower cement content indicate lower reductions in strength (Schneider, 1982). The reduction of concrete tensile strength with temperature is strongly influenced by the type of the aggregate as well, such as that the reduction of tensile strength of calcareous aggregate is as twice as high as siliceous aggregate concrete at 500°C. From measuring tensile strength in direct tension tests at different temperatures, Felicetti (2000) deduced that residual (cold) state does not influence the concrete tensile strength reduction, i.e. it is the same as in the hot state.

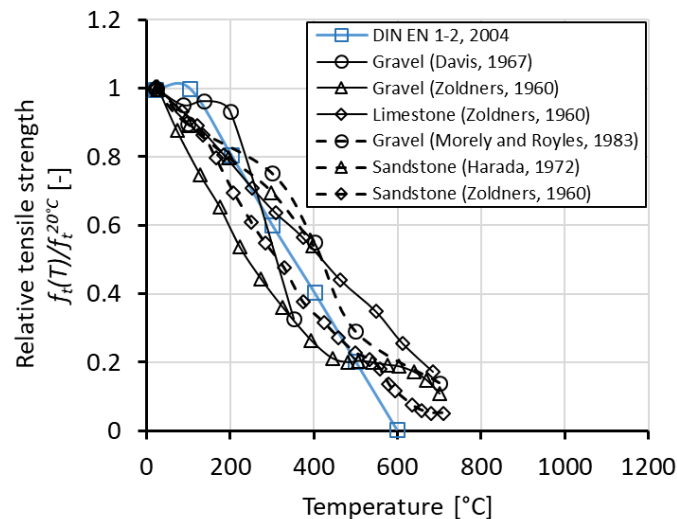


Figure 2-10. Relative tensile strength of concrete as a function of temperature.

Concrete density

The density of concrete depends mainly on the density of its aggregates and their moisture content in the temperature range between 20 and 150°C. Figure 2-11 shows a comparison of density change with temperature increase for different concrete compositions. Schneider (1982) pointed out that the specimens previously stored at 20°C and 65% relative humidity, when heated from 20 to 150°C, gave off relatively little water and therefore underwent a small change in density. It appears that Harmathy (1970) used a rather dry limestone concrete since it exhibited a density decrease from 150°C to the start of decarbonation (600°C), compared to the concrete from Hildenbrand et al. (1978) with the medium moisture range, which showed a very minor decrease in the density.

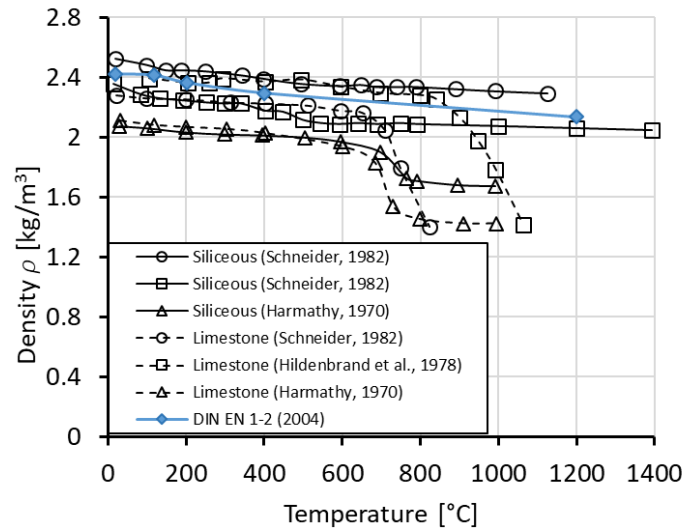


Figure 2-11. Density of concrete with different aggregates as a function of temperature.

Furthermore, concrete made with siliceous aggregates exhibits a somewhat steeper decline in density in the range between 20 and 700°C, due to the greater thermal expansion of quartzite. The reason why siliceous aggregates are in the similar range of density decline as the concrete with gravel aggregates is the addition of quartzitic sand as fine aggregate.

Fracture energy of concrete

Currently, it is generally accepted that fracture energy first increases with temperature up to 300°C and then decreases. The summary and an overview of the literature concerning the behavior of concrete fracture energy at elevated temperatures is provided in Chapter 3, as it is a part of the experimental study.

2.1.1.3 Thermal properties of concrete

Concrete thermal conductivity

Thermal conductivity is described as the ability of material to conduct heat and it is defined as the ratio of the heat flow rate to temperature gradient. At normal temperatures, the thermal conductivity of concrete is mainly dependent on the moisture content at the time of the heating and the conductivity of the aggregates. Harmaty (1970) indicated that the behavior of the cement paste heated up to 1000°C does not show any significant changes in thermal conductivity. As shown in Figure 2-12, in the temperature range between 400 and 800°C there was an increase in thermal conductivity for limestone reported (Hildenbrand et al., 1978). In

general, however, it can be stated that it reduces significantly with the temperature increase. The recommendations of the EN 1992 1-2 (2004) are plotted in Figure 2-12b. for comparison.

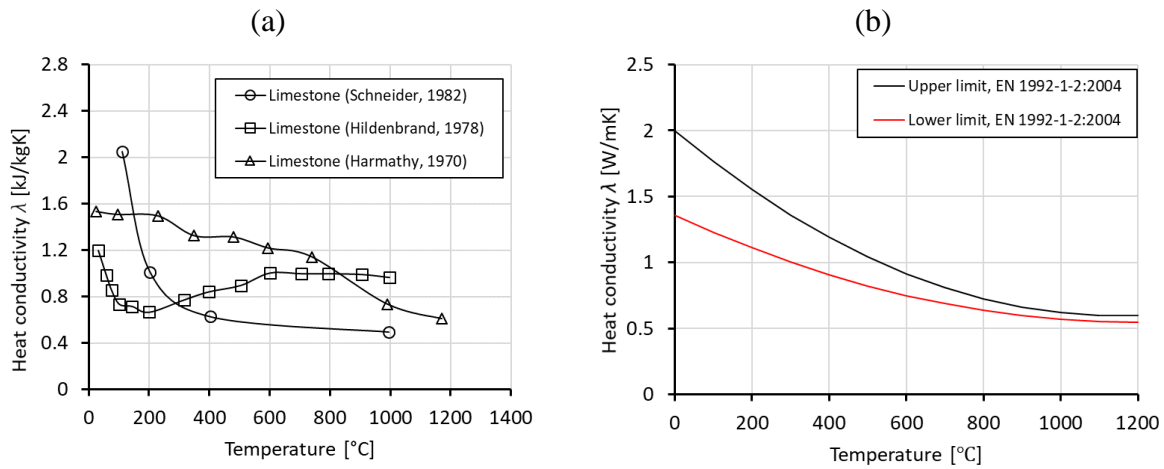


Figure 2-12. Heat conductivity of concrete with different aggregates (a) and from the EN-1992 Part 1-2 (b) as a function of temperature.

Concrete specific heat capacity

Specific heat capacity is defined as the amount of heat per unit mass required to raise the temperature by 1°C (or K). It is important to note that the Eq. (2-1) for specific heat capacity does not apply if the phase change is taking place due to the isothermal latent heat release. If the heating process is accompanied by chemical reactions of phase transitions, the resulting enthalpy is a function not only of the temperature but also the degree of conversion of the reactants into the products (Bažant and Kaplan, 1996):

$$c_p = \left(\frac{\partial H}{\partial T} \right)_{p,\xi} + \left(\frac{\partial H}{\partial \xi} \right)_{p,T} \frac{d\xi}{dT} = \bar{c}_p + \Delta H_p \frac{d\xi}{dT} \quad (2-1)$$

where ξ is the conversion degree of the reactants ($1 \geq \xi \geq 0$), c_p is the apparent specific heat and H is the enthalpy of the system. The first term on the right hand side in Eq. (2-1) represents the contribution of the sensible heat to the specific heat (no phase change) and the second term is the latent heat contribution (phase transition of the reactants). The contribution of the latent heat is significant and can be several times higher than the sensible heat due to the absorption of heat in the dehydration reactions (100-850°C). A review of the effect of temperature on the specific heat capacity increase for various concretes is summarized in Figure 2-13a. The curves indicate that for some siliceous and limestone aggregate concretes the specific heat increases up to 700°C. Depending upon whether or not the decarbonation of limestone is taken into account,

Hildenbrand et al. (1978) reported an increase in specific heat from 1.65 to 3.6 kJ/kgK. Principally, the specific heat of concrete is very dependent on the moisture content having a rapid increase when the specimens are heated from initially wet state to 90°C (Figure 2-13b). Harmathy and Allen (1973) performed tests on 16 different concretes at temperatures up to 650°C and the rate of heating 5°C/min. It was reported that the specific heat of concrete was not very sensitive to either the type of the aggregate or the mix proportions.

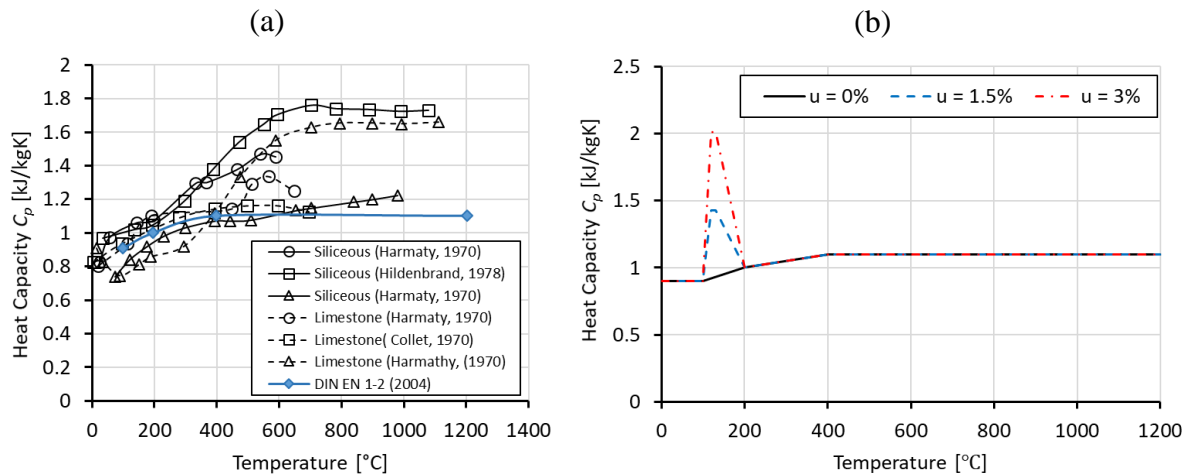


Figure 2-13. Heat capacity of concrete with different aggregates (a) and with different moisture levels (b) as a function of temperature.

Pan et al. (2016) conducted a series of measurement tests with the half-open dynamic method based on the mixing principle and applied it to determine the specific heat of concrete at temperatures up to 600°C. It was established that the specific heat increases linearly within the range of thermal storage applications of 300-600°C.

Concrete thermal diffusivity

Thermal diffusivity measures a rate of heat transfer through a medium, i.e. how fast a material reacts to a temperature change. It is obtained by dividing the thermal conductivity λ_c with the multiplication of heat capacity c_p and density ρ , which is also called the volumetric heat capacity. Thermal diffusivity is, better formulated, a term describing the balance between the passage of heat and the heat storage, because a greater thermal diffusivity does not necessarily manifest itself in a better heat dissipation. Principally it means that the higher the diffusivity is, the faster will be the temperature increase in inner concrete member region.

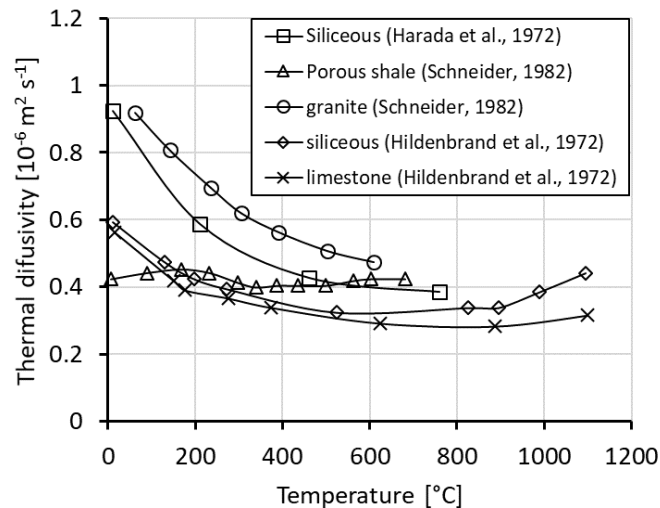


Figure 2-14. Thermal diffusivity of concrete as a function of temperature.

Figure 2-14 depicts the thermal diffusivity of different types of concrete with the temperature increase. The rapid decrease of diffusivity with temperature is observed, having its initial value reduced to 50% after 400°C. For example, the limestone diffusivity reduction is attributable to its mostly constant heat capacity and rapidly reducing thermal conductivity with temperature (density is mostly constant). Schneider (1982) states that this decrease takes place because of the influence of the moisture content reduction on concrete density and thermal conductivity.

2.1.2 Concrete spalling

Concrete spalling is a phenomenon occurring in an area close to the surface of concrete when exposed to elevated temperature and it can be divided to: (i) non-explosive and (ii) explosive spalling. The non-explosive spalling occurs due to the thermally induced stresses and related damage of concrete surface. The explosive spalling, however, presents a greater risk taking places suddenly (explosion) and it materializes with the release of high kinetic energy.

One of the three theories for the initiation of explosive spalling in concrete, the *pore pressure spalling theory*, assumes that the process itself is associated with the moisture transport in the region close to the surface. The moisture travels fundamentally in both directions, to and from the fire-exposed surface. One part evaporates towards the heated surface and the other part, having a large percentage of moisture transported towards the inner region of the concrete, condensates upon reaching cooler area. When the inner region becomes fully saturated, it is preventing the moisture close to the surface to advance to that region resulting in the one directional moisture transport (evaporation outwards to the heated surface) and the build-up of

pore pressure. When the pore pressure exceeds the tensile strength of concrete, explosive spalling occurs. (Shorter & Harmathy, 1965; Meyer-Ottens, 1972).



Figure 2-15. Explosive spalling on a concrete structural member (Source: see bibliography).

In the second theory, the thermal stress spalling, it is assumed that the severe thermal gradients occurring in the region near to the heated surface lead to a thermal shock that causes spalling. Saito (1965) initiated a theory where the explosive spalling is commenced by thermal stresses leading to a compressive failure. He has pointed out that the spalling caused by compressive failure occur mainly in pre-stressed concrete members where the tensile cracking in the central region is restricted. The specimens without pre-stress or longitudinal restraint exhibited reduced compressive forces near the heated surface due to the internal tensile cracking. Dougill (1972) indicated a shortcoming to Saito's theory, stating that concrete is a nonlinear material and therefore, the failure does not necessarily occur when the compressive stresses reach a maximum at a certain point. He pointed out that the explosive nature of the failure could be described with a type of a spring effect caused by internal tension region.

The combined pore-pressure spalling theory assumes that the main cause of the explosive spalling is the combined action of the accumulated pore pressure and the thermally induced compressive stresses in the region exposed to fire. In a premise pointed out by Zhukov (1970), the material strength of concrete can be compared with the summation of the superimposed stresses developed within a heated concrete specimen. Khoury (2000), based on Zhukov's idea, proposed a sketch describing explosive spalling based on this theory (Figure 2-16). This was recently confirmed by means of numerical simulations which clearly showed that the pore

pressure together with thermally induced stresses cause explosion spalling (Bošnjak, 2014). It was shown that the pore pressure is a trigger, i.e. it initiates the explosive spalling.

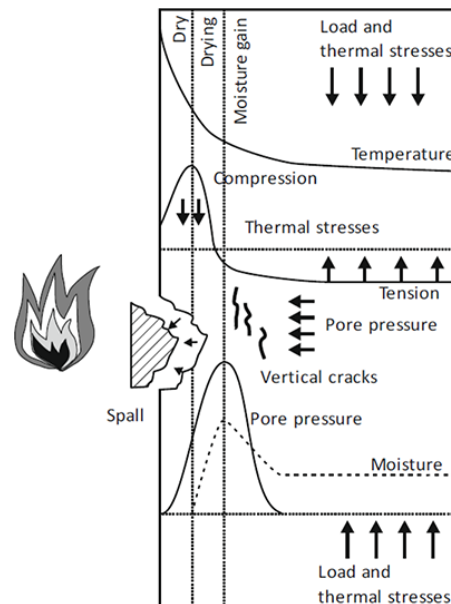


Figure 2-16. Explosive spalling caused by a combined action of thermal stresses and pore pressure (Khoury, 2000 – based on Zhukov, 1970).

2.1.3 Behavior of concrete subjected to high loading rates

Dynamic effects in concrete materials and RC structures can be introduced by applying a rapid load of short duration into structural element. Therefore, the interactions occurring in the contact zone between the impacting bodies is considered as impact of impulsive loading. From the load velocity viewpoint, dynamic load can be classified into four groups:

Table 2-2. Load classification (Sierakowski et al., 1985).

Load Classification	t/t_{resp}^*	Type of load
Quasi-static	> 4	Conventional testing of concrete
Quasi-Impact	≈ 1	Transient loading on structures
Impulsive and Impact	< 0.25	Kinetic energy, blast loads
Shock loads	$< 10^{-6}$	High energy explosives

* t/t_{resp} is the ratio of load duration (t) to characteristic response time (t_{resp})

Dynamic loads typically occur during events like projectile impact, earthquake, blast wave propagation, vehicle collision with buildings, bridge collapse etc. The behavior of concrete materials under dynamic load differs greatly from the quasi-static one. This is due to the strain-rate influence on the strength, stiffness and ductility and the influence of the inertia forces at structural and micro-crack level. Figure 2-17 summarizes different strain rates for different loading conditions.

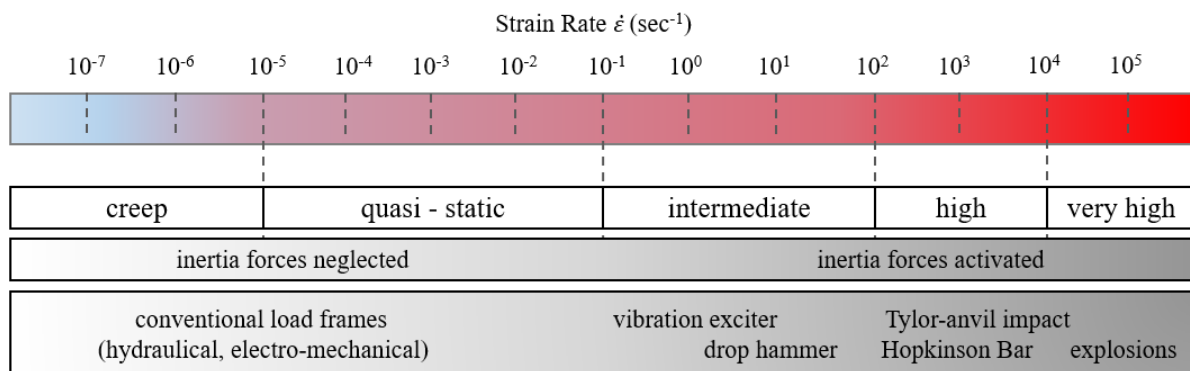


Figure 2-17. Loading range with respect to strain rate and corresponding experiments.

Principally, the response of the structure is affected by time dependent loading through three effects (Reinhardt, 1982; Bischoff and Perry, 1991; Weerheijm, 1992; Ožbolt and Reinhardt, 2005a; Pedersen et al., 2006; Ožbolt et al., 2011): (i) through the rate dependency of the growing microcracks (influence of inertia at micro-crack level), (ii) through the viscous behavior of the bulk material between the cracks (creep of concrete or viscosity due to the water content) and (iii) through the influence of inertia, which can significantly change the state of stresses and strains of the material (Ožbolt et al., 2011). In the case of quasi-brittle materials such as concrete, the first two effects are important for relatively low and medium strain rates. The third effect, the influence of the structural forces, dominates, however, at higher strain rates (impact and explosion). In principle, the resistance of the material increases with increasing loading rate, and above a certain loading rate the increase is progressive. The numerical investigations show that this progressive increase in resistance is due to the inertia and not to the strength of the material. However, this is very difficult to prove by experiments, as it is not possible to filter out the influence of inertia completely in the experiments. This is because the experiments to determine the dynamic properties of the material are carried out on structures (e.g. concrete cylinders) and in such investigations, various inertial effects are always present, especially at very high strain rates.

Figure 2-18 shows the dynamic increase factor (DIF) obtained by various researchers for the effect of loading rate on apparent tensile and compressive strength of concrete (Malvar and

Ross, 1998; Freund, 1972a, b; Reinhardt, 1982; Dilger et al., 1978; Banthia et al., 1987; Bischoff and Perry, 1991; Weerheijm, 1992; Ozbolt and Reinhardt, 2005a; Ozbolt et al., 2011; Larcher, 2009). Furthermore, the rate sensitivity of concrete is different in tension and compression (Figure 2-18).

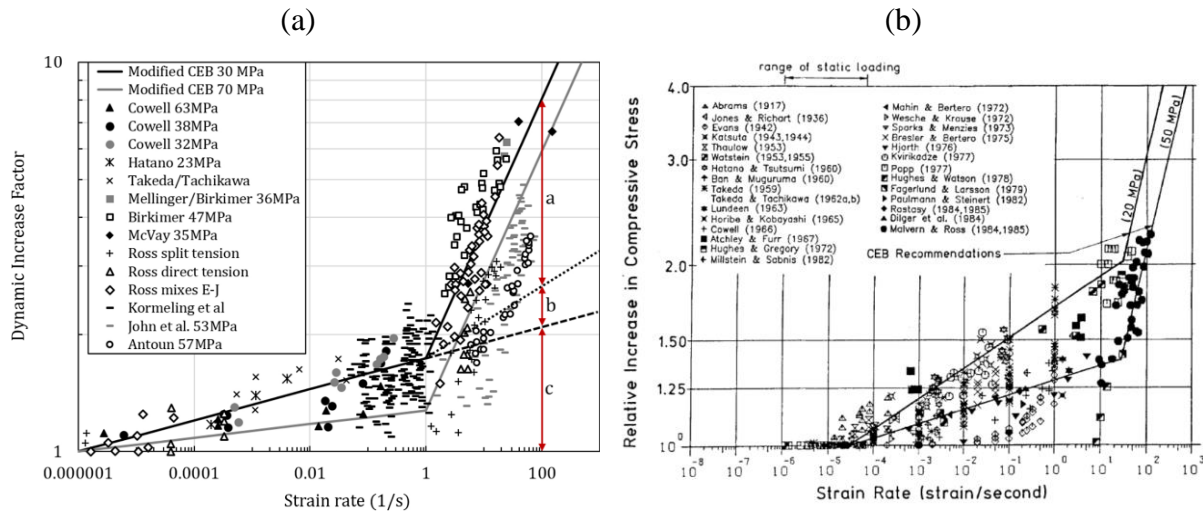


Figure 2-18. Dynamic increase factor for concrete loaded in tension (Malvar and Ross, 1998; Hwang et al., 2020) (a) and compression (Bischoff and Perry, 1991) (b) as a function of strain rate.

Low-level loading rates that correspond to quasi-static conditions could be achieved with the conventional testing methods with hydraulic or electro-mechanical machines. At these loading rates, inertia is not important and can be neglected. However, at high and very high strain rates, the influence of inertia is significant and must be accounted for. Suitable experimental tests at high loading rates are Tylor-anvil impact test, the split Hopkinson bar test or the modified split Hopkinson bar. Even numerically, it is difficult to evaluate the direct dynamic uniaxial tensile behavior of concrete since, at high loading rates, the failure always occurs locally, near the loading points. Therefore, under dynamic loads, the problem is studied through indirect tests such as split Hopkinson bar tests (Zielinski et al., 1982; Rossi et al., 1994; Weerheijm et al., 2007).

Split Hopkinson bar test (Hopkinson, 1914; Kolsky, 1953) is widely used for determining the dynamic compressive and tensile strength for concrete and steel materials. Its theory is based on the uni-axial wave propagating through elastic media. The procedure requires placing a small specimen between two identical long bars equipped with strain gauges. The projectile is then launched against one bar inducing a compressive longitudinal elastic wave that propagates into the incident bar. Only a portion of the wave is propagated in the specimen from the incident bar, while other portion is conducted through the output bar. However, several research studies

(Wu et al., 2005; Li and Meng, 2003) indicated that the SHPB test are reliable only for ductile materials such as metals and that the apparent dynamic strength enhancement beyond the strain rate of 100/s is strongly influenced by the hydrostatic stress effect due to the lateral inertia confinement in the SHPB test. Li and Meng (2003) further emphasized that the apparent dynamic strength increase due to the strain-rate effect may lead to the over-prediction on the dynamic strength of quasi-brittle materials.

The strain and strain rate is obtained by applying the theory of uniaxial wave propagation through an elastic body:

$$\varepsilon_s = -\frac{2c_0}{L} \int_0^T \varepsilon_r dt \quad (2-2)$$

$$\dot{\varepsilon}_s = -\frac{2c_0 \varepsilon_r}{L} \quad (2-3)$$

where c_0 corresponds to the wave propagation velocity, ε_r is the strain coming from the wave reflection in the output bar and L is the specimen length (Ožbolt et al., 2014). The stress in the specimen is obtained as:

$$\sigma_s = E \varepsilon_t \frac{A}{A_s} \quad (2-4)$$

where E , A and ε_t are Young's modulus, cross-sectional area and strain due to transmitted pulse in the transmitter bar, respectively, while A_s is the cross-sectional area of the specimen. The setup of the bar, as well as the initial impact velocity or the tested materials can be easily changed to achieve different loading conditions and strain rates.

The extremely rapid loads influence not only the mechanical behavior of concrete, but also the type of failure (Ožbolt et al., 2016). Based on experimental and numerical investigations it has been confirmed (Ožbolt et al., 2006) that for various problems (e.g. uniaxial tension, bending or pulling of anchor bolts) the Mode I failure mode changes to the Mode II shear failure mode with increasing loading speed. The phenomenon can be explained by the influence of inertial forces (Ožbolt et al., 2006, 2011, 2015).

2.2 Steel at extreme loading conditions

2.2.1 Behavior of steel at elevated temperatures

2.2.1.1 Mechanical properties

Stress – strain relationship at elevated temperature

Kodur et al. (2011) performed a series of tests investigating the influence of temperature on the stress-strain curve for tension. The steel type A325 was tested and evaluated at eight temperature levels ranging from 20 to 800°C. The corresponding stress-strain curves are plotted in Figure 2-19. At 20 and 250°C, a linear-elastic response up to the yielding point is observed followed by the plastic nonlinear behavior after the ultimate stress is reached. At 400°C, steel material goes into softening and experience a slight reduction in strength. At 500 and 600°C, it exhibits further softening and large deformations, with peak and yield stresses occurring in early stages. At higher temperatures, the failure strain increases due to higher ductility. Furthermore, the specimens subjected to lower heating rates are prone to the influence of high-temperature creep, which affects the stress-strain curve

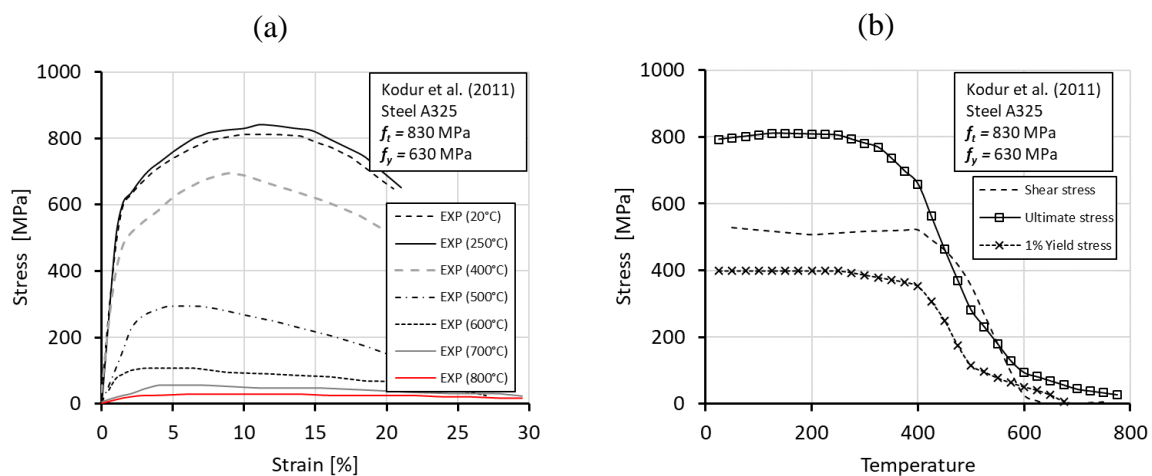


Figure 2-19. Stress- strain relationship of steel (a) and the ultimate, yield, and shear stress (b) as a function of temperature for steel type A325 (adapted from Kodur et al., 2011).

Yield stress and modulus of elasticity

The yield stress and the modulus of elasticity are generally obtained from tensile tests due to the elimination of geometric instabilities and the confinement of specimen. Furthermore, there is a lack of experiments obtained from compressive tests and it is assumed that the modulus of elasticity for steel is the same for compression state (Kodur, 2010).

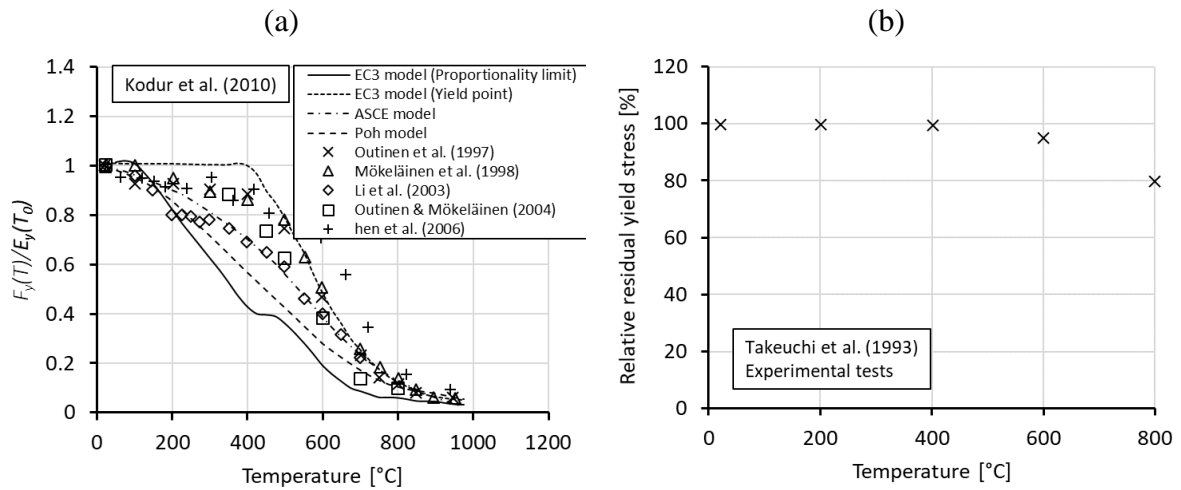


Figure 2-20. (a) Relative yield stress of steel as a function of temperature (adapted from Kodur et al., 2010) and (b) relative residual yield stress upon cooling.

As shown in Figure 2-20a, the yield stress of steel remains constant until approx. 200°C and then decrease as temperature increases. This can be attributed to the nucleus of iron atoms in steel moving apart due to the rising temperature, resulting in reduced bond strength and thus the reduced yield stress and modulus of elasticity. Variable test conditions, such as the heating rate and strain/load rates are responsible for the large scatter of data after 200°C. Furthermore, steel upon cooling exhibits remarkable recovery capabilities. According to the literature (Takeuchi, 1993), steel, when cooled down from 800°C, recovers about 80% of its initial yield stress value (Figure 2-20b). The Eurocode, ASCE and Poh (2001) models are plotted and used as a reference. The relative Young’s modulus of steel as a function of temperature is shown in Figure 2-21.

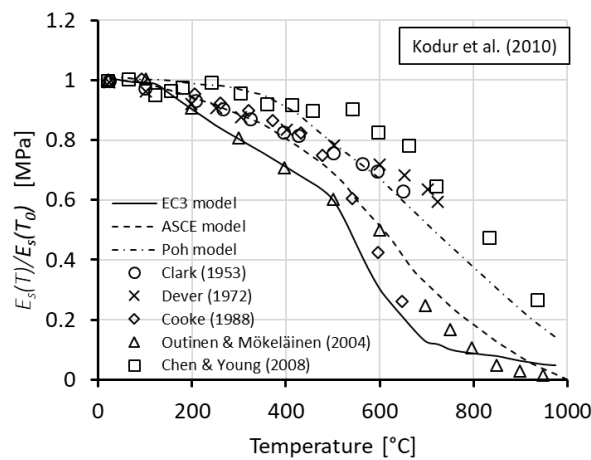


Figure 2-21. Relative elasticity modulus of steel as a function of temperature adapted from Kodur et al., 2010).

Thermal strain and thermal elongation

Thermal expansion (elongation) of steel is evaluated as the percentage of change in length compared to its original length, as shown in Figure 2-22. Principally, steel exhibits an almost linear increase in length with the increase in temperature, with the exception of high carbon steel, which displays a plateau in the range 700-800°C. This is due to the phase change, taking place in that temperature range and energy absorbed in this process is used for the changes in the microstructure.

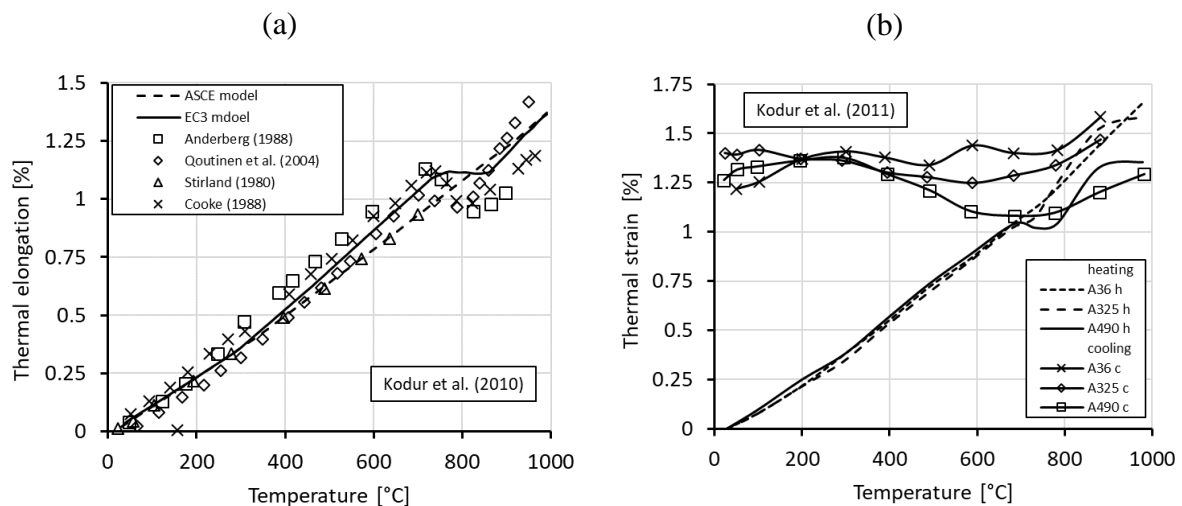


Figure 2-22. Thermal elongation (a) and Thermal strain (b) of steel as a function of temperature.

In the cooling phase, thermal strain of steel (low, medium and high carbon) follows a constant trend (Figure 2-22b.). This is due to the microstructural changes that occur when steel undergoes heating and cooling cycles.

2.2.1.2 Steel thermal and physical properties

Thermal properties such as thermal conductivity and heat capacity of steel are influenced not only by the change in temperature but by the chemical composition (carbon content) as well. The most common methods for determining these two thermal properties is the “steady-state” and the “transient” test methods. The latter is used more widely because it can realistically capture the physicochemical changes that occur in steel material.

Thermal conductivity of steel

The thermal conductivity of mild steel at room temperature is in the range from 45 to 60 W/mK. The increase of the carbon content in steel leads to the increase of the thermal conductivity (Yafei et al., 2009). Kodur et al. (2011) compared the thermal conductivity of high strength

structural steels A36, A325 and A490 in the heating and cooling phases. Thermal conductivity of all three specimens was dropping gradually with the increase of temperature with the lowest values of steel A490 because of its high carbon content. However, with the increase of temperature the influence of the carbon content diminishes and it is negligible after 700°C (at approx. 700°C steel undergoes phase change). At 735 °C thermal conductivity drops to 28 W/m°C for all three types of steel. After cooling, as temperature decreases, thermal conductivity increases to its initial value. Thus, without taking the microstructural changes that occur as a result of temperature variation into account, the thermal conductivity of steel is similar in the heating and cooling phases.

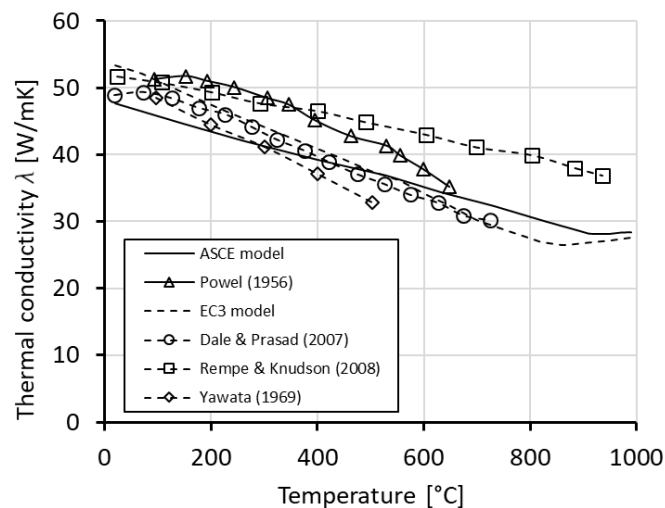


Figure 2-23. Thermal conductivity of steel as a function of temperature.

Specific heat capacity of steel

The specific heat coefficients of conventional steel is around 400 – 500 kJ/kgK at room temperature. The specific heat gradually increases with temperature up to 600°C following by a faster increase rate in the temperature range between 600 and 700°C. At 735°C a sudden jump to 1500-1700 kJ/kgK takes place. Moreover, the specific heat capacity from Eurocode 3 Part 1-2 reaches even values of 5000 kJ/kgK at its peak. The reason for this is that the microstructure of steel, when heat above 700°C, undergoes a transition from body-centered cubic “ α -ferrite” to face-centered cubic “ γ -austenite” crystal structure. In this process, steel absorbs substantial amount of thermal energy in the form of latent heat, resulting in the sudden increase of heat capacity.

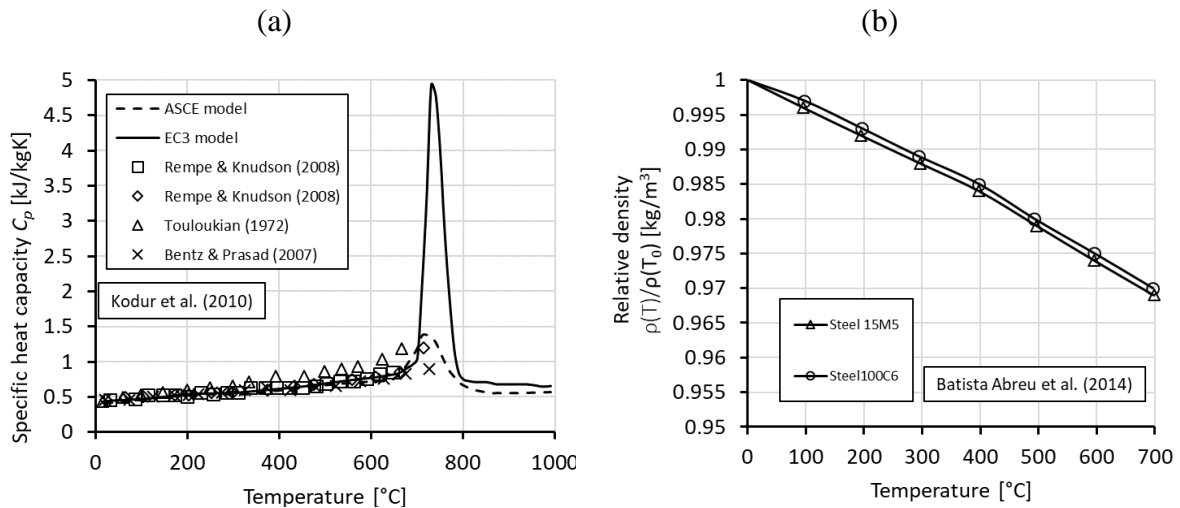


Figure 2-24. Specific heat capacity of steel (adapted from Kodur et al., 2010) (a) and the relative density of steel (b) as a function of temperature.

Density of steel

Density and Poisson's coefficient of steel are assumed to be constant with the increase of temperature. Nonetheless, mass density has a slight declining tendency and Poisson's ratio a slightly increasing trend with increasing temperature as shown in Figure 2-24b (Clark, 1953; Costes, 2004). However, this data is available and could be useful to infer other constitutive parameters, such as shear modulus.

2.2.2 Behavior of steel subjected to high loading rates

As in the case of concrete materials, the behavior of steel and steel structures is strongly influenced by the loading rate. It was demonstrated that the progressive increase in resistance relying on tensile strength, such as concrete, is attributed primarily to inertia effects (Cusatis 2011; Ožbolt et al. 2014; Bede et al. 2015). It is well known that metallic materials, such as steel of high toughness and ductility, do not exhibit significant strain rate sensitivity (Boyce et al. 2007). The influence of the strain rate on the response of steel is shown in Figure 2-25. The steel loaded in a tensile test and the strain rates varied from 0.0002 to 200/s. The strain rates up to 200/s have obviously no influence on the resistance of the steel material. This can be attributed to the homogeneity of steel, unlike concrete, and non-porosity with very few defects. Nevertheless, steel exhibits a strong sensitivity to the loading rate. Due to the strain rate insensitivity and its ductility, its loading rate dependency comes primarily from inertia.

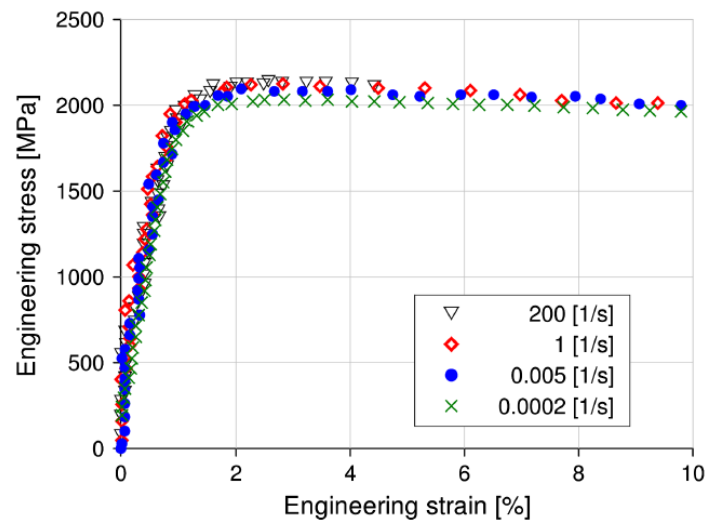


Figure 2-25. Strain rate sensitivity of steel (adapted from Boyce et al., 2007).

Inertia that manifests itself when steel is subjected to high loading rates can be divided into three parts: (i) inertia at the crack tip related to high nonlinearity of steel, (ii) large plastification zone and (iii) structural inertia. Steel exhibits rate-dependent resistance and failure modes, crack branching and decreases of ductility with the increase of loading rate.

Ozbolt et al. (2016) investigated the problems related to the dynamic fracture of steel by performing a numerical analysis on a compact tension specimen. A 3D finite element code based on the microplane model for steel was employed, discussed and verified. The predicted crack patterns from the analysis for loading rates 0.002, 1, 50 and 100m/s was provided. Up to the loading rate of 50 m/s no crack branching phenomena was observed, i.e. single crack and mode I failure was observed. However, at loading rates around 90 m/s, soon after the crack initiation at the notch tip, the crack branched into two cracks. Similar phenomena was observed in the experimental tests (Bousquet et al., 2011).

Bousquet (2011) performed a study that encompassed the physical mechanisms of cleavage cracks and criteria related to the brittle fracture of steel. A compact tension specimen made from 16MND5 /A508) grade ferritic steel, used in a French Pressurized Water Reactor (PWR) vessel ring blank was used in the experimental work. Pravel, Rossol and Tanguy (Prabel et al., 2008; Rossoll, 1993; Tanguy, 2001) have already studied this kind of steel subjected to dynamic loading but the range of strain rates were up to 5.5/s. In the study performed by Bousquet the experiments were done with Split-Hopkinson Pressure Bar for a strain rate range from 10^2 to 10^4 /s and for seven temperatures from 175°C to 25°C. The fracture tests and the observation of the CT specimen surface exhibited two kinds of crack path, a straight and branched crack. The branching crack appear at high loading rates, which increases the effect of the plastic zones.

Hahn et al. (1973) discusses the behavior of the unstable fracture and arrest in steel materials (4340 Steel). From the results of crack speed and arrest measurements compared with the results from the dynamic analysis the conclusion has been made that the inclusion of the inertia forces in the equation of motion substantially improve the prediction of crack speed, crack propagation, arrest and possible retaining events in specimens of finite geometry.

One of the most convenient ways to evaluate dynamic characteristics of deformation in materials like metals and alloys is by using the Taylor anvil-on-rod impact test (Taylor, 1948; Whiffin, 1948). Principally, at the end of the rod colliding with anvil, the high-rate stresses are developed and should these stresses exceed the corresponding dynamic yield strength of the material, the plastic wave will appear and propagate thorough the cylinder causing permanent plastic damage. In the part of the rod, where stresses do not exceed yield limit, deformation remains elastic (Wilkins et al., 1973; Volkov et al. 2017). Further development of experimental methods made it possible to track deformation of the sample during impact with high time resolution and record the oscillation profile of the back surface of the rod using laser interferometry (Eakins et al., 2006). The occurrence of plastic mushrooming, i.e. "mushroom" deformation shape of the rod end is often appearing as the result of deformation for a number of metals and alloys (Borodin et al., 2015; Rakvåg et al., 2013). Five distinct failure and fragmentation modes in the Taylor bar impact test are shown in Figure 2-26.

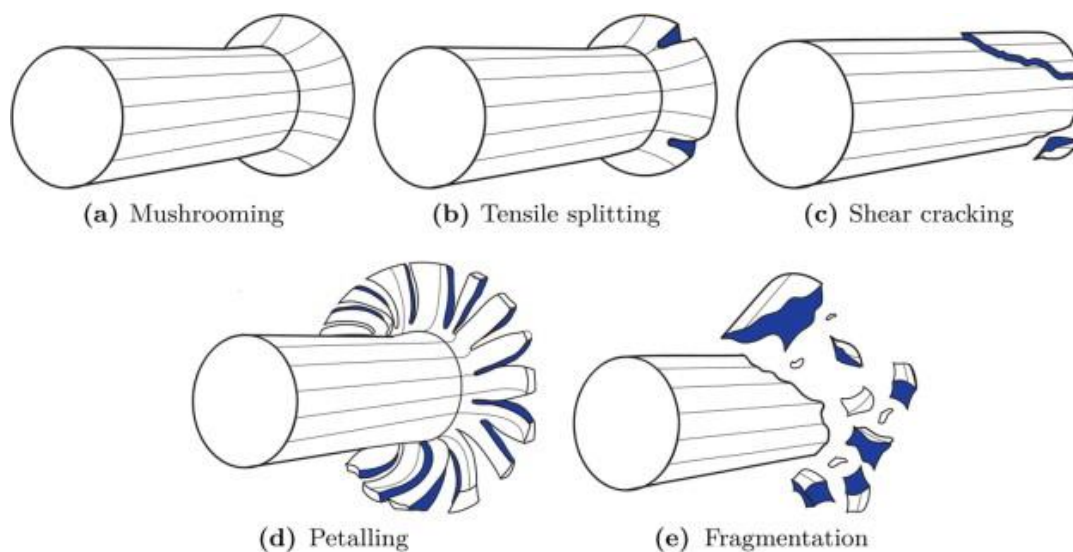


Figure 2-26. Deformation and fracture modes in the Taylor bar impact test (Rakvåg et al., 2013).

The dynamic increase factor (DIF) for steel material loaded in tension shown in Figure 2-27 and obtained from the dynamic analysis of the CT specimen (Ožbolt et al., 2016) clearly shows that up to the strain rate of approx. 100/s there is a linear increase of DIF in semi-log scale. However, for higher loading rates, a progressive increase in DIF is observed which yields a conclusion that the progressive increase in resistance is closely related to inertia generated at the crack tip. This means that two inertia effects are taking place, inertia at the crack tip and structural inertia of the specimen, whose contribution is linearly proportional to the loading rate. At a critical value of strain rate the crack starts to branch and the resistance of the material increases.

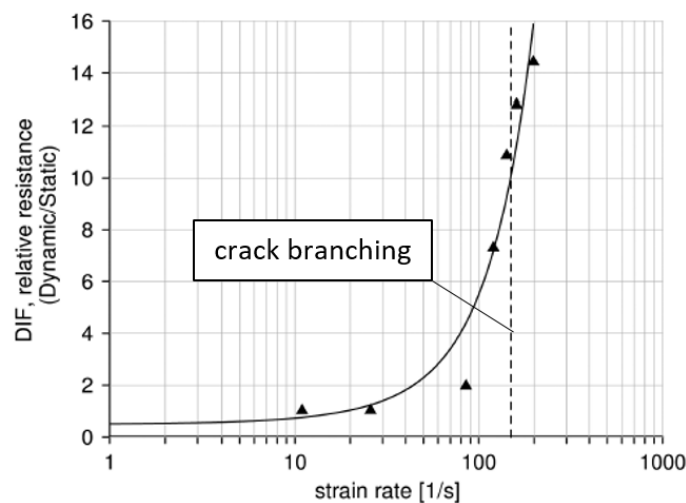


Figure 2-27. Relation of the dynamic increase factor and strain rate at the onset of cracking (Ožbolt et al., 2016).

Kazenawa (1981) performed tests to examine the brittle crack propagation and arrest on structural steels on double-tension and double-cantilever type (DCB) specimens. The relation of DIF factor with material toughness (apparent) and crack velocity was experimentally obtained. According to tests, toughness increases progressively after the crack velocity reaches its critical value. However, it should be noted that the progressive increase of resistance (apparent strength) and toughness (apparent toughness), is because of the effect of inertia and is not the consequence of higher material strength or higher material toughness (Ožbolt et al., 2016).

Due to the steel insensitivity to strain rate, true toughness should be independent of the crack velocity and strain rate. More realistically would be to decrease the stress intensity factor while keeping toughness constant (Freund, 1972a, 1972b). However, the stress intensity factor should be in that case obtained from dynamic and no quasi-static analysis, which must account for inertia effects.

2.3 Combined thermal and static/dynamic loading

2.3.1 Influence of fire on anchors loaded in shear perpendicular to the concrete edge

The decrease in the mechanical properties of concrete and steel due to thermally induced damage causes a decrease of the load-bearing capacity of fasteners and a significant increase of deformations. Moreover, thermally induced strains and the associated constraint stresses can also have a strong influence on the resistance of fasteners. In the past, the behavior of fasteners under fire exposure was mainly investigated by anchor manufacturers as part of approval procedures. The Eurocode 2 provisions for fasteners under fire were proposed based on the anchor failure tests under tension and shear loads tested in different laboratories and summarized by Reick (2001). Since steel as a reinforcement material is considered to be well protected against high temperature fire events with various sprays, castings and claddings, the emphasis in this work will be on the concrete failure. Eligehausen & Reick (1996) investigated a total of 21 fasteners including the ceiling hangers, displacement-controlled expansion anchors, undercut anchors, and headed bolts. Reick (1998) conducted additional 6 tests on loaded reinforced concrete slabs to measure the temperature distribution in the concrete and along the fastener. Based on these tests, Reick (2001) developed a proposal for the design of fasteners under fire exposure.

Periškić (2009) carried out an extensive experimental and numerical study to investigate the influence of the fire exposure of single and anchor groups located close and away from the concrete edge on the load bearing capacity. The anchors were loaded with tensile load employing the fire boundary conditions on one and two sides of the concrete member. Principally, the anchor embedment depth had a significant influence on the residual tensile capacity. It was observed that the anchors located close to the edge experienced a greater sensitivity in terms of load bearing capacity reduction when two-sided fire was imposed. Based on these investigations, the design rules were then proposed.

Mirza and Uy (2009) performed a series of numerical studies to investigate the influence of temperature on composite-steel anchors loaded in shear. Observing the results, some inconsistencies were recorded between the experimentally measured temperature distribution and the numerical analysis. Specifically, the high thermal conductivity of steel was not encompassed by the model reflecting in slower temperature elevation in the area around the steel anchor. However, the load-slip curves were in a good agreement with the experimental data. The relative resistance after 10 min of fire exposure was reduced by 35% compared to its

value at ambient temperature. The relative resistance reduction equation as a function of time was recommended.

Wang (2012) simulated the push-out tests using a nonlinear 3D thermo-mechanical coupled model. It was reported the higher thermal conductivity of steel increases significantly the difference in temperature distribution between the headed stud and the surrounding concrete. The difference that was obtained from the numerical simulation was 100 to 150°C leading to faster deterioration of the shear connectors. A negative displacement was observed in the specimens with solid and composite slabs caused by major thermal expansion. Due to high temperatures at the bottom layer of the concrete specimen, failure occurred in an overturning mode with a reduced load-bearing capacity. Overall, it was verified that the thermo-mechanical model can properly simulate the headed shear connectors in push-out tests subjected to elevated temperature.

Mashiri et al. (2017) experimentally tested the behavior of shear connectors at both ambient and elevated (post-fire) temperature conditions subjected to push-out tests. The tests were performed on thermally pre-damaged specimens heated up to 200, 400 and 600°C. The results indicated the reduction in resistance and the increase of ductility with the temperature increase. The load capacity reduction in the case of headed stud specimens was recorded to be 25, 43 and 60% at 200, 400 and 600°C, respectively. Furthermore, no yield failure was observed in the shear connectors at both ambient and post-fire temperature conditions.

Tian, (Tian et al., 2018a; Tian et al., 2018b; Tian, 2019) performed a series of experimental and numerical investigations on stud fasteners loaded in shear perpendicular and towards the free edge of the concrete member at high temperature up to failure. Since it was found that there are still very few experimental studies, in addition to the numerical studies, missing, fire tests were carried out for single and group fasteners (double and quadruple fasteners) close to the concrete edge. In the numerical and experimental studies, both geometry (edge spacing, anchorage depth and bolt diameter) and concrete properties (concrete C20/25 and C40/50) were varied. A total of about 190 tests on single fasteners and 50 tests on group fasteners were performed. The tests were then used to calibrate and verify the thermo-mechanical model previously implemented into a 3D finite element (FE) code. Studies of the anchorage behavior were conducted at elevated temperature and ambient temperature after heating (cold state, residual state). The cold state was found to have a most critical impact on the reduction of the load-bearing capacity of the single and group of anchors. This is explained by the fact residual mechanical properties of cementitious composites are known to worsen after cooling. Based on the experimental tests

and numerical simulations a design formula is proposed, which accounts for the influence of the high temperature on the residual capacity of anchors loaded in shear.

Fuchs et al. (1995) proposed the CC (concrete capacity) method for predicting the fastening capacity of brittle failures (concrete breakout) in uncracked concrete. He compared the fastening capacities of concrete obtained with the CCD method with the design recommendations of ACI Committee 349 and a large number of test results. The comparison was made for 36 fasteners, close and far from the edge, under tension load, for single and double fastenings loaded with shear load towards the edge. Further, the following equation for the prediction of the concrete edge failure load of a single anchor in concrete was proposed:

$$V_{u,c}^0 = \sqrt{d_{nom}} \cdot (l_f/d_{nom})^{0.2} \cdot \sqrt{f_{cc,200}} \cdot c_1^{1.5} \quad (2-5)$$

where:

d_{nom} = the nominal diameter of fastener, which equates shank diameter d for headed stud,

l_f = the effective load transfer length, which is h_{ef} for anchors with constant flexural stiffness over the length of the anchor,

c_1 = is the edge distance measured from the longitudinal axis of the anchor perpendicular to the free edge of concrete.

Several conclusions can be drawn from Eq. (2-5). The failure load $V_{u,c}^0$ is strongly influenced by the edge distance c_1 to the power of 1.5. This differs from the strength theory where the exponent is set to 2. Furthermore, the failure load is proportional to the nominal diameter of the fastener and the compressive strength, but a lesser extent than to the edge distance. This equation is mainly valid for anchors with a diameter under 25 mm (Tian, 2019).

Hofmann et al. (2004) and Hofmann (2005) proposed a more accurate equation for obtaining the mean shear resistance of a single anchor in an un-cracked concrete at ambient temperature (Tian, 2019):

$$V_{u,c}^0 = 3.0 \cdot d_{nom}^{\alpha_0} \cdot l_f^{\beta_0} \cdot \sqrt{f_{cc,200}} \cdot c_1^{1.5} \quad (2-6)$$

where $\alpha_0 = (l_f/c_1)^{0.5}$ and $\beta_0 = 0.1 \cdot (d_{nom}/c_1)^{0.2}$.

Equation (2-3) can be rewritten as:

$$V_{u,c}^0 = 3.27 \cdot d_{nom}^{\alpha_0} \cdot l_f^{\beta_0} \cdot \sqrt{f_{cm}} \cdot c_1^{1.5} \quad (2-7)$$

where f_{cm} is the mean concrete cylinder compressive strength measured on a cylinder with dimensions of 150×300 mm.

Grosser (2012) summarized the previous research data on the subject of shear-loaded anchors close to the concrete and conducted a series of tests. An Equation for predicting the resistance of anchors close to the edge and loaded perpendicular to the free edge was obtained:

$$V_{u,c} = 16.5 \cdot c_1^{4/2} \cdot \sqrt{f_{cc,200}} \cdot (0.02d + 0.5) \cdot (l_f/12d)^{c_1^{-0.4}} \quad (2-8)$$

where all of the terms are in analogy with previous Equations (2-5 and 2-6).

The shear failure of anchor groups can be calculated using the CC-Method by means of projected areas (Fuchs et al., 1995; Eligehausen et al., 2006):

$$V_{u,c} = \frac{A_{c,V}}{A_{c,V}^0} V_{u,c}^0 \quad (2-9)$$

where $A_{c,V}^0$ represents the projected area of the fully developed failure surface for a single anchor idealized as a half-pyramid with height c_1 and base lengths $1.5c_1$ and $3c_1$, which equals $4.5c_1^2$; $A_{c,V}$ is the projected area of the failure surface for the anchorage as defined by the overlap of individual idealized failure surfaces of adjacent anchors ($s < 3c_1$); $V_{u,c}^0$ refers to Eq. (2-5).

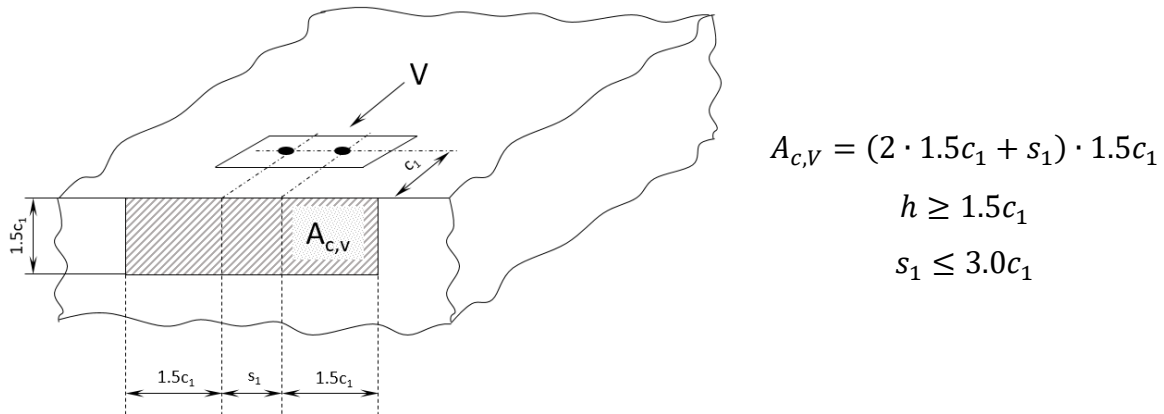


Figure 2-28. Projected area for pair of anchors close to the edge acc. to Eq. (2-9) (adapted from Eligehausen et al., 2006)

2.3.1.1 Design provisions for fasteners loaded in shear exposed to fire

An overview of the design formulas for fire resistance of anchors loaded in shear is shortly discussed. The design formulas given with a 90% confidence level that over 95% of the failures occur above the calculated resistance limit state.

Eurocode 2 EN 1992-4

The design method in Eurocode 2 (European Committee for Standardization, 2018) covers only fasteners exposed to fire from one side only. If the concrete specimen is loaded with fire from multiple sides, additional geometric requirements should be considered ($c \geq 300$ mm and $c \geq 2h_{ef}$). The characteristic resistance of concrete is only provided for 90 and 120 min of fire exposure according to EN 13501-2.

The following design formula for shear resistance was proposed by Hofmann (2005):

$$V_{Rk,c}^0 = k_9 \cdot d_{nom}^\alpha \cdot l_f^\beta \cdot \sqrt{f_{ck}} \cdot c_1^{1.5} \quad (2-10)$$

where $k_9 = 1.7$ for cracked concrete

= 2.4 for uncracked concrete

The characteristic resistance of concrete edge failure for headed stud in concrete exposed to fire up to 90 minutes and 120 minutes reads:

$$V_{Rk,c,fi(90)}^0 = 0.25 V_{Rk,c}^0 \text{ for fire exposure up to 90 min} \quad (2-11)$$

$$V_{Rk,c,fi(120)}^0 = 0.2 V_{Rk,c}^0 \text{ for fire exposure up to 120 min} \quad (2-12)$$

Note that the above given Equations do not give an insight whether the specimens is loaded in hot or cold (residual) state. Based on the equations (2-11 and 2-12), the resistance of a single anchor after fire exposure of 90 and 120 min is reduced to 17.5% and 14% of its value at ambient temperature, respectively.

Eurocode 4 EN 1994-1-2

The fire resistance of composite steel and concrete connectors is principally obtained by applying a partial factor for the strength of the material and for the concrete failure subjected to shear load is as follows:

$$P_{fi,Rd} = k_{c,\vartheta} \cdot P_{Rd} \quad (2-13)$$

where P_{Rd} is the design shear resistance as obtained from *EN 1994-1-1 (European Committee for Standardization, 2004b)* and $k_{c,\vartheta}$ is the reduction factor for stress-strain relationship of concrete at high temperature.

ACI 318

Currently the fire resistance and fire safety design of fasteners are not covered in the ACI 318. However, the design formula for the concrete edge failure of a single anchor in cracked concrete loaded in shear was determined according to Fuchs et al. (1995):

$$V_b = 7 \cdot \sqrt{d} \cdot (l_f/d)^{0.2} \cdot \sqrt{f'_c} \cdot c_1^{1.2} \quad [\text{lb}] \quad (2-14)$$

For the un-cracked concrete, the Eq. (2-14) should be multiplied by 1.4 (Tian, 2018).

2.3.2 Dynamic behavior of concrete at high temperatures

In the literature, a large number of studies are available for concrete loaded under high loading rates at ambient temperature and even more on thermally exposed concrete structures. However, there is a relatively low number of studies for the structures that are exposed to combined loading, e.g. impact after fire (Li, et al. 2012; Huo et al., 2013; Caverzan et al., 2013; Weidner et al., 2015; Colombo et al., 2015; Zhai et al., 2016).

The behavior of concrete at high strain rates and simultaneously at high temperature has been relatively little studied so far. In principle, there are two load scenarios: (i) Damage of concrete due to temperature load and subsequent dynamic loading. Such cases are relevant for safety, e.g. in case of an explosion or impact during a fire load and (ii) Fire loading after dynamic loading, e.g. the occurrence of fire after an earthquake is the relevant scenario for practical application.

For the first scenario, the behavior of concrete at relatively low temperature gradients is decisive. The behavior of concrete structures under high temperature changes very much compared to the behavior at normal temperature (Schneider 1988; Zhang & Bićanić, 2002). The physical processes that take place in concrete at high temperatures, which are the basis for realistic modelling, have been discussed and described in detail by Bažant and Kaplan (Bažant & Thongutai 1978, Bažant & Kaplan 1996) and Khoury (Khoury et al. 1985a; Khoury 1996). An unloaded test specimen under high temperature expands unhindered (free thermal expansion). The same test under mechanical load shows a completely different overall elongation behavior. The effect that leads to this difference is called "load-induced thermal strain" (LITS) (RILEM, 1998). As mentioned before, the numerical investigations on the meso scale have shown that the reason for such behavior is the interaction between the load-induced

damage and the free thermal strains (Bošnjak, 2014). In numerical modelling, both strain components have a significant influence on the behavior of the components under fire load. The decrease of mechanical properties of concrete at high temperature as well as the non-elastic strains and relatively high pore pressure lead to damage and to decrease of the load-bearing capacity. A major type of damage is spalling (erosion) of the concrete at its surface (Ožbolt et al., 2005b, 2008, 2014; Lakhani et al., 2014; Sharma et al., 2016). Damage of concrete by thermal stress has an impact on the behavior of the concrete under dynamic load. In this respect, however, there are virtually no test results available in the literature. The sources available in the literature are mainly focused on investigation of steel under combined thermal and dynamic load (Song et al., 2000)

He et al. (2011) carried out several dynamic tests using the split Hopkinson pressure bar with concrete at different temperatures (200, 400, 600 and 800°C) in hot state. He concluded that with the temperature increase, the compressive dynamic resistance of concrete decreased and the compressive deformation increased. Furthermore, he pointed out that concrete at higher temperatures tends to be more strain-rate sensitive with the exception of the case at 200°C. Li et al. (2012) performed similar experiments on concrete cubes and cylinders, only on cold (residual) state. It was found out that the thermal exposure to 400°C to be the critical point concerning the change of mechanical properties. Further, a strong strain-rate dependency was recorded with the temperature increase.

Huo et al. (2013) performed a series of compressive dynamic tests to investigate the influence of fire exposure on the concrete dynamic behavior. The tests were performed in the cold state after being cooled down from 100, 300, 500 and 700°C using a SHBT. It was deduced that the Dynamic Increase Factor (DIF) decreases with the increase in temperature. However, the DIF increased with the increase of strain rate.

Weidmer et al. (2015) showed that the strength of normal strength concrete (NSC) is permanently reduced after high temperature fire exposure, even when the structure is cooled down to ambient temperature. He investigated the influence of temperature on NSC and fiber reinforced concrete (FRC) cylinders in hot and cold state. A conclusive comparison of the cylinder compressive strength at various elevated temperatures was made and it was shown that NSC heated to 204°C and cooled down exhibited 80% higher dynamic compressive resistance than those at higher temperatures under static load.

Colombo et al. (2015) studied the event of an explosion (internal blast event) inside a tunnel with geometrical parameters same as the one in the metro line in Brescia. The aim of the study

was to devise a design procedure that can provide a valuable tool for engineers to check the safety of a tunnel in the case of an explosive event. After a series of dynamic analysis were carried out in order to reproduce the blast event, pressure-impulse diagrams for underground tunnels were generated and an ultimate limit state criterion that includes fire –blast interaction is presented. Furthermore, he compared the quantitative performance of fiber-reinforced layered solution with the traditional RC one and indicated, in terms of all loading domains (impulsive, dynamic and quasi-static), that the layered solution performs better. Further, it was shown that the fiber reinforced layered solution gives better results in terms of internal and external bending moments for all fire exposure times in comparison with the traditional RC solution.

Zhai et al. (2016) performed a series of model tests on RC beams in order to investigate the performance of RC structures subjected to blast after fire exposure. The tested RC beams were 2500 mm long with square cross-section of 200 mm side length and were being exposed to 90 and 120 min of fire. The beams were then transported to the blast site where they were loaded by detonating 7 kg of rock emulsion explosive. The test results showed that the peak and residual displacements of the RC beams increased linearly with the fire duration and the thermally damaged beams suffered greater blast-induced damage as opposed to the undamaged ones. After 90 and 120 min of fire exposure, the peak and residual displacement were 51.4% and 123.0%, respectively, larger than that measured on the thermally undamaged beams.

Ruta (2018) conducted a series of experiments to study the effect of thermally induced damage at 200°C and 400°C on the dynamic properties of concrete compact tension specimens. The specimens were loaded in tension under different displacement rates (40 - 4000 mm/s) in the cold (residual) state. The results indicated that the increase of resistance due to the loading rate, decreases with temperature elevation. Due to the degradation of mechanical concrete properties at high temperatures, for temperature of 400°C almost no increase of resistance was observed. The evaluation of crack patterns showed that the change of crack pattern is observed for test series at 400°C at high loading rates (>3000 mm/s), changing from branching failure mode to a crack profile with two single cracks.

2.4 Behavior of concrete structures subjected to seismic loading

Earthquakes are very often regarded as a low-occurrence but high-consequence event and it is difficult to account for all possible loading scenarios that could occur. The most vulnerable part of the reinforced concrete (RC) structure, when subjected to shear load, is the beam-column joint. By designing the section of beams and columns in a way that the reinforcement bars reach yield stress before the concrete reaches its limiting strain in compression under bending moment, the shear failure could be avoided. (Sharma, 2013). To improve the performance of the beam-column joints, a retrofit solution is recommended (Pampanin et al. 2006).

2.4.1 Structures subjected to post-earthquake fire

Several existing experimental and numerical studies that include a PEF (post-earthquake fire) or FFE (fire-following earthquake) scenario consist of three stages: loading the RC structures in a quasi-static cyclic manner to a certain maximum story drift corresponding to different performance levels, i.e. IO (immediate occupancy), LS (life safety) and CP (collapse prevention), unloading the structure and exposing it to fire and finally performing a monotonic pushover to obtain the residual capacity. Although large-scale fire conflagrations can be caused by a number of destructive events, earthquake definitely takes the precedence.

RC frame is a heterogeneous structure consisted of steel and concrete, which exhibit different thermal characteristics at elevated temperatures. Since concrete has a low thermal conductivity compared to steel, when an RC structure is exposed to elevated temperature without being subjected to cyclic load, the steel reinforcement bars are protected by the concrete cover. However, in a PEF event involving a high temperature fire exposure, major concrete spalling occurrences are observed. During spalling (explosive), large pieces of concrete are being detached from the structural members leaving the steel directly exposed to fire.

Sharma et al. (2012) was first to investigate the behavior of RC frames exposed to fire. The RC frame has been first been subjected to lateral cyclic story drift (simulated earthquake) which was followed by the exposure to compartment fire. Although massive spalling and high temperatures were recorded in several locations along the structural members, no global structural failure was observed. Based on the design modifications, the damage during initial mechanical loading phase was first noted in beams rather than in columns. The experimental results in terms of temperature distribution, recorded displacements and strains in beams, columns and slabs were provided.

Ronagh & Behnam (2012) performed a sequential nonlinear analysis in which the RC frames were exposed to PEF scenario. The analysis encompassed two RC frames designed based on ACI 318-08 code with different geometries ($L=1.5H$ and $L=3.5H$). The concrete material used in the analysis was NSC with compressive strength of 25 MPa and reinforcement steel bars with yield stress of 400 MPa. A constant live and dead load with magnitude 2.5 kPa and 8.0 kPa, respectively, was imposed on the slab. The frames were first exposed to gravity load (constant) and fire exposure before being subjected to monotonic pushover, i.e. being pushed to arrive at three different lateral displacements corresponding to three different performance levels (IO, LS, CP). Successive loading, consisting of gravity loads, lateral loads and fire exposure was performed using software SAFIR, while the pushover analysis is carried out in the SAP2000 software according to FEMA356. Analysis results suggest that the structures that suffered greater damage from the initial earthquake loads experienced lower fire resistance than lesser-damaged structures. This can be a consequence of the residual lateral displacements, degradation in stiffness or the direct exposure of steel to fire as a result of the concrete cover removal during spalling. Furthermore, it was observed that the fire resistance of the frames is mostly dependent on the resistance of the beams.

Behnam & Ronagh (2013) further experimented with the effect of PEF on the load bearing capacity of the RC structures. The investigated frames were initially subjected to a lateral load with a peak ground acceleration (PGA) of 30g. The structure was then exposed to fire according to ISO 834 and natural fire curves. An extensive numerical analysis was performed to investigate the time taken for structures weakened by earthquake and fire to collapse. As a benchmark, a case with fire-only scenario without earthquake pre-damage was investigated as well. From the fire resistance viewpoint, it was established that the structures damaged by earthquake exhibited higher vulnerability to fire than undamaged ones and behavior of structures exposed to ISO 834 fire curve behaved differently than the ones exposed to natural fire curves.

Demir et al. (2020) investigated the behavior of seismically loaded full-scale reinforced concrete columns after fire exposure. The aim of the parametric study was to analyze the influence of the fire duration and the thickness of the concrete cover on the average reduction of the maximum load. An extensive crushing (spalling) of concrete cover and the initial yielding of longitudinal reinforcement resulted in the flexural failure of columns. Naturally, an observation was made that the fire exposed columns exhibited lower load capacities than the reference thermally undamaged columns. The reduction in the average maximum bearing load was found to be 13%, 19%, and 19% for fire durations of 15, 60 and 90 min, respectively. Since

the residual tests were performed in the cold state and steel strength was assumed to recover completely, the decrease in lateral load capacity is mostly impacted by the deterioration in the concrete material properties. This was the reason why the load bearing reduction at 60 and 90 min were approximately the same. The monitored ductility in columns was approx. the same for all fire duration except column heated to 90 min, which exhibited lower ductility. With the increase of the fire duration, the initial stiffness decreased.

Wen et al. (2018) carried out an experimental and numerical study to determine the structural performance of seismically damaged RC beams subjected to PEF scenario. The RC frames were first tested in a shake table test and subsequently the thermal field distribution, the bearing capacity and reduction coefficient were validated with the numerical model in ABAQUS. Cracking and spalling were determined to be the main factors influencing the bearing capacity during the shake table experiment. Formula for determining the bearing capacity reduction coefficient of RC beams subjected to a PEF event is proposed. The effect of thermal spalling on the flexural capacity of the beam proved to have a significant influence. The prediction equations for the reduction factor of the flexural bearing capacity is proposed.

2.5 Conclusions

Exposure to fire, high temperature gradients and high loading rates have a considerable influence on the behavior of concrete and RC structures, as they in isolated or successive sequence, change significantly the mechanical and thermal properties of concrete material. In this chapter, an overview of existing research on the following topics was summarized: (i) Mechanical and thermal properties of steel and concrete under thermal, dynamic and combined thermal-dynamic loading; (ii) the behavior of thermally pre-damaged anchors under shear load perpendicular to the edge; (iii) RC structures under dynamic loads exposed to fire; (iv) the influence and aftermath of post-earthquake fire on the load bearing behavior of RC structures.

The literature overview indicates that the aggregate type and moisture content (curing conditions) have a significant impact on the reduction of mechanical and thermal properties of concrete with the temperature increase. High loading velocities do not only influence the mechanical behavior of concrete (strain-rate dependence) but also the type of failure (Mode I changes to mixed mode failure). Furthermore, steel exhibits sensitivity on the carbon content on elevated temperature and the phase change occurring at 700-800°C. Steel materials under dynamic loading do not exhibit significant strain-rate sensitivity. However, for high loading

rates ($>10/s$) a progressive increase in DIF (resistance) in tension is observed which indicates that the progressive increase in resistance is closely related to the inertia at the crack tip as a consequence of high ductility of steel.

Thermally induced strains and the associated constraint stresses have a strong influence on the resistance reduction of fasteners. After 15 min of fire exposure, the reduction of resistance can be more than 50% of the reference resistance. The studies have shown that the reduction in the load bearing capacity is more pronounced when the fasteners were loaded in cold state (after being cooled down to the ambient temperature) than in the hot state.

There is a relatively small number of published papers on the topic of RC structures under dynamic loads exposed to fire. The dynamic response of the RC structures is influenced by the temperature state (hot or residual state) the RC structure is loaded in. The reason for this are the recovery capabilities of steel in the cold state. The DIF (resistance) of concrete decreases with the temperature increase.

RC structures subjected to seismic and subsequently thermal load are understudied from the numerical point of view. The numerical studies indicate that it is difficult to simulate a realistic response of the structure subjected to a PEF scenario. The effect of the post-earthquake fire on the residual capacity of RC frames was predominantly investigated in the experimental tests and the need for a suitable numerical tool that can link the seismically damaged structure with the thermally induced damage during the fire exposure is needed.

3. EXPERIMENTAL INVESTIGATIONS

3.1 Measurement of fracture energy

3.1.1 Influence of temperature on fracture energy

In fracture mechanics, it is assumed that the energy required to extend the crack is supplied by the energy released through the system during the crack propagation (Naus et al., 1974; Krausz and Krausz, 1988). It is generally accepted that the fracture is a thermally activated rate process implying that the energy of thermal vibration is responsible of the atom bond rupture that constitutes the mechanism of fracture (Cottrell, 1964). Since the thermal vibrations are statistically distributed, defined by the Maxwell distribution, the rise in temperature increases the probability that the atom's energy would exceed the activation energy of the bond (Bažant and Prat, 1988). This suggests that the rise in temperature would increase the rate of growth of fracture.

Fracture energy (work of fracture) is calculated as the integral under the stress-crack opening curve and when the concrete is exposed to temperature, the curve becomes flatter (more ductile). The dependence of the tensile stress-crack opening curve on the temperature elevation is shown Figure 3-1b from the experiments carried out by Schneider (1982). The already mentioned decrease of the modulus of elasticity and strength is clearly visible. Up to date, there has been a limited number of studies measuring the fracture properties (fracture energy and fracture toughness) with the increase of temperature. The experimental studies analyzing the influence of temperature on the fracture energy of normal strength concrete (NSC) have been limited to wedge-splitting methods (Yu et al., 2012) and three point bending tests on notched preheated specimens (Bažant and Prat, 1988a; Baker, 1996; Zhang et al., 2000; Nielsen and Bićanić, 2002; Bošnjak et al., 2018). Most of these tests exhibited an increase-decrease tendency with the increase of temperature.

The measurements of Zhang & Bićanić (2002) showed that the fracture energy initially increases with increasing temperature and reaches its maximum value at about 300°C (Figure 3-1a). This increase is explained firstly by the progressive hydration and secondly by the increased friction between the individual aggregate grains due to thermal expansion. A further increase in temperature above 300°C leads to increased microcracking, dehydration and degradation of the cement paste. This leads to a decrease of the fracture energy. At about 600°C, the value measured at 20°C is reached again. The tests were performed on the concrete beams

of dimensions $100 \times 100 \times 500$ mm and an initial notch depth of 50 mm in a three point bending test.

Yu et al. (2012) experimentally investigated the influence of temperature on the residual fracture properties of NSC using the wedge splitting tests. The specimens had a notch of 80 mm height and 3 mm thickness, each with dimensions of $150 \times 150 \times 300$ mm. He observed that the weight loss of the specimens gradually increased with the increase of temperature. The Young's modulus was decrease to 7.18 GPa at 600°C , indication a net drop of 78%. The fracture energy G_F and fracture toughness K_{ic} both experienced an increase-decrease tendency with the increase of temperature. According to Yu et al., the mechanism for the increase in G_F is the thermal damage making the crack path more tortuous, passing around the aggregates instead of through them. The initial fracture toughness K_{ini} was observed to decrease monotonically with the temperature elevation. The tests were carried out in cold (residual) state.

Yu et al. (2016) studied the influence of elevated temperature on the residual fracture properties of high strength/high performance concrete C80 and C100 with compressive strengths of 76.5 and 96.5 MPa, respectively. To avoid spalling, 0.3% polypropylene fibers (PP) were added to the admixture. It was found out the fracture energy of both concretes, as well as both initial and unstable fracture toughness decreased with temperature increase. In the case of HSC, the bond between the cement paste and the aggregates has not deteriorated as much as in the case of NSC resulting in the cracking of aggregates in numerous locations and inducing a much flatter crack surface. The tests were carried out in cold (residual) state.

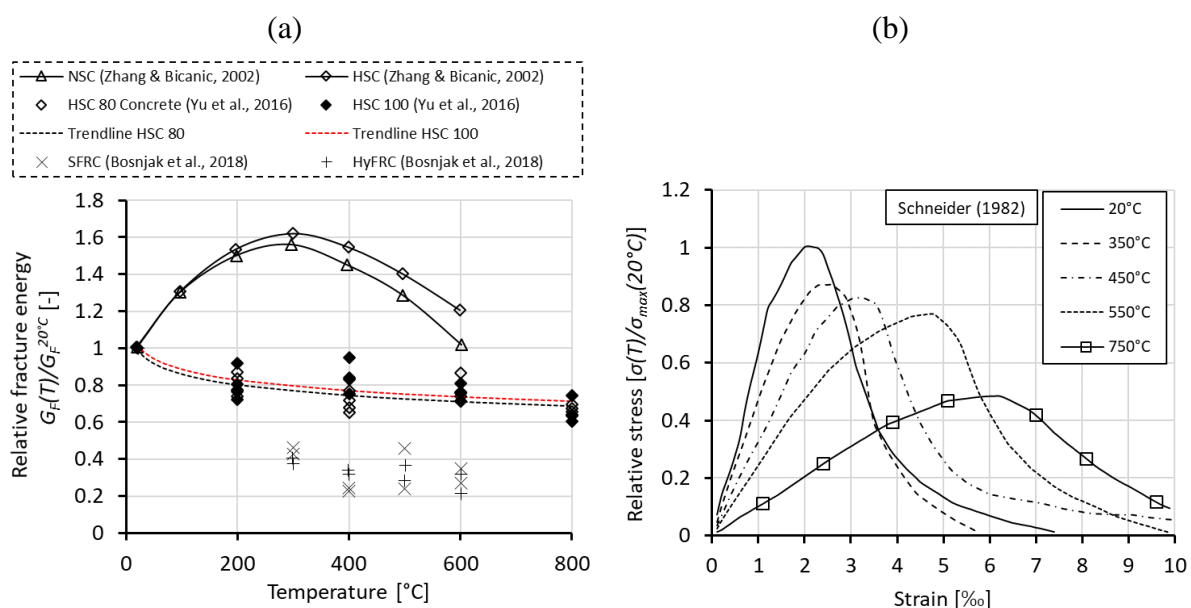


Figure 3-1. Relative fracture energy of concrete as a function of temperature (a) and relative stress-strain curves at different temperature exposures in the cold state (b).

Bošnjak et al. (2018) conducted a series of tests to determine the influence of high temperature on the mechanical and physical properties of high strength concrete (HSC) with and without steel fibers. Three types of HSC were investigated: normal concrete (NC) without fibers, steel fiber reinforced concrete and a hybrid reinforced concrete with both steel and 1 kg/m³ PP fibers. It was pointed out that the presence of fibers increased the fracture energy by two orders of magnitude compared to NC throughout the complete temperature range. Both fiber reinforced concretes had a decreasing tendency of fracture energy with the increase in temperature. The tests were carried out in cold (residual) state.

3.1.2 Methods of determining fracture energy

The fracture energy, as a measure of specific (average) energy consumption due to crack propagation, can be measured using various methods, some of which will be summarized in this chapter with the focus on the three point bending tests (Khalilpour et al., 2019).

Peterson method

Peterson (1980) discussed the possibility of determining the energy release rate G_c subjected to three point bending test by using the LEFM when the maximum load is known. In fact, to obtain the correct amount of fracture energy on the notched beam, the amount of input energy via force applied on the top midspan of the rectangular beam section and the beam weight should be equal to the energy consumed by the crack propagation. He pointed out that the weight of the beam could be ruled out in Eq. (3-1), if the length of the beam is as twice as the distance between the supports. Peterson (1980) proposed a couple of weight compensation methods to compensate for the weight of the beam and to eliminate the midspan moment in short beams. The following equation can be used to calculate the fracture energy including the weight of the beam:

$$G_F = \frac{A_1 + Mg\delta_0}{b(d - a)} \quad (3-1)$$

where A_1 is the area underneath the load displacement curve where the mass of the beam is excluded; M is the total mass of the beam; g is the gravity acceleration; δ_0 is the maximum deflection at the ultimate peak; d is the depth of the beam; b the beam width and a the depth of the crack.

Hillerborg recommendation (RILEM)

Hillerborg (1985) put forward certain geometrical parameters such as span, length, depth and D_{max} for determining fracture energy. He also proposed a set of requirements for the three point bending testing, some of which are: (i) the depth and width of the fracture area can't be less than three times the maximum size of the aggregate; (ii) the minimization of the energy absorption effect from then zone outside the fracture area; (iii) the stiffness demand on the machine should be limited. RILEM (1985) based on Hillerborg's set of requirements proposed the following equation for obtaining the fracture energy:

$$G_F = \frac{(W_t + mg\delta)}{b(d - a)} \quad (3-2)$$

where the parameters b , d , a and δ represent the same dimensions as in the *Peterson* method; W_t is the area under the entire load-displacement curve; $m = m_1 + 2m_2$, where m_1 is the mass between the two supports and m_2 is the portion weight which is not connected to the machine but follows the beam up to failure. Hilleborg (1983) proposed that the initial depth of the initial notch should not be less than 1/3 of the specimen depth.

Guinea, Planas and Elices model (Khalilpour, et al., 2019)

As one of the important factors influencing the measurement error of fracture energy according to Guinea, Planas and Elices are: (i) energy dissipation, (ii) using fixed rollers as supports and (iii) effect of weight on fracture energy and the tail of the load displacement curve.

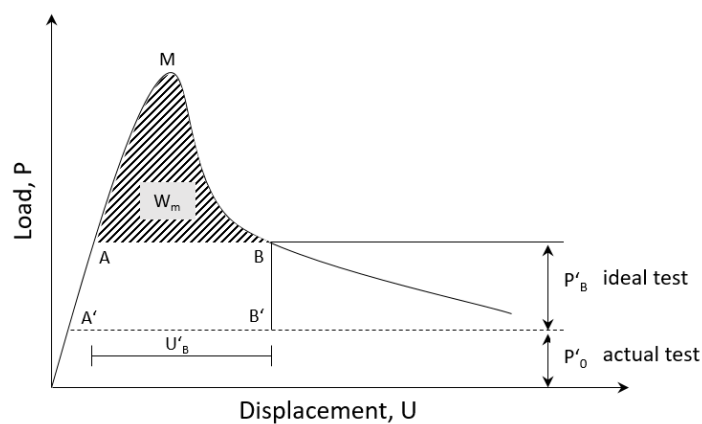


Figure 3-2. Load-displacement curve (adapted from Guinea et al., 1992).

The equation for obtaining the work of fracture was proposed:

$$W_F = W_m + 2 \left(\frac{A}{U_B - U_A} \right) \quad (3-3)$$

$$P - P_B = A \left[\frac{1}{(U - U_A)^2} - \frac{1}{(U_B - U_A)^2} \right] \quad (3-4)$$

where W_m is the area under the curve AMBA, U_A and U_B are the displacements at the point A and B, and A is a constant derived from the Eq. (3-4) suggested by Guinea et al. (1992).

European standard

The European standard method for testing concrete metallic fiber implies the use of specimens with the length in the range $550 \text{ mm} \leq L \leq 700$, mm with the maximum aggregate size of 32 mm and the maximum length of the metallic fiber of 60 mm (BS EN, 2007). The recommended notch size is to be $25 \text{ mm} \pm 1$ with one side of the frame being fixed with a slider and the other with rotating fixture. The LVDTs are used in the experiment for midspan deflection measurement.

Other methods of obtaining fracture energy include: the four point bending test, compact tension test, wedge splitting test, uniaxial tensile test, size-independent test and meso-mechanical modeling.

3.1.3 Parameters affecting the work of fracture (load – displacement curve)

Water-cement ratio (w/c)

The water to cement ratio can affect the interfacial transition zone (ITZ), i.e. the aggregate-paste interface with thickness approx. between 10 and 50 μm . The interface zone has lower strength than aggregates and the cement paste (Garboczi et al., 1996).

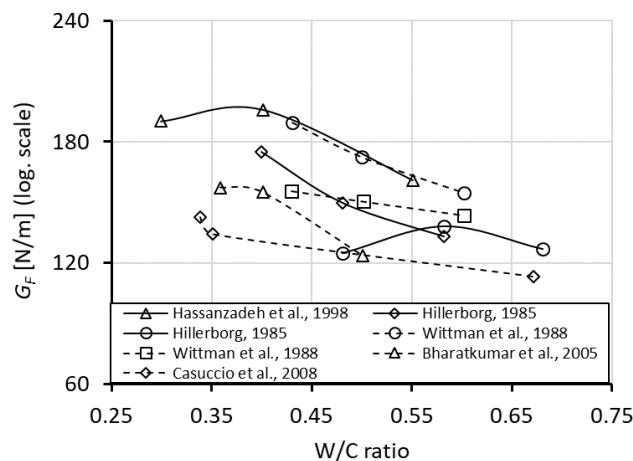


Figure 3-3. Normalized fracture energy G_F as a function of water to cement ratio.

By reducing the water to cement ratio, the porosity between the paste and the ITZ decreases resulting in a stronger paste and as a consequence, the bond strength increases. Having this in mind, it is more likely that the cracks will not pass around the aggregate but rather through the aggregate. From the fractal theory perspective, concrete with lower water to binder ratio (higher strength) will have a smoother cracking surface.

Aggregate size

The interfacial zone properties and the aggregate size, distribution and surface texture can have an important role in resisting the crack opening (Khalilpour et al., 2019; Siregar et al., 2017). Increasing the biggest dimension of aggregate in concrete with similar water to binder ratio, fractal dimension increase resulting to an increase in fracture energy (Yan et al., 2001). Furthermore, the aggregate properties like the size, type and smoothness influence the crack control capacity with smoother aggregates having a decrease in fracture energy (Nallathambi, et al., 1984). Some of the works reported the increase in fracture toughness with the increase of aggregate size or by increasing the coarse-to-fine aggregate ratio. (Giaccio et al., 1993)

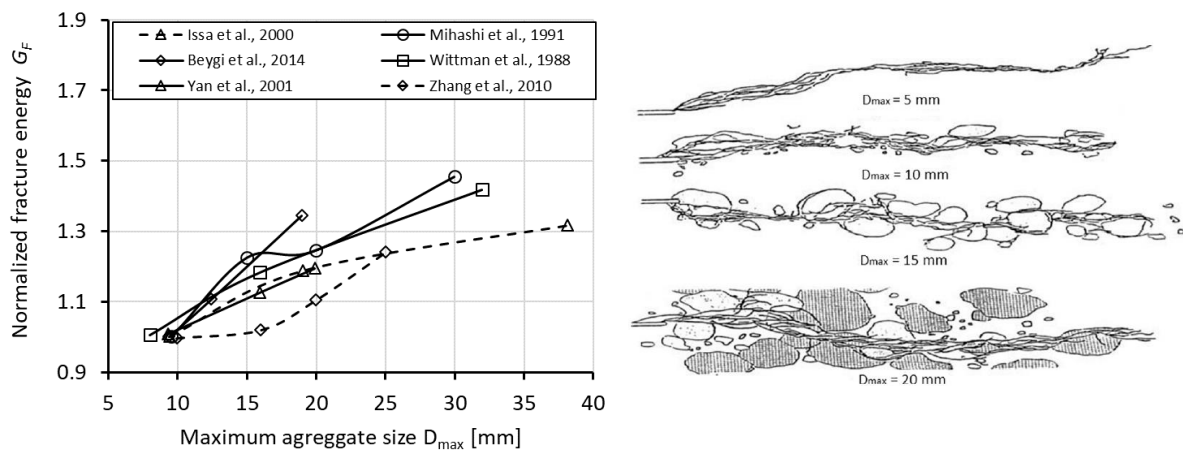


Figure 3-4. Normalized fracture energy G_F as a function of maximum aggregate size (left) and the aggregate size effect on the crack path in concrete (right, Chen et al., 2004).

Size of the specimen and notch/depth ratio

It is well known that the fracture process zone (FPZ) largely influences the crack propagation and the energy required to its growth. Furthermore, as the size of the concrete specimen increases, the relative size of the process zone decreases leading to a conclusion that the infinitely sized specimens are size-independent (Bažant et al., 1991). Increasing in size lead to an increase in fracture toughness and the fractal dimensions. Some experimental studies (Issa et al., 2000) show that if the dimension of the specimen is three times enlarged, the fracture

toughness and the stress intensity factor significantly increase. However, the stable fracture energy remains almost a constant irrespective of the specimen size, the unstable fracture energy increases with increasing ligament length. Stable fracture energy is taking place during the crack stable extension (pre-critical crack growth) and the unstable energy is occurring in the fracture period, where the stored energy is completely released until the deformation reaches its maximum value and the load fails to zero (Xu et al., 2006).

Fibers

Adding fibers of any kind in the concrete mix improves the durability and the mechanical properties of hardened concrete including the resistance to fatigue, flexural strength, impact strength, toughness, vulnerability to cracking and spalling (Nanni, 1988; Malhotra et al., 1994). Fibers differ from themselves in their type (steel, polypropylene, polyethylene, glass, carbon etc.), size (length to diameter ratio), volume content, ultimate tensile strength and distribution (Shah et al., 1971; Gopalaratnam et al., 1991). Fibers have a considerable influence on the post-peak behavior and increase the non-linear fracture properties. Mo et al. (2014) determined that adding 0.5 to 1% of steel fibers in the mixture, the fracture toughness is increased from 6 to 17 times, indicating the effect of steel fibers on the bond between the microcracks. Furthermore, the highest rate of fracture energy increase is associated to steel fibers and the lowest to Basalt fibers. (Khalilpour et al., 2019)

3.2 Experimental investigation: temperature dependent fracture energy

3.2.1 Test preparation

The experimental tests for temperature dependent fracture energy were carried out at the MPA laboratory (*Materialprüfungsanstalt Stuttgart*). The work was performed in two steps; initially, the notched beams were placed in the electrical oven, subjected to thermal load and left to cool down naturally to the ambient temperature. In the second step, the three point bending test according to RILEM test specifications for determination of fracture energy was carried out (RILEM committee, 1985).

Test specimens of two different sizes with their corresponding dimensions are shown in Figure 3-5. For consistency and unambiguous comparison in the numerical analysis later (Chapter 5), the smaller specimens have been pre-cut from the cracked compact tension specimens (CTS) already used in the dynamic experimental analysis (Ruta, 2018), as shown in Figure 3-6. Since the CT specimens used in the preceding research were thermally damaged only up to 400°C, one part of the sliced specimens at the ambient temperature were additionally heated up to 600°C.

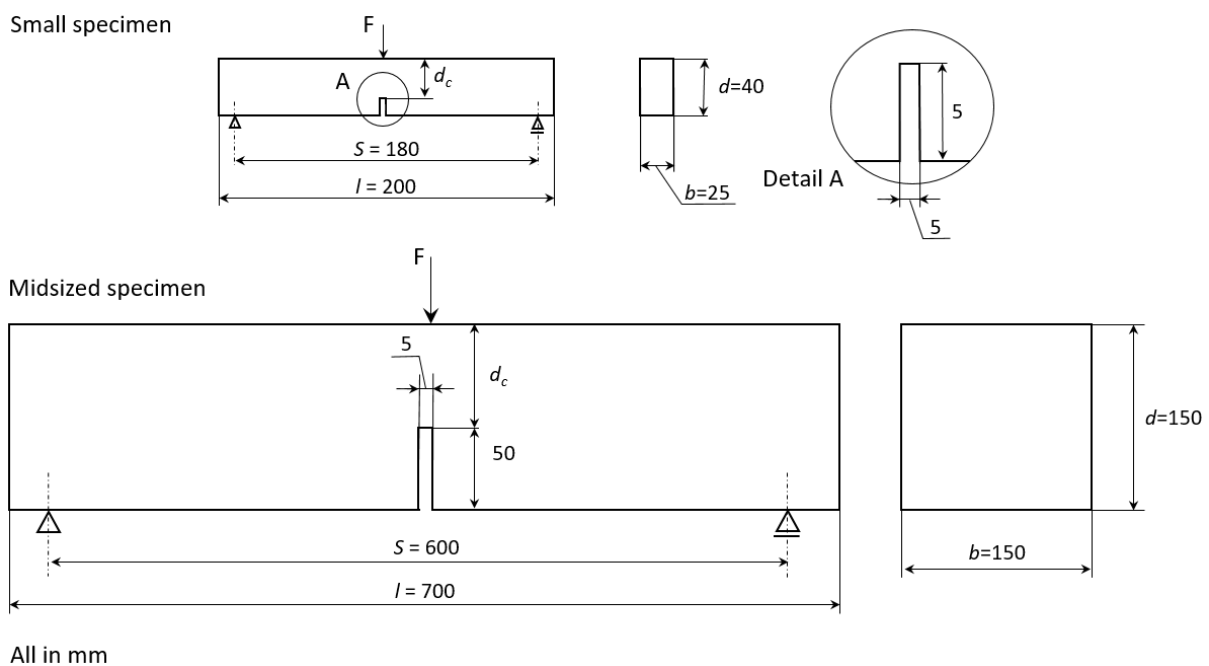


Figure 3-5. Dimensions of the test specimens used in the experiments.

The concrete specimens were cured for 7 days under constant temperature of 20°C and relative humidity (RH) of 100%. Subsequently, the specimens were exposed to the relative humidity of 60% for 3 weeks and afterwards, they were placed in the oven at 80°C for 2 weeks. The beams were additionally set aside for three months at room temperature to mitigate the possibility of

any remaining free water in the material. Altogether, 20 smaller-sized and 16 midsized specimens were produced for the tests. Since the midsized beams were too big for one mixing batch, the mixing process had to be repeated three times. The concrete recipe for the midsized concrete specimens is summarized in Table 3-1.

Table 3-1. Concrete mixture properties (Midsized specimens).

Batch	Cement		Aggregates				w/c	Plasticizer	f_c	Density
	type	ρ [kg/m ³]	0-2	2-4	4.8	8-16	-	kg/m ³	N/mm ²	kg/m ³
1	CEM I 32.5	250	553	410	375	446	0.73	0.0027	46.53	2.21
2	CEM I 32.5	250	553	410	375	446	0.73	0.0027	48.06	2.24
3	CEM I 32.5	250	553	410	375	446	0.73	0.0027	45.47	2.25

The cement type for all test specimens was CEM I | 32.5. The water to cement ratio was taken as 0.73 in the case of midsized specimens in order to reduce the strength of the concrete and to obtain a smooth and stable post-peak curve. Additionally, polypropylene fibers (PP) with a diameter of 15.4 μm and a length of 6 mm from the company Baumhüter were added to the mixture to avoid concrete spalling. Midsized specimens with addition of PP fibers contained 1.5 kg of fibers per m³ of concrete. A high length to diameter ratio combined with small diameter leads to more interconnected network of fibers and capillaries.

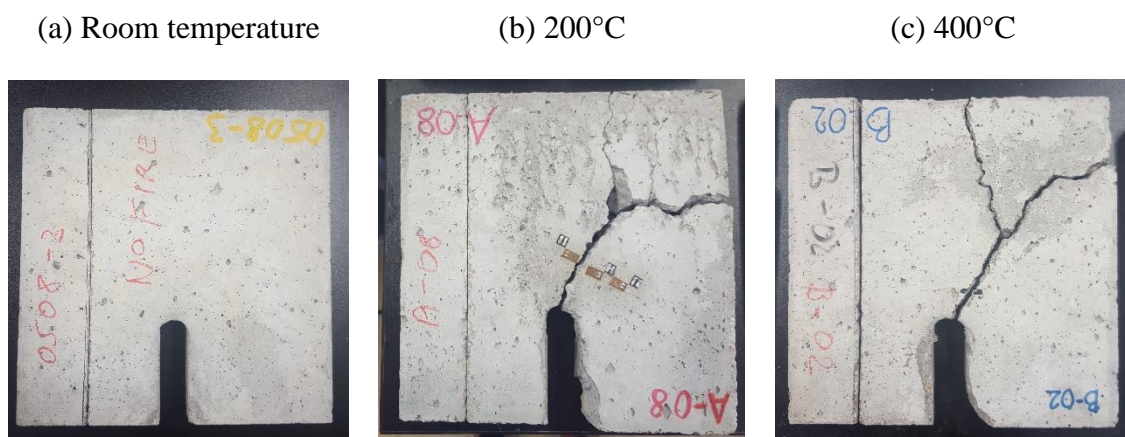


Figure 3-6. Sliced specimens from the original CT probes (small specimens).

The uniaxial concrete compressive strength for midsized specimens was measured before the tests on three standard 150 mm cubes for every casted mixture (Table 3-2). Concrete compressive strength is then reported as the mean value of those three specimens. The

properties of hardened concrete and calculated compressive mean value are summarized in Table 3-2.

Table 3-2. Properties of hardened concretes for small (S) and mid-sized (M) specimens.

Mixture No.	Specimen No.	Specimen size*	Weight [kg]	Density ρ [kg/m ³]	Compressive strength [N/mm ²]	Compressive strength – mean value [N/mm ²]
S1*	1	S	7.245	2.162	50.46	
S1	2	S	7.338	2.110	46.91	48.96
S1	3	S	7.118	2.124	49.52	
M1*	1	M	7.665	2.270	46.82	
M1	2	M	7.441	2.210	46.95	46.53
M1	3	M	7.209	2.140	45.83	
M2	4	M	7.356	2.180	48.04	
M2	5	M	7.518	2.230	47.75	48.06
M2	6	M	7.568	2.240	48.4	
M3	7	M	7.598	2.250	45.41	
M3	8	M	7.621	2.260	47.55	45.47
M3	9	M	7.598	2.250	43.5	

* S – small; M – mid-sized.

Based on the compressive strength, the concrete properties of small specimens were estimated as: Young's modulus $E_c = 36$ GPa, Poisson's ratio $\nu = 0.18$ and tensile strength $f_t = 3.8$ MPa.

Figure 3-7 shows the beams of both sizes before the TPB test.

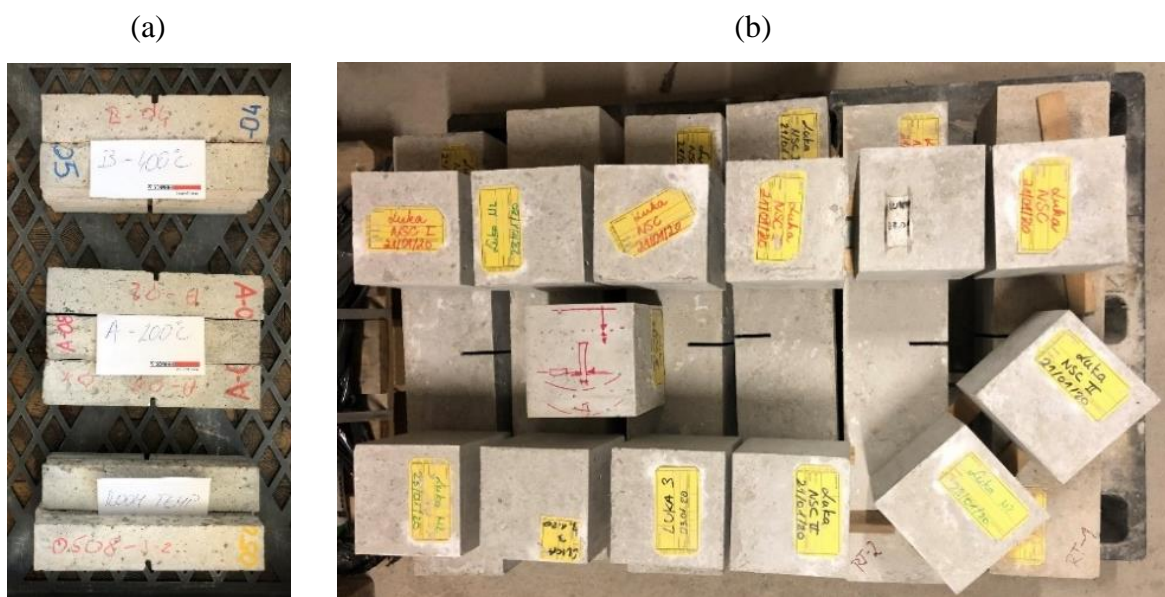


Figure 3-7. Small (a) and mid-sized (b) specimens before the TPB tests.

3.2.2 Thermal exposure

The specimens were heated up in the oven *Kittec XT-330* from the company Bentrup that was equipped with a pre-programmable temperature history option. This option was mainly used for adjusting heating gradients and retaining time on a certain temperature level.

Table 3-3. Testing procedure and number of specimens used in the tests.

Target temperature [°C]	Size of the specimen	Number of specimens	Heating regime
20	150x40x25	4	1°C/min
200	150x40x25	4	1°C/min
400	150x40x25	4	1°C/min
600	150x40x25	5	1°C/min
20	700x150x150	4	1°C/min
200	700x150x150	4	1°C/min
400	700x150x150	4	1°C/min
600	700x150x150	4	1°C/min

The specimens were heated up with a constant heating rate of 1 °C/min to their target temperatures of 200, 400 and 600°C, where they were kept for another 2 hours to obtain a uniform temperature throughout the complete specimen. During the heating process, no extensive thermal spalling occurred in mid-sized specimens due to the presence of PP-fibers. The fibers lose their thermal stability at 120°C, melt at approximately 160°C and burn at 320°C.

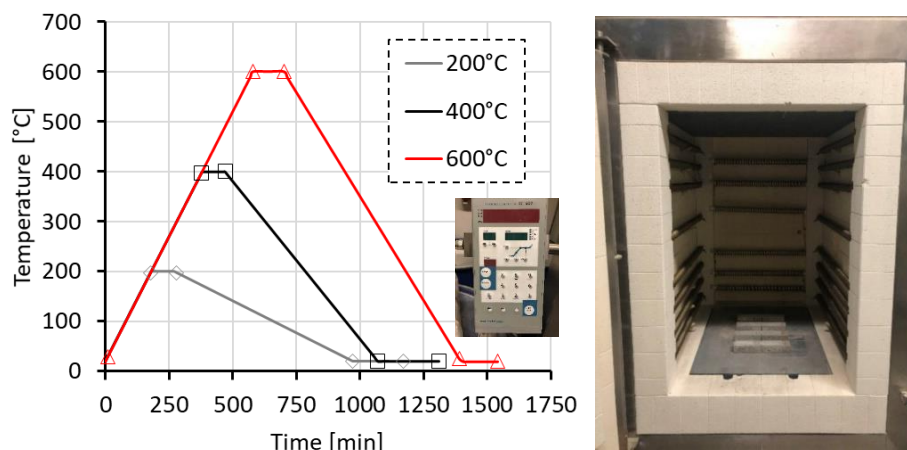


Figure 3-8. Heating and cooling regime for both specimen sizes and the oven.

The used temperature time curve (heating regime) that was programmed in the machine's interface is depicted on Figure 3-8. For all test cases, the heating gradient of 1°C/min was kept the same. Figure 3-9 shows the thermally induced damage (cracks) that occurred during the

heating and cooling regime in the case of 600°C in both specimen sizes. Majority of cracks in the mid-sized specimens originate at the notch tip and tortuously propagate towards the peripheral parts on the side. Positioning the beams in an upward position during heating caused the initiation of cracks on the side of the specimens. Smaller beams were placed in the oven in a horizontal position without any major cracks observed at the end of heating regime (Figure 3-9; 600°C).

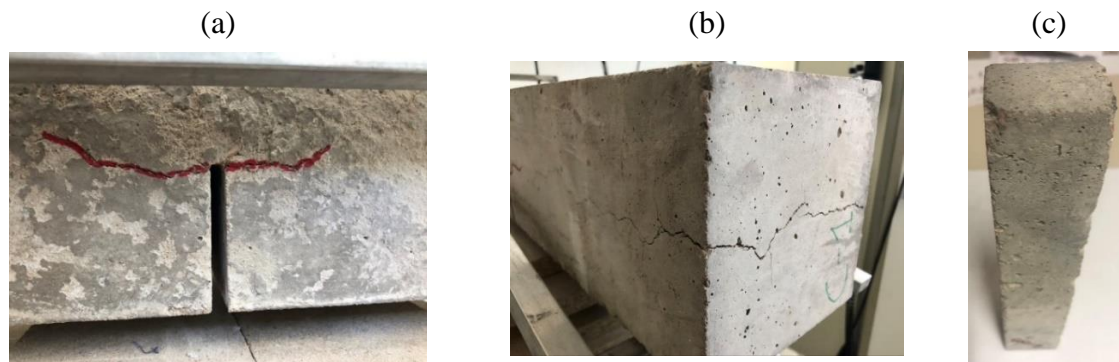


Figure 3-9. Observed cracks after being cooled down from 600°C in mid-sized specimens (a and b) and in small specimens (c).

Measured weight loss with the temperature increase indicates that smaller beams lost more in weight than mid-sized beams (Figure 3-10). However, smaller beams exhibited a more pronounced scatter of results. The initial weight loss at low temperatures occurred due to the evaporation of capillary water followed by the weight loss due to the evaporation of gel water at temperatures of 200-400°C and finally the dehydration and decomposition of hardened cement paste and aggregates at 600°C. Since different cooling rates have no influence on the weight loss, these results are comparable (Zhang & Bićanić, 2002).

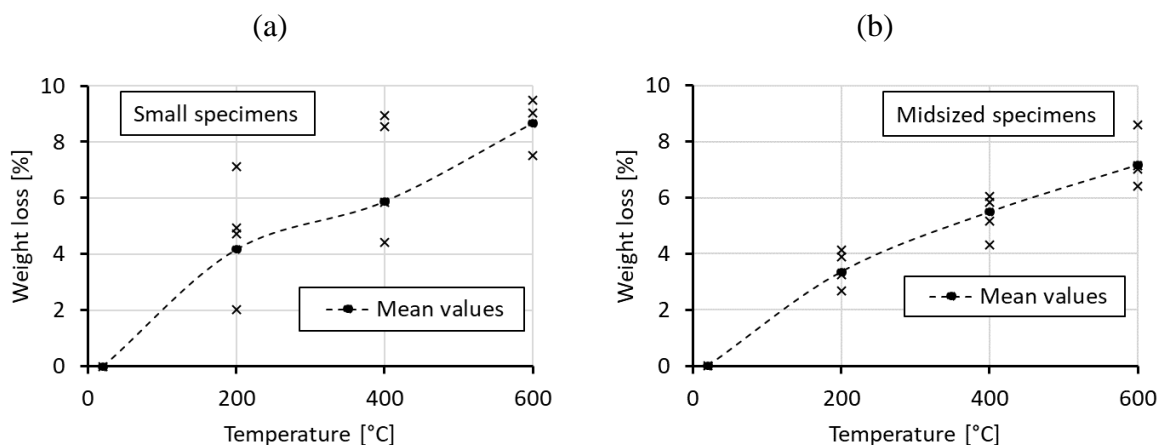


Figure 3-10. Weight loss for different target temperatures: small specimens (a) and mid-sized specimens (b).

3.2.3 Small concrete specimens

The first batch of specimens (small sized) with the dimensions of $25 \times 40 \times 200$ mm ($b \times d \times l$) were fixed between the rollers in a 10 kN Zwick/Roell machine and the distance between the supports where the specimens were placed on, was set to $S = 180$ mm (Figure 3-11d). The three point bending test was performed on four series of specimens; one at ambient temperature and three that were previously heated up to 200°C , 400°C and 600°C . The beams were tested in the cold (residual) state, i.e. after being cooled down to the room temperature. The testing was carried out at normal ambient conditions (Figure 3-11a).

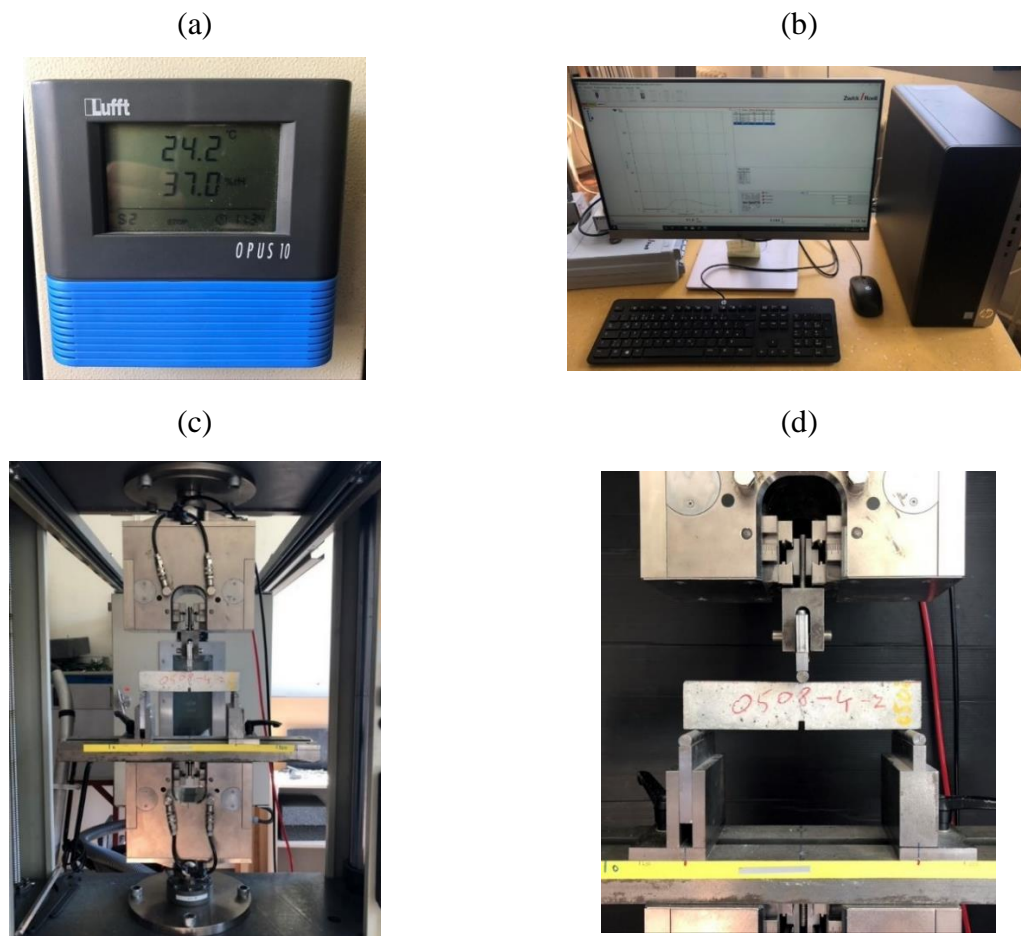


Figure 3-11. Thermometer (a), Acquisition unit (b), testing machine (c) and loading jack (d).

Due to the small dimensions of the specimens, it was inconvenient to mount the LVDT sensors or clip-on extensometers to measure the crack mouth opening displacement (CMOD). Therefore, the midspan deflection of tested probes was measured through the movement of loading jack (Figure 3-11d) and the information was sent to the computer for displacement processing (Figure 3-11b). The data acquisition rate of the load-displacement results was set to 0.005 s. The distance between the supports at the bottom was set at 180 mm and the loading

speed was kept constant at 0.02 mm/s. The load displacement (L-D) curves from the TPB tests on small specimens with their corresponding crack patterns are shown in Figure 3-12. The test was aborted at approx. 5% of the corresponding peak load value.

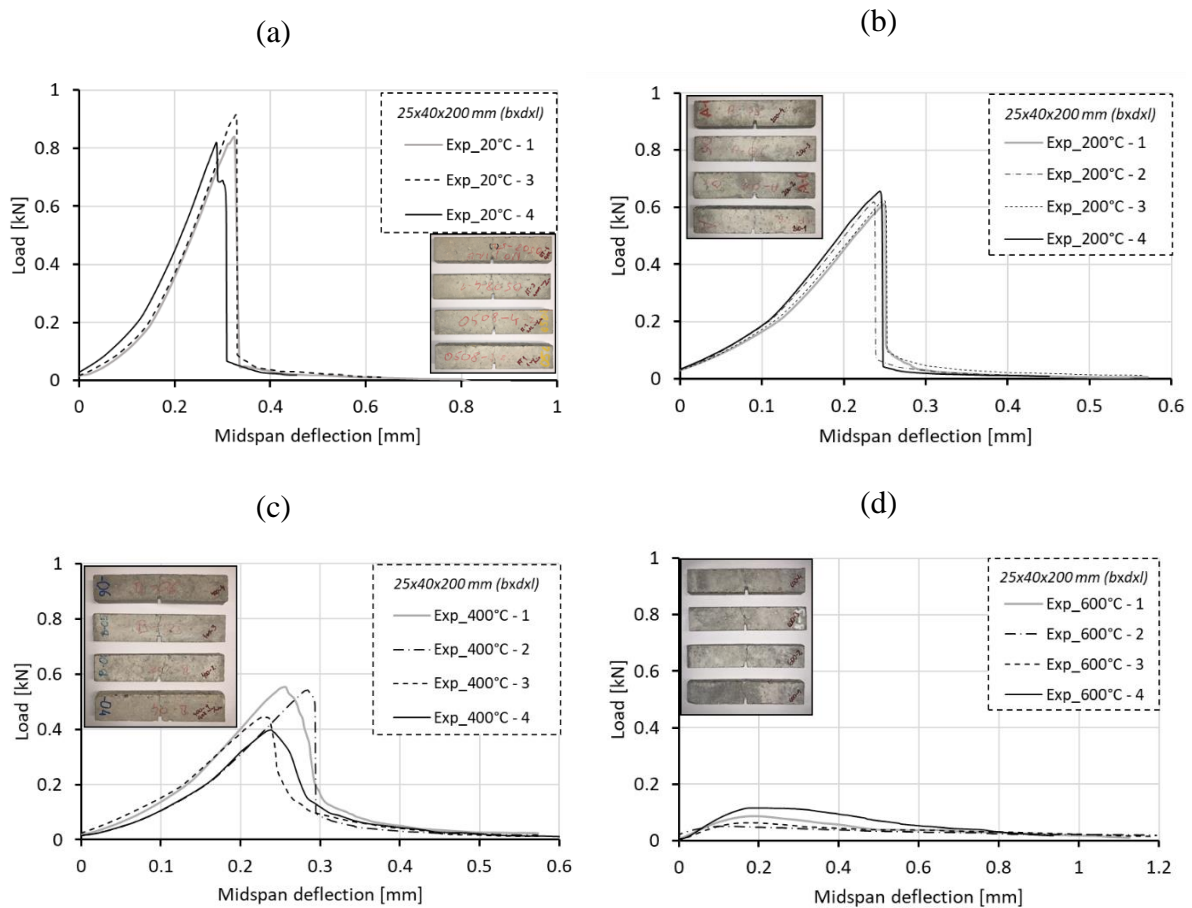


Figure 3-12. Load displacement curves from the three point bending test of mid-sized beam specimens at: 20°C (a), 200°C (b), 400°C (c) and 600°C (d).

The L-D curves for the specimens at ambient temperature and at 200°C indicate a brittle failure after the peak load is reached. Since the midspan displacement was measured on the machine and not with the LVDT (Linear Variable Differential Transformer) or CMOD (crack mouth opening displacements) gauges, the loading nose was not controlled by the crack opening and exhibited insensitivity in the post-peak zone. In 200°C case, a slightly tortuous crack path can be observed which indicates that these specimens already experienced noticeable thermally induced damage. In both temperature cases, 20°C and 200°C, in terms of deflections at peak load, don't differentiate as much. Specimens which underwent a heating regime up to 400°C and 600°C prior to the TPB test, exhibited a more pronounced ductile failure with a rounded peak (occurring at high temperature). The initial slope of the ascending branches in these two cases, compared with specimens at 20 and 200°C, decreased and the curve became generally

flatter and more extended. Figure 3-13 shows the experimental results in terms of relative peak load values and the displacement at the onset of cracking as a function of temperature. The reduction in average relative peak load values compared to the case at room temperature amounts to 25.4%, 42.3% and 91.4% at 200°C, 400°C and 600°C, respectively. The results also indicate that the displacement at the onset of cracking increases with the temperature increase.

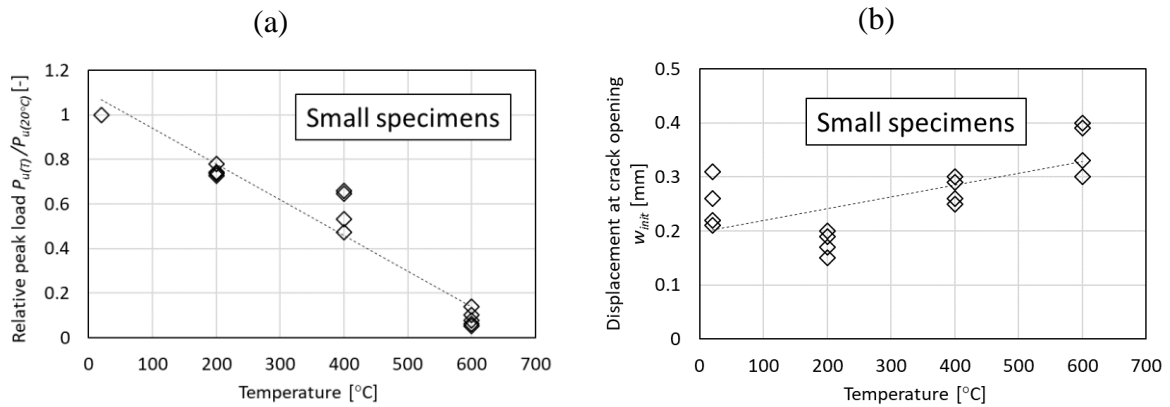


Figure 3-13. Values of peak loads (a) and the displacement at the onset of cracking (b) at different temperatures from the TPB test of small sized beams.

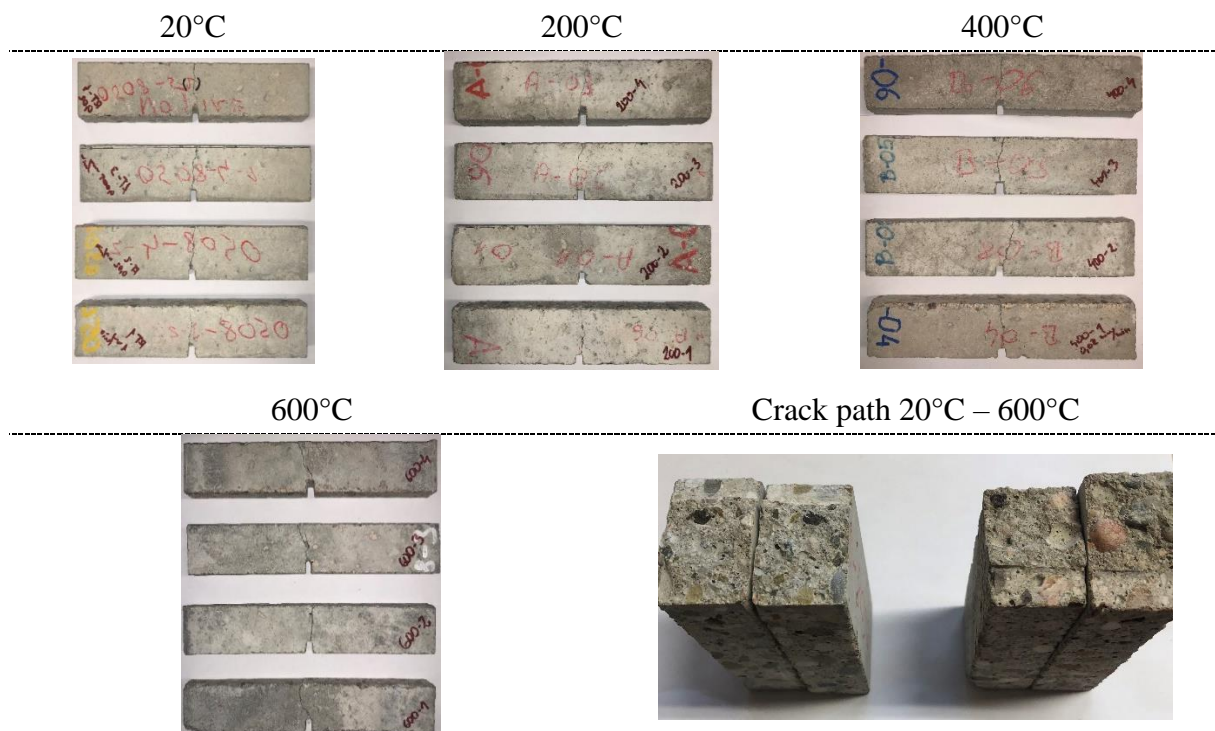


Figure 3-14. Observable crack paths at the surface in the complete temperature range and the crack path difference between specimens at 20 and 600°C.

The cracked specimens at their corresponding temperature levels are shown in Figure 3-14. As the temperature increased, the crack path became more tortuous and the change in specimen

surface color was observed. Moreover, the crack at 600°C went around the aggregates while the crack at 20°C through them, which indicates the degradation of the bond between the aggregates and the cement paste as well as the existence of the micro cracks in the interface zone.

3.2.4 Midsized concrete specimens

The three point bending (TPB) tests in the case of mid-sized specimens were carried out according to the recommendations of RILEM (RILEM Committee, 1985). The beam specimens, after being left to completely dry out at room temperature for 3 months, were placed in the servo-controlled hydraulic jack WALTER+BAI ZDEM 20/600 with a maximum loading capacity of 20 kN. Three LVDT sensors for tracking the mid-span deflection were installed on each specimen and glued with a molten ethylene-vinyl-acetate copolymer.

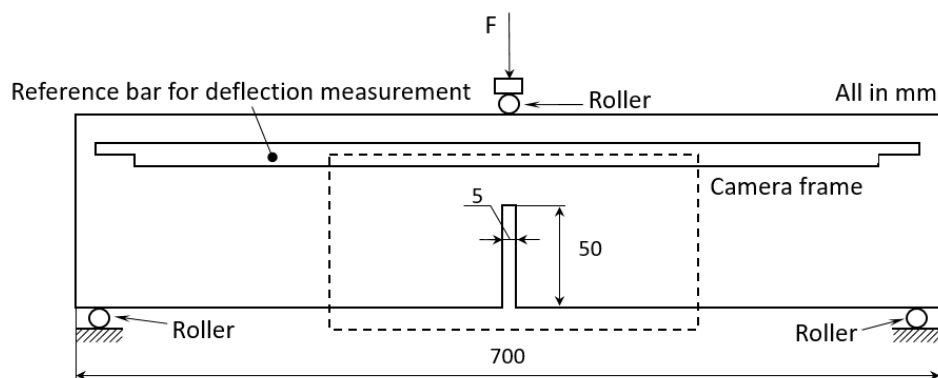


Figure 3-15. Complete test setup (top) the schematic side view of the specimen in the camera frame (bottom).

The test set-up was equipped with a monitoring unit that had a recording frequency of 0.05 seconds (Figure 3-15). The tests were filmed with a GoPro Black 5 camera in order to track the crack path in real time. To obtain the complete load-displacement curves in reasonable time, the testing rate was fixed at 0.025 mm/min. Due to the high sensitivity of the LVDT sensors that were measuring the midspan deflection, a high-frequent oscillation of displacement during the tests could be observed. To circumvent the oscillation, a program in Matlab© was created to calculate a smoothed function by obtaining the coherent tangents of each point and the inclination between them. Each point with an inclination higher than 5° was discarded. Figure 3-16a. shows an example of the test with frequent displacement oscillations with its corresponding smoothed curve expressed as a red dotted line. The LVDT connected directly to the motion regulation channel is shown in Figure 3-16b.

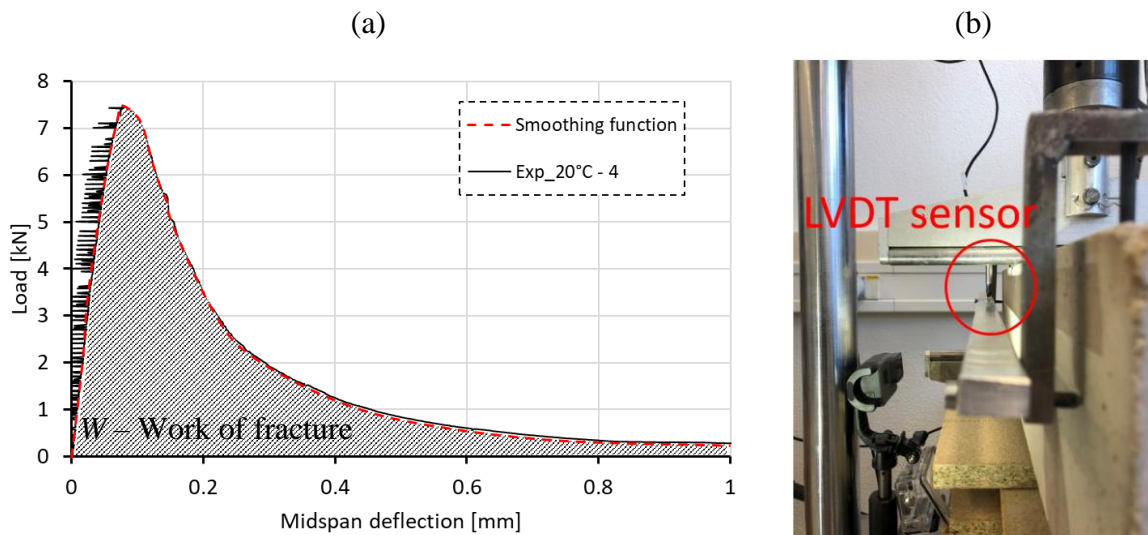


Figure 3-16. Load-deflection curve from the TPB test of the mid-span beam at 20°C and its corresponding smoothed curve (a) and the position of the LVDT sensors (b).

Test results for four target temperatures at 20°C , 200°C , 400°C and 600°C with their corresponding load displacement curves are shown in Figure 3-17. Between the specimens in tested cases, individually, no particular peak load deviation has been observed. The horizontally placed beams were each loaded with a constant loading rate, whereby at approx. 5% of the corresponding peak value, the test was aborted. Therefore, the time of the tests increased with the temperature level as they became more ductile and needed more time to reach the prescribed test termination load. The initial slope of the curve, representing the initial stiffness, decreased with the temperature increase. The L-D curves at 600°C exhibited expressed ductile behavior and reduction of peak load compared to its value at 20°C . The largest scatter of the peak loads and the curves itself was observed at 200 and 400°C .

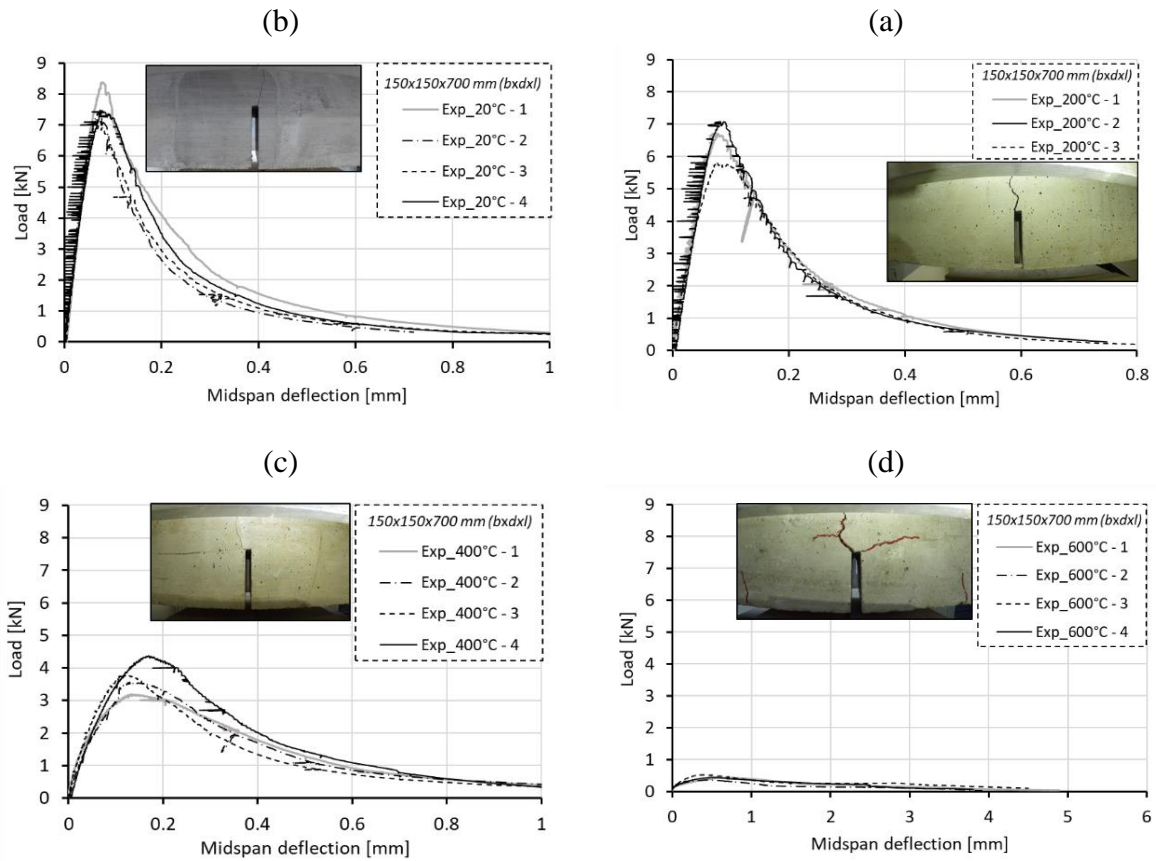


Figure 3-17. Load displacement curves from the three point bending test of midspanned beam specimens at: 20°C (a), 200°C (b), 400°C (c) and 600°C (d).

The peak loads exhibit a strong declining tendency as the temperature increases. Comparing the average peak loads of thermally pre-damaged specimens with the case at ambient temperature, a decline of 25% at 200°C, 50% at 400°C and 90% at 600°C is detected. The highest relative decrease of the peak load was observed at 600°C compared to the values at 400°C (Figure 3-18a).

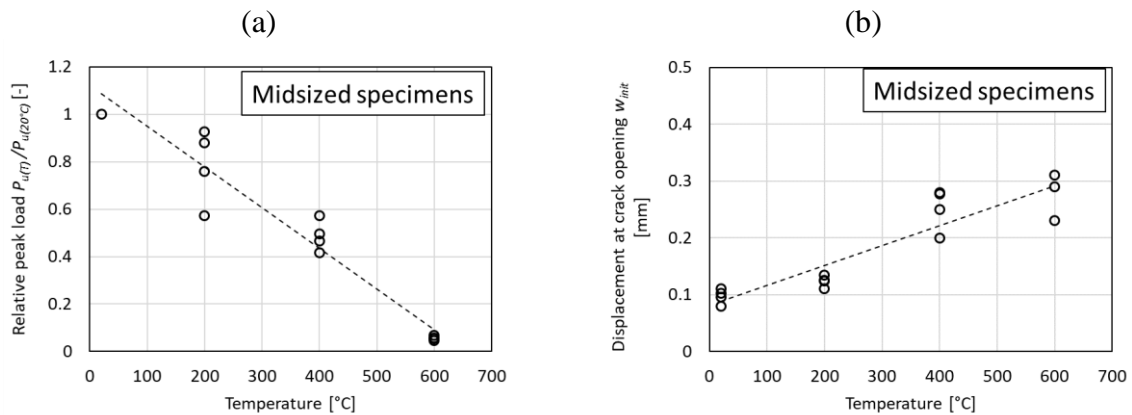


Figure 3-18. Values of peak loads (a) and the displacement at crack opening (b) at different temperatures from the TPB test of midspanned beams.

The displacement at the crack onset as a function of temperature shown in Figure 3-18b. With the increase of temperature, the displacement at which the crack initiate is slightly increasing. As the temperature increased, the color of the specimen surface changed and the crack path became more tortuous, as shown in Figure 3-19. Due to the increase in target temperature, the crack started to circumvent the aggregates instead of going through them (Figure 3-20).

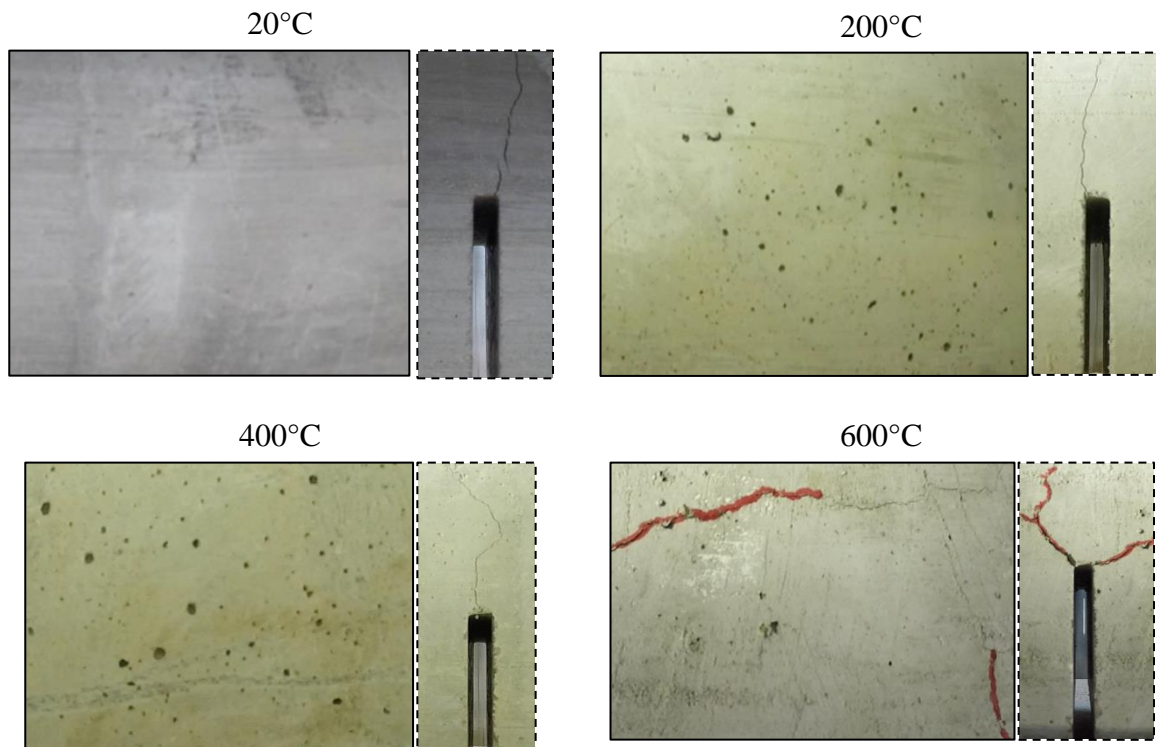


Figure 3-19. The surfaces of mid-sized concrete specimens after exposure to elevated temperature and their corresponding crack pattern during the three point bending test.

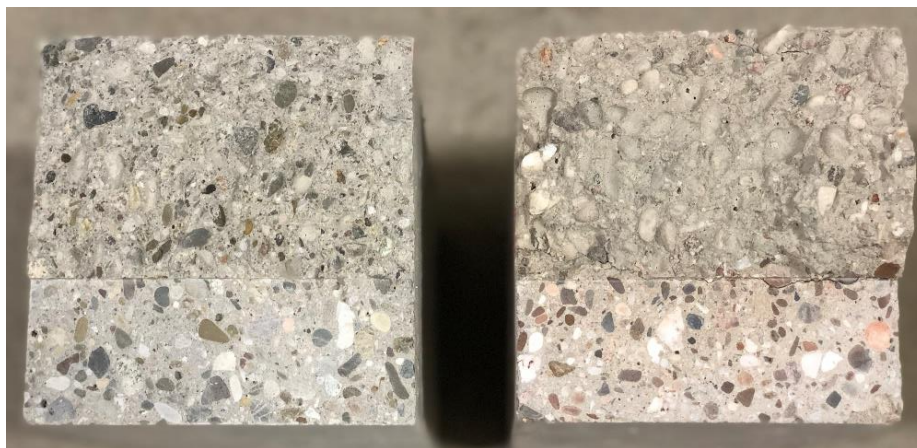


Figure 3-20. Cross section along the crack path of the mid-sized specimens at 20°C (left) and 600°C (right).

3.2.5 Fracture energy measurements

The fracture energy, G_F defined as the total energy dissipated over a unit area of the cracked ligament, should be calculated by taking the work of fracture imposed by the acting force and the self-weight of the specimen. However, since in the case with smaller beams, the self-weight was not taken in to account, the same was also neglected in the case of midsized beams:

$$G_F = \frac{\int_0^{\delta_0} P(\delta)d\delta}{A_{lig}} \quad (3-5)$$

where G_F is the fracture energy (J/m^2), A_{lig} is the area of the ligament (m^2), δ_0 is the mid-span deflection (m), and P is the load (N). The fracture energy as a function of temperature is shown in Figure 3-21 for the tested beams. In the case of smaller beams, a declining trend with the increase of temperature can be observed. The biggest relative decrease in fracture energy is visible at 200°C and it amounts to 71% of the value at ambient conditions. The average fracture energy at 600°C is 61% compared to its initial value at the room temperature.

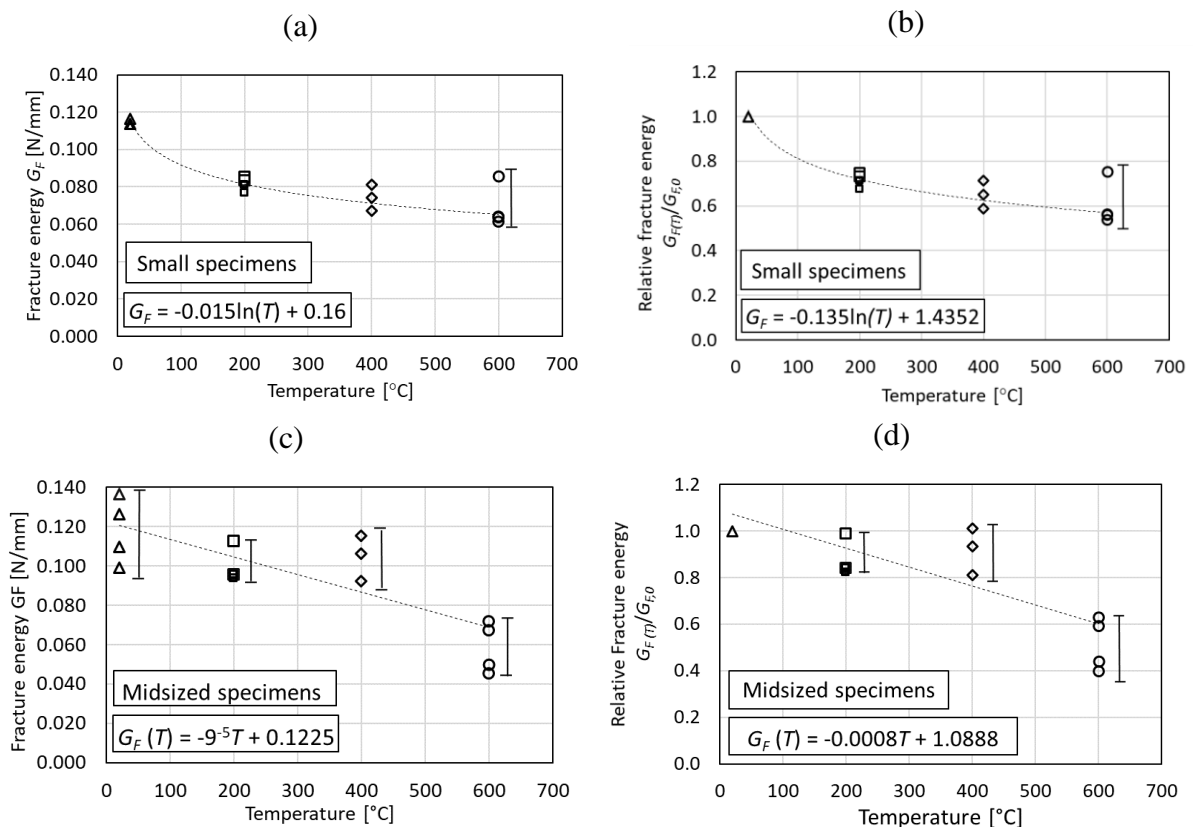


Figure 3-21. Fracture energy as a function of temperature given in absolute and relative values for: Small (a and b) and midsized specimens (c and d).

It should be emphasized that the displacement in the tests with smaller beams was measured directly from the loading jack movement and the probes at 20 and 200° showed quite a brittle

response in the post peak zone. Considering this fact, it can be concluded that the fracture energy at those temperatures, measured with LVDT sensors or CMOD method, would be probably slightly larger. Equations (3-6) and (3-7) describe the experimentally obtained temperature dependence of fracture energy plotted in Figure 3-21.

$$\text{Small specimens:} \quad G_F^S = -0.135 \ln(T) + 1.4352 \quad (3-6)$$

$$\text{Midsized specimens:} \quad G_F^M = -0.0008 (T) + 1.0888 \quad (3-7)$$

Since the midspan deflection in the case of larger specimens was measured with the help of LVDT sensors and the notch length was relatively large, the obtained load displacement curves were more stable in the post peak zone. Although the measured G_F at 200 and 400°C are similar to each other, their average values compared with G_F at room temperature still show a decreasing trend. The average value of fracture energy at 600°C is 61% of the initial value at room temperature and compared to the smaller specimens, only 5% higher. The G_F decline at 200 and 400°C is more pronounced in the case of smaller specimens (logarithmic function), in spite of the heating gradient being the same in both cases (1°C/min). Having smaller size, the small concrete beams reached their uniform temperature much faster causing higher thermally induced strains in the inner regions. Naturally, this led to higher damage already at 200°C and 400°C and a higher reduction of G_F . This reduction equalized in both cases at 600°C with approx. 60% of their reference value at ambient temperature. It should be emphasized that for the purposes of this work, the relative values are more important.

3.2.6 Tensile strength

The tensile strength was obtained by calculating the bending strength assuming the elastic beam theory formula $\sigma_B = 3P_U S / 2bd_c^2$ with P_U as the corresponding peak load, d_c as the distance from the notch top to the upper specimen surface (the length of the ligament) and S as the distance between the supports. Accounting for the size effect on the bending strength σ_B , tensile strength f_t is calculated as $f_t = \sigma_B / \alpha_t$ where $\alpha_t = 2.85$ and 1.64 for small and midsized beams, respectively. In both cases, a linear decrease in tensile strength with the temperature increase is observable. The relative decrease with 95% at 600°C, compared to the case at 20°C, is more pronounced in the midsized specimens.

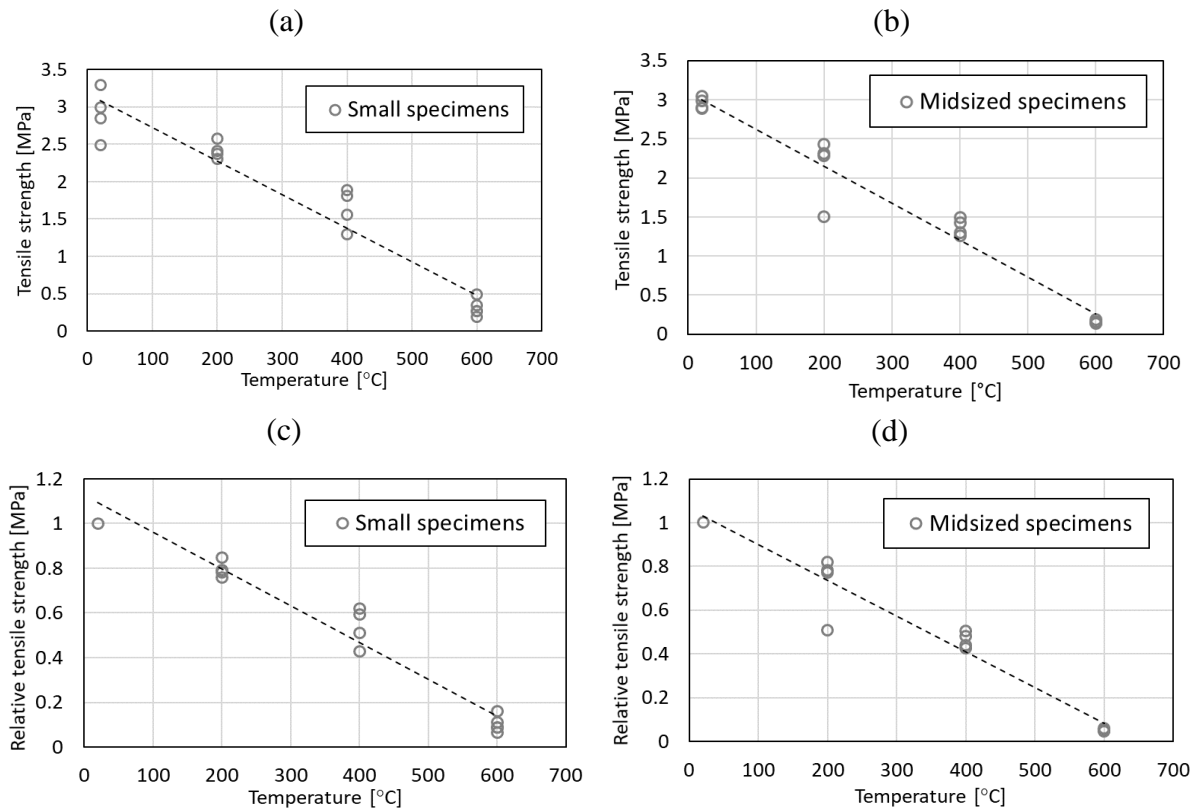


Figure 3-22. Tensile strength as a function of temperature given in absolute and relative values for: Small (a and b) and midsized specimens (c and d).

3.3 Conclusions

In the framework of the present experimental study, the influence of temperature on tensile strength and fracture energy was investigated. The tests were carried out using the three point bending method according to RILEM recommendation on specimens with two dimensions, small and midsized beams. The results confirmed the initial premise that the fracture energy has a steady decrease with the increase of temperature, similar to tensile strength and Young's modulus. The smaller sized specimens needed less time to reach the uniform temperature across in the specimen, hence were the inner regions longer exposed to higher temperature. The difference in reduction between the specimen sizes was observed already at 200 and 400°C, as the smaller specimens had higher thermally induced damage during the heating phase. In spite of this difference, both small and mid-sized beams had approx. similar 40% reduction of fracture energy at 600°C. Figure 3-23 illustrates the comparison of the results from literature (Zhang and Bićanić, 2002) and the experimental results for both specimen sizes. Had the fracture energy been measured up to 800°C, the trends indicate that the experimental results would conjoin in one point. The aim of the study was not only to obtain the fracture energy

curve but also to determine its influence on the dynamic response of CT specimen, as it will be discussed later in the numerical studies.

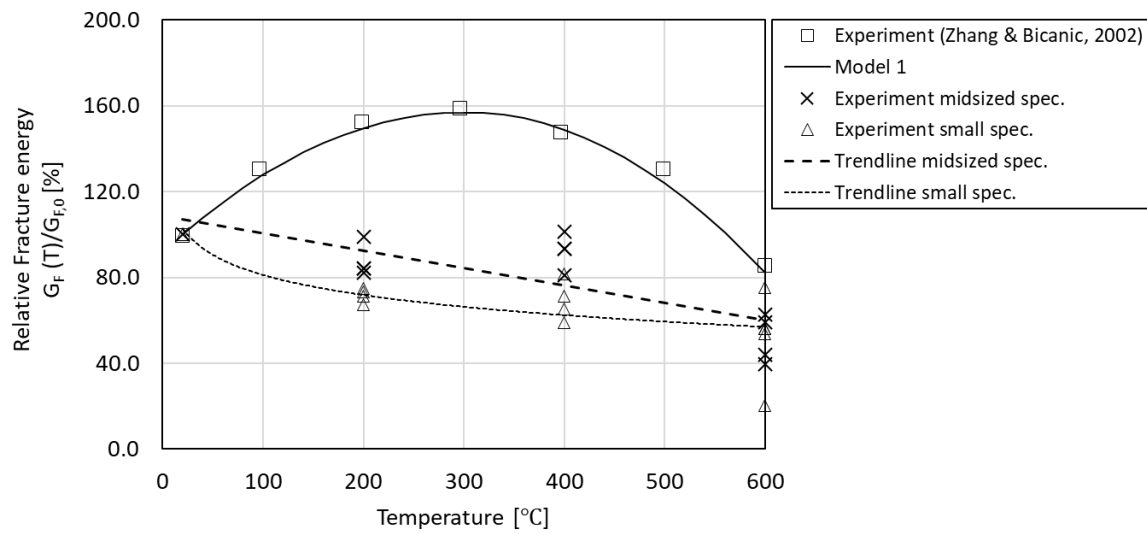


Figure 3-23. Comparison of the experimentally obtained fracture energy with the data from literature as a function of temperature given in relative values.

4. THERMO-MECHANICAL MODEL FOR CONCRETE AND THE 3D FE ANALYSIS

4.1 Introduction

In order to properly simulate the structural response under complex loading scenarios, such as fire and impact, a proper numerical approach has to be chosen. The non-mechanical influences, such as fire, can have a great impact on the resulting material behavior, cracking phenomena and the integrity of the structure making the numerical prediction of material failure a very demanding task. The simultaneous or successive loading of fire (elevated temperatures) and dynamic loading (impact) can lead to damage localization in a narrow zone accompanied by a progressive stress relaxation (material softening). Moreover, when two materials with different dynamic response in terms of strain rate sensitivity such as concrete and steel are modelled together, a proper computational approach plays a crucial role. In the used FE program MASA different constitutive laws are available (microplane model, plasticity and damage based models). However, for the application of the FE code to the problem at hand, a rate-dependent thermo-mechanical microplane model will be utilized. To account for the temperature influence on the material properties of the simulation constituents, the thermal dependencies of these properties were implemented in the model. A brief description of the mechanical and thermal parts of the microplane model, as well as the implementation of the nonlocal temperature field in the code will be discussed.

Two groups of coupled thermo-mechanical constitutive models exist currently: (i) thermo-mechanical models (de Borst and Peeters, 1988; Luccioni et al., 2003; Ožbolt et al., 2005b) and (ii) thermo-hygro-mechanical models (Bažant and Kaplan, 1996; Gawin et al., 1999; Ožbolt et al., 2008; Periškić 2009; Tenchev et al., 2005). In the first group, the mechanical properties of concrete are temperature dependent, while the temperature distribution is independent of the mechanical properties of the concrete. In the second group, the physical processes that take place at the micro level are coupled, i.e. there is an interaction between the mechanical properties, temperature, moisture, pore pressure, hydration, etc. These models are rather complex and interesting from a theoretical point of view. Due to the extremely complex structure of concrete, especially in the cracked state, the theoretical assumptions of these models are often very questionable and can therefore lead to incorrect results (e.g. transport of water and steam in damaged concrete at high temperatures). Consequently, for practical applications, the first group are more suitable.

4.2 Microplane mechanical model with relaxed kinematic constraint

In contrast to classical macroscopic constitutive laws, such as plasticity or damage models, which are based on tensorial invariants of stresses and strains, in the microplane model, the material response is computed based on the monitoring of stresses and strains in different predefined directions (Ožbolt et al., 2016). The constitutive law for concrete in the present work is rate sensitive temperature dependent microplane model, which is an extension of the microplane model with relaxed kinematic constraint (Ožbolt et al., 2001).

4.2.1 Isothermal constitutive law for concrete – Microplane model

In the microplane model formulated for concrete, the material is described by the relationship between the stress and strain components on planes of different orientation. These planes can be interpreted as microcrack planes or as "weak surfaces", such as contact surfaces between the aggregate and the cement matrix or slip planes in the theory of plasticity (Ožbolt et al., 2001). Few uniaxial stress and strain components are present on the microplanes and no tensor invariance requirements need to be considered. The tensor invariance constraints are automatically satisfied because the microplanes directly reproduce, to some extent, the behavior at various weak levels in the material. The basic concept of the microplane model was defined by Taylor (1938). The model was subsequently optimized by Bažant and his co-workers for the modeling of quasi-brittle materials (Bažant & Gambarova 1984, Bažant & Prat 1988b, Bažant & Ožbolt 1990, Carol et al. 1992). The model has been changed and adapted to obtain a unique solution for softening materials (replacement of the static constraints with the kinematic one; Bažant, 1984) and subsequently extended to model cyclic and rate sensitive material behavior (Ožbolt and Bažant, 1992). The version used in the framework of this thesis is based on the so-called relaxed kinematic constraint concept (Ožbolt et al., 2001). Each microplane is defined by its normal n_i (Figure 4-1). The microplane strains are assumed to be projections of the macroscopic strain tensor ε_{ij} (kinematic constraint). In the integration point of the finite element, normal (σ_N, ε_N) and two shear mutually perpendicular ($\sigma_K, \sigma_M; \varepsilon_K, \varepsilon_M$) stress-strain components are considered. To realistically model concrete behavior, the normal component is further decomposed into volumetric and deviatoric part ($\sigma_N = \sigma_V + \sigma_D; \varepsilon_N = \varepsilon_V + \varepsilon_D$).

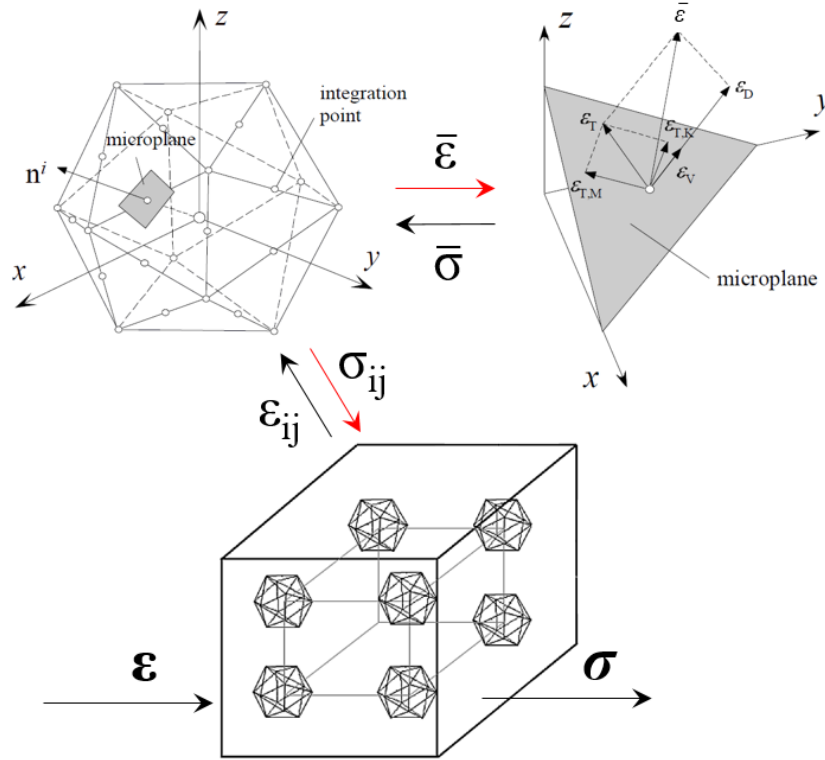


Figure 4-1. The concept of the microplane model: Discretization of the unit volume sphere for every FE integration point in 21 microplane directions and the microplane strain components.

Figure 4-1 is representing the implementation of the aforementioned equation in a 3D finite element. As an example, a solid finite element in Figure 4-1 is consisted of 8 integration points and the macroscopic strain tensor is first projected to each of that 8 integration points followed by the spatial decomposition (microplane). The projected strains are further decomposed into normal and shear components. Stress-strain relations on each microplane are then employed to determine the respective micro-stress components. Finally, using the principle of virtual work, a numerical integration over the total number of microplanes representing the material point is performed to determine the macroscopic stress components.

Based on the micro-macro work conjugacy of volumetric-deviatoric split and using the defined microplane stress-strain constitutive laws, the macroscopic stress tensor is then calculated as an integral of microplane stresses over all pre-defined microplane orientations:

$$\sigma_{ij} = \sigma_V \delta_{ij} + \frac{3}{2\pi} \int_S \left[\sigma_D \left(n_i n_j - \frac{\delta_{ij}}{3} \right) + \frac{\sigma_K}{2} (k_i n_j + k_j n_i) + \frac{\sigma_M}{2} (m_i n_j + m_j n_i) \right] dS \quad (4-1)$$

Where S denotes the surface of the unit radius sphere, δ_{ij} denotes Kronecker delta and k_i and m_i are directions of shear microplane components. The integration in Eq. (4-1) is performed by numerical integration using 21 microplanes for the symmetric part of the unit sphere. According

to present experience, 21-point integration formula (Bažant and Oh, 1986) gives a good balance between results accuracy and computational effort.

For each component of the microplane, the uniaxial stress-strain relationships are defined as follows:

$$\sigma_V = F_V(\varepsilon_V); \quad \sigma_D = F_D(\varepsilon_{D,eff}); \quad \sigma_S = F_S(\varepsilon_{S,eff}, \varepsilon_V) \quad (4-2)$$

where F_V , F_D and F_S represent the uniaxial stress-strain relations for the volumetric, deviatoric and shear components. For the deviatoric and shear components, only the effective part of the strain is used to calculate the stress. Eq. (4-2) is then used to calculate the macroscopic stress tensor from Eq. (4-1). In order to model the cracking of the concrete realistically for all load histories, the effective strain was used in Eq. (4-2). This strain is calculated as follows:

$$\varepsilon_{M,eff} = \varepsilon_M \psi_M(\varepsilon_M, \sigma_I) \quad (4-3)$$

where M stands for the corresponding components of the microplane (V , D , S), ε_M is the strain calculated by the projection of the total strain tensor (kinematic bond) and ψ is the so-called discontinuity function, which depends on the strain component and the maximum principal stress σ_I . The discontinuity function takes into account the discontinuity of the macroscopic strain field (cracking) at the individual levels. It is calculated in a way that for predominant tensile loading, the ratio between the positive volumetric and deviatoric strain components remains constant over the entire loading history remains constant. This function "relaxes" the kinematic constraint, which is unrealistic for the case of strong localization of strains. Furthermore, the discontinuity function ψ in the smeared crack method allows localization of strains in both tension and compression failures. The relaxation of the kinematic constraint to prevent the unrealistic model response for dominate tensile load is what makes this model unique, unlike most microplane models, which are based on the kinematic constraint approach. (Ožbolt et al., 2001; Ožbolt et al., 2005b).

The further advantage of the model is that the tensorial invariant restrictions are automatically fulfilled and they do not need to be directly enforced (Ožbolt et al., 2001). To account for large strains and large displacements, the Green-Lagrange finite strain tensor is used. Furthermore, to account for the loading history of concrete, the Cauchy co-rotational stress tensor is employed. Detailed discussion of the features and various aspects related to the finite strain

formulation of the microplane model are beyond the scope of the present paper (Bažant et al., 2000; Ožbolt et al., 2001).

4.2.2 Cyclic loading in the microplane model

Initially, Bažant and Prat (1988b) introduced the simplistic rules for unloading in the framework of their study, which was focused on monotonic loading. The model was able to represent only the first unloading and, compared to the experiments, even then showed some errors. Later, Ožbolt and Bažant (1992) introduced a new set of rules for unloading, reloading and cyclic loading considering arbitrary triaxial stress states for each microplane stress-strain component. The virgin loading for each microplane strain component ε occurs if:

$$\varepsilon \Delta \varepsilon \geq 0 \text{ and } (\varepsilon - \varepsilon_{max})(\varepsilon - \varepsilon_{min}) \geq 0 \quad (4-4)$$

where ε_{max} and ε_{min} are the maximum and minimum values of the effective microplane strain (ε) that have occurred so far; otherwise unloading or reloading takes place. In the contrast to virgin loading, the cyclic loading the stress-strain relations have to be written in the incremental form for every microplane strain component (volumetric, deviatoric and shear):

$$d\sigma_i = E_i d\varepsilon_i \text{ for } i = V, D, M \text{ and } K \quad (4-5)$$

where E_i represents the unloading-reloading tangent moduli which is generally defined as (Ožbolt et al., 2001):

$$\begin{aligned} E &= E_0 \alpha_e + \sigma \left(\frac{1 - \alpha}{1 - \varepsilon_0} \right) \\ \varepsilon > \varepsilon_p, \quad \varepsilon_1 &= \varepsilon_p - \frac{\sigma_p}{E_0} + \beta_e (\varepsilon - \varepsilon_p) \\ \varepsilon \leq \varepsilon_p, \quad \varepsilon_1 &= 0 \end{aligned} \quad (4-6)$$

where σ_p and ε_p denote the positive or the negative peak stress and the corresponding strain for each microplane component using the values σ_{p+} , ε_{p+} and σ_{p-} , ε_{p-} for positive and negative peaks; α_e and β_e are empirically chosen constants between 1 and 0 and E_0 is the initial elastic stiffness moduli for the corresponding microplane component. Figure 4-2 shows the loading-unloading-reloading rules for the volumetric and deviatoric microplane component. The loading-unloading-reloading rules for shear are principally the same as for the deviatoric component.

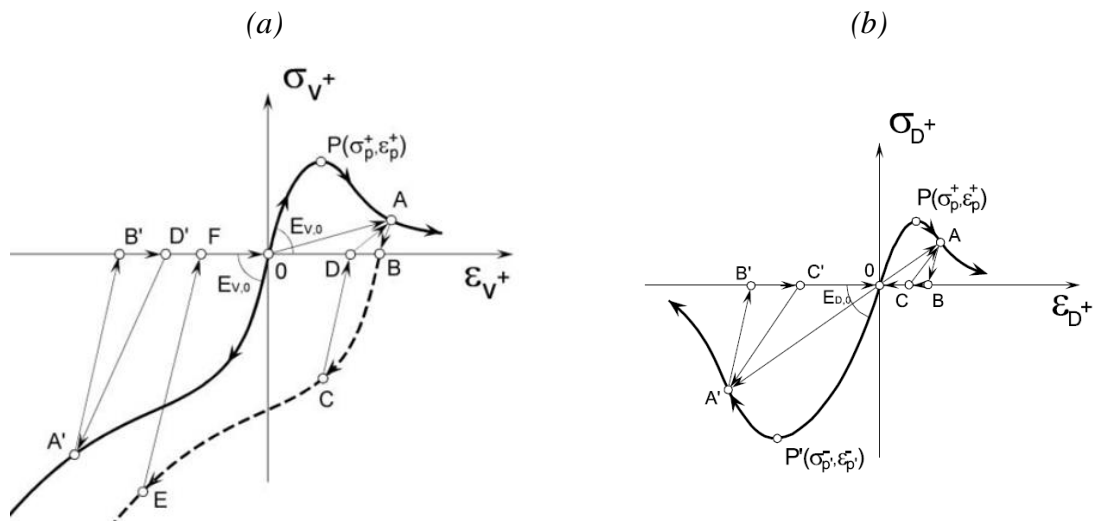


Figure 4-2. Loading-unloading and reloading rules for microplane strain components: Volumetric component (a) and deviatoric component. (Ožbolt et al., 2001).

4.2.3 Microplane model for steel

Currently several versions of the microplane model exist for concrete (e.g., Bažant and Prat 1988b; Bažant et al. 2000a, b; Ožbolt et al. 2001). Although several versions of the microplane model for steel were proposed (Jirásek and Bažant 2002), for the modelling of metallic materials, such as steel, almost exclusively macroscopic models based on the rate theory of plasticity are employed. Apart from the so-called *vertex effect*, these models are principally able to realistically predict failure of metallic materials under quasi-static loading. However, similar to the modelling of concrete, within the framework of standard finite elements these models are not capable to predict phenomena related to dynamic fracture of metals, for instance, crack branching, without additional failure criteria (Ožbolt et al., 2016). The microplane model for steel is based on the modification of the microplane model for concrete (Bažant and Prat, 1988b; Ožbolt et al. 2001). Similar to the microplane model for concrete, the microplane strains (ϵ_V , ϵ_D , ϵ_M and ϵ_K) are assumed to be the projections of macroscopic strain tensor ϵ_{ij} (with kinematic constraint) and the corresponding microplane stresses are computed by employing, in advance defined, uniaxial constitutive law for volumetric, deviatoric and shear components. However, there are several major differences in modelling quasi-brittle materials like concrete and metals. The nonlinearity of the quasi-brittle materials is mainly attributable to damage and therefore the constitutive laws for microplane components are based on the concept of damage. For metal materials, the nonlinearity is a consequence of the plastic slip, which is insensitive to lateral confinement, and therefore the tensile and compressive strength are the

same. Furthermore, metals exhibit a phenomenon, called the Bauschinger effect, where the yield stress is reduced when the material has been previously loaded in the opposite direction beyond the yield limit. This effect was also successfully implemented in the microplane model by proposing the following microplane stress-strain relationships (Ožbolt et al., 2016):

$$\text{Volumetric: } \sigma_V = C_V \varepsilon_V, \quad C_V = E_{V,0} \quad (\text{Linear elastic}) \quad (4-7)$$

$$\begin{aligned} \text{Deviatoric: } \dot{\sigma}_D &= \dot{C}_D \varepsilon_D + C_D \dot{\varepsilon}_D, \quad C_D = E_{D,0} e^{-|\varepsilon_D| a |^p} \quad (\text{Loading}) \\ \dot{\sigma}_D &= \dot{C}_D \varepsilon_D, \quad C_D = E_{D,0} \quad (\text{Unloading}) \end{aligned} \quad (4-8)$$

$$\begin{aligned} \text{Shear } (T \equiv M, L): \sigma_T &= C_T \varepsilon_T, \quad C_T = E_{T,0} e^{-|\varepsilon_T| b |^q} \quad (\text{Loading}) \\ \sigma_T &= C_T \varepsilon_T, \quad C_T = E_{T,0} e^{-|\varepsilon_{T,max}| b |^q} \quad (\text{Unloading}) \end{aligned} \quad (4-9)$$

where C and E_0 = secant and initial stiffness of the corresponding microplane component (V , D , T), respectively; a , b , p and q = internal model parameters obtained from the calibration of the model. The volumetric and the shear components are written in total (secant) form, whereas the deviatoric component is written in the rate form to account for its cyclic loading history.

4.2.4 Rate sensitivity

The components of the microplane stresses $\sigma_{Ms}^0(\varepsilon_{Ms})$ (Ms stands for microplane volumetric, deviatoric and shear component) are calculated from the known microplane strains ε_{Ms} using pre-defined microplane uniaxial stress–strain constitutive relations (Ožbolt et al., 2001). The rate dependency for each microplane component is based on the rate process theory and can be written in the following form:

$$\begin{aligned} \sigma_{Ms}(\varepsilon_{Ms}) &= \sigma_{Ms}^0(\varepsilon_{Ms}) \left[1 + c_2 \ln \left(\frac{2\dot{\gamma}}{c_1} \right) \right] \\ \text{with } \dot{\gamma} &= \sqrt{\frac{1}{2} \dot{\varepsilon}_{ij} \dot{\varepsilon}_{ij}} \quad \text{and} \quad c_1 = \frac{c_0}{s_{cr}} \end{aligned} \quad (4-10)$$

where c_0 and c_2 are material rate constants obtained by fitting the test data (Dilger et al., 1978), $\dot{\varepsilon}_{ij}$ represents the components of the macroscopic strain rate tensor. Here is obvious that the rate magnitude is not measured on the individual microplanes, which would be not objective, but on the macroscale. Eq. (4-10) applies to all microplane components except to volumetric compression, which is assumed to be rate insensitive. This is because for volumetric compression there is no crack development, i.e. the material is compacted. The rate dependency in the rate-sensitive microplane model for concrete accounts for two effects: (i) the rate dependency related to the formation (propagation) of the micro-cracks, which is the effect of

inertia forces at the level of the micro-crack tip, and (ii) the rate dependency due to the viscosity of concrete (bulk material) between the micro-cracks (Ožbolt et al., 2011).

On the other hand, metallic materials such as steel, that display high toughness and ductility, do not exhibit significant strain rate sensitivity (Boyce et al., 2007). Up to strain rates of 200/s there is almost no observable influence of strain rate on the strength due to its homogenous and nonporous structure. Because steel is nearly strain rate insensitive but very ductile, its loading rate dependency comes primarily from inertia, such as inertia at the crack tip that is related to high nonlinearity of steel, relatively large plastification zone, and structural inertia. (Ožbolt et al., 2016)

4.3 Thermo-mechanical coupling

In the thermo-mechanical model, the influence of temperature is accounted for through the following (Ožbolt et al., 2005b):

- (i) Formation of thermal strains: Free thermal strains (FTS) and the load induced thermal strain (LITS),
- (ii) The degradation of material properties due to thermal damage.

Furthermore, in the here presented temperature dependent microplane model the overall strain tensor ε_{ij} is decomposed as follows (Khoury, 1985a; Schneider, 1986; Thelandersson, 1987):

$$\varepsilon_{ij} = \varepsilon_{ij}^m(T, \sigma) + \varepsilon_{ij}^{ft}(T) + \varepsilon_{ij}^{tm}(T, \sigma) \quad (4-11)$$

where:

ε_{ij}^m - Mechanical strain tensor

ε_{ij}^{ft} - Free thermal strain tensor

ε_{ij}^{tm} - Thermo-mechanical strain tensor (LITS)

It is assumed that the mechanical component is decomposed in elastic and non-elastic part (plastic and damage part). Here, these strain components are obtained from the constitutive law (temperature dependent microplane model). Important to note is the fact the free thermal strain is stress independent component and it is measured on the unloaded concrete. As discussed in chapter 2, the thermo-mechanical strain is a load dependent component which occurs only in the first temperature cycle (Khoury, 1985b).

4.3.1 Thermally dependent mechanical properties in the microplane model

The non-linear thermal analysis is incremental where the load increment is defined by a time step Δt . In the present model, it is assumed that during the load increment the temperature remains constant. Consequently, the temperature-dependent material properties are also constant during the load step. Temperature dependent thermal properties of concrete based on the recommendations from Eurocode 2 (DIN EN 1-2, 2004) have been implemented in the microplane model. Contrary to this, the mechanical temperature dependent properties depend on the loading history of the problem. This temperature dependency of the mechanical concrete properties is accounted for in the model based on the experimental evidence.

Young's modulus – Concrete

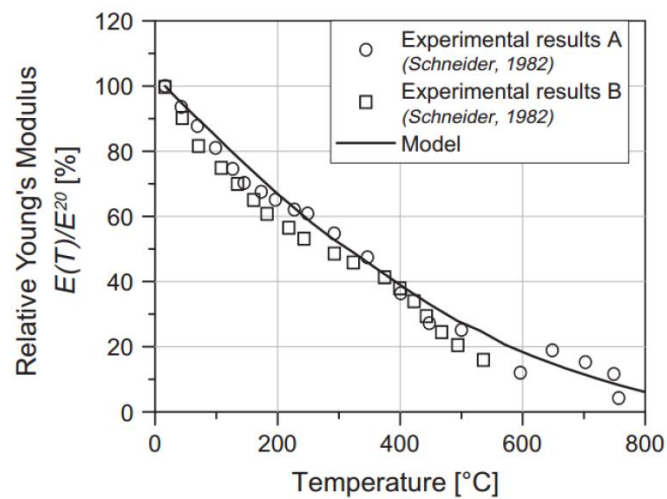


Figure 4-3. Concrete Young's modulus as a function of temperature (Periškić, 2009).

In the present model, the Young's modulus is implemented as the scalar function of temperature, as plotted in Figure 4-3 (Stabler, 2000):

$$E(T) = (1 - \max(\omega_{t,E}))E_{20}$$

$$\begin{cases} \omega_{t,E} = 0.2\vartheta - 0.01\vartheta^2 & \text{for } 0 \leq \vartheta \leq 10 \\ \omega_{t,E} = 1.0 & \text{for } \vartheta > 10 \end{cases} \quad (4-12)$$

where E_{20} is the Young's modulus at temperature $T_0 = 20$ °C and $\vartheta = (T - T_0) / 100$ °C is the relative temperature. The dependency (4-12) is implemented in the FE code and it is valid for standard normal strength concrete. As can be observed, it exhibits good agreement with the experimental evidence (Periškić, 2009).

Compressive strength – Concrete

The model assumes the constant compressive strength up to 300°C followed by a linear decrease to approx. 50% of its initial value at 600°C. From a physical viewpoint, this phenomena occurs due the fact that the thermal strains, aggregate locking and frictional phenomena are even more pronounced than at room temperature whereby at high temperatures, concrete strength decreases due to microcracks in the matrix and damage of the cement paste and aggregate.

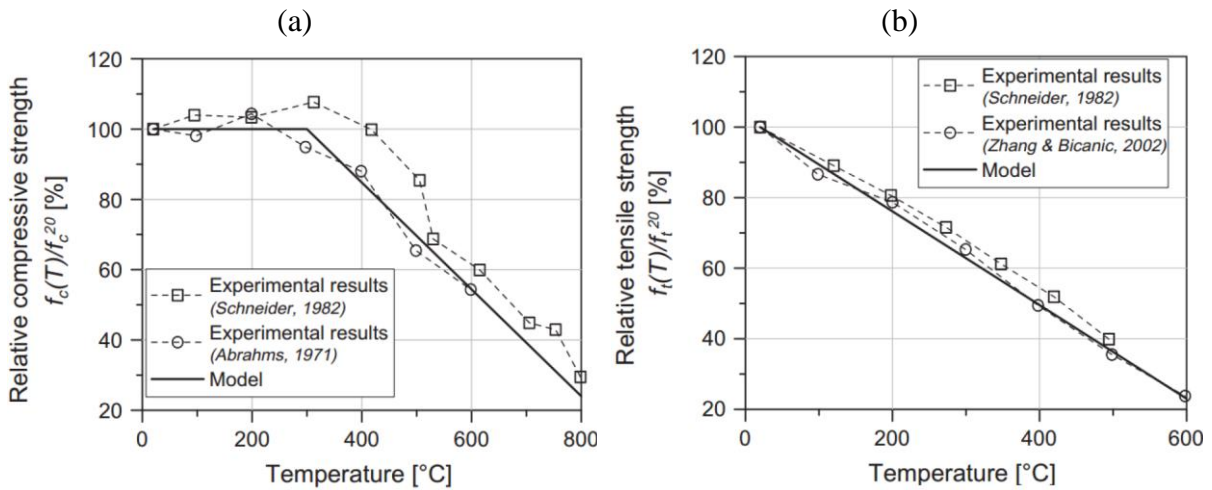


Figure 4-4. Concrete relative compressive (a) and tensile strength (b) as a function of temperature (Ožbolt et al., 2014).

The temperature dependency implemented in the model reads (Periškić, 2009):

$$f_c(T) = \max(\omega_{t,f_c})f_{c,20}$$

$$\begin{cases} \omega_{t,f_c} = 1.0 & \text{for } 0 \leq \vartheta \leq 2.80 \\ \omega_{t,f_c} = 1.43 + 0.153\vartheta & \text{for } \vartheta > 2.80 \end{cases} \quad (4-13)$$

where $f_{c,20}$ is uniaxial compressive strength at $T = 20^\circ\text{C}$. The above exposed relation is plotted together with the experimental data in Figure 4-4a.

Tensile strength – Concrete

The temperature dependency of the concrete tensile strength and its comparison with the experimental data from the literature is shown in Figure 4-4b. The trend shows an immediate decrease of tensile strength, already at 50°C, with temperature increase.

$$f_t(T) = \max(\omega_{t,f_t})f_{t,20} \quad (4-14)$$

$$\omega_{t,f_t} = 1.0 - 0.13\vartheta$$

where $f_{t,20}$ is the uniaxial tensile strength at $T = 20^\circ\text{C}$ and $\vartheta = (T - T_0) / 100^\circ\text{C}$ relative temperature.

Fracture energy – Concrete

In the course of this work, the thermo-mechanical model will account for two temperature dependencies of the concrete fracture energy. The first curve (Model 1) has been implemented by fitting the experimental data obtained by Zhang et al. (2002). The results indicate the increase of fracture energy by 60% up to 300°C followed by the decrease to approx. 90% of its initial value at 600°C . The second curve (Model 2) was obtained by fitting the test data from the fracture energy measurements performed in the framework of this thesis using the three point bending test. The experimental data, as discussed in Chapter 3, show a decreasing tendency with the temperature increase.

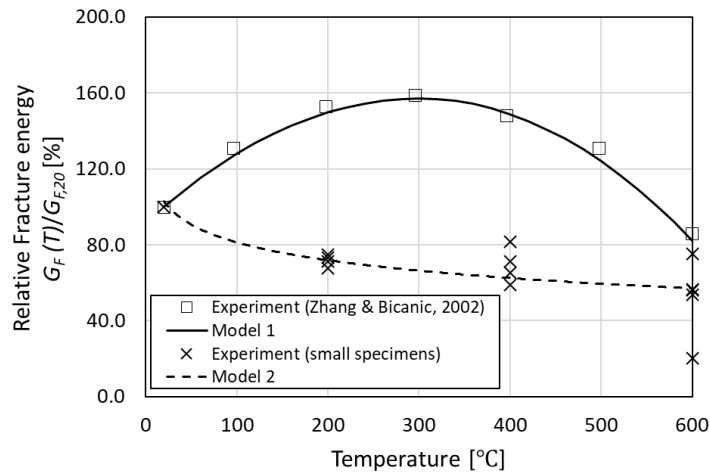


Figure 4-5. Fracture energy as a function of temperature with the implemented curves in the thermo-mechanical model.

Figure 4-5 depicts two curves implemented in the thermo-mechanical model obtained by fitting the test data from the literature and own experimental work. The adopted relation for Model 1 reads (Periškić, 2009):

$$G_F^1(T) = \max(\omega_{t,G_F}^1)G_{F,20}$$

$$\begin{cases} \omega_{t,G_F}^1 = 1.0 + 0.407\vartheta - 0.07272\vartheta^2 & \text{for } 0 \leq \vartheta \leq 2.80 \\ \omega_{t,G_F}^1 = 0.917 + 0.467\vartheta - 0.0833\vartheta^2 & \text{for } \vartheta > 2.80 \end{cases} \quad (4-15)$$

where $G_{F,20}$ is the fracture energy at $T = 20^\circ\text{C}$. The relation representing the second model curve obtained from the experimental investigation on small specimens is assumed to be a scalar function that reads:

$$G_F^2(T) = \max(\omega_{t,G_F}^2) G_{F,20} \quad (4-16)$$

$$\omega_{t,G_F}^2 = -0.0008\vartheta + 1.0888 \quad \text{for } 0 \leq \vartheta \leq 6$$

The test data from the fracture energy measurements of thermally pre-damaged mid-sized concrete specimens in the cold state is given and discussed in chapter 3.

Temperature dependent mechanical properties of steel

As discussed in detail in Chapter 2, the mechanical behavior of steel changes with the increase of temperature. The adopted mechanical relationships dependent on temperature used in the analysis for yield stress and Young's modulus are shown in Figure 4-6. (Periškić, 2009). In both cases a bi-linear reduction with the increase of temperature is adopted.

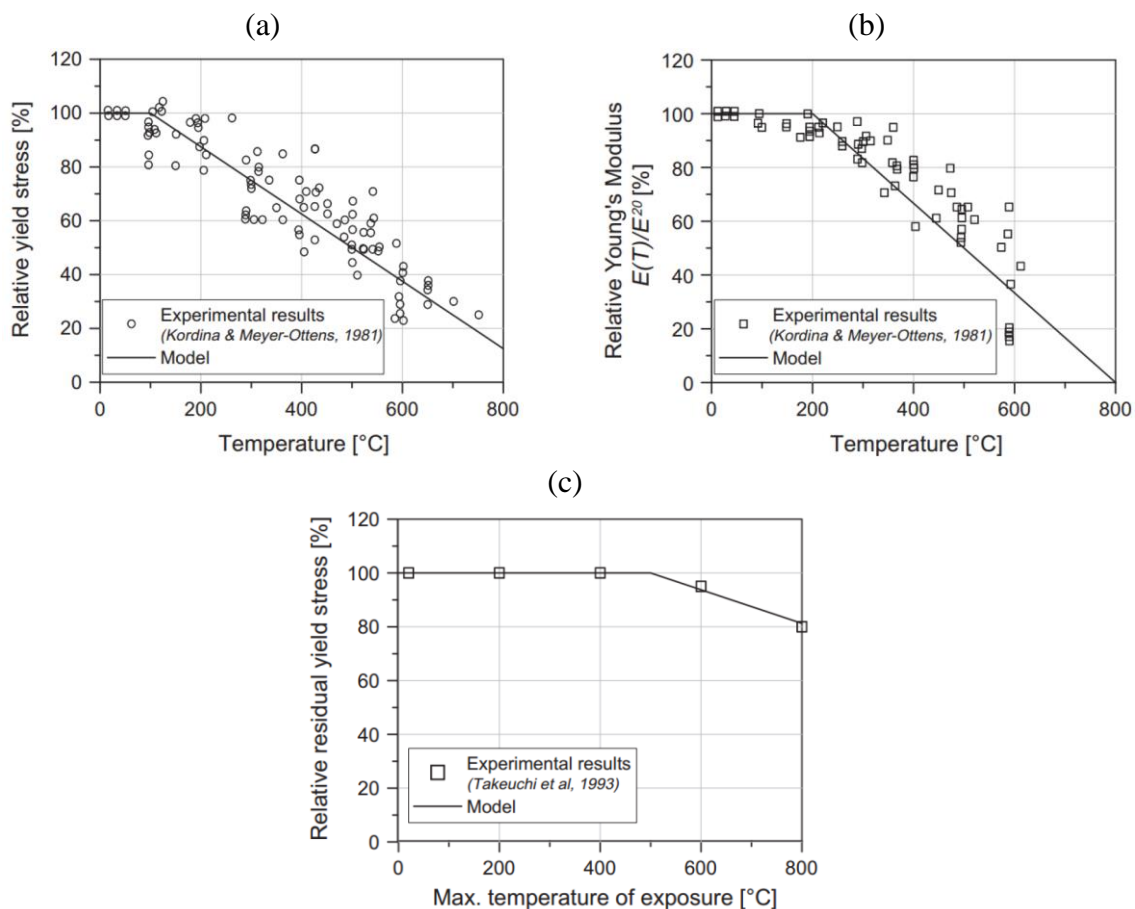


Figure 4-6. The reduction of relative yield stress (a) and Young's modulus (b) of steel with temperature increase and the relative yield stress of steel after recovery upon cooling (c); (Ožbolt et al., 2014).

4.3.2 Thermal strains

Free thermal strains

As already discussed, thermal strains depend on factors such as the type of the aggregate, connection between the aggregate and the cement paste or the chemically bound water in the hydration products. The present model (Periškić, 2009) does not account for the aggregate type, but it gives an average behavior of concrete exposed to temperature. In a stress-free body, it is assumed that the behavior of free thermal strains is isotropic, i.e. equal free thermal strains in all three directions (Cartesian coordinate system). The following equation is implemented into the model (Periškić, 2009):

$$\dot{\sigma}_{ij}^{ft} = \alpha \dot{T} \delta_{ij}$$

$$\text{for } 0 \leq \vartheta \leq 6 \quad \alpha = \frac{6.0 \times 10^{-5}}{7.0 - \vartheta} \quad (4-17)$$

$$\text{for } \vartheta > 6 \quad \alpha = 0$$

where δ_{ij} is the Kronecker delta, whereas the relative temperature ϑ is calculated as follows:

$$\vartheta = (T - T_0)/100^\circ\text{C} \quad (4-18)$$

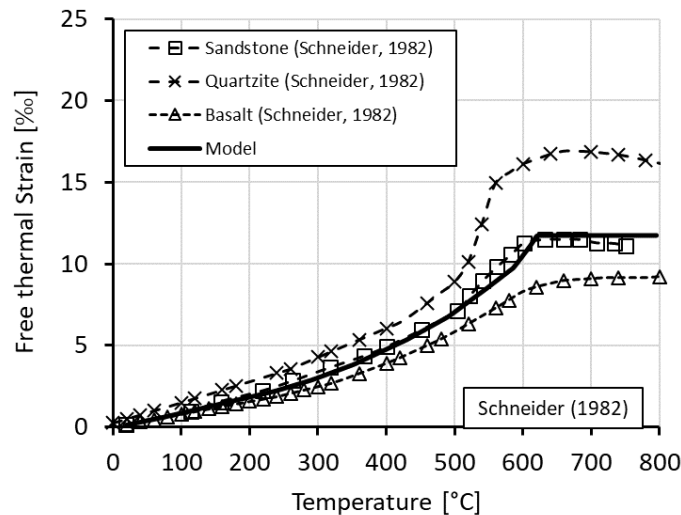


Figure 4-7. Free thermal strain as a function of temperature (adapted from Periškić, 2009) and the implemented curve in the thermo-mechanical model.

Figure 4-7 depicts the free thermal strain as a function of temperature in concretes with different aggregate type (Schneider, 1982) and the function implemented in the thermo-mechanical model. The model curve is, as shown, non-linear up to ca. 600°C and the further increase in temperature has no influence on the free thermal strain.

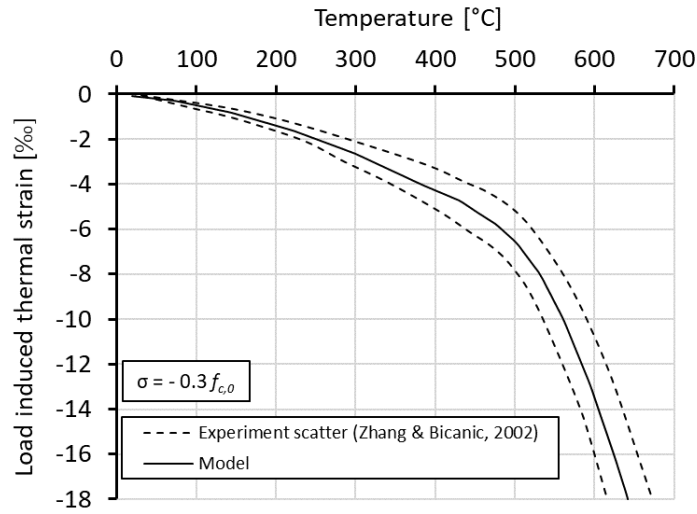
Load induced thermal strains (LITS)

Figure 4-8. Load induced thermal strains as a function of temperature under the compressive load $\sigma = -0.3 f_{c,0}$ (adapted from Periškić, 2009).

The typical curve describing the LITS for $\sigma = -0.3 f_{c,0}$ is shown in Figure 4-8. In the present model, the LITS formation is described with a bi-parabolic thermo-mechanical strain function. The uniaxial (scalar) differential equation of the model is adopted (Periškić, 2009):

$$\dot{\varepsilon}^{lits}(T, \sigma) = \frac{\sigma}{f_{c,0}} \beta \dot{T}$$

$$\beta = 0.01 \begin{cases} 2A\vartheta + B & \text{for } 0 \leq \vartheta \leq \vartheta^* = 4.5 \\ 2C(\vartheta - \vartheta^*) + 2A\vartheta^* + B & \text{for } \vartheta > \vartheta^* \end{cases} \quad (4-19)$$

with ϑ^* describing the dimensionless transition temperature (470°C) between the two expressions for β and $\vartheta = (T - T_0) / 100^\circ\text{C}$, the relative temperature. These two expressions were introduced to account for the sudden change in behavior observed in experiments. A, B and C are constants derived from experiments, which are set in the model to $A = 0.0005$, $B = 0.00125$ and $C = 0.0085$.

4.3.3 Nonlocal temperature model

The temperature in thermo-mechanical models usually comes from the local transient finite element analysis. This is however not always ambiguous when quasi-brittle materials such as concrete are a part of dynamic problem involving high loading rates. To make the thermo-mechanical analysis more objective with respect to the size of the finite elements, a new nonlocal temperature field is introduced. The temperature dependent mechanical properties of concrete are therefore calculated based on the nonlocal temperature.

4.3.3.1 Formulation

The calculation of the nonlocal temperature field follows the same principle as in the nonlocal strain approach (Bažant and Ožbolt, 1990; Jirasek et al., 2005). To alleviate the non-objective temperature influence, e.g. in the region close to the impact region in the dynamic analysis on the mechanical properties, a new nonlocal temperature field, that averages local temperature field in a homogenous continuum, has been proposed. The algorithm uses the temperatures in nodes calculated for a given time step and averages them in the representative volume of the material. The parameter that defines the radius of the averaging volume is the so-called characteristic length l_c of the nonlocal continuum, which is a material property that defines the size of the averaging volume and is determined by the size of the inhomogeneities of the material. (Bažant and Ožbolt, 1990).

The temperature, which is to be averaged, must be chosen such that the nonlocal solution exactly agrees with the local solution in a homogenous temperature field. Firstly, the local temperature variable is calculated based on the input material data and the boundary conditions in each Gauss point of the continuum and subsequently, the nonlocal temperature variable is obtained from the neighboring temperatures in advance defined domain V_R . In order to define the influence of the nonlocal region around a certain point, a suitable weight function has to be introduced. Although a weight function that is uniform over a certain finite representative volume could be used, it is more efficient to use a smooth, Gauss or bell shaped function (Bažant and Ožbolt, 1990). If $T(x)$ is the local temperature variable, then the corresponding nonlocal variable is defined as:

$$\begin{aligned} \bar{T}(x) &= \frac{1}{V_R(x)} \int_V \alpha_n(x, s) f(s) dV(s) = \int_V \alpha_n'(x, s) f(s) dV(s) \\ V_R(x) &= \int_V \alpha_n(x, s) f(s) dV(s) \\ \alpha_n'(x, s) &= \frac{\alpha_n(x, s)}{V_R(x)} \end{aligned} \tag{4-20}$$

where the bar overscript denotes the averaging operator; $\alpha_n(x)$ = nonlocal weighting function; x = coordinates of the averaging point; s = coordinates of the contributing point; V = volume of the entire structure and V_R = representative volume.

After implementing the suitable nonlocal weighting function, the temperature in a point is calculated as an average of temperatures in the surrounding Gauss points. The spatial averaging integral is approximated by a finite sum over all integration points in the representative volume. As will be shown later, this is proved useful in the current model due to the large temperature gradients occurring in the zone around the fire-exposed surface.

4.3.3.2 Weight function

In order to investigate the influence of the weight function on the nonlocal temperature distribution, a parametric study was carried out. Three weight functions were implemented ranging from the largest to the smallest influence of the temperature of neighboring Gauss points (see Figure 4-9).

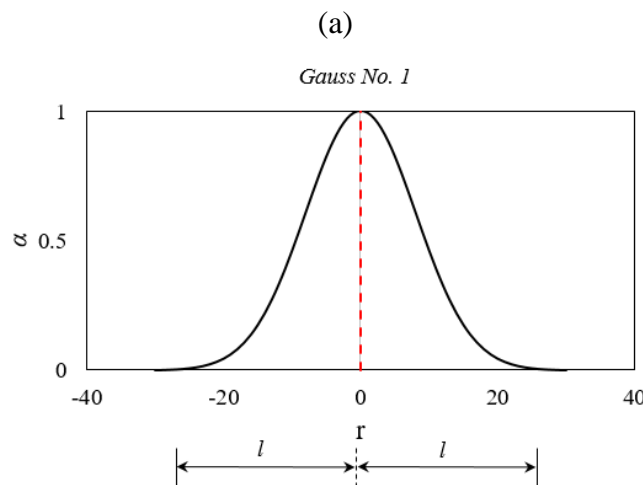


Figure 4-9. Initial weight functions used for the calculation of nonlocal temperature: Gauss No.1 (a), Gauss No. 2 (b) and Bell-shaped (c).

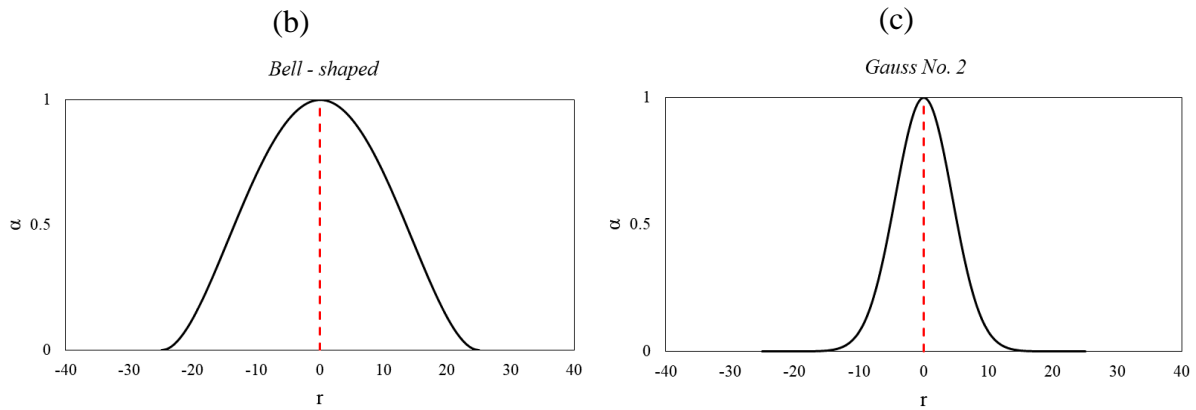


Figure 4-9. (Continued).

A concrete column with dimensions of 300x300x600 mm was utilized in the simulations. The column was discretized with 8-noded solid elements with 15 mm in size. The column's bottom nodes were constrained in the vertical direction and each side was exposed to elevated temperature (red surfaces in Figure 4-10). The column was initially exposed to 15 mm fire duration according to ISO 834 fire curve. The temperature distribution was measured along the cross-section of a concrete column after the heating phase.

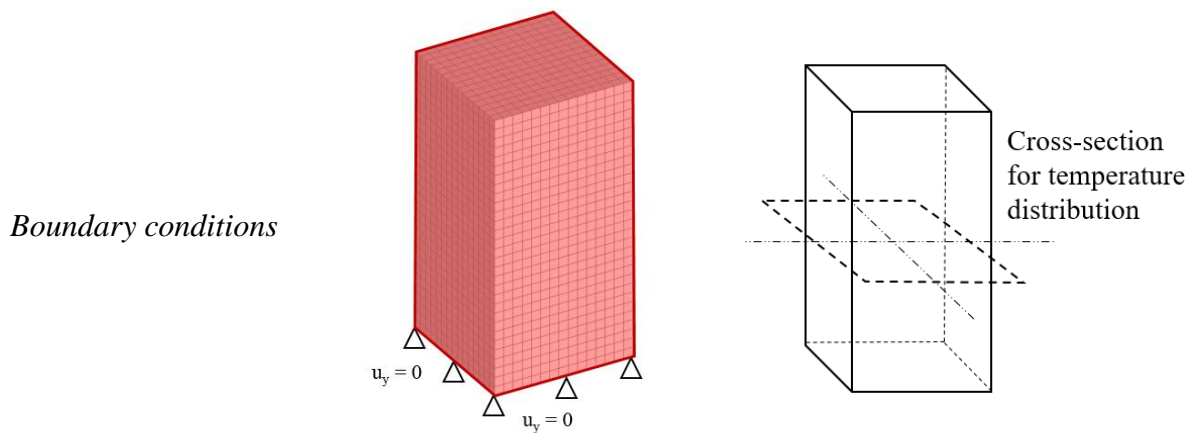


Figure 4-10. The boundary conditions employed in the numerical analysis and the display of the cross-section for the temperature evaluation.

Figure 4-11 shows the results in terms of temperature distribution as a function of the cross-section distance (mid-height of the specimen). The effect of the nonlocal temperature can be observed only in the region close to the surface since these values deviate from their corresponding local values. Therefore, the effect of minimizing the temperature influence on the material properties only in the surface zone (impact zone) is achieved, where large localization of damage can occur due to large temperature gradients.

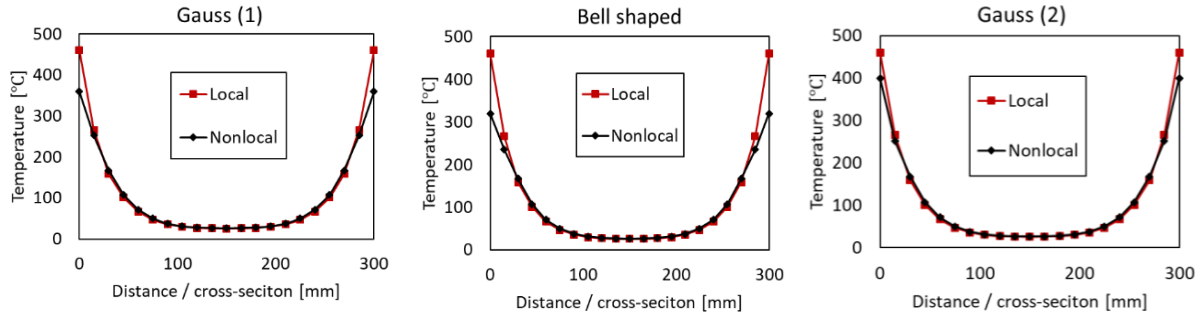


Figure 4-11. Influence of different shape functions on the temperature distribution across the cross-section of the model.

It can be seen that the model with the first Gauss function exhibits a median value of surface temperature in comparison with the other two functions. Consequently, the first modified Gauss distribution function is adopted as a nonlocal weighting function:

$$\alpha_n(r) = \exp\left(-\left(2.1989 \frac{r}{l_c}\right)^2\right), \quad r = |s - x|; \quad l_{ch} = 3d_{ag} \quad (4-21)$$

where l_c represents the characteristic length, which is assumed to be approximately three times maximum aggregate size ($l_{ch} = 3d_{ag}$). Note that if the size of the finite elements is significantly larger than the characteristic length, the nonlocal and local temperatures are the same. Furthermore, free thermal strains and load induced thermal strains are also calculated based on the nonlocal temperature, i.e. in Equation (4-11) T is replaced with \bar{T} . The main effect of the nonlocal temperature \bar{T} is obvious at the exposed concrete surface if the FE are very small. In such situations the surface elements get unrealistically damaged and the load transfer from the exposed surface of concrete will possibly not take place.

4.4 3D FE analysis

In the present work, the thermo-mechanical model for concrete is used. The model employs the temperature dependent microplane model as constitutive law for concrete and it is formulated within the framework of continuum mechanics based on the principles of irreversible thermodynamics. The nonlinear three-dimensional (3D) analysis of concrete and reinforced concrete (RC) structures is performed in the finite element (FE) program MASA. For given geometry and material data, FE mesh is generated and the initial and boundary conditions for the calculation are defined. The pre- and post-processing is performed in the commercial program FEMAP (Siemens PLM Software, 2016).

4.4.1 Static analysis

The static analysis is of implicit type, based on the secant stiffness matrix (Belytschko et al., 2001). The finite element formulation is the total Lagrange formulation. The equilibrium between external and internal forces [Eq. (4-22)] is obtained iteratively by employing Newton-Raphson iterative scheme:

$$[K_S]\{u\} + \{f_e\} = 0 \quad (4-22)$$

where $[K_S]$ is the stiffness matrix, u are the nodal displacements and f_e are the external nodal forces.

Damage and cracking are modelled in the framework of smeared crack approach which means that the crack is smeared over a row of finite elements. To assure the objectivity of the analysis with respect to the size of the finite elements the crack band method is used (Bažant and Oh, 1983). Furthermore, it should be noted that the area under the compression or tension stress-strain curves multiplied by the mean element size h , should correspond to the compression or tension fracture energy, respectively.

4.4.2 Nonstationary (transient) thermal analysis

The transient incremental analysis consists of two parts: (i) the evaluation of temperature distribution (thermal part) and (ii) the calculation of stresses and strains due to degradation of mechanical properties as a consequence of elevated temperature and mechanical loading. The load increment is defined as a time step in which the boundary conditions, such as ambient temperature or load, change stepwise. In the present model, it is assumed that during the load increment the temperature remains constant. Consequently, the temperature-dependent material properties are also constant during the time step.

The non-mechanical part of the problem is solved using direct integration scheme of implicit type, whereas the equilibrium between external and internal forces is obtained iteratively by employing the Newton-Raphson iterative scheme, the same as in static analysis. After completion of the second calculation step (mechanical part), the distributions of the stresses and strains are known. The procedure described above (staggered solution scheme) is repeated for each further time step Δt , until the specified total time t is reached.

The first step towards the coupling of the mechanical concrete properties and the temperature is the calculation of temperature distribution in a continuum (body). In each time step t , the energy conservation in the volume Ω , which is described in Cartesian coordinates, has to be fulfilled (Ožbolt et al., 2005b):

$$\lambda \Delta T(x, y, z, t) + W(x, y, z, t, T) - c\rho \frac{\partial T}{\partial t}(x, y, z, t) = 0 \quad (4-23)$$

with T = Temperature, λ = Heat conductivity, c = specific heat capacity, ρ = density of the material, W = internal heat source (if any, e.g. for hydration processes), Δ = Laplace operator.

Two basic thermodynamic boundary conditions govern the solution of the Eq (4-23), the Neumann boundary condition, where the values of the derivative are specified on the boundary domain (e.g. the heat flux) and the Dirichlet condition that specifies the fixed boundary solution (e.g. the surface temperature). The spatial boundary conditions can be described with Newton-type transition law:

$$\lambda \frac{\partial T}{\partial \mathbf{n}} = \alpha_h (T_M - T) \quad (4-24)$$

where \mathbf{n} = normal on the concrete surface, α_h = heat transfer coefficient, T_M = Temperature of the medium, to which the surface of the concrete volume is exposed to (e.g. air temperature). The temperature distribution is calculated in the current load step by solving differential Eq. (4-23) considering the thermal boundary condition defined by Eq. (4-24).

In order to solve the differential Eq. (4-23) numerically using the finite element method, it must first be rewritten into an integral (weak) form (Belytschko et al. 2001). If the test function is considered as stationary, the following system of linear equations is obtained (Voight notation):

$$[C]\{\dot{T}\} + [K]\{T\} = \{R\} \quad (4-25)$$

$$\text{with:} \quad [K] = \int_{\Omega} b[B]^T [\lambda][B] d\Omega + \int_{\Gamma} \alpha [N]^T [N] d\Gamma \quad (4-26)$$

$$\text{and:} \quad [C] = \int_{\Omega} c\rho [N]^T [N] d\Omega; [R] = \int_{\Gamma} [N]^T \alpha T_M d\Gamma \quad (4-27)$$

where $[N]$ is the matrix that couples the temperature field with the nodal temperatures, $[B]$ represents the connection between the temperature gradient field and the nodal temperatures, b is the thermal conductivity, F is the surface area of unit volume and Ω is the unit volume. The non-stationary, linear Eq. (4-25) is solved with a direct Crank-Nicholson integration procedure with a backward difference coefficient applied ($\beta = 1$), which leads to unconditional numerical stability. In the direct integration method, the following relationship is assumed for the solution in the $(r + 1)^{th}$ step:

$$\{T\}_{r+1} = \{T\}_r + \Delta t \left((1 - \beta)\dot{T}_r + \beta\dot{T}_{r+1} \right) \quad (4-28)$$

where T denotes the temperature and t is time.

After the temperature distribution is calculated, the thermo-mechanical coupling is performed. It is important to note that the cracks and damage in concrete do not influence the temperature distribution in the structure (Ervin et al., 2012).

4.4.3 Transient dynamic analysis

In the 3D transient explicit dynamic FE analysis the system of unknown displacements in each time step t is calculated by solving the following system of equations (Voigt notation) (Ožbolt et al., 2011):

$$[M]\{\ddot{u}(t)\} + [C]\{\dot{u}(t)\} + \{f(t)\} = 0 \quad (4-29)$$

where $[M]$ is the mass matrix, $[C]$ is the damping matrix, \ddot{u} are nodal accelerations, \dot{u} are nodal velocities and f are the resulting nodal forces. The resulting nodal forces are calculated as:

$$\{f(t)\} = \{f^{ext}(t)\} - \{f^{int}(t)\}$$

with: $f^{ext}(t)$ = external nodal forces (4-30)

and: $f^{int}(t)$ = internal nodal forces

The system of Eqs. (4-29) is solved using an explicit direct integration scheme (Belytschko et al., 2001). The external nodal forces are known nodal loads. The internal nodal forces are unknown and they are calculated by the integration of the stresses over the finite elements. In

the FE code used in the numerical study the mass and damping matrices are assumed to be diagonal (Ožbolt et al., 2011).

4.5 Conclusions

In the present chapter, the topics related to the solving of boundary value problem in thermo-mechanical FE analysis are briefly discussed: (i) the used thermo-mechanical model based on the microplane model for concrete is presented and the brief summary of 3D FE procedure employed in the mechanical and thermal analysis is provided; (ii) the implemented rate-dependent thermo-mechanical microplane model is further developed by introducing a nonlocal temperature field and the method of obtaining the nonlocal temperature is discussed; (iii) as will be demonstrated on numerical example, substituting the nonlocal temperature field results in higher objectivity of the simulation at the loading surface of concrete.

5. INFLUENCE OF EXPERIMENTALLY OBTAINED FRACTURE ENERGY ON DYNAMIC RESPONSE OF THE CT SPECIMEN

5.1 Introduction

The aim of the present numerical study was to investigate the dynamic response of the compact tension (CT) specimen using the experimentally obtained fracture energy as a function of temperature, implemented in the rate sensitive thermo-mechanical model. The influence of the loading rate and temperature on the response of the CT specimen has been already thoroughly investigated, numerically and experimentally (Ruta, 2018; Ožbolt et al., 2013). However, the obtained peak reactions from the FE analysis at higher temperature levels did not correspond well with the experiment. This inconsistency of the obtained reactions in terms of displacement rate can be possibly contributed to the temperature dependence of fracture energy that was implemented in the original thermo-mechanical model (Periškić, 2009).

Ožbolt et al. (2013) performed a numerical study where the response of the thermally undamaged CT specimen under dynamic load was investigated, which was later validated experimentally. Ruta (2018) used the same geometry and boundary conditions to investigate the influence of temperature on the dynamic response of the CT specimen. The temperature dependency of fracture energy used in the preceding FE analyses was taken from Zhang & Bićanić (2002). As specified in Ruta (2018), the influence of the loading rate with increasing temperature was significantly less pronounced in the tests than in the numerical investigations. The tests show, as illustrated in Figure 5-1, that at a temperature of 400°C there is practically no influence of the loading rate on the resistance. This is explained by the fact that at this temperature the concrete becomes more brittle and therefore the influence of inertia on the resistance becomes relatively small (as is the case with brittle materials, e.g. glass). Although the numerical results show the same tendency in principle, the influence of the loading velocity is much more pronounced than in the tests. Therefore, the aim of the presented numerical parametric study was to investigate the influence of fracture energy under elevated temperatures on the dynamic response of the CT specimen. As discussed before, based on very few experiments (Zhang and Bićanić, 2002), in the original model it is assumed that up to the temperature of about 350°C the fracture energy increases and then decreases. The question is whether this is possibly the reason for the differences between the numerical and experimental results. It was recently reported that with increasing temperature the fracture energy decreases continuously, similar to the tensile strength (Barragan et al., 2001). In this manner, a new

numerical study is performed where the dynamic response of the CT specimen together with the experimentally obtained fracture energy (see Section 3) was compared with numerical and experimental results from the initial investigation (Ruta, 2018). In the experimental tests, the CT specimens were first exposed to the temperatures of 200°C and 400°C, cooled down to room temperature and then dynamically loaded at various loading rates until failure.

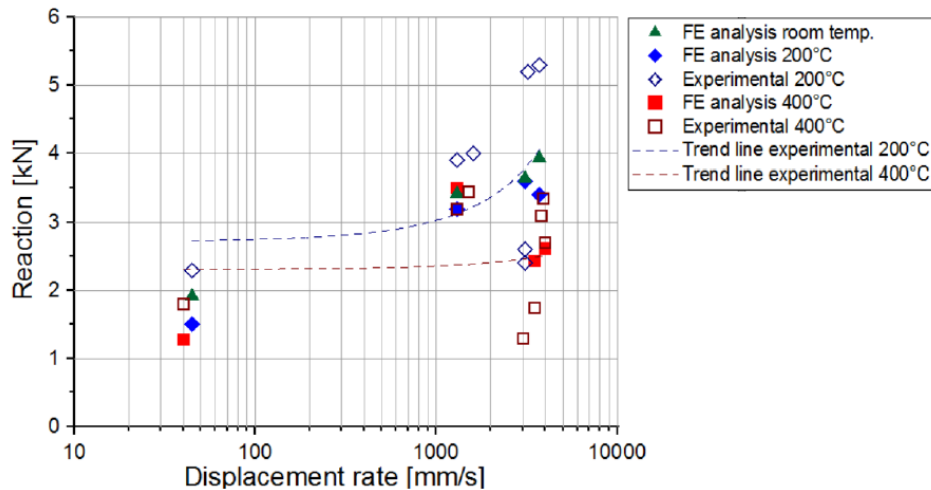


Figure 5-1. Numerically and experimentally obtained peak reactions as a function of the displacement rate for thermally undamaged, pre-damaged at 200°C and 400°C obtained both (Ruta, 2018).

5.2 Experimental studies of plain concrete CT specimen subjected to thermal and dynamic loading

Following the experimental and numerical study on dynamic fracture of thermally undamaged CT specimens carried out by Ožbolt et al. (2013), Ruta (2018) investigated the influence of the temperature on the dynamic response of the CT specimens. Experimentally tested plain concrete CT specimens without thermal preloading showed a very good agreement with the numerical analysis. However, as already mentioned, the dynamic response of thermally pre-damaged CT specimens in the numerical study exhibited some deviation from the experimental investigation. To investigate the influence of the temperature dependent fracture energy on the dynamic response of the CT specimen, the FE model and boundary conditions utilized in the present numerical study were adopted from the experimental investigations of Ruta (2018), hence a brief summary of the experimental work is here discussed.

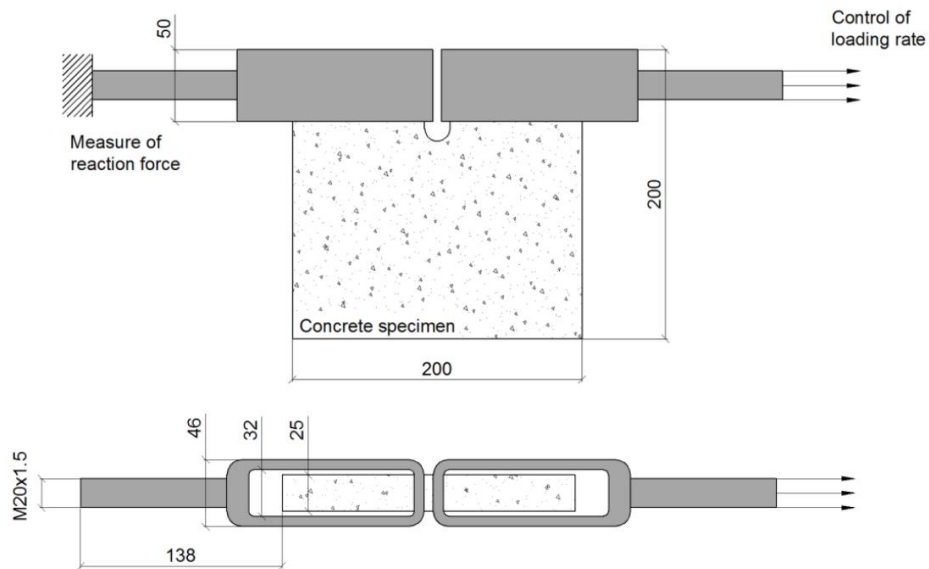


Figure 5-2. Dimensions and the boundary conditions of the experimentally investigated CT specimen (Ožbolt et al., 2013; Ruta et al., 2018).

The experimentally tested CT specimens were constrained vertically on one side to the top of the loading machine with the help of a steel frame (depicted with the dark grey color in Figure 5-2), where the reaction forces were monitored. The load was applied on the other steel frame attached to the second half of the CT specimen in the direction opposite to the constrained frame.



Figure 5-3. Strain gauges placed on the CT specimen and the experimental setup (Ruta, 2018).

For the evaluation of crack patterns and the crack propagation velocity, optimal visual and recording conditions were provided. The test setup was equipped with two different cameras, Photron Fastcam APX RS for studying the crack propagation velocity in the crack notch tip and an additional camera to record the global cracking process of the complete area on the specimen (Figure 5-3). The experiment was carried out using the following procedure (Ruta, 2018). The CT specimens were initially heated in an oven in two sets, test series A (to 200 °C) and test

series B (to 400 °C) with an additional set of thermally undamaged specimens that was set aside for obtaining reference values. In all cases, a heating rate of 1°C/min was supplied in the oven (Figure 5-4). When the temperature reached the prescribed temperature, it was kept constant for 90 minutes to assure the uniform temperature distribution across the cross-section of the specimen. In the final step of the thermal phase, the specimens were naturally cooled down inside the oven. Subsequently, the oven doors were unlatched and the specimens were let to cool down to the room temperature.

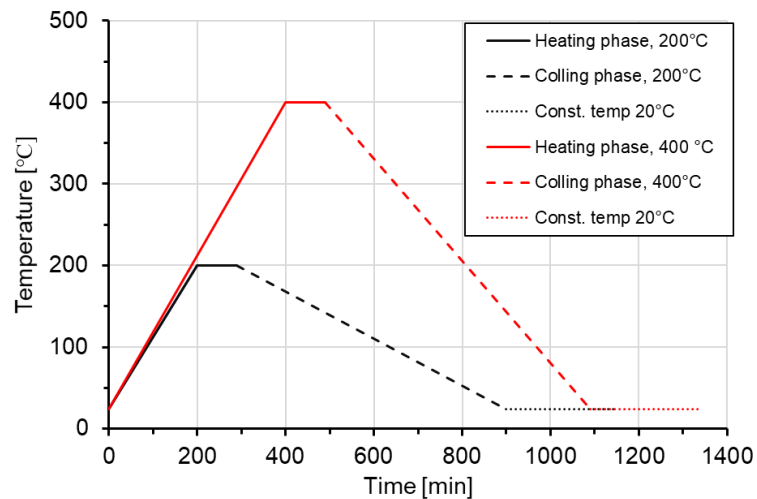


Figure 5-4. The thermal phase carried out in the experiment (Ruta, 2018).

In the second phase, dynamic loading with four different loading rates was applied on one metal frame attached to the specimen. The reaction time curves for different thermal exposures and loading rates from the experiments are shown in Figure 5-5 and the typical crack patterns are shown in Figure 5-6.

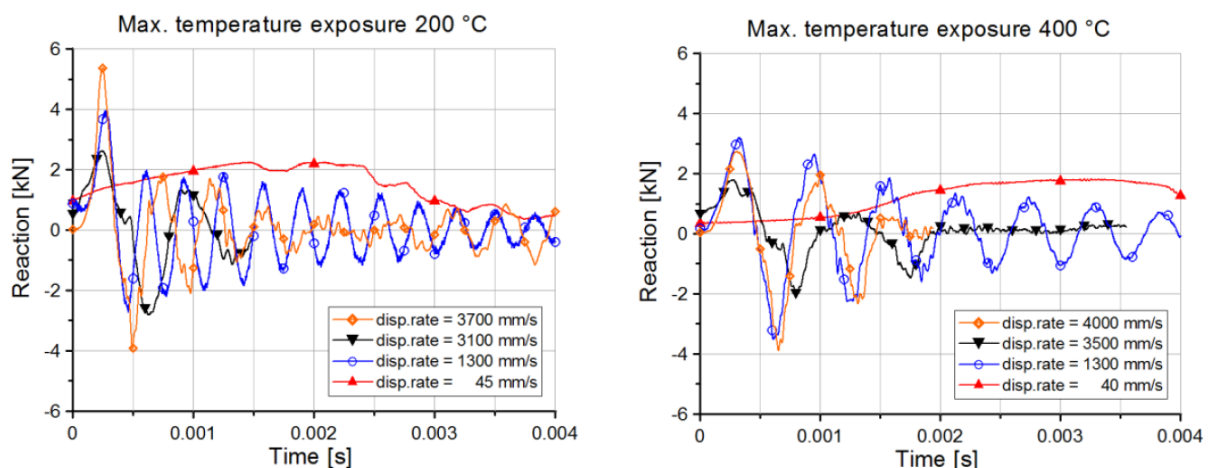


Figure 5-5. Experimentally obtained reaction time histories for thermally predamaged CT specimens at 200°C and 400°C (Ruta, 2018).

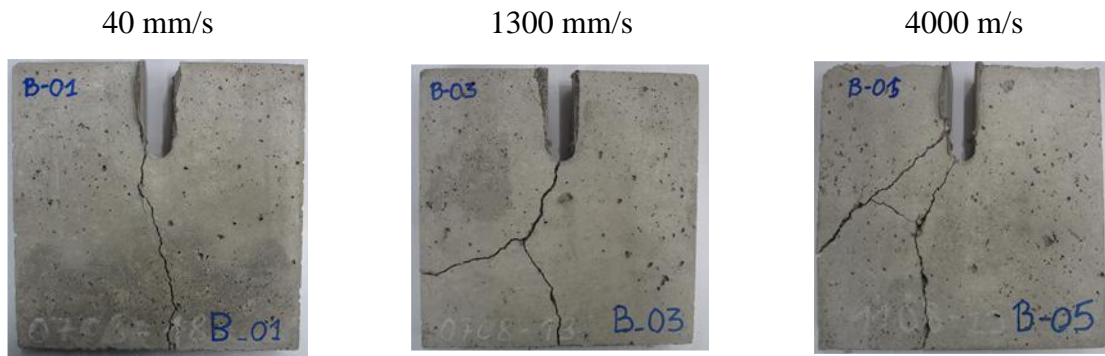


Figure 5-6. Crack patterns observed in the experiments for thermally pre-damaged CT specimens at 400°C loaded with different displacement rates (Ruta, 2018).

5.3 FE analysis of CT specimens

5.3.1 FE discretization and material properties

To compare the numerical results of both present and preceding numerical studies, the geometry, boundary and initial conditions were taken from the aforementioned experimental tests (Ruta, 2018). The finite elements utilized in the analysis are 4-node linear strain tetra elements, as shown in Figure 5-7. The model is, as in the experimental setup, constrained on one and loaded in the opposite direction at the end of the other metal profile. The thermal load is applied on all concrete surfaces facing outwards and corresponds to the experiment as well. The finite element analysis was carried out using the rate sensitive thermo-mechanical model for concrete.

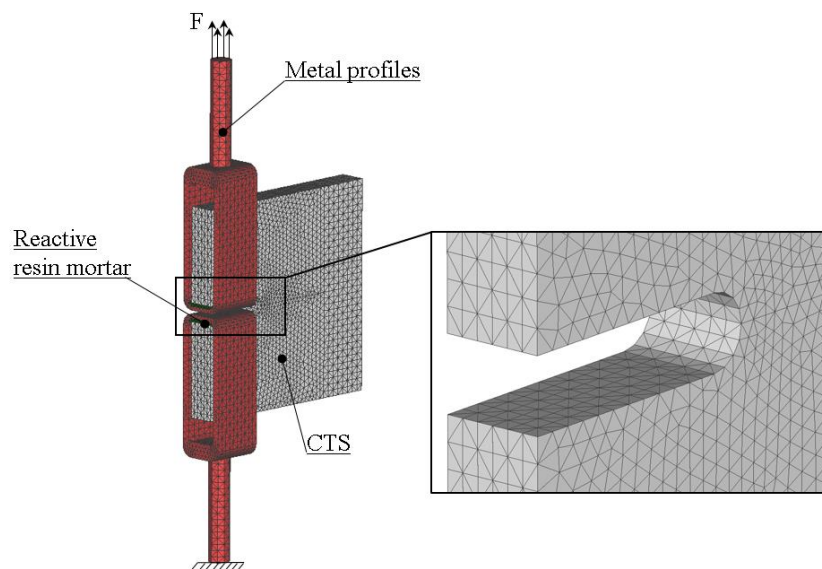


Figure 5-7. Discretized FE model with 4-node linear strain elements and a detailed view of the elements around the notch tip.

The discretization was performed uniformly in the steel material, while the number of elements around the concrete notch zone was larger than in the peripheral areas. In the notched zone, the

nodes on the concrete surface are in full contact with the nodes of the steel profiles. In Table 5-1, the mechanical and thermal properties of concrete and steel materials used in the simulations are summarized. The material parameters that have been utilized in the FE analysis were the same as in the experiment. The temperature dependent thermal conductivity and heat capacity are taken according to Eurocode 2 (EN 1992-4: Part 4, 2015).

Table 5-1. Mechanical and thermal properties of steel and concrete material used in the numerical simulation of the CTS.

<i>Property</i>	<i>Steel</i>	<i>Concrete</i>
ρ [kg/m ³]	7800	2130
E [MPa]	210000	33140
f_c [MPa]	-	39.17
f_i [MPa]	-	2.97
G_F [N/m]	-	52.0
ν [-]	0.33	0.18
c_p (J/kgK)	490.0	900
λ (W/mK)	43.0	1.36

5.3.2 Results of the numerical analysis

To investigate the influence of fracture energy on the dynamic response of the CT specimens, a 3D FE numerical study has been carried out using the proposed temperature dependent G_F obtained for small specimens (see Chapter 3) that was implemented into the FE code. A total of 16 simulations have been performed under different loading conditions matching the experimental setup in the preceding experimental study (Ruta, 2018). The numerical analyses consist of two steps: (i) transient-thermal analysis is carried out to obtain the temperature distribution in the CT specimen and (ii) an explicit dynamic analysis is performed where the specimen is subjected to four displacement rates: 45, 1300, 3100 and 3700 mm/s. The specimens were loaded in the cold state, i.e. before loading they had been cooled down to the ambient temperature. The summary of the simulations is given in Table 5-2.

Table 5-2. List of investigated cases in the numerical study.

Target temperature	Applied displacement rate [mm/s]			
	Experimental and numerical (Ruta, 2018)	G_F dependency on the temperature	Numerical (Present work)	G_F dependency on the temperature
20°C	45; 1300; 3100; 3700	increase - decrease	45; 1300; 3100; 3700	descending
200°C	45; 1300; 3100; 3700	increase - decrease	45; 1300; 3100; 3700	descending
400°C	45; 1300; 3100; 3700	increase - decrease	45; 1300; 3100; 3700	descending

5.3.2.1 Dynamic behavior of thermally undamaged CT specimen

The first set of simulations were aimed to obtain the reference values of peak reactions and fracture patterns from the dynamic analysis of thermally undamaged CT specimens. Since the used fracture energy at ambient conditions was the same as in the previous simulations (Ruta, 2018), the results of the analysis are therefore identical. Typical reaction history response and failure modes are shown in Figure 5-8 and Figure 5-9, respectively.

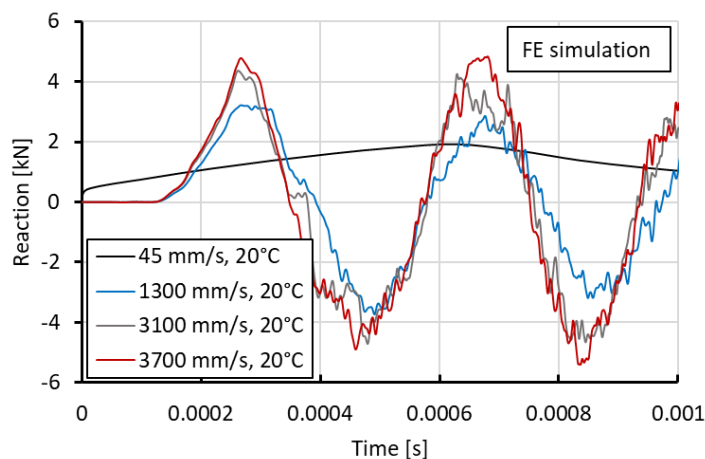


Figure 5-8. Measured reactions in terms of reaction-time histories for thermally undamaged CTS with four displacement rates: 45, 1300, 3100 and 3700 mm/s.

A strong increase in reaction peaks with the increase of loading rate can be observed from Figure 5-8. This rise can be attributed to the effect of inertia and not to a real material strength increase (Ožbolt et al., 2013). The red zones in Figure 5-9 represent cracks, in terms of maximum principal strains, which correspond to the crack width equal or greater than $c_w = 0.1$

mm. With the increase of loading rate, the failure mode changes. At displacement rate of 1300 mm/s crack branching can be observed in the direction of the applied load.

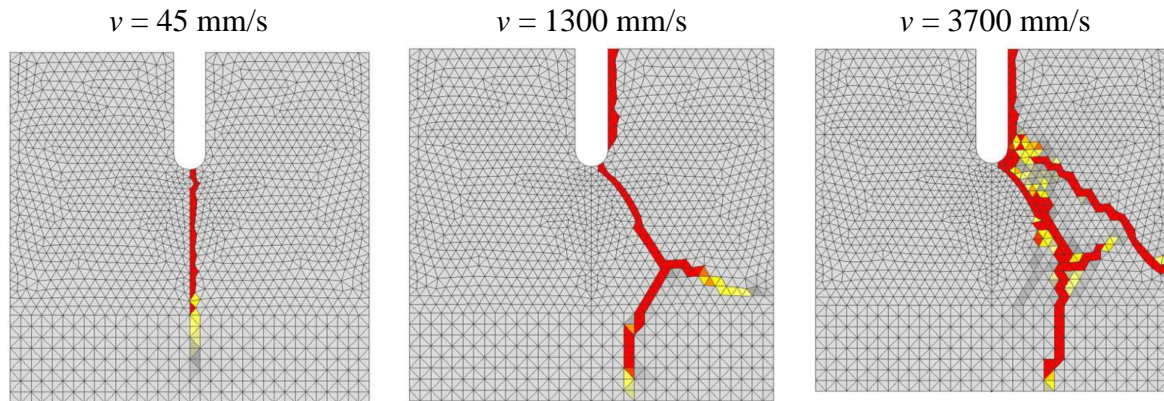


Figure 5-9. Fracture patterns for loading rates of 45, 1300 and 3700 mm/s (red zones = maximum principal strain that corresponds to crack width of 0.1 mm).

5.3.2.2 Dynamic behavior of thermally pre-damaged specimen (200°C)

Experimentally obtained fracture energy exhibited a descending tendency with the temperature increase. In this example, a quantitative comparison of the results from the numerical analyses carried out with the fracture energy according to Zhang and Bićanić (2002) and the experimentally obtained one is presented. Both numerical cases are compared with the experiment.

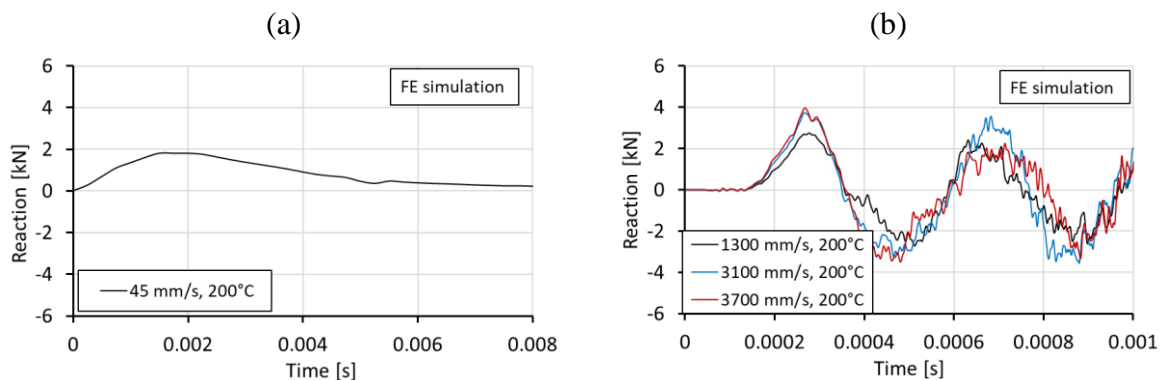


Figure 5-10. Measured reactions in terms of reaction-time histories for thermally pre-damaged CTS at 200°C.

Figure 5-10 shows the results given in terms of reaction – time histories. Comparing the dynamic response of CT specimens at ambient temperature and 200°C, the thermally pre-damaged specimens exhibited lower values in terms of reaction and displacements. From Figure 5-10, it can be observed that although the maximum reaction increases with the increase of displacement rate, it is less expressed than in the case at 20°C.

Table 5-3. Calculated fracture parameters from the static and dynamic analysis of thermally pre-damaged CTS at 200°C measured at the onset of cracking.

Displacement rate (mm/s)	Tensile strength (N/mm ²) (Ruta, 2018)	Strain rate (1/s) (Ruta, 2018)	Fracture energy (N/m) (Ruta, 2018)	Tensile strength (N/mm ²) Present work	Strain rate (1/s) G_F Present work	Fracture energy (N/m) Present work
Static	1.86	-	31.7	2.01	-	21.41
45	2.65	1.28	48.4	2.25	2.52	29.0
1300	2.88	79.81	51.6	3.17	77.28	32.06
3100	2.94	99.94	53.9	3.19	105.81	31.27
3700	2.91	108.4	51.9	3.2	122.67	32.53

Figure 5-11 represents the numerically obtained maximum principal strains and stress curves in time at the crack tip, which were used for obtaining the values given in Table 5-3. The strain rate $d\varepsilon/dt$ was calculated as a tangent of the strain –time curve at a point where the maximum principal stress reached its peak value on the onset of cracking. Fracture energy was obtained as the area under the stress-strain curve of the same finite element. The principal stress curves do not exhibit any increase in the true strength with the increase of the loading rate. Note that the stress at the start of dynamic analysis is not equal to zero due to the thermally induced stresses after cooling.

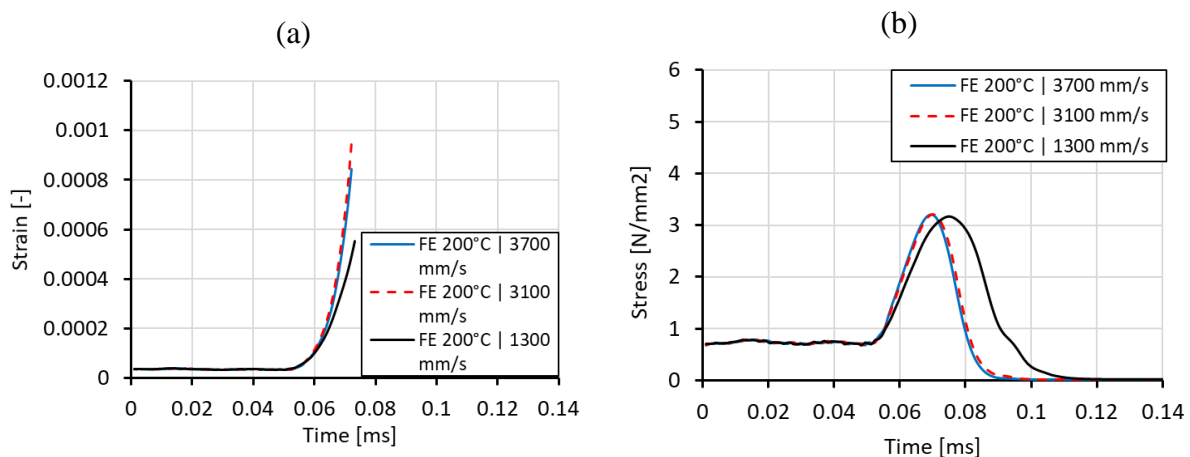


Figure 5-11. Numerically obtained: maximum principal strains (a) and maximum principal stresses (b) for three loading rates at 200°C measured at the onset of cracking.

The previous numerical analyses (Ruta, 2018) exhibit similar values in terms of tensile strength. However, the strain rate and fracture energy values differ from the values obtained in the present numerical analysis. The reason for this is the continuously decreasing nature of fracture energy

with temperature increase. Figure 5-12 illustrates the crack patterns of thermally pre-damaged CT specimens at 200°C from the experimental tests, previous and the present numerical study (red zones are the maximum principal strains, which correspond to the crack width equal or greater than 0.1 mm).

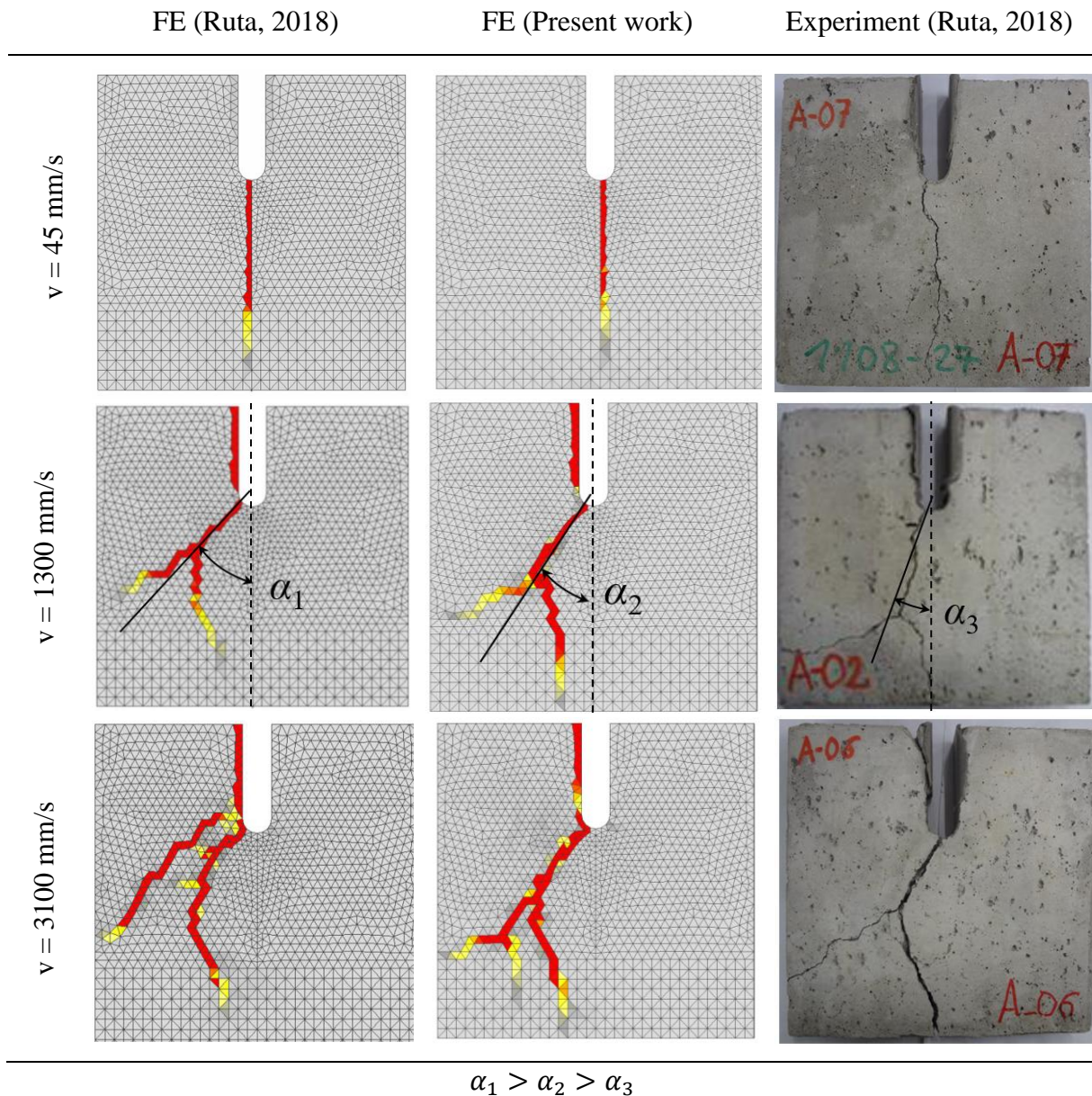


Figure 5-12. Numerically calculated and experimentally obtained crack patterns for thermally pre-damaged CT specimens at 200°C (red zones are the maximum principal strains, which correspond to the crack width equal or greater than 0.1 mm).

Compared to the preceding numerical analysis, the crack pattern at 1300 mm/s indicates that the G_F already exhibited some effect on the dynamic response of the CT specimen, showing a smaller inclination angle between the midline of the specimen and the crack direction before it branches. It is especially interesting to observe the behavior of the crack path at the displacement rate of 3100 mm/s. In the experimental work the crack path propagates in the form

of a straight line until it reaches the critical crack velocity and the crack branching occurs. Comparing this with the numerically calculated crack patterns, the present numerical analysis correlates better with the experimentally obtained crack path. Figure 5-13 shows the comparison for the numerically obtained reaction time histories of dynamically loaded CT specimens at 200°C with the experiment and previous simulations (Ruta, 2018). The reactions from the present study show a very good agreement and converge better with the experiment, not only in the magnitude but in the period of oscillation as well.

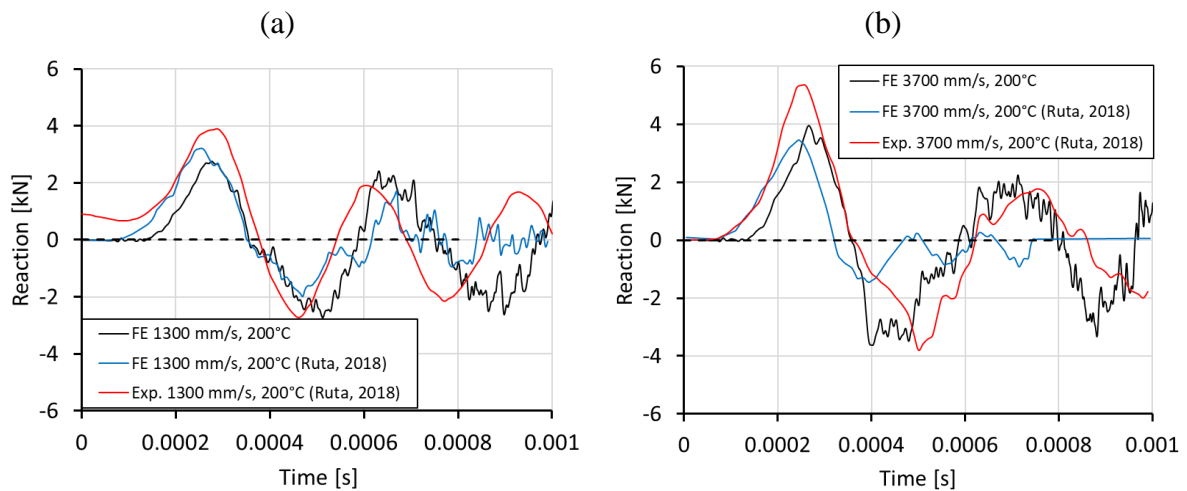


Figure 5-13. Comparison of numerically and experimentally obtained reaction time histories from the present analysis and from the analysis performed by Ruta (2018) for the thermally pre-damaged CT specimens at 200°C with displacement rates of 1300 mm/s (a), 3700 mm/s (b).

In Table 5-4, the summary of reaction forces obtained from the numerical and experimental work of the preceding study and from the present numerical analysis is given. Although the reactions deviate in both cases from the experimental values, for some displacement rates (45 and 3700 mm/s), the present study agrees better with the experiment.

Table 5-4. Experimentally and numerically obtained reaction values at 200°C.

Displacement rate [mm/s]	Reaction forces (Ruta, 2018) [kN]		Reaction forces [kN] - present work
	Experimental	Numerical	
static	-	0.99	1.1
45	2.3	1.5	1.81
1300	3.9	3.2	2.70
3100	2.6	3.6	3.72
3700	5.3	3.4	3.94

5.3.2.3 Dynamic behavior of thermally pre-damaged specimen (400°C)

The here employed fracture energy, in terms of relative values at 400°C, is at 70% of its initial value at 20°C, while the fracture energy used in the previous numerical analyses had a 30% increase compared to its reference value at room temperature. Figure 5-14 depicts the reaction – displacement curves of thermally pre-damaged CT specimens at 400°C where it is shown that, however small, with the increase of loading rate, an increase in reactions can be observed as well.

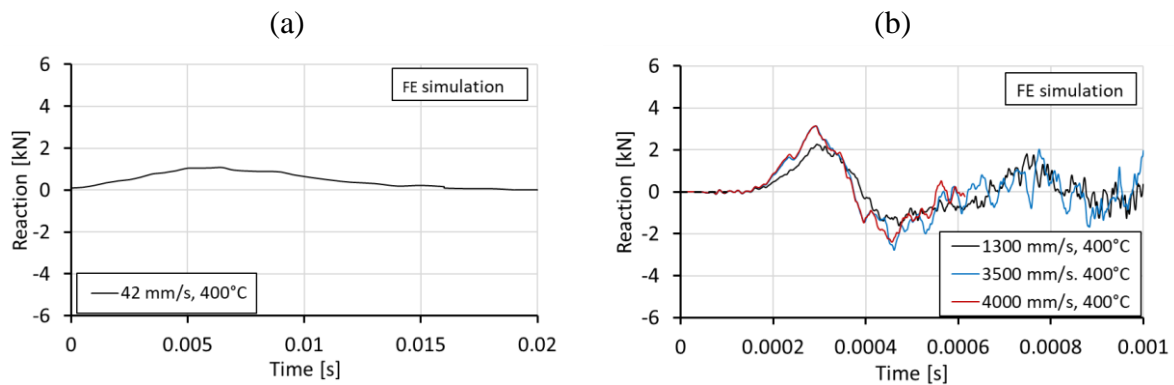


Figure 5-14. Measured reactions in terms of reaction-time histories for thermally pre-damaged CTS at 400°C.

Table 5-5 summarizes the values of tensile strength, strain rates and fracture energies at the onset of cracking for different displacement velocities of the CT specimen thermally pre-damaged at 400°C. The values were obtained using the curves shown in Figure 5-15. The fracture energy is much lower compared to the values from the previous numerical study. This is in correlation with the descending pattern of fracture energy with the temperature increase.

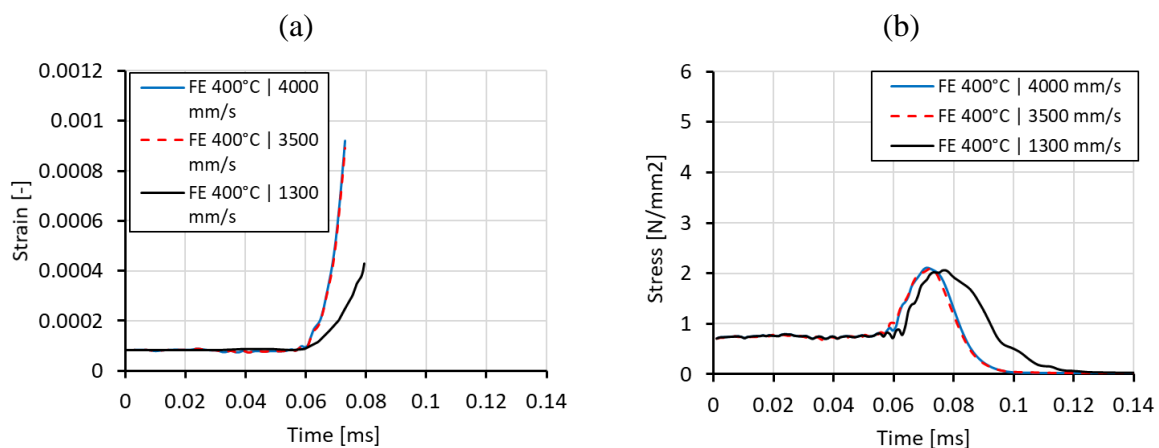


Figure 5-15. Numerically obtained: maximum principal strains (s) and maximum principal stresses (b) for three loading rates at 400°C, measured at the onset of cracking.

The strain rates are in a good agreement with the experimentally obtained values. However, it should be noted that the strain rates obtained in the experiment (Ruta, 2018) are only approximate values since the strain gauges have not been installed at the notch tip due to the technical difficulties.

Table 5-5. Calculated fracture parameters form the static and dynamic analysis of thermally pre-damaged CTS at 400°C, measured at the onset of cracking.

Displacement rate (mm/s)	Tensile strength (N/mm ²) (Ruta, 2018)	Strain rate (1/s) (Ruta, 2018)	Fracture energy (N/m) (Ruta, 2018)	Tensile strength (N/mm ²) Present work	Strain rate (1/s) Present work	Fracture energy (N/m) Present work
Static	1.19	-	32.8	1.32	-	18.87
42	1.69	1.12 ^{num}	49.0	1.99	1.7	28.23
1300	1.89	84.09 ^{num} ----- 61.52* ^{exp}	54.0	2.07	70.42	26.77
3500	1.91	130.78 ^{num} ----- 155.4* ^{exp}	56.5	2.1	144.34	27.92
4000	1.90	156.73 ^{num} ----- 82.17* ^{exp}	56.0	2.11	121.2	28.59

* Experimentally obtained data (Ruta, 2018)

The crack patterns depicted with red color shown in Figure 5-16 represent the maximum principal strains that corresponds to the critical crack opening of 0.1 mm. The obtained crack paths correspond to the ones from the previous numerical study and to the experimental work, exhibiting no major change in the crack behavior. At 1300 mm/s crack branching phenomena is observed approximately at the same place in both numerical studies. However in the present study, one of the branches nearly reached the end of the specimens, similar to the experimentally obtained crack path.

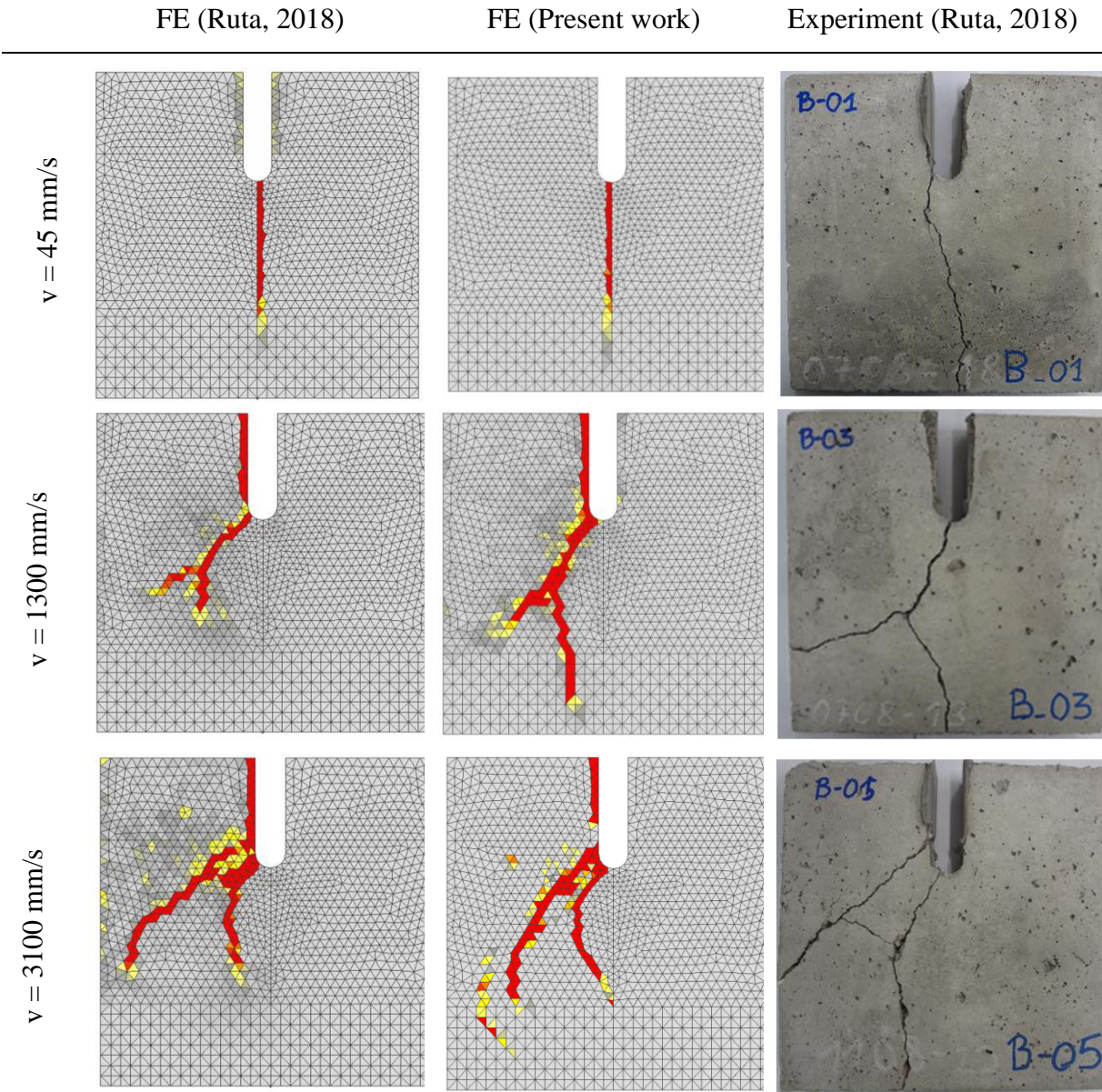


Figure 5-16. Numerically calculated and experimentally obtained crack patterns for CT specimens at 400°C (red zones = maximum principal strain that corresponds to crack width of 0.1 mm).

Comparison of the numerically obtained reaction – time curves against their corresponding experimental results are depicted in Figure 5-17a and Figure 5-17b. Although the reactions at displacement rate of 1300 mm/s exhibit a slight mismatch from the experimental values, the amplitudes of the curve correlate better than in the preceding numerical study (Figure 5-17c and d). In the case with 4000 mm/s, the CT specimen reached its reaction peak somewhat later than the experimental one.

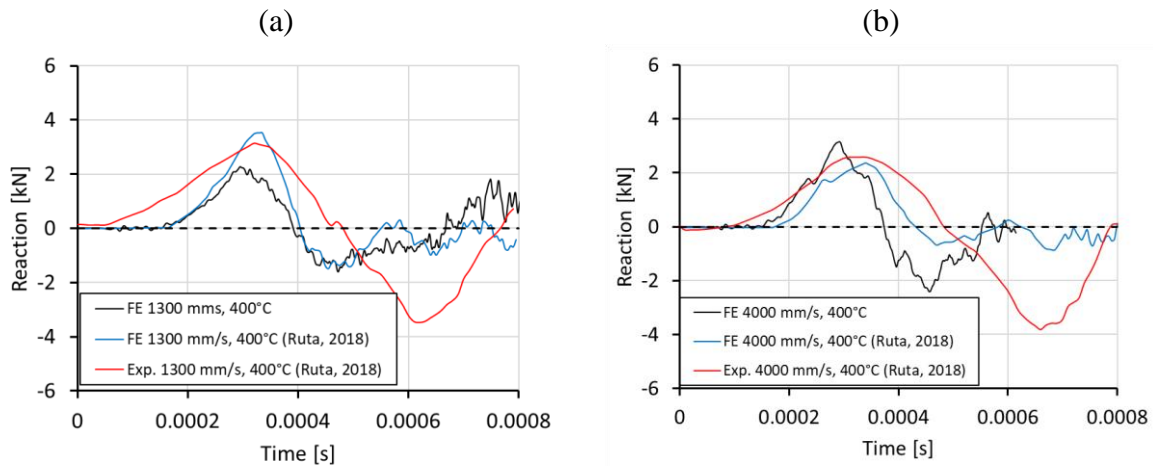


Figure 5-17. Comparison of numerically and experimentally obtained reaction time histories from the present analysis and from the analysis performed by Ruta (2018) for the thermally pre-damaged CT specimens at 400°C with displacement rates of 1300 mm/s (a), 3700 mm/s (b).

The reaction forces summarized in Table 5-6 indicate less pronounced deviation compared to the experimentally obtained values.

Table 5-6. Numerically and experimentally (Ruta, 2018) obtained reaction values at 400°C.

Displacement rate [mm/s]	Reaction forces (Ruta, 2018) [kN]		Reaction forces – present work [kN]
	Experimental	Numerical	
static	-	0.71	1.21
45	1.8	1.28	1.31
1300	3.2	3.5	2.1
3500	1.75	2.44	2.82
4000	2.7	2.62	2.84

In spite of the increase in the reaction forces with the increase of displacement rate, the scatter of results is reduced meaning that the increase in temperature leads to the less pronounced rate sensitivity and higher material degradation. The reaction peaks values are lower than in the previous numerical cases at 20°C and 200°C due to the stronger reduction of concrete fracture energy with higher temperature, however, the differences are not significant.

5.4 Conclusions

The aim of the present numerical study was to clarify the mismatch of the numerical and experimental results in the preceding work (Ruta, 2018) and to investigate whether this difference is possibly a consequence of the temperature dependent fracture energy. The dynamic response of the CT specimen together with the experimentally obtained fracture energy (decreasing tendency) was compared with the preceding numerical and experimental investigations. Having in mind that concrete becomes more brittle and therefore the influence of inertia on the resistance becomes relatively small (as is the case with brittle materials, e.g. glass), the following conclusions can be drawn: (i) the decreasing tendency of fracture energy with temperature increase has an effect on the dynamic response of the specimens, however, the influence is less than expected; (ii) the numerically obtained reaction-time curves are in a better agreement with the test results in terms of reaction amplitudes and trendlines compared to previous FE analyses; (iii) the fracture patterns obtained in the present FE analysis correlate better with the experiment; (iv) although the influence of displacement rate on the reaction force at 400°C is still more pronounced than in the experiment, the results of the numerical analysis at 200°C correspond well with the test (Figure 5-18); (v) further numerical and experimental studies are needed.

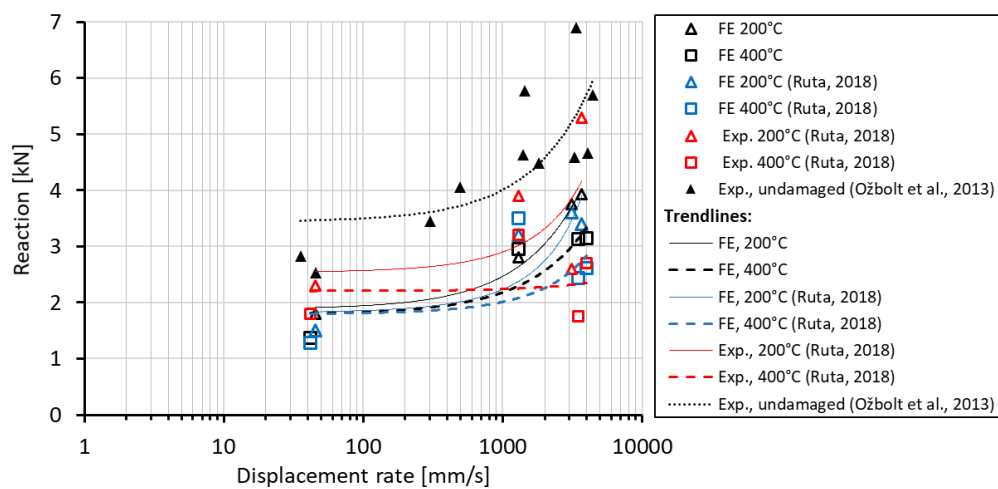


Figure 5-18. Summary and comparison of peak reactions for different exposure temperatures and displacement rates.

6. INFLUENCE OF PRELOADING ON THE CONCRETE EDGE FAILURE OF STUD ANCHORS AFTER FIRE EXPOSURE

The aim of the present study was to numerically investigate of the influence of preloading on the residual edge failure capacity of a single anchor and anchor groups after fire exposure. Headed stud anchors with single stud, two- and four anchor groups were exposed to various fire durations and loaded in shear perpendicular and towards to the free edge of concrete member, in hot and cold state (after cooling), up to failure. The influence of the edge distance, embedment depth, anchor diameter, number of anchors and fire duration on the residual edge failure capacity were taken into account and evaluated numerically. To demonstrate that the used 3D FE code, which is based on the thermo-mechanical microplane model for concrete, is able to realistically replicate the response of a single anchor and group of anchors for concrete edge failure after fire exposure, the numerical results for fasteners without preloading are compared with the available test data. Subsequently, the numerical results from the parametric study of preloaded anchors, for the hot and cold state, are presented and discussed. Finally, the concluding remarks are provided.

6.1 Introduction

In the field of modern construction technology, it is often necessary to economically transfer loads in reinforced concrete structures using fasteners (Eligehausen et al., 2006). The behavior of fasteners has already been investigated in detail for environmental temperatures that are common in engineering practice (Fuchs et al., 1995; Anderson and Meinheit, 2005; Kim et al., 2013; Grosser, 2012; Jebara et al., 2016). However, their behavior changes significantly at high temperatures, such as those that can occur in case of fire (Reick, 2001; Bamonte et al., 2020; Periškić, 2009; Tian et al, 2018a; Tian et al, 2018b; Tian, 2019). The decrease in the mechanical properties of concrete and steel due to thermally induced damage causes a decrease of the load-bearing capacity of fasteners and a significant increase of deformations. Moreover, thermally induced strains and the associated constraint stresses can also have a strong influence on the resistance of fasteners (Tian, 2019).

To better understand the behavior of fasteners under shear load at high temperatures, fire tests with single headed stud anchors and group of anchors loaded perpendicular to the free edge of the concrete slab and exposed to fire have been recently carried out (Tian et al, 2018a; Tian et al, 2018b; Tian, 2019). The tests were then used to calibrate and verify the thermo-mechanical

model previously implemented into a 3D finite element (FE) code (Ožbolt et al., 2001; Ožbolt et al., 2005b; Ožbolt et al., 2014). After calibration and verification of the model, extensive numerical studies for a single and group of fasteners close to an edge were performed to investigate the influence of high temperature on their behavior. Studies of the anchorage behavior were conducted at elevated temperature and at ambient temperature after heating (i.e., during and after the fire, respectively). The former condition was found to be most critical, as should be expected, since the residual mechanical properties of cementitious composites are well-known to be worse after cooling than at high temperatures. Based on the experimental tests and numerical simulations a design formula is proposed, which accounts for the influence of the high temperature on the residual capacity of anchors loaded in shear (Tian, 2019).

Due to the difficulties in the design of experimental tests for in shear preloaded fasteners exposed to fire, almost all available investigations were carried out without preloading. With the preloading of anchors there is a number of difficulties, for instance during fire it is not simple to keep the anchor load constant and then in the hot state load them up to the failure. However, since in the engineering practice almost all fasteners are preloaded, the question is to what extent preloading may influence the residual shear failure capacity of anchors close to the edge after fire exposure. Therefore, the numerical investigations were carried out for single anchors, as well as for double and quadruple anchor groups preloaded with design load according to Eurocode 2 (European Committee for Standardization: Part 4, 2015).

6.2 Geometry and material properties

The numerical parametric study is carried out for geometries that have recently been experimentally tested (Tian, 2019). The tested configurations were single anchors, two- and four anchor groups close to the edge, loaded in shear perpendicular to the edge (see Table 6-1 and Figure 6-1). In the experiments and analysis the most severe heating conditions were assumed. The concrete slab was heated from two sides (Figure 6-1c) according to ISO 834 fire curve (Figure 6-1a) and then naturally cooled down to the environmental temperature ($T = 20^\circ\text{C}$). Subsequently, the fasteners were loaded in shear (cold state) up to failure. The experiments were carried out for fastenings without preloading and only for the cold state. The obtained experimental results are here used only to verify the employed numerical model. The example of identification meaning of anchors from Table 6-1 is as follows: ‘‘G2’’ stands for two-stud anchor group, ‘‘c100h95d25’’ stands for anchor with concrete edge distance $c = 100$ mm, embedment depth $h_{ef} = 95$ mm and diameter $d_a = 25$ mm.

Table 6-1. Anchor configurations in the experimental tests (Tian, 2019).

Identification	Number of studs	c_1	s_1 & s_2	h_{ef}	d_a	Concrete grade	Fire duration (min)
G1c100h95d25	1	100	-	95	25	C20/25	0; 15; 60
G2c100h95d25	2	100	100	95	25	C20/25	0; 15; 60
G4c100h95d25	4	100	100	95	25	C20/25	0; 15; 60

$c_1/d = 4.0$ & $h_{ef}/d = 3.8$; For single anchor and for two anchors: $c=c_1$; for group of four anchors $c= c_1=c_{1,1}$

In the numerical parametric study the following geometrical parameters were varied: (1) edge distance $c_1 = 75, 100$ and 150 mm; (2) anchorage embedment depth $h_{ef} = 75$ and 95 mm, anchor bolt diameter $d_a = 16$ and 25 mm and anchor spacing $s_1 = s_2 = 100$ and 150 mm (Figure 6-1b). The simulations are carried out for concrete that approximately corresponds to the class C20/25 (Eurocode 2 EN 1992-4: Part 4, 2015). Note that the concrete compressive strength in the simulations was taken from the experimental measurements (Tian, 2019) (see Table 6-2). In order to exclude the failure of steel, it was assumed that steel is linear-elastic, i.e. heating of steel does not affect its mechanical properties (strength and Young’s modulus). Note that the numerical parametric study was not carried out for all possible combinations of the above mentioned parameters (geometry, fire load and mechanical load), as the number of possible combinations would be very high. Some calculations were already available and some combinations were excluded, depending on the results during the investigations.

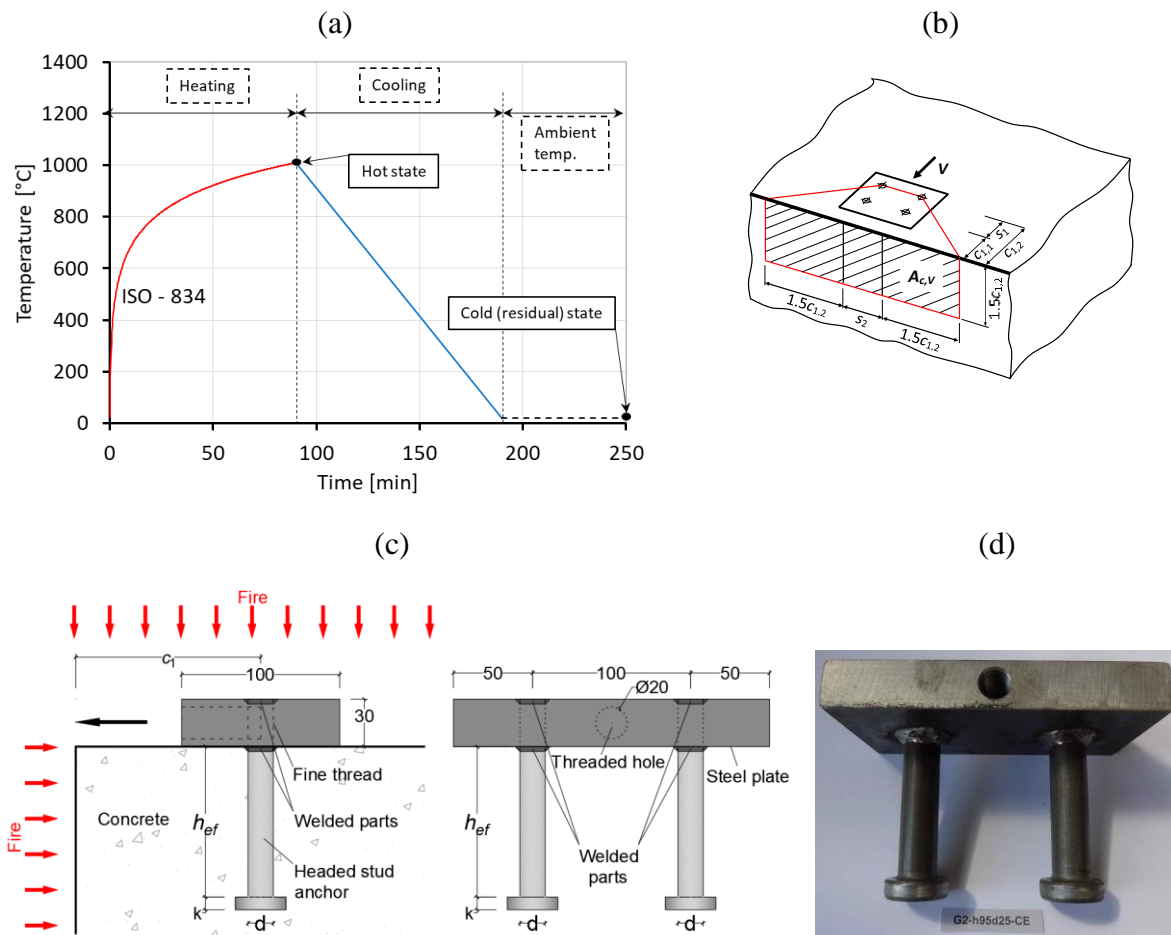


Figure 6-1. (a) Heating curve according to ISO 834, (b) group of four anchors, (c) and (d) example of two-stud anchor group in the fire test (Tian, 2019).

6.3 Numerical analysis

6.3.1 Geometry, material properties and FE model

In the 3D FE simulations as the constitutive law for concrete, the original thermo-mechanical microplane model for concrete is used (Ožbolt et al., 2001; Ožbolt et al., 2005b; Ožbolt et al., 2014). The finite element discretization (see Figure 6-2) is performed according to the geometry and boundary conditions from the experimental tests (Tian, 2019) by employing 4-node constant strain solid finite elements. The connection between steel and concrete is performed by using contact elements that can transfer only compressive contact forces. To assure mesh size-independent results, the regularization based on the crack band method is used (Bažant and Oh, 1983). The properties of concrete and steel employed in the analysis are specified in Table 6-2. The temperature-dependent thermal properties of concrete and steel are taken according to Eurocode 2 EN 1992-1-2: 2004 Part 1-2 (International Organization for Standardization, 1999).

Note that temperature dependent properties of concrete and steel were calculated using the local temperature. As already mentioned, since the aim of the analysis was to investigate the failure of concrete, the behavior of steel was assumed to be linear elastic. In all simulations, one symmetry plane was utilized (see Figure 6-2). Note that the only numerical tests were performed with and without preloading.

Table 6-2. Material properties used in the simulations.

Material	Young's modulus (GPa)	Poisson's ration	Uniaxial compressive strength (MPa)	Tensile strength (MPa)	Fracture energy (J/m ²)	Heat conductivity (W/mK)	Heat capacity (J/kgK)	Weight density (Kg/m ³)
Concrete C20/25	27	0.18	32	2.9	60	1.33	900	2300
Steel 1.4828	200	0.33	-	550-750	-	18.00	500	7900

The fire load was enforced by heating the environment (air) temperature according to the standard ISO 834 curve. The fire exposure times were varied from $t = 0$ (reference case) to 15, 30, 60 and 90 min. The fire was applied on two sides of the concrete specimen (see Figure 6-2a). The pre-loading (shear service load according to Eurocode 2, see Table 6-3) was applied perpendicular to the free edge. The shear resistance of fasteners was calculated for both, hot and cold state. In the hot state, the fasteners were loaded immediately after the heating by displacement control until failure (see Figure 6-2b). In the cold state, the specimens were after heating naturally cooled down to the room temperature and subsequently loaded by displacement control until failure. The summary of simulated cases for the cold and hot state, with and without preloading, is given in Table 6-3 (hatched block).

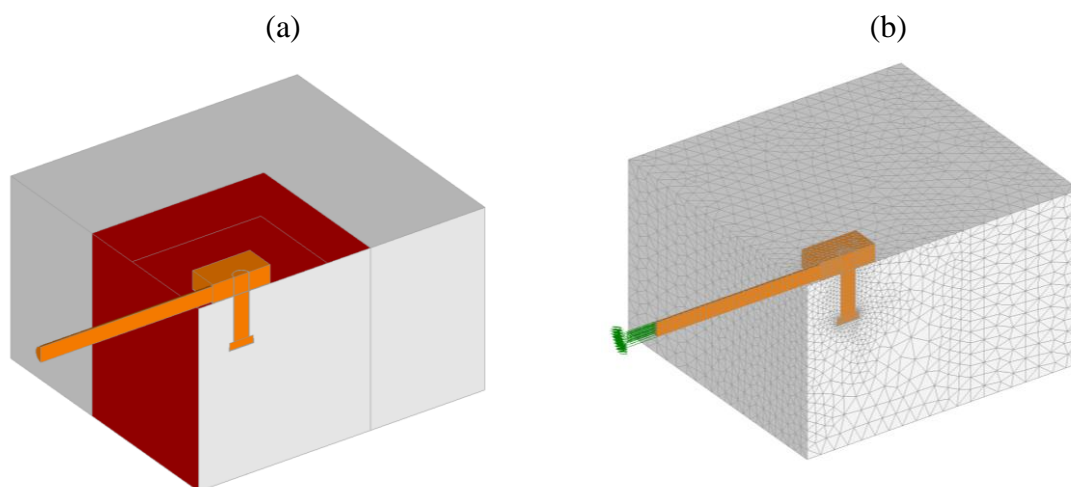


Figure 6-2. Single headed stud anchor at the edge: (a) Two-sided fire exposure according to ISO-834 and (b) FE discretization (one symmetry plane).

Table 6-3. Simulated models in the numerical parametric study (length and size units in [mm]; load in [kN]).

Number of anchors	Edge distance, c	Embedment depth, h_{ef}	Anchor diameter, d_a		Preloading	
			16	25	$d_a = 16$	$d_a = 25$
Single – anchor system	75	75	-	+		7,56
		95	-	+		8,02
	100	75	-	+		10,93
		95	+	+	10,71	11,52
	150	75	-	+		18,6
		95	-	+		19,46
Two anchors	75	75	-	+		10,92
		95	-	+		11,58
	100	75	-	+		14,57
		95	+	+	14,28	15,36
	150	75	-	+		22,73
		95	-	+		23,78
Four anchors	100	75	-	+		17,29
		95	-	+		27,18
	100	75	-	+		28,36
		95	+	+	31,35	33,17
	150	75	-	+		33,47
		95	-	+		34,74
100	75	-	+		43,42	
	95	-	+			

“+” = simulated; “-” = not simulated

6.3.2 Verification of the model

The mechanical part of the model is based on the thermo-mechanical microplane constitutive law for concrete and in the employed model, the total strain tensor is decomposed into mechanical strain, free thermal strain and load induced thermal strain (LITS) as discussed in Chapter 4. Principally, with increase of temperature there is degradation of mechanical properties of concrete. Moreover, thermal strains and LITS together with constrains (boundary conditions) can cause additional thermally induced damage. To confirm that the employed thermo-mechanical model is able to realistically predict the behavior and resistance of fasteners after fire, the numerical results are compared with the recently performed experimental tests. Typical response is illustrated in Figure 6-3 which shows the results for single anchors ($c = 75$, 100 and 150 mm, $h_{ef} = 95$ mm and $d_a = 25$ mm, concrete C20/25) heated without the applied shear load and then loaded up to failure after the specimen had cooled down.

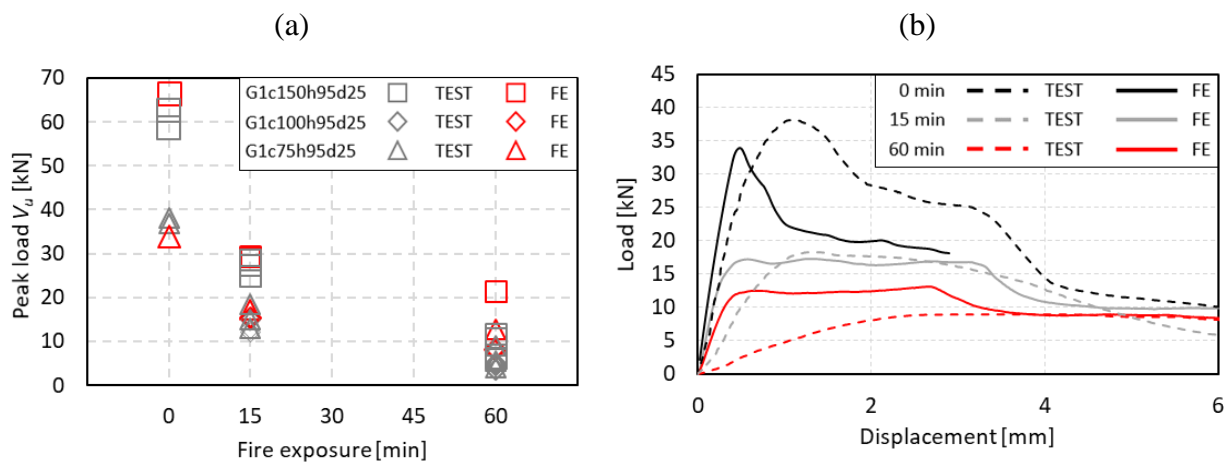


Figure 6-3. Comparison between experimental and numerical results: (a) Resistance as a function of fire exposure and (b) load-displacement curves for a single anchor.

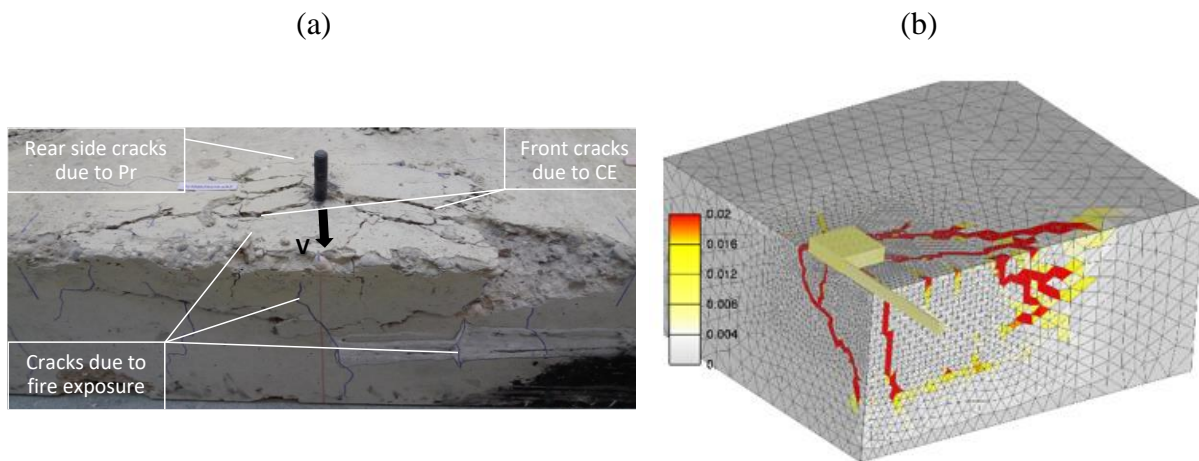


Figure 6-4. Typical failure mode observed in the experiment (Tian, 2019) (a) and simulation (b).

As can be seen from Figure 6-3a, the experimentally and numerically obtained results show for all anchor configurations strong degradation of shear resistance as a function of fire duration. Figure 6-3b shows the measured and computed load-displacement curves for a single anchor. It can be seen that with an increase in fire duration the response becomes more ductile. The numerically obtained resistance reasonably well fit experimental values. However, the initial stiffness observed in the simulations is higher than in the analysis and the shape of the curves is not the same. The main reasons can be attributed to the local damage effects that cannot be properly accounted for in the macroscopic FE analysis. Furthermore, in the analysis the ideal heating boundary conditions are not exactly the same as in the experimental tests. The reduction of concrete mechanical properties and calculation of thermal strains are based on the local values of temperature in the integration points of finite elements. In order to eliminate the

influence of the element size on the thermal properties, it would be probably more realistic to use nonlocal (average) temperature of the representative volume for the calculation of thermally dependent concrete properties. However, having on mind the complexity of the problem from the mechanical and thermal point of view, it is rather difficult numerically obtain exactly the same load-displacement curves as in the experimental tests.

The typical failure modes are compared in Figure 6-4. Red zones shown in Figure 6-4b are maximum principal strains, which correspond to the crack width equal or greater than 0.10 mm. Despite the high complexity of the problem, Figure 6-3 and Figure 6-4 confirm that the 3D FE thermo-mechanical model is able to reasonably well replicate temperature-dependent failure of anchors loaded in shear against the free edge of the concrete member.

6.3.3 Parametric study

6.3.3.1 Single anchor

The typical load-displacement (L-D) curves ($h_{ef} = 95$ mm, $c_1 = 75$ mm, $d_a = 25$ mm) with and without preloading, for cold and hot state, are shown in Figure 6-5. The plotted displacement corresponds to the applied displacement control. It can be seen that the load-bearing capacity decreases with increase of fire exposure. This applies to both cold and hot conditions, with and without preloading of anchors. The highest relative drop of ultimate load takes place after fire duration of only 15 minutes. Moreover, the reduction of resistance is higher for the cold state than for the hot state. Comparing the L-D curves, it can be seen that the fasteners with preloading show a greater decrease in load-bearing capacity as a result of the fire exposure (see also Figure 6-6). For longer fire exposures ($t \geq 60$ min) the load immediately after application of displacement of anchor reduces and the resistance becomes smaller than the applied service load. This means that the pre-loaded fastener fails during the fire exposure, i.e. the residual load-bearing capacity is smaller than the service load. Note that during the thermal process (heating and cooling) the analysis is carried out by the load control of the fasteners. The employed numerical procedure is not able to account for the descending part of the L-D curve, i.e. after reaching the peak resistance the equilibrium is not assured. However, since the fasteners are loaded by displacement control after thermal analysis, the equilibrium between external load and internal forces is again established with the consequence that the resulting load (the highest value of the L-D post-peak response shown in Figure 6-5) actually represents the residual resistance, i.e. the load at which the fasteners fails as a consequence of the

preloading and thermally induced damage. In the experimental tests, this would take place during the thermal loading of fasteners (heating or cooling).

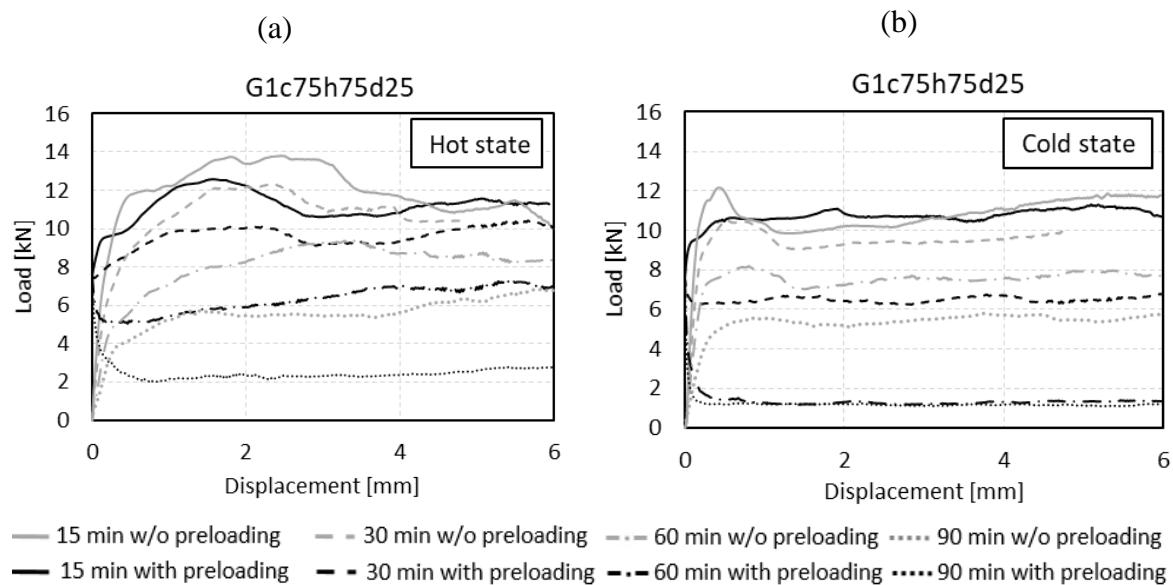


Figure 6-5. Single anchor: L - D curves for $c_1 = 75$ mm, $h_{ef} = 75$ and $d_a = 25$ mm with preloading (solid) and without preloading: (a) hot condition; (b) residual condition.

Figure 6-6 shows the decrease of the resistance for two typical cases as a function of fire duration. It can be clearly seen that, as in the tests (Tian, 2019), the strongest relative decrease of load-bearing capacity takes place in the first 15 minutes. In most cases the load-bearing capacity appears to decrease more in residual conditions than in hot conditions. As already reported (Tian, 2019), the reason for this is the fact that the concrete is additionally damaged by the cooling process. Furthermore, it is also evident that the preloading has a relatively strong influence on the residual load-bearing capacity of fasteners. It can be seen that the design load (approx. 20% of the resistance at room temperature) leads to an additional reduction of the resistance after fire exposure. This applies to both, cold and warm condition. The influence increases significantly with longer exposure to fire and is more pronounced for the cold state. The reason for this is the fact that the damage of concrete caused by preloading, which in interaction with the temperature-induced damage causes additional damage and consequently leads to additional reduction in the load-bearing capacity.

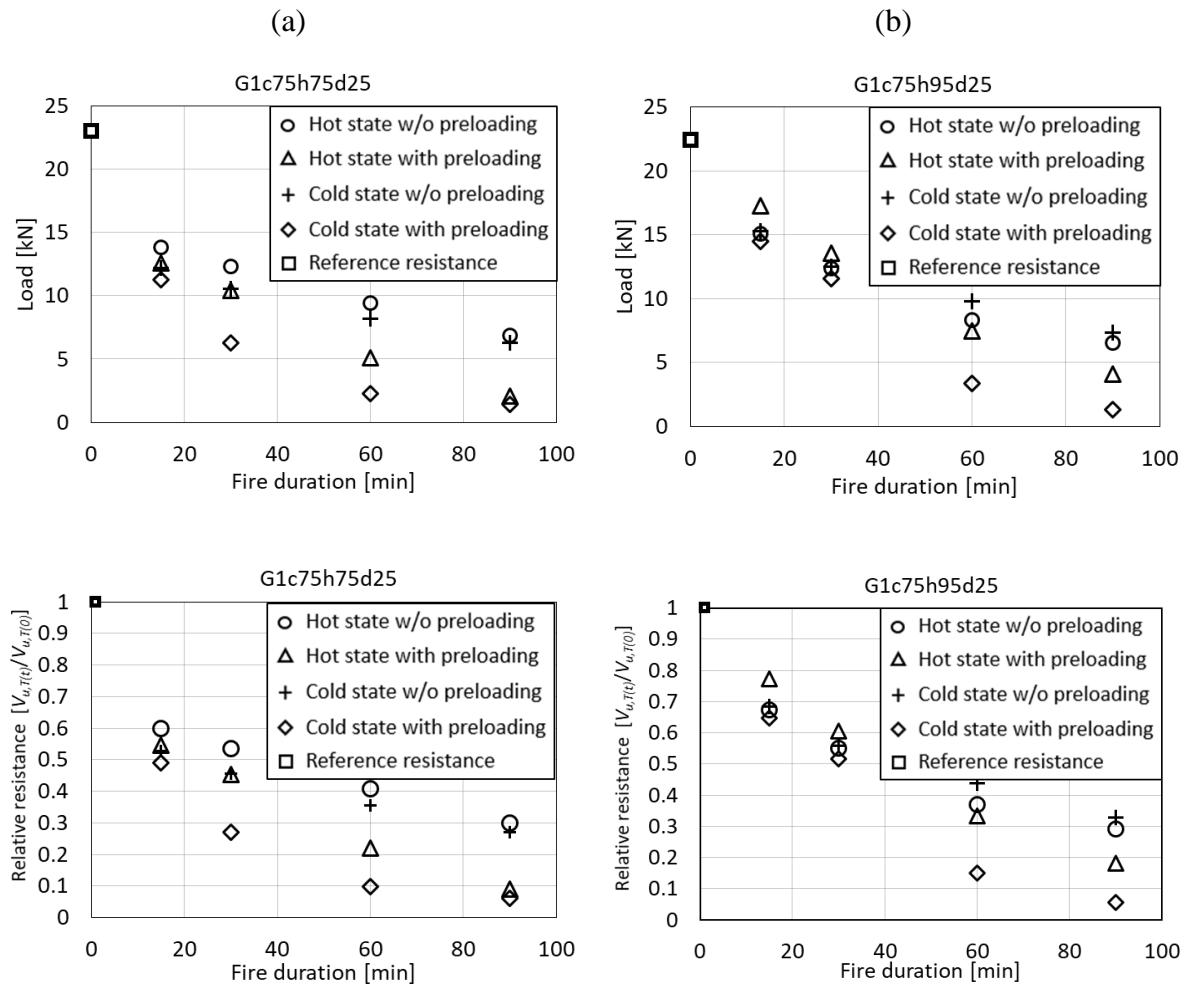


Figure 6-6. The load capacity reduction as a function of fire duration for: (a) $c_1 = 75$ mm, $h_{ef} = 75$ and $d = 25$ mm and (b) $c_1 = 75$ mm, $h_{ef} = 95$ and $d_a = 25$ mm.

The typical crack patterns (damage) after cooling of the specimen and loading until failure are shown in Figure 6-7, for the cases with and without preloading. It can be seen that for both cases the crack pattern is relatively similar. However, already after 15 min. of heating, damage of concrete close to the anchor position and directly in front of the anchor is more pronounced for the pre-loaded anchors. With further increase of fire exposure this tendency continues to increase. As a consequence, the decrease in the load-bearing capacity after fire exposure is higher for pre-loaded anchors.

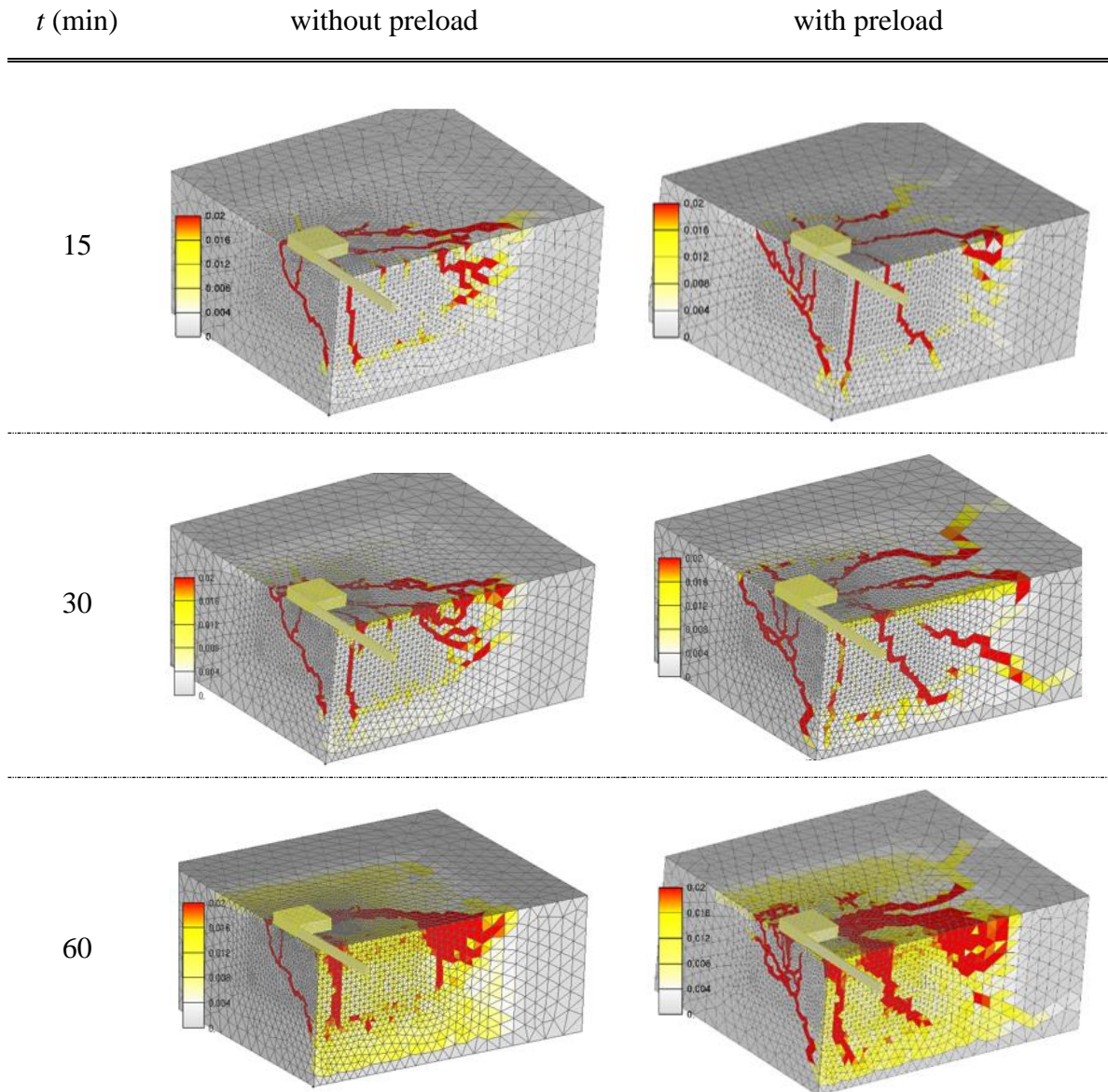


Figure 6-7. Crack formation at the residual load in the cold state, with and without preloading.

Influence of edge distance – single anchor

Figure 6-8 shows the influence of the edge distance on the relative resistance of the concrete specimens with and without preloading, in hot and cold state. The influence of preloading is more expressed in the specimens with lower edge distance having a bigger scatter with respect to the load bearing capacity in the complete fire exposure range. This scatter is amplified when comparing the influence of edge distances in the cold state implying that bigger edge distance (with preloading) exhibits lower relative load bearing reduction as a function of temperature. In spite of the trend being similar for the cases without preload, the scatter is still less pronounced.

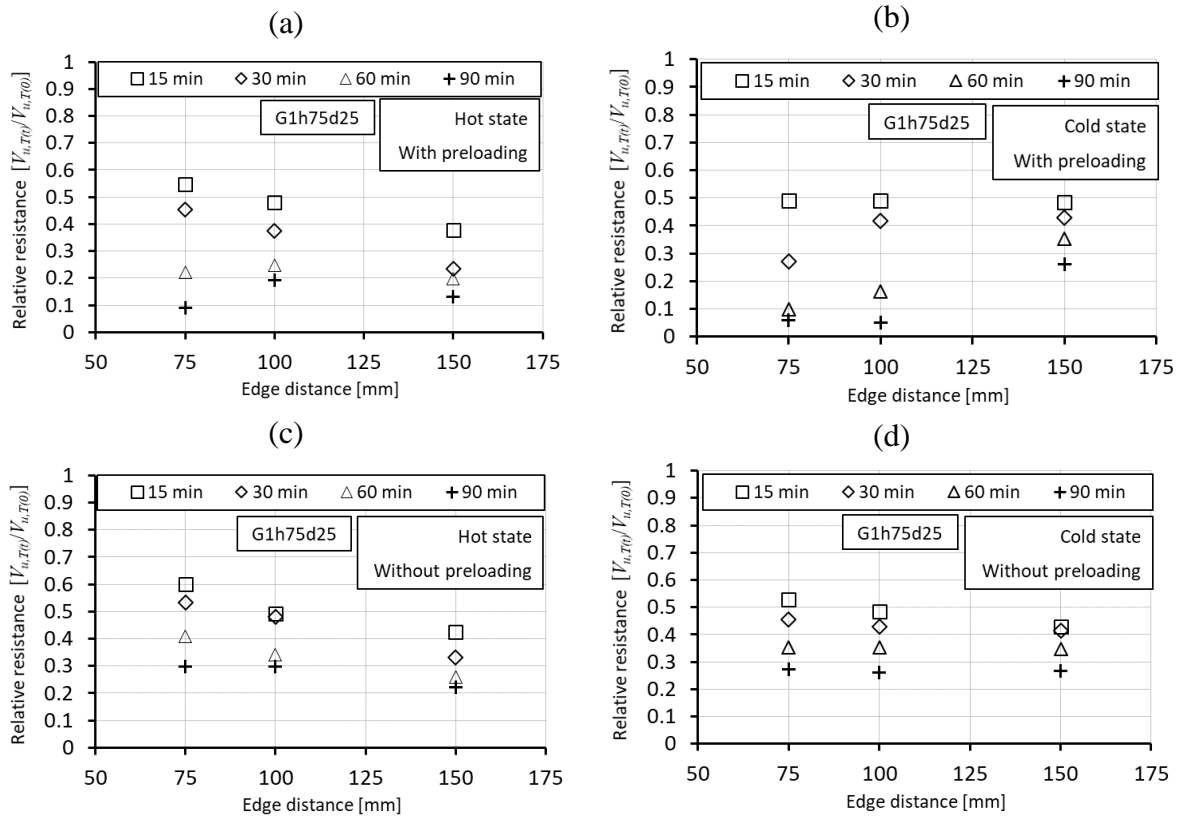


Figure 6-8. The load capacity reduction as a function of fire duration and edge distance for $h_{ef} = 75$ and $d_a = 25$ mm in the case of: (a) Hot state with preloading, (b) Cold state with preloading, (c) Hot state w/o preloading and (d) Cold state w/o preloading.

6.3.3.2 Group of anchors

Figure 6-9 shows the typical L-D curves for a group of two anchors ($h_{ef} = 75$ mm, $c_1 = 75$ mm, $s_1 = 100$ mm, $d_a = 25$ mm), with and without preloading, for hot (a) and cold state (b).

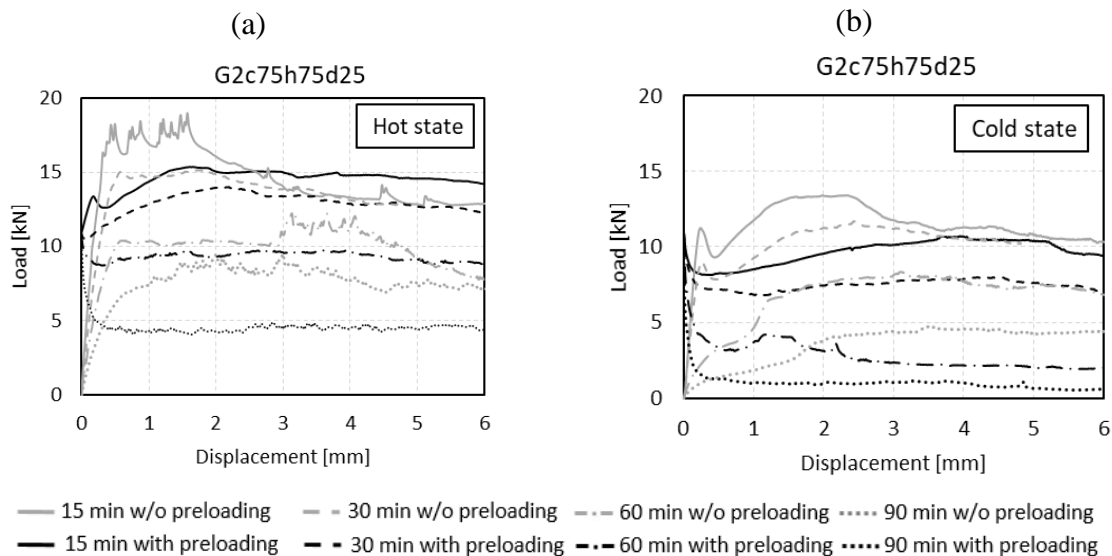


Figure 6-9. Two anchor group: L-D Curves for $c_1 = 75$ mm, $s_1 = 100$ mm, $h_{ef} = 75$ and $d_a = 25$ mm with preloading and without preloading: (a) hot state; (b) residual (cold) state.

The same as for the single fasteners, it can be observed that with increased fire duration, the load-bearing capacity decreases, and ductility increases. This applies to cold and hot states, with and without preloading. It is also obvious that the resistance for the cold state is significantly lower than for the hot state. The highest decrease in the load-bearing capacity occurs after a fire duration of only 15 minutes.

The decrease in the load-bearing capacity as a function of fire duration is shown in Figure 6-10. In principle, the same applies as for the single anchors. The preloading shows a relatively strong influence on the load-bearing capacity of fasteners. In some cases, the residual resistance is smaller than the applied design load. This implies that the anchor fails already during the fire exposure or during the cooling phase.

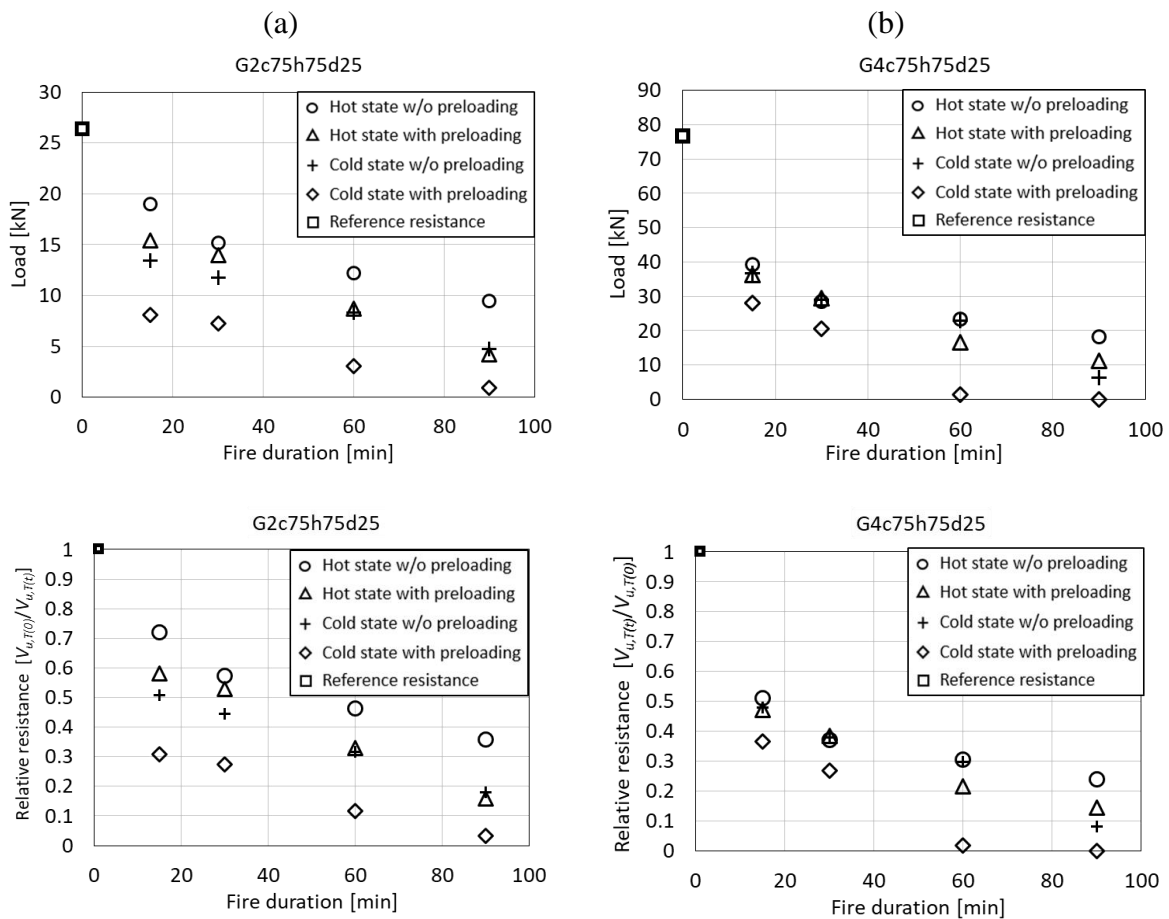


Figure 6-10. The reduction of the load-bearing capacity as a function of fire duration for: (a) two anchor group with $c_1 = 75$ mm, $s_1 = 100$ mm, $h_{ef} = 75$ and $d_a = 25$ mm and (b) four anchor group with $c_1 = 75$ mm, $s_1 = s_2 = 100$ mm, $h_{ef} = 95$ and $d_a = 25$ mm.

Influence of edge distance – group of anchors

The relative resistance as a function of edge distance for four anchor configuration with and without preloading, in both hot and cold state are shown in Figure 6-11. The results indicate similar behavior for all edge distances in all cases. The resistance reduction after 90 minutes of thermal exposure is least pronounced in the case with edge distance of 150 mm for almost all cases. Furthermore, the specimens with $c_l = 150$ mm exhibit the smallest relative resistance reduction after 15 min of fire duration. The most unfavorable loading condition is cold state with preloading for all edge distances.

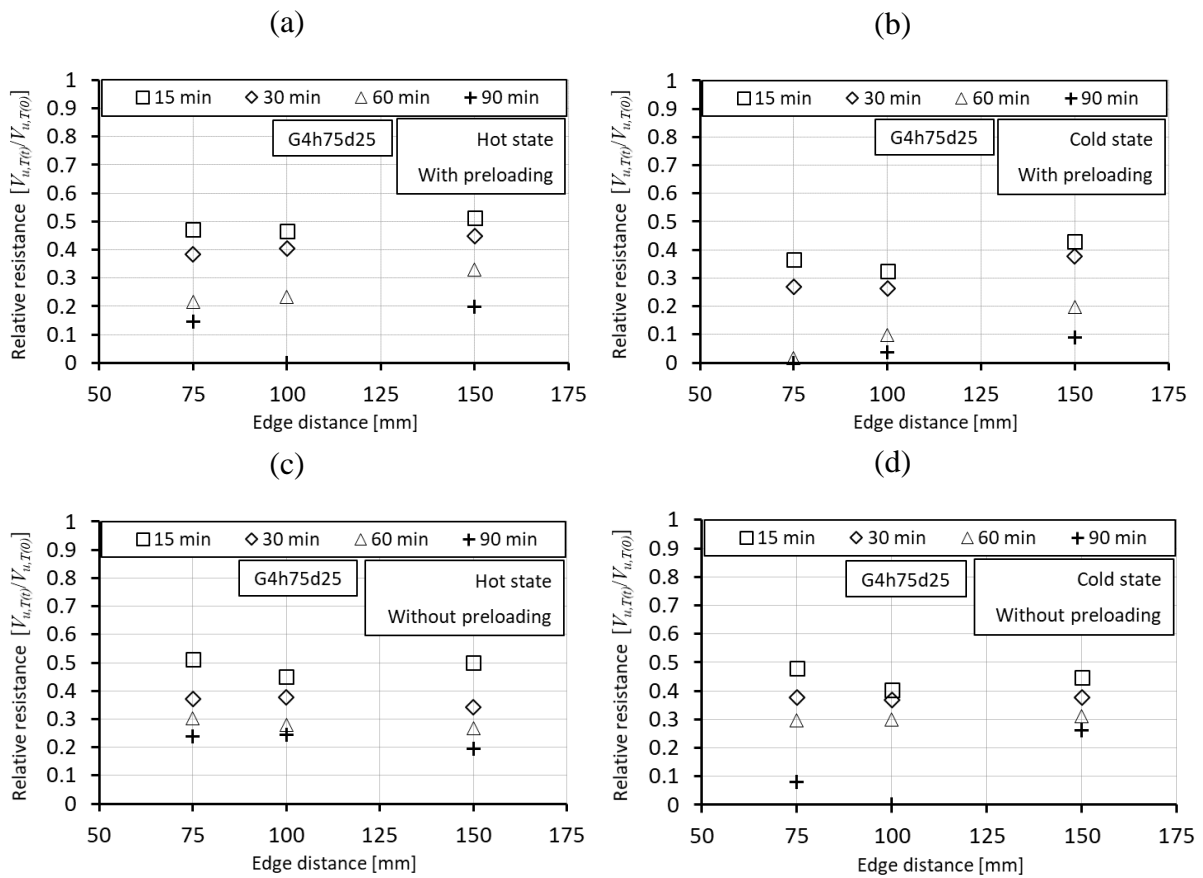


Figure 6-11. The load capacity reduction as a function of fire duration for: (a) $c_l = 75$ mm, $h_{ef} = 75$ and $d = 25$ mm and (b) $c_l = 75$ mm, $h_{ef} = 95$ und $d_a = 25$ mm.

6.4 Conclusions

The aim of the study was to investigate the influence of preloading on the load bearing capacity of a single headed stud anchor and groups of anchors loaded in shear perpendicular to the concrete edge after thermal exposure. The numerical model had to be initially validated against the experimental test data and subsequently, an extensive parametric analysis including not only the influence of preloading, but also the influence of hot and cold (residual) state on the relative

resistance was to be carried out. From the numerical study following conclusions can be drawn: (i) the 3D FE code adopted in this study, based on the thermo-mechanical microplane model for concrete, is able to reasonably well replicate the corresponding resistance of the experimental tests. However, due to the complexity of the problem, it was not possible to sufficiently accurately replicate the experimentally measured L-D curves; (ii) as expected, the simulation shows that with an increase of fire exposure time, the shear load capacity of anchors decreases significantly. The decrease is more pronounced in the first 15 minutes of fire and greater for cold than for hot state; (iii) the preloading has a relatively strong negative influence on the shear load-bearing capacity of anchors. The reduction of residual resistance increases with increasing fire exposure time. The study indicates that for the fire exposure larger than 30 min there is a relatively high possibility that the residual resistance becomes smaller than the design load. Obviously, with increase of pre-loading level, the residual resistance should decrease; (iv) the design formula for the shear resistance of fasteners should account for the influence of the preloading on the residual load-bearing capacity of anchors after the fire (Ožbolt et al., 2021).

7. RC FRAME SUBJECTED TO THERMAL AND DYNAMIC LOADING

7.1 Introduction

Reinforced concrete structures subjected to combined thermal and dynamic loading are characterized with high loading rates and high temperature gradients related to fire outbursts resulting in fast and strong degradation of mechanical and physical material properties and ultimately in their failure. Therefore, it is important to investigate the behavior of RC structures exposed to these conditions to predict the failure mode, damage localization zones, temperature fields and the load bearing capacity. With this in mind, it is important to investigate numerically the behavior of complex structures under extreme loading conditions in order to avoid the failure and to make structures more resistant.

The mechanical properties of concrete such as strength and Young's modulus, when exposed to elevated temperature, decrease. Exposed to fire, boundary conditions of the structure can prevent deformation due to thermal strains, which in result cause thermally induced stresses and damage. Effects that can occur during fire exposure such as explosive concrete spalling and load induced thermal strains (thermal creep) can significantly decrease the resistance of reinforced concrete (RC) structures. It is well known that the resistance, failure mode, crack pattern and crack velocity in concrete are strongly influenced by the loading rate. (Bažant and Thonguthai, 1978; Bažant and Kaplan, 1996; Khoury et al., 1985; Ožbolt and Reinhardt, 2002; Ožbolt et al. 2008; Ožbolt et al., 2014a; Sharma et al., 2016).

As already discussed in Chapter 2, there are relatively low number of studies related to the topic of structures subjected to successive thermal and dynamic loading. Recently, it has been demonstrated (Ruta, 2018) that through high temperature pre-damaged concrete is less sensitive on the influence of high strain rates. Therefore, the dynamic response of reinforced concrete (RC) structures that are thermally pre-damaged can change significantly when compared to initially undamaged RC structures. Here, the influence of thermally induced damage of RC frame on its dynamic impact properties is investigated numerically. The frame is first exposed to elevated temperature, cooled down to room temperature and then loaded by the side impact with a stiff pendulum. To verify the numerical model, the results of experimental test on one thermally pre-damaged RC frame are compared with the results of the numerical simulation (Ruta, 2018; Parmar et al., 2014). Subsequently, the results of parametric study are presented and discussed. Finally, the role of rate dependent constitutive law and structural inertia in dynamic (impact) and static analysis of RC frame is investigated and concluding remarks are

given. The study is also conducted in order to clarify some open questions stated in the work of Ruta (2018).

7.2 Finite element analysis

As discussed in Chapter 4, in the existing thermo-mechanical models, the temperature dependency of thermal and mechanical properties of concrete is based on the calculated temperature T that comes from finite element analysis. However, such approach in cases where the quasi-brittle materials such as concrete are a part of a multi body dynamic problem (impact) preceded by thermal damage, can exhibit localization of thermally induced damage and mesh dependent results. When the impact takes place into an already thermally pre-damaged structure, the combination of mechanical and thermally induced damage can cause nonobjective results and lead to unrealistic degradation of structural resistance. As will be shown later, this is especially true when the heated surface of concrete is loaded by impact, e.g. hammer.

To make the numerical analysis more objective from this viewpoint, a new nonlocal (average) temperature variable is introduced. The nonlocal temperature field, which will replace the one calculated from the finite element analysis, is going to be used for calculating the thermally dependent mechanical properties. Similar to the nonlocal strain approach (Jirásek, 2005; Bažant and Ožbolt, 1990), the nonlocal temperature \bar{T} is calculated as an average of local temperatures T inside representative volume V_R . The adopted nonlocal weighting function is the modified Gauss distribution function as discussed in Chapter 4. Note that if the size of the finite elements are significantly larger than the characteristic length or if the temperature field is homogeneous, the nonlocal and local temperatures are the same. Furthermore, free thermal strains and load induced thermal strains are also calculated based on nonlocal temperature, i.e., in Eq. (4-11) T is replaced with \bar{T} .

Thermo-mechanical model for steel is formulated in the framework of classical rate theory of plasticity. It is based on the von-Mises yield criteria, isotropic hardening and associated flow rule. As discussed in Chapter 2, its mechanical properties, i.e., Young's modulus, yield stress and strength, as well as thermal properties (free thermal strains, heat capacity and conductivity) depend on temperature (Ožbolt et al., 2008; Ožbolt et al., 2014; *fib* Model Code, 2010) and are taken from Eurocode 2 EN 1992-1-2 (European Committee for Standardization, 2004). The total strain tensor is decomposed into mechanical strain and free-thermal strain, similar to concrete. Note, however, that after cooling down to the ambient temperature, the mechanical

properties of steel are almost fully recovered. Furthermore, temperature dependent properties of steel are calculated using local temperature field obtained from transient heat analysis. Steel is almost rate insensitive, however, if it is loaded under high loading rates; after threshold strain rate the resistance (apparent strength) starts to increase progressively. The reason is that the non-linear response of steel (strain hardening) that generates strong inertia induced resistance (Ožbolt et al., 2016).

The finite element analysis consists of two parts: (i) transient thermo-mechanical and (ii) dynamic analysis. The spatial discretization is performed using standard 3D solid finite elements. Thermal transient analysis is performed using direct integration scheme of implicit type (Ožbolt and Reinhardt, 2002; Ožbolt et al. 2008; Ožbolt et al. 2010; Ožbolt et al. 2014; Belytschko et al., 2001). The mechanical part is implicit and based on the Newton–Raphson iteration scheme. The global stiffness matrix is secant, which assures stable convergence for the pre- and post-peak response. In the mechanical part, maximum residual is set to be 1.0% (Euclidian norm). Coupling between the mechanical and non-mechanical part of the model is performed by continuous update of governing parameters during the incremental transient finite element analysis using a staggered solution scheme. After finishing thermo-mechanical analysis, explicit dynamic finite element analysis is conducted. The analysis is performed in the framework of total Lagrange formulation assuming small strains. To obtain analysis objective with respect to the size of finite elements, regularization scheme based on the crack band method is employed (Bažant and Oh, 1983).

7.3 Experimental study and verification of the numerical model

The experimental tests to investigate the effect of combined thermo-dynamic load on RC frames were carried out at Bhabha Atomic Research Center (BARC) in Mumbai, India (Parmar et al., 2014). In the experimental work, the influence of extreme loading conditions including a combination of fire exposure and side impact of pendulum was investigated. To validate the numerical model employed in the subsequent numerical study, only one of the performed experimental tests is simulated here.

7.3.1 Geometry, FE discretization and material properties

To fit in the oven, the dimensions and the reinforcement area of RC frame in the experiment were scaled down by factor 0.50 and it was designed for gravity load, with no ductile detailing present (see Figure 7-1). The concrete used in the experiment was a class M25 (mean measured cube strength was approximately 22 MPa) and a steel grade Fe 415, characterized by yield stress of $f_{yk} = 415$ MPa. The length to width ratio was 1 with 1750 mm in size and the frame height of 1500 mm (excluding the footings). The following reinforcement configuration was utilized in the test: (i) the beams (100 x 150 mm) with 2- $\phi 8$ bars in both compression and tension zones and $\phi 6$ stirrups with spacing of 100 mm; (ii) columns (150 x 150 mm) with $\phi 6$ stirrups and the spacing of 100 mm and (iii) slab (70 mm thickness) with the top reinforcement layer consisting of $\phi 6$ mesh reinforcement and 80 mm spacing.

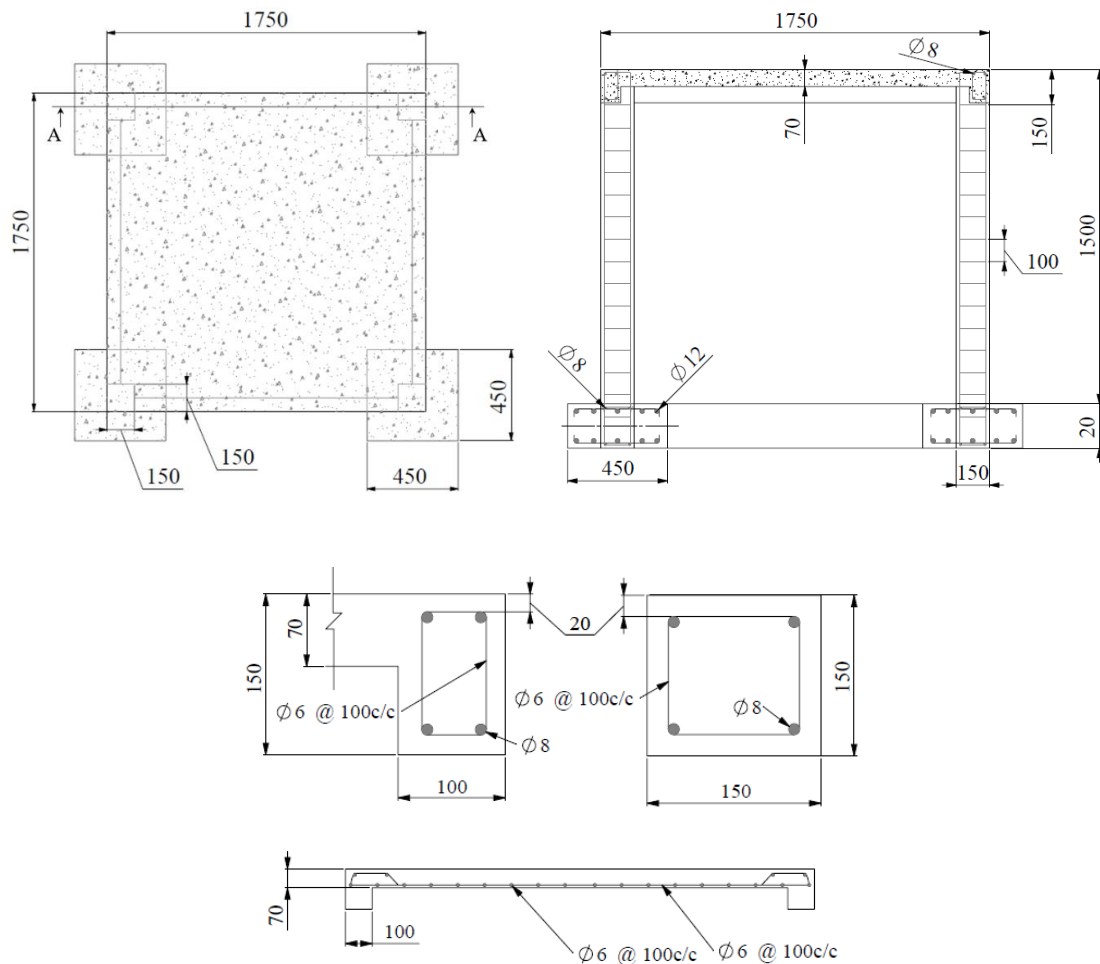


Figure 7-1. Geometry of the experimentally tested reinforced concrete (RC) frame (Parmar et al., 2014) (all in mm).

The experimental test was performed in two stages. First, the RC frame was pushed into the oven and subjected to one hour compartment fire by utilizing the ISO 834 fire curve and

subsequently, loaded on the side with a steel pendulum. The RC frame structure was fixed on the four contact-point pendulum facility. In the absence of anchorage bars, a supporting structure was made to anchor the frame (see Figure 7-2). To mitigate the maneuver issues during the fire test, the frame was additionally mounted on an oven trolley and pushed into the oven.

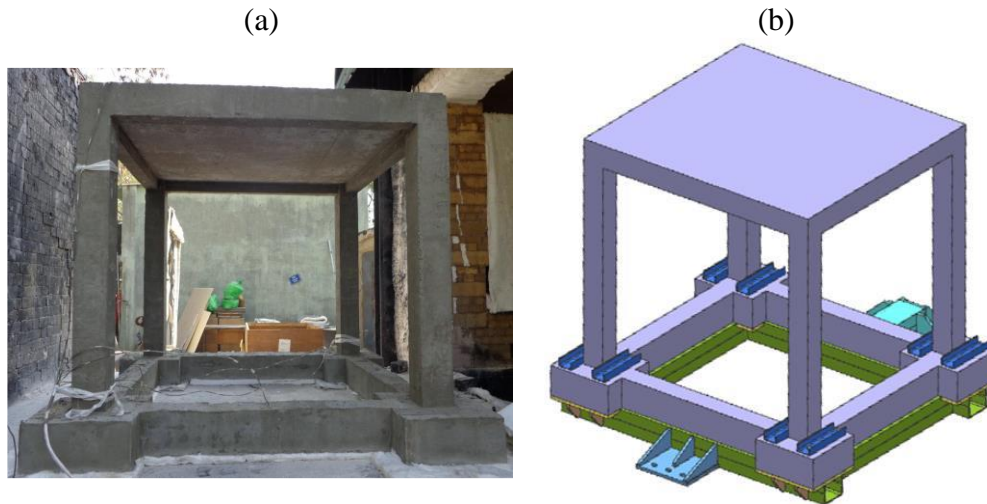


Figure 7-2. (a) RC frame before testing and (b) fixing of the base of the frame (Parmar et al., 2014).

Two bodies are involved in the numerical finite element simulations, the RC frame and the steel impact pendulum. As in the experiment, the first simulation step was characterized with the frame being exposed to thermal load, which consisted of heating and subsequent cooling down to the ambient temperature. The thermo-mechanical analysis is then followed with the dynamic analysis in form of a side impact of steel pendulum. The FE discretization of the complete RC structure is shown in Figure 7-3a, whereby the steel plate represents the pendulum and the steel reinforcement are shown in detail. The experience with the modeling of concrete-like materials shows that relatively simple constant strain finite elements and randomly generated finite element mesh are most suitable to realistically model fracture and damage phenomena. Moreover, the same elements can also be employed for modeling of reinforcement due to the fact that reinforcement bars are mainly loaded in direct tension or compression. The concrete, main reinforcement, stirrups and pendulum are discretized with standard 4 node constant strain solid finite elements sizing from 8 to 13 mm. For pendulum (steel) and foundation (concrete), linear elastic behavior is assumed. The connection of the pendulum and concrete is performed using contact elements that can transfer only compressive contact forces. Full connection between steel and concrete was assumed (perfect bond). To alleviate the stiffness of the connection between stirrups and main reinforcement, the contact elements (stirrups-main reinforcement) are assumed to have reduced stiffness. The surfaces exposed to elevated

temperature are depicted with red color in Figure 7-3c. Note that also the bottom side of the slab was exposed to fire.

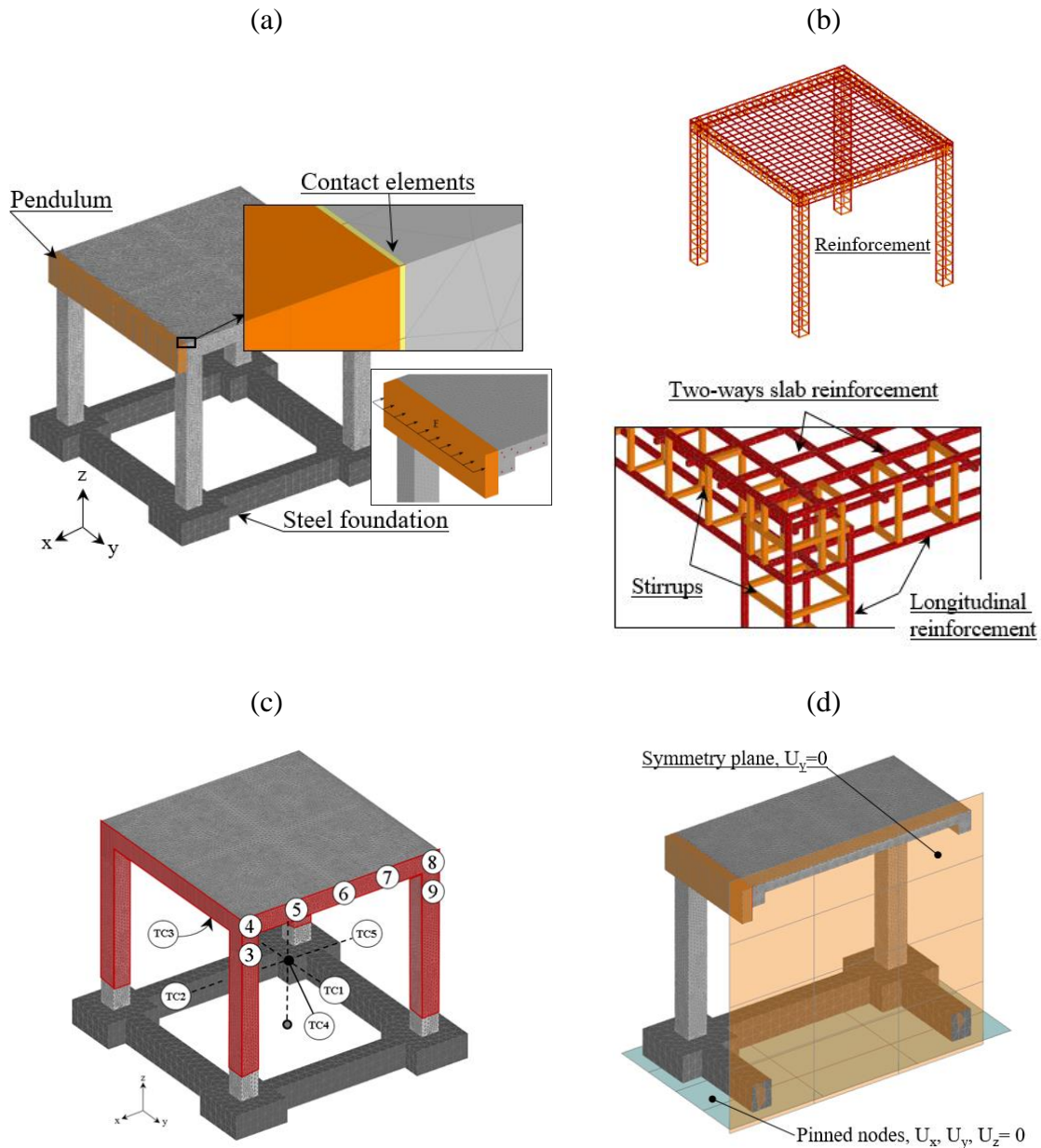


Figure 7-3. 3D finite element discretization of the frame: (a) RC frame, pendulum and contact elements, (b) main reinforcement and stirrups, (c) heated surfaces of the frame in red including bottom surface of the slab and (d) symmetry plane and boundary conditions.

In each simulation, one symmetry plane was utilized, as shown in Figure 7-3d, together with the kinematic constraints of the model. The mechanical and thermal material properties of concrete and steel are summarized in Table 7-1. Note, that the FE discretization, with minor modifications, was principally the same as in Ruta (2018).

Table 7-1. Material properties used in numerical simulations

Property	Concrete	Reinforcement Steel
Weight density (kg/m ³)	2400	7800
Young's modulus (MPa)	26300	210000
Compressive (cylinder) strength (MPa)	18.20	-
Tensile strength (MPa)	1.40	-
Fracture energy (J/m ²)	46.00	-
Poisson's ratio	0.18	0.33
Yield stress (MPa)	-	480
Strength (MPa)	-	550
Heat capacity (J/kgK)	900	490
Heat conductivity (W/mK)	1.36	43.0

7.3.2 Loading history (fire exposure and side impact)

As mentioned before, the frame was first exposed to fire, cooled down to ambient temperature, and subsequently laterally loaded with a side impact of pendulum. The fire load was applied following the fire scenario according to the ISO 834 curve (Figure 7-4) for the duration of 60 min, reaching the maximum ambient temperature of approximately 950 °C (Eurocode 2). Subsequently, the frame was cooled down, with linear decrease of temperature in 120 min, to the ambient temperature of 24 °C with a relatively fast cooling rate of 500 °C/h, where the oven temperature was kept constant for the next 10 h. The first 200 min of the fire loading, compared against the standard ISO 834, is shown in Figure 7-4.

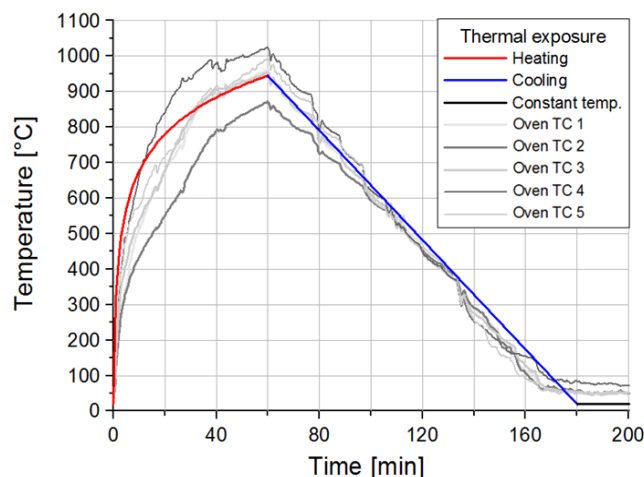


Figure 7-4. ISO 834 heating curve compared against measured temperature (Parmar et al., 2014).

All of the surfaces except the top slab surface and the four footings, which were thermally insulated, were exposed to fire. The frame was pushed on an oven trolley into it. For measuring the temperatures in the oven, 5 thermocouples were placed in the center of the frame and at the

center of each bay. Additionally, 80 thermocouples were installed in the frame to measure the temperature distributions across the columns, beams and the slab cross-sections. To measure the temperature along the height of the frame, five thermocouples were installed on one of the columns.

In the second loading stage, the thermally damaged frame was laterally loaded with a pendulum under an initial impact angle of 23° . The structure was additionally equipped with strain gauges and accelerometers to measure the strain and acceleration histories at different locations on the frame. The horizontal displacement was measured with high-speed camera, with a frame rate of 1000 fps, which kept track of the stickers placed along the frame and the steel pendulum. The horizontal displacements were monitored on the pendulum and at different locations on the frame as well (see Figure 7-5a). The displacement measured in the mid of the pendulum (location 4 from Figure 7-3c) was taken as the displacement loading history applied in the middle of the pendulum in numerical simulation (see Figure 7-5b). Note that in the numerical analysis only the first 0.15 s of loading history (first rebound) was simulated.

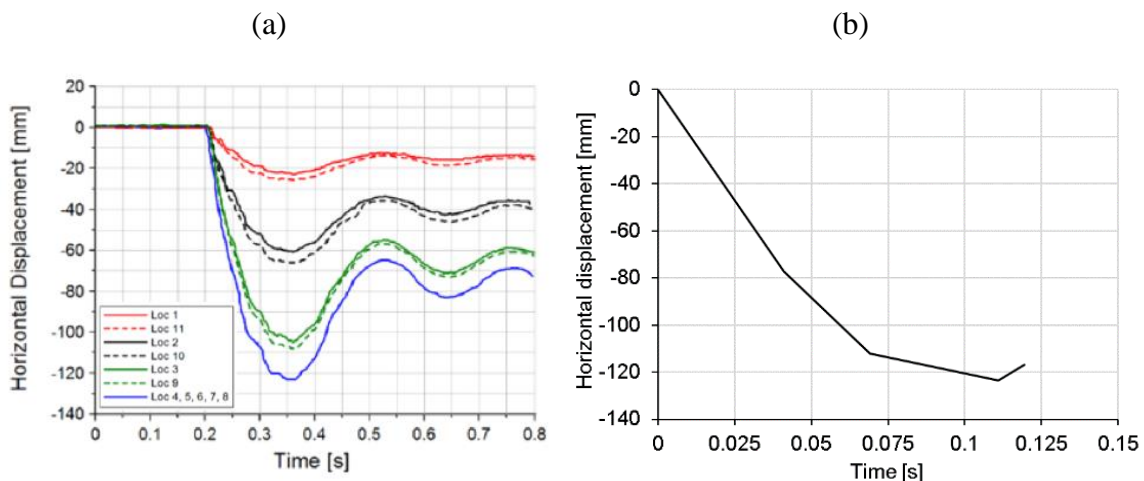


Figure 7-5. (a) Measured displacement load history obtained from the experiment (Parmar et al., 2014; Ruta 2018) and (b) displacement load history applied in the finite analysis at the midline of the pendulum (see Figure 7-3c).

7.3.3 Comparison of the experimental and numerical results

In the following, the typical results obtained from the thermo-mechanical and dynamic simulations are presented and compared with the experimental results. Figure 7-6 shows the distribution of both local and nonlocal temperatures obtained from the transient thermal analysis in column and beam at different locations.

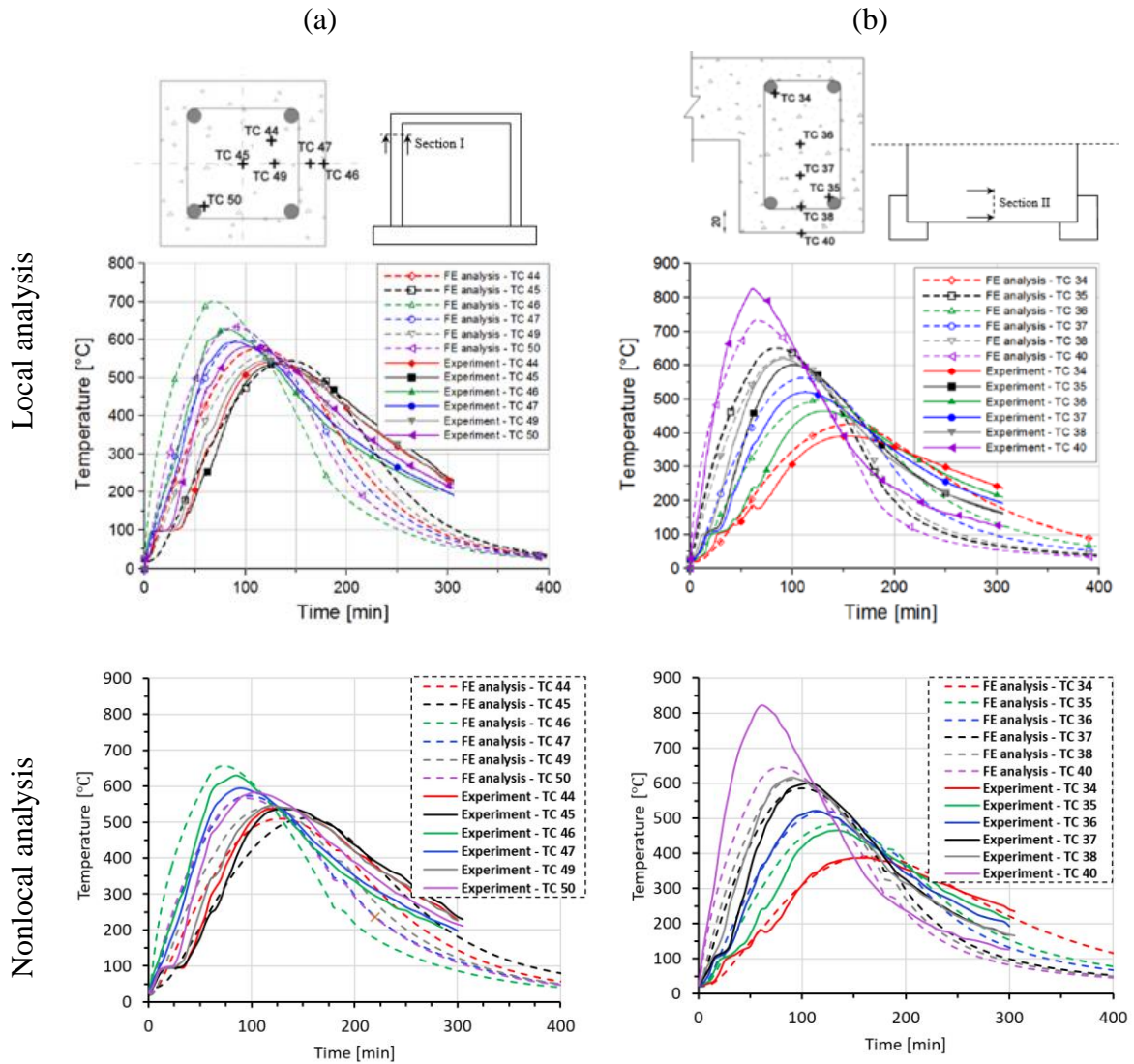


Figure 7-6. Experimentally measured and numerically obtained distribution of temperatures at different locations in local (Ruta, 2018) and nonlocal analysis: (a) column and (b) slab.

Note that heat sources in the furnace cannot assure the same temperature conditions at every position, i.e. the experiment cannot exactly follow the ISO 834 curve as the analysis does. Bearing this in mind, the agreement between measured and computed temperature distributions is relatively good, especially for the beam. Although a peak temperature reduction of approx. 70°C is observed in the nonlocal analysis at the beam edge location, the temperature distribution inside the beam corresponds well to the experimentally obtained ones. As already mentioned,

this effect is only related to the reduction of mechanical properties of concrete. The comparison between local and nonlocal temperature distribution is shown in Figure 7-7. As discussed above, to prevent unrealistic localization of thermally induced damage in concrete, temperature dependent mechanical properties of concrete are assumed to be dependent on nonlocal temperature. In the present study, the characteristic length is taken as $l = 25$ mm. It should be noted that the main differences between local and nonlocal temperature exist close to the exposed surfaces, i.e. in these zones, nonlocal temperatures are slightly lower than the local, due to the relatively large temperature gradients. Local temperature causes unrealistically high thermally induced damage of the concrete surface (impact zone), as will be shown later, which leads to the unrealistic failure of concrete slab.

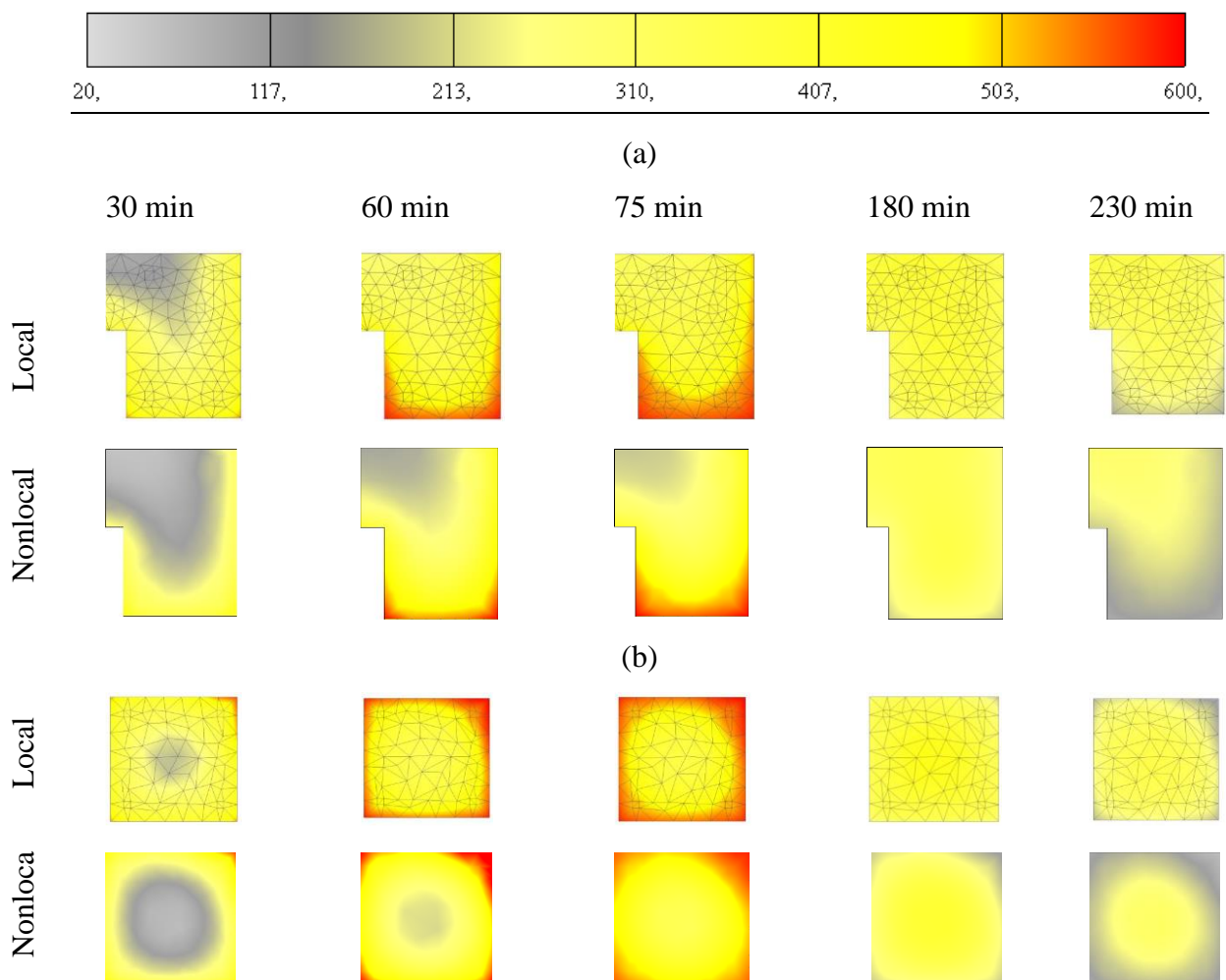


Figure 7-7. Numerically calculated temperature distributions in: (a) beams and (b) columns.

Figure 7-8 shows the comparison between numerical and experimental results in terms of damage of RC frame after thermal exposure and side impact of the pendulum. The red zones represent cracks, in terms of maximum principal strains, which correspond to the crack width equal or greater than $c_w = 6$ mm. Bearing in mind the complexity of the problem, the agreement between experimental and numerical crack patterns is reasonably good.

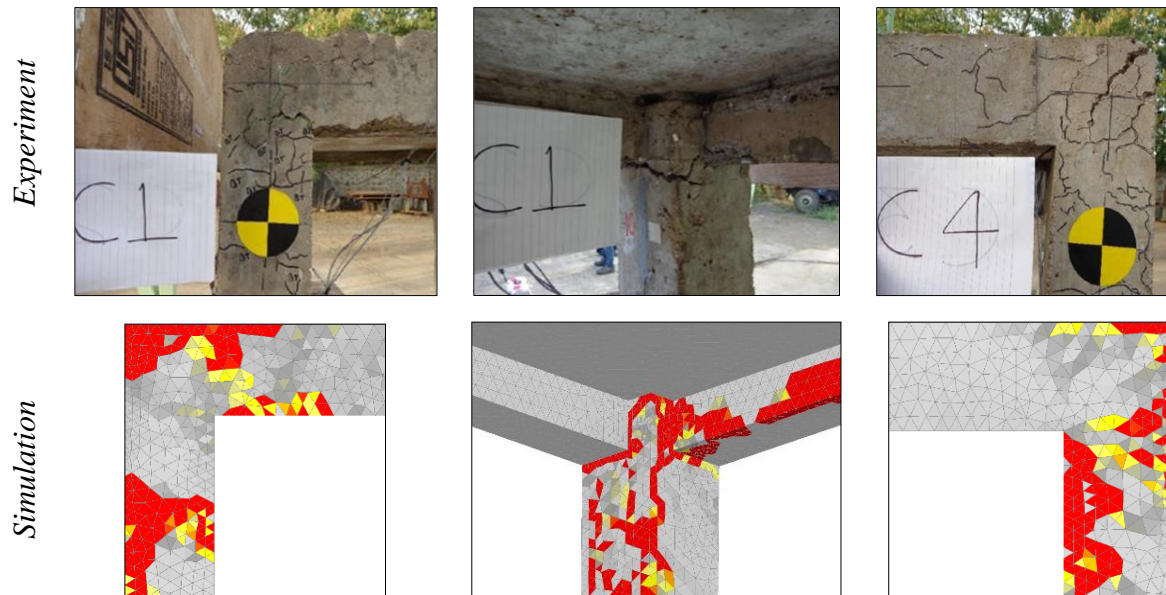


Figure 7-8. Damage of RC frame after thermal exposure and subsequent side impact of the pendulum.

Experimentally measured and numerically obtained time displacement histories at different locations are shown in Figure 7-9. Figure 7-9a displays the comparison between measured and simulated displacements at the contact between RC frame and pendulum using local and nonlocal temperature, respectively. As can be seen, the agreement between the experiment and simulation for the case when nonlocal temperature distribution was employed in the thermo-mechanical model for concrete is very good. However, if the thermally induced damage of concrete is calculated using local distribution of temperature, the failure takes place too early. As mentioned above, this is due to the unrealistic thermally induced damage of concrete slab, not observed in the experiment. The importance of employing nonlocal temperature when accounting for temperature induced damage of concrete seems to be significant. If the local temperature of the concrete surface is used, which in the present case is in the range of $800\text{ }^{\circ}\text{C}$, the concrete cover is unrealistically damaged and not able to transfer the impact load as in the experimental test. Therefore, in all further simulations, nonlocal temperature is used to account for more realistic temperature induced damage of concrete. Note, however, that for steel (reinforcement) local temperature has to be employed.

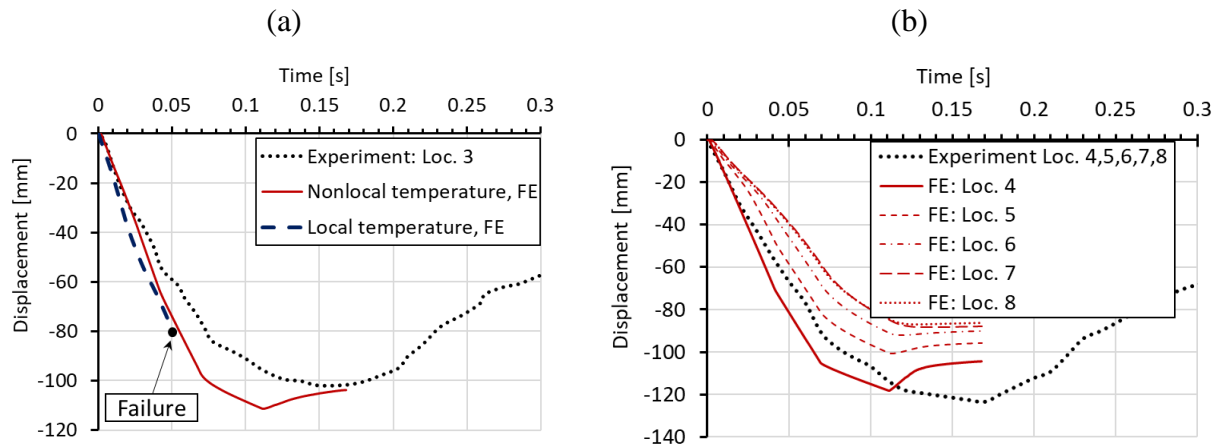


Figure 7-9. Experimentally measured and calculated displacement time histories: (a) Location 3 and (b) Locations 4 to 8.

7.4 Parametric study

To investigate the influence of thermally induced damage of RC frame under static and dynamic loading on its response and resistance, a parametric numerical study was carried out. The simulations were performed for static and dynamic loading, with and without thermal pre-damage. In the case of dynamic loading, the side impact of pendulum was performed for three different displacement rates. Moreover, the importance of the rate sensitive analysis in static and dynamic analysis was investigated. The geometry, boundary conditions and loading were the same as in the above presented experimental and numerical investigations.

7.4.1 Static analysis

Static analysis was performed by controlling horizontal displacement at the pendulum mid-line. Considered are the following cases: (i) initially undamaged frame, (ii) thermally damaged frame, hot and cold state after 30 min of fire exposure and (iii) hot and cold state after 60 min of fire duration. The reactions on the frame foundation are shown in terms of reaction-displacement (RD) responses (see Figure 7-10). The displacement-monitoring node was chosen on the left side of the structure in the contact area of the pendulum and the frame. It is obvious that the thermally induced damage leads to significant decrease in resistance, increase in ductility and decrease of initial stiffness of the frame. The reduction of 22% of the peak reaction between cold and undamaged state can be observed (60 min exposure). However, the response in the hot state exhibits reduction of 42%. The reason for this is the fact that the steel after cooling almost completely restores its strength and stiffness, resulting in higher resistance of

the cold state. Furthermore, by analyzing the initial slope of the RD curves, further differences between the hot and cold states can be observed in terms of stiffness. The initial stiffness is mainly governed by damage of concrete. Therefore, the highest reduction is observed for cold state after 60 min of fire exposure. The accumulation of concrete damage after cooling leads to the overall reduction of initial stiffness. Hot conditions are, on the other hand, unfavorable for the steel reinforcement resulting in overall reduction of resistance since the reinforcement has relatively low contribution to the initial stiffness. It is also interesting to observe that for the hot state after 30 and 60 min of fire exposure, the resistance has not significantly changed. This is because the temperature of the main reinforcement in columns critical sections for $t = 30$ and 60 min is not notably different, i.e., 600 °C vs. 730 °C, respectively.

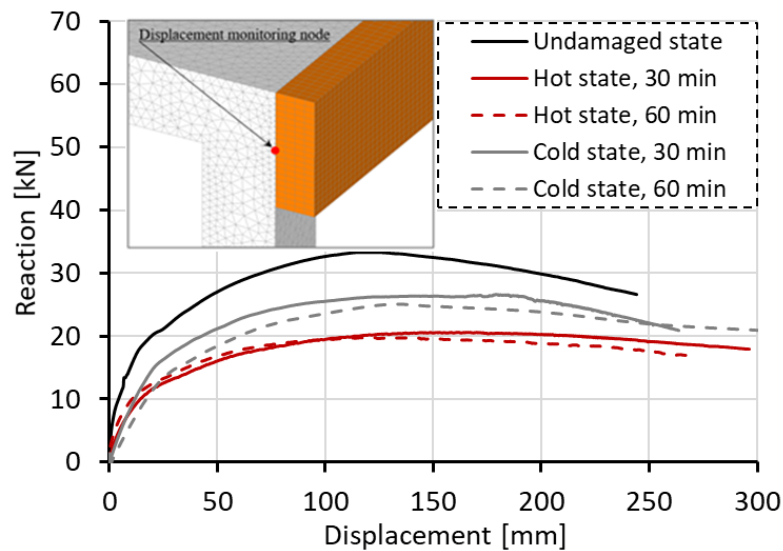
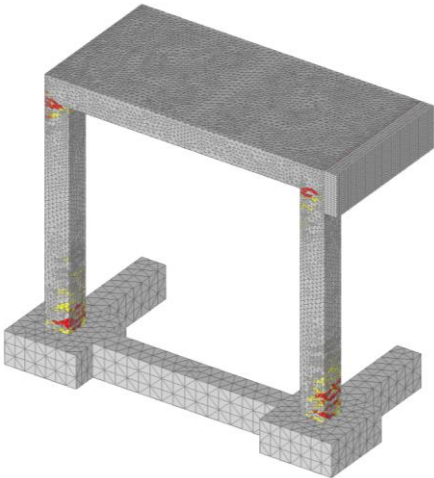


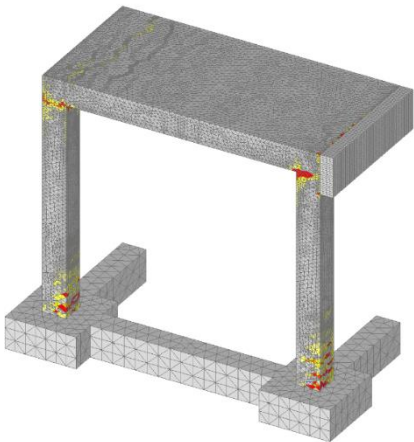
Figure 7-10. Static analysis - reaction-displacement curves.

The typical failure modes are shown in Figure 7-11. The red zones are maximum principal strains, which correspond to the crack width equal or greater than 1.30 mm. It can be seen that in the localization zones (top and bottom of columns) damage is more pronounced for the hot than for the cold state. This is because in hot state, the reinforcement is weaker and consequently, the damage zone is larger and as well as the crack widths.

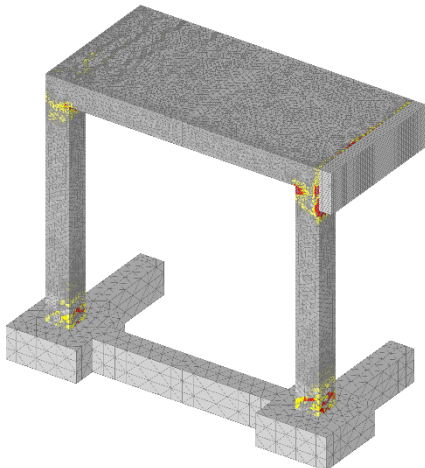
Initially undamaged



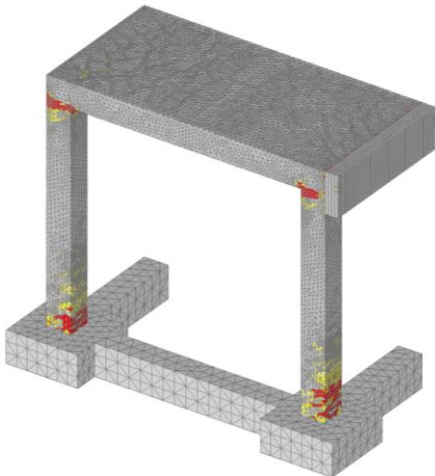
Cold state, 30 min



Cold state, 60 min



Hot state, 30 min



Hot state, 60 min

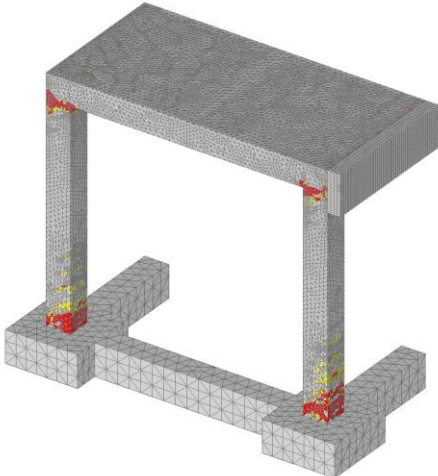


Figure 7-11. Static analysis - Localization of damage in concrete after peak resistance.

7.4.2 Dynamic analysis

In the dynamic analysis, the loading time history was the same as in the experimental test and simulation from chapter 7.3.2 (see Figure 7-5b). The initial displacement rate of 1885 mm/s was applied through the control of the mid-line of the pendulum. The same cases are investigated as in above-discussed static analysis. The RC curves are shown in Figure 7-12 and the predicted peak reactions, together with reactions obtained in static analysis, are summarized in Table 7-2. Note that displacement is monitored in the same node as in the static analysis (see Figure 7-10).

Comparing the RD curves, it can be seen that principally the same is valid as for the static analysis, i.e., with increase of temperature induced damage, the peak resistance and initial stiffness decreases, especially for the hot state. The degradation of peak reaction for cold state is lower than in the case of static analysis. When compared to dynamic resistance of undamaged frame with that of thermally pre-damaged (60 min of fire, cold state), the degradation is only 16%. Moreover, the reduction of initial stiffness is smaller than in the case of static loading and ductility of the response is not strongly influenced by the thermal damage. However, for the hot state, besides concrete, the reinforcement is damaged as well and consequently, relatively high reduction of dynamic resistance (48%) and initial stiffness is observed for a duration of 60 min of fire. The reason for relatively large differences in the responses of cold and hot state is that in hot state concrete and reinforcement are damaged, however, in cold state the mechanical properties of steel are almost fully recovered.

Table 7-2. Summary of the peak reactions for static and dynamic analysis.

State	R_{stat} (kN)	R_{dyn} (kN)	$RDIF$ (R_{dyn}/R_{stat})
Undamaged	33.28	65.43	1.97
Hot state (30 min)	20.45	51.29	2.51
Cold state (30 min)	26.56	62.46	2.35
Hot state (60 min)	19.70	33.97	1.72
Cold state (60 min)	24.82	55.01	2.22

The comparison between RD curves for static and dynamic loading shows that dynamic resistance is higher and the response stiffer. There are two principal reasons for this: (i) rate sensitive constitutive law for concrete and (ii) inertia effects of different kinds (e.g., inertia due to damage and crack propagation, yielding of reinforcement, structural inertia). In Table 7-2

the relation between dynamic and static peak resistance of the frame ($RDIF$) is also shown. As can be seen, the dynamic resistance of the frame for different states and given loading conditions is not very different, as it varies between 1.72 and 2.51.

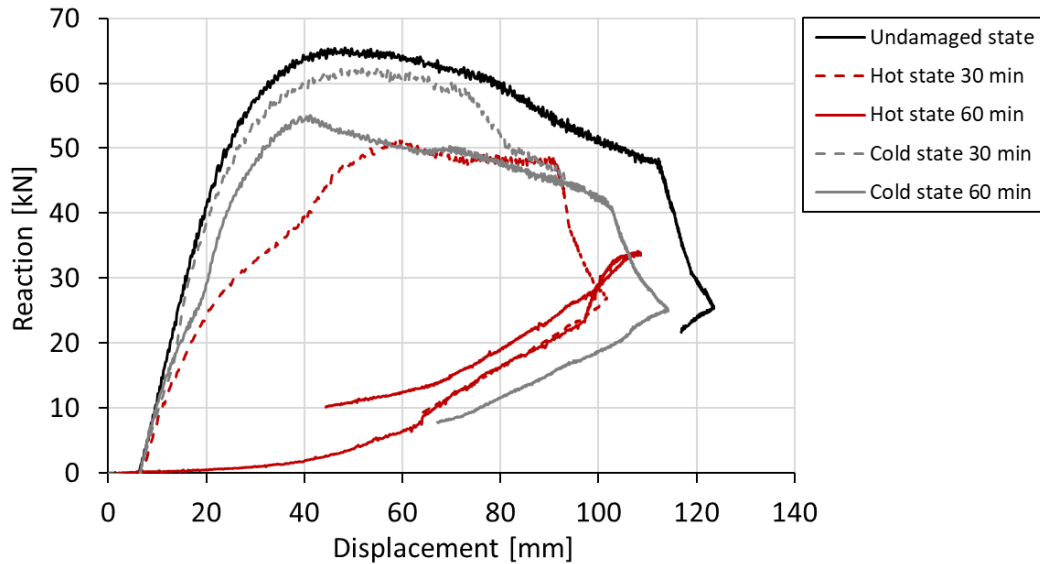


Figure 7-12. Dynamic analysis - reaction-displacement curves.

The typical failure modes are shown in Figure 7-13. The red zones are maximum principal strains, which correspond to the crack width equal or greater than 11 mm. In contrary to the static analysis, damage of the frame is for all loading histories localized in the slab and the top zone of the columns. With increase of thermally induced pre-damage, the size of damage due to impact of pendulum also increases. As shown above, the highest reduction of resistance and initial stiffness was observed for the hot state after 60 min of fire exposure. The reason is thermally induced damage of concrete and reduction of strength and stiffness of reinforcement. The comparison between cold and hot state is shown in Figure 7-14. Stresses in reinforcement on deformed geometry are also shown. It is obvious that for the hot state deformations, and therefore stiffness, are significantly larger than for the cold state.

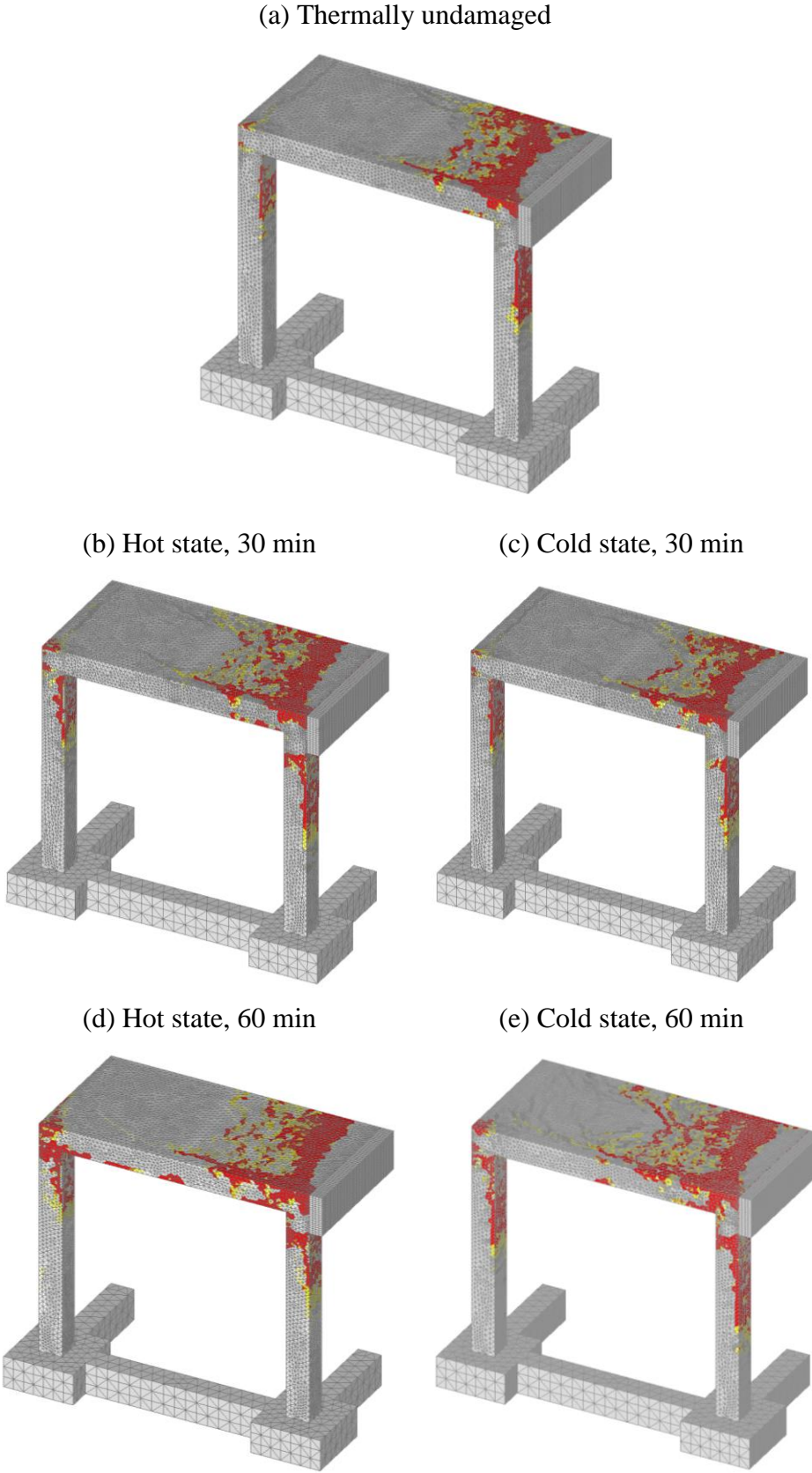


Figure 7-13. Dynamic analysis - Localization of damage in concrete after peak resistance.

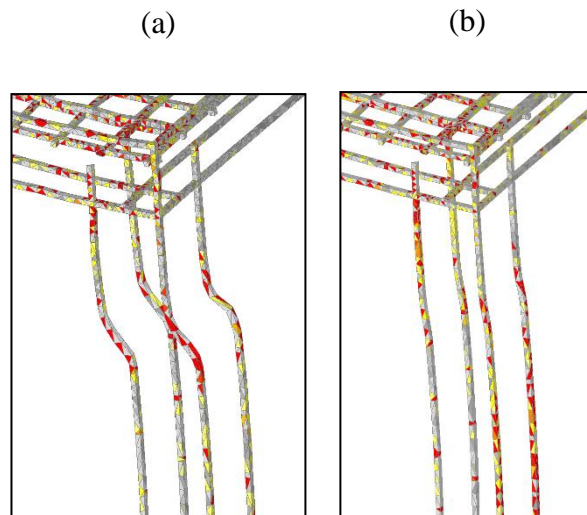


Figure 7-14. Stresses and deformations in column reinforcement after 60 min of fire exposure at peak reaction: (a) hot state and (b) cold state; red corresponds to the maximum principal stress of approximately 300 MPa.

7.4.3 Rate sensitivity study

As discussed above, the dynamic response exhibits higher resistance and stiffness. This is a consequence of the contribution of the rate dependent constitutive law of concrete and inertia effects. To investigate the contribution of these two effects on the dynamic response of the initially undamaged RC frame, additional parametric study is carried out. Static and dynamic analysis with and without rate sensitivity for three different displacement-loading histories of the pendulum (see Figure 7-15): low (241 mm/s), medium (725 mm/s), and high (1885 mm/s, same as above) are performed. The analyses are carried out only for initially undamaged RC frames.

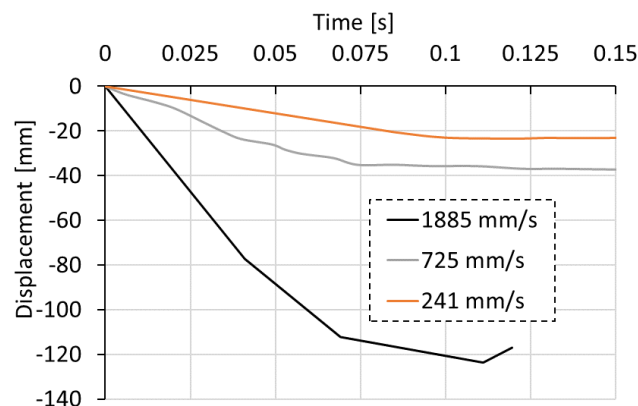


Figure 7-15. Applied displacement time histories of the pendulum.

The typical reaction vs. pendulum-displacement responses are shown in Figure 7-16. As expected, for quasi-static load the resistance (reaction) only slightly increases with increase of

loading rate (Figure 7-16a). The increase approximately follows the rate dependent constitutive law since the failure mechanism is independent of the loading rate and there are no inertia effects (Figure 7-17). The concrete strength and fracture energy increases with the increase of loading (strain) rate, according to the rate sensitive constitutive law, and the structural resistance also increases.

However, interesting behavior can be observed for dynamic loading. For relatively high loading rate (1885 mm/s), the rate sensitivity has a significant contribution to the resistance (reaction) and failure mode, i.e., the resistance is approximately double compared to the case without rate sensitivity (Figure 7-16b). The main reason is due to the different failure modes. Namely, without rate sensitivity the failure takes place in the slab, at the front of the pendulum impact zone (see Figure 7-18). Therefore, the load is not transferred to the second row of columns of the frame. In contrary to this, when the strain rate is activated, the concrete resistance increases and the transfer of load over the slab to the second row of columns becomes possible. According to the rate dependent constitutive law, tensile and compressive strength become higher than in the case of no rate sensitivity and there is no local failure of concrete slab in the impact zone. Obviously, because of the higher dynamic resistance of the concrete slab, the failure mode changes with the consequence that the dynamic resistance of the frame increases.

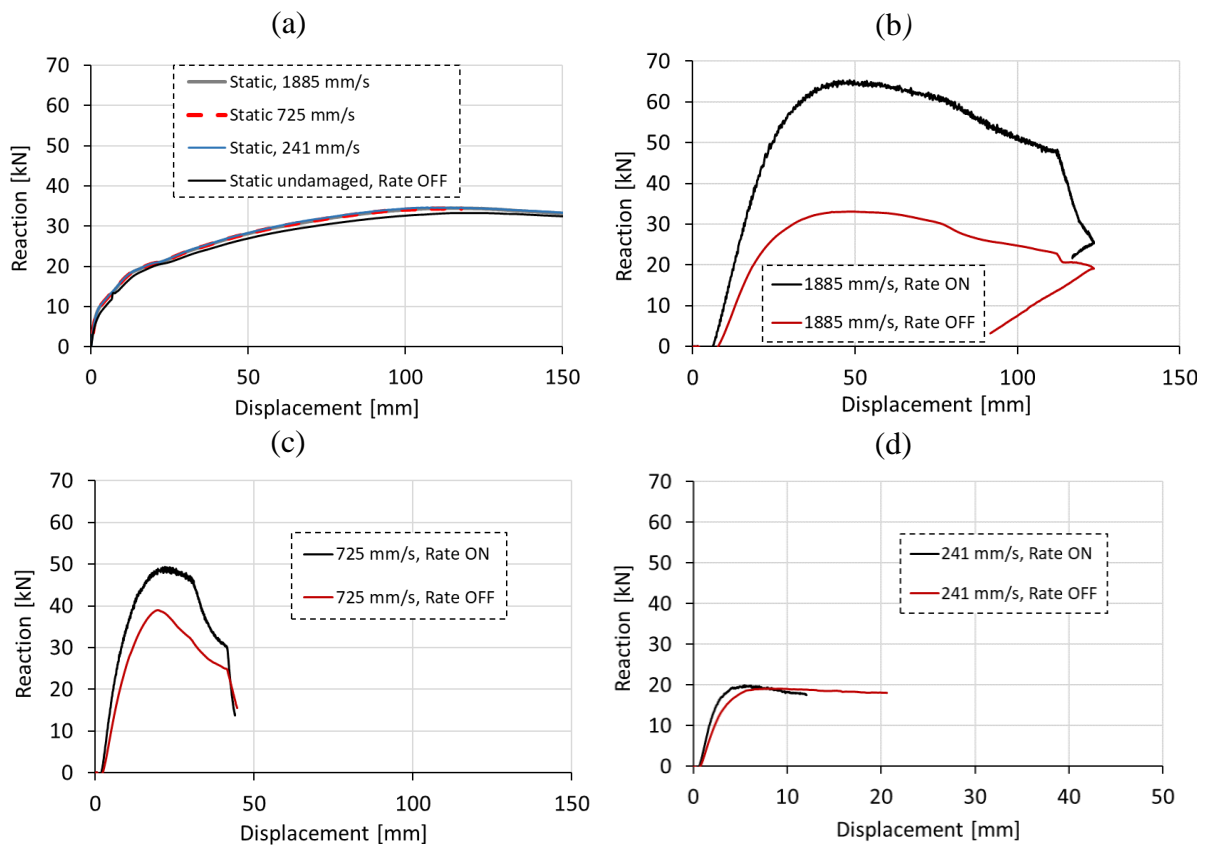


Figure 7-16. Reaction vs. displacement: (a) quasi-static and dynamic for initial loading rates: (b) 1885 mm/s, (c) 725 mm/s and (d) 241 mm/s.

For the medium impact velocity (725 mm/s), the impact force can be transferred over the slab in both cases, i.e., with and without rate sensitive constitutive law. Therefore, the effect of rate sensitivity is less important. However, compared to the structural inertia, its contribution is still relatively high. For instance, by comparing RD curves for the loading rate of 725 mm/s (Figure 7-16c) with the quasi-static RD curve (Figure 7-16a), it can be concluded that the contribution of strain rate sensitivity is still relatively high. The static resistance is approximately 33 kN, dynamic with rate sensitivity 49 kN, and dynamic without rate sensitivity is 39 kN, respectively. This means that the contribution of rate sensitivity to dynamic resistance is 10 kN and the contribution of inertia 6 kN ($33 + 10 + 6 = 49$ kN). Of course, this is valid only for this example; however, it principally depends on a number of parameters such as loading rate, structure geometry, size, etc. Figure 7-16d shows the comparison of RD curves for relatively low loading rate (241 mm/s), which does not lead to the failure of the frame. The peak load is lower than the static resistance and it can be seen that for this case, where the impact load does not cause the collapse of the frame, the effect of rate sensitivity is relatively small. By comparing the failure modes obtained from quasi-static and dynamic analysis, it can be seen that in static analysis the critical sections are the top and bottom of the columns (Figure 7-17). However, in the dynamic analysis critical sections are the top zones of the columns and the slab, especially at the front of the impact surface. It is also obvious that the damage is more pronounced if the rate sensitivity is not accounted for (Figure 7-18).

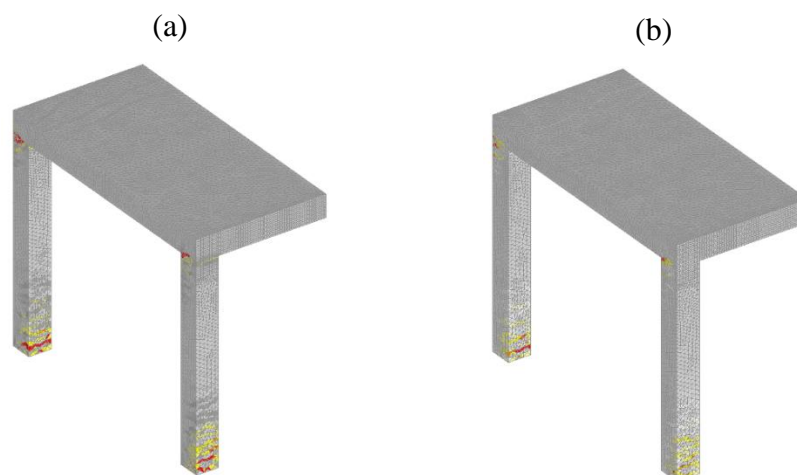


Figure 7-17. Crack pattern at peak load, quasi-static analysis for loading rate 1885 mm/s: (a) no rate sensitivity and (b) with rate sensitivity (red = maximum principal strain that corresponds to crack width = 1.30 mm).

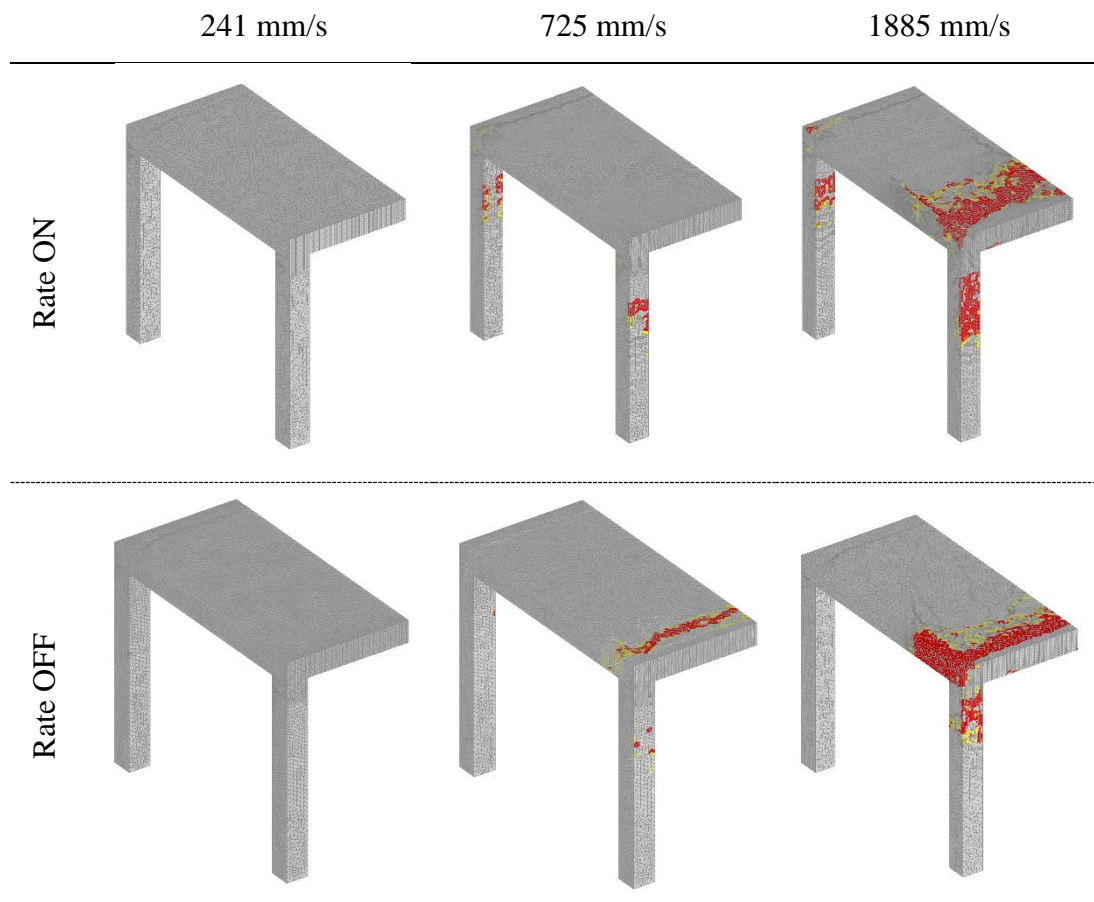


Figure 7-18. Dynamic analysis, failure modes for different loading rates with and without rate sensitivity (red = maximum principal strain that corresponds to crack width = 3 mm).

7.5 Conclusions

In the framework of the present numerical study, the rate dependent thermo-mechanical model was initially validated and subsequently, a parametric study including the static and dynamic 3D FE simulations of initially undamaged and thermally pre-damaged damaged RC frames were carried out. Based on the results, the following conclusions can be drawn: (i) comparing the numerically calculated results with the experimental data, it can be concluded that the thermo-mechanical transient analysis based on the temperature dependent microplane model is able to realistically replicate the experimental dynamic test of thermally pre-damaged RC frame; (ii) the temperature degradation of concrete mechanical properties should be calculated with the nonlocal (average) temperature instead of local temperature obtained from the standard transient thermal analysis This has been verified and it is mainly applicable in conjunction with dynamic (impact) analysis; (iii) the parametric analysis showed that the fire exposure of RC frames and related thermally induced damage significantly influence their behavior and resistance; (iv) for quasi-static loading, the reduction of structural resistance is the highest for

the hot state because the steel reinforcement after cooling almost fully recovers. In the contrary to the peak resistance, the initial stiffness is controlled by concrete properties and it decreases with increasing of fire exposure. Consequently, the initial stiffness is lower for cold state. Ductility of the response was increased with the increase of fire duration; (v) compared to quasi-static analysis, in dynamic analysis the reduction of resistance and initial stiffness is principally similar, however, it was established that the RC frame exhibits different responses loaded in either hot or in cold (residual) state. The results show that the reduction of resistance and the initial stiffness is significantly higher for the hot state. The overall response is more brittle due to the contribution of inertia; (vi) it was demonstrated that with the increase of the loading rate, the influence of strain rate becomes more pronounced than the contribution of effects due to inertia. Conclusively, the rate sensitive constitutive law for concrete significantly contributes to dynamic structural resistance and failure mode. However, it should be pointed out that its contribution to the overall structural response does not depend only on the loading rate but also on a number of other parameters (e.g., structure type and size, loading, material properties, etc.) and should be investigated for each case separately (Ožbolt et al., 2020).

8. RC FRAME SUBJECTED TO THERMAL AND CYCLIC LOADING (POST-EARTHQUAKE FIRE)

8.1 Introduction

Considering the loading conditions and its sequence discussed in the previous chapter, where the RC frame was first exposed to fire and subsequently loaded with impact; the aim of the present study is to numerically investigate the cyclic response of a single story RC frame structure subjected to post-earthquake fire (PEF). The PEF scenario constitutes the case where the structure is first cyclically loaded and then exposed to fire, which ultimately represents a more realistic scenario in terms of load sequence. Furthermore, the PEF can cause a rapid collapse of structures previously damaged as a consequence of a prior earthquake. The geometry and boundary conditions of the investigated RC frames were taken from the experimental work on full scale tests of RC frames exposed to PEF carried out by Shah et al. (2017). In the experimental study, the influence of the pre-damage level, the reinforcement detailing and masonry infill on the performance of the RC frames subjected to PEF was investigated. In the numerical validation cases, however, the case with the masonry infill was omitted. Furthermore, to show the influence of the reinforcement configuration, the validation of the numerical model was performed for the cases with and without ductile detailing. After the thermo-mechanical model has been properly calibrated and validated, the parametric study with different fire exposure durations according to ISO 834 fire curve was carried out.

8.2 Experimental studies on RC frame structures in post-earthquake fire scenario

An extensive experimental work carried out on a full scale RC frames was performed by Shah et al. (2017) within the facilities of civil engineering department of IIT Roorkee, India. The tested frames were initially subjected to predetermined earthquake loading before being exposed to a compartment fire with the duration of one hour. Subsequently, the frames were again tested for residual resistance. The aim of the experiment was to investigate the influence of the following loading and structural parameters on the performance of the RC frames in the PEF scenario:

- (i) Seismic cyclic loading: two different magnitudes of lateral displacement were imposed on the RC frame corresponding to 2% and 4% of the story drift as per FEMA 356 (FEMA 356, 2000),
- (ii) Reinforcement detailing: Two types of reinforcement level were embedded in the geometry of the frame. One designed as per guidelines of the Indian standard code

IS 456:2000 without the use of ductile detailing and one per guidelines of the IS 13920:1993 with ductile detailing,

- (iii) In one of the frames, a masonry infill was added in between the beams and columns (not considered in the framework of this study).

The sizes and the configuration of the RC frame elements is provided in Table 8-1.

Table 8-1. Configuration of the RC frames used in the experiments (Shah et al., 2017).

RC frame element	Number of elements	Size of the element (cross-section)	Concrete grade
Column	4	300 × 300	M30
Plinth beam	4	230 × 230	
Roof beam	4	230 × 230	
Roof slab	1	120 mm thick	
RC raft	1	6900 × 8700	
foundation	1	(900 mm thick)	

All in mm

The reinforcement of the frames was designed with steel bars of grade Fe500 having the yield strength of 500 MPa. The typical reinforcement details and the concrete dimensions in the RC frame with and without ductile detailing are provided in Figure 8-1 and Figure 8-2, respectively.

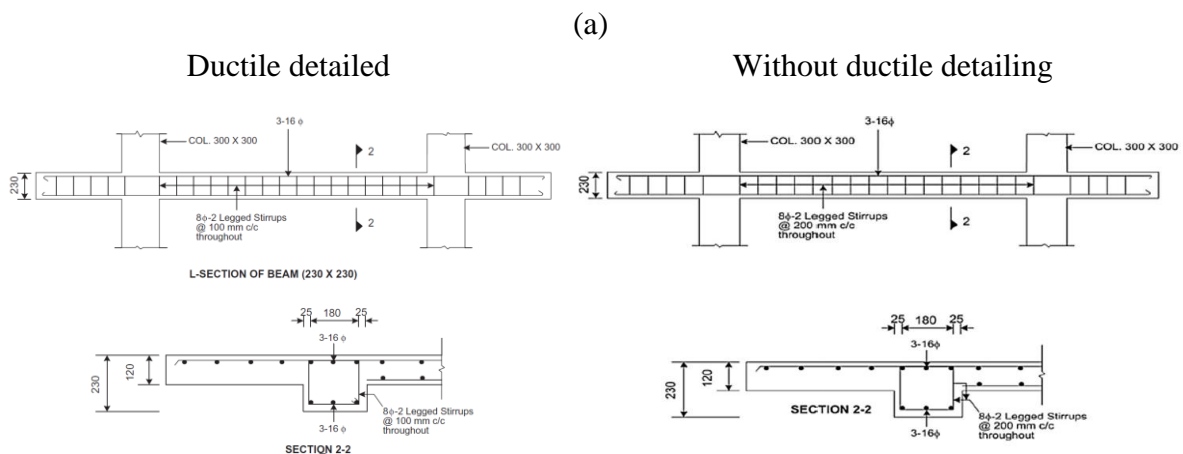


Figure 8-1. Reinforcement details in the cross-section view of different frame elements: (a) Beam reinforcement for both reinforcement configurations, (b) Ductile column detailing (IS 13920, 1993) and (c) Column without ductile reinforcement detailing (IS 456, 2000), (Shah et al., 2017).

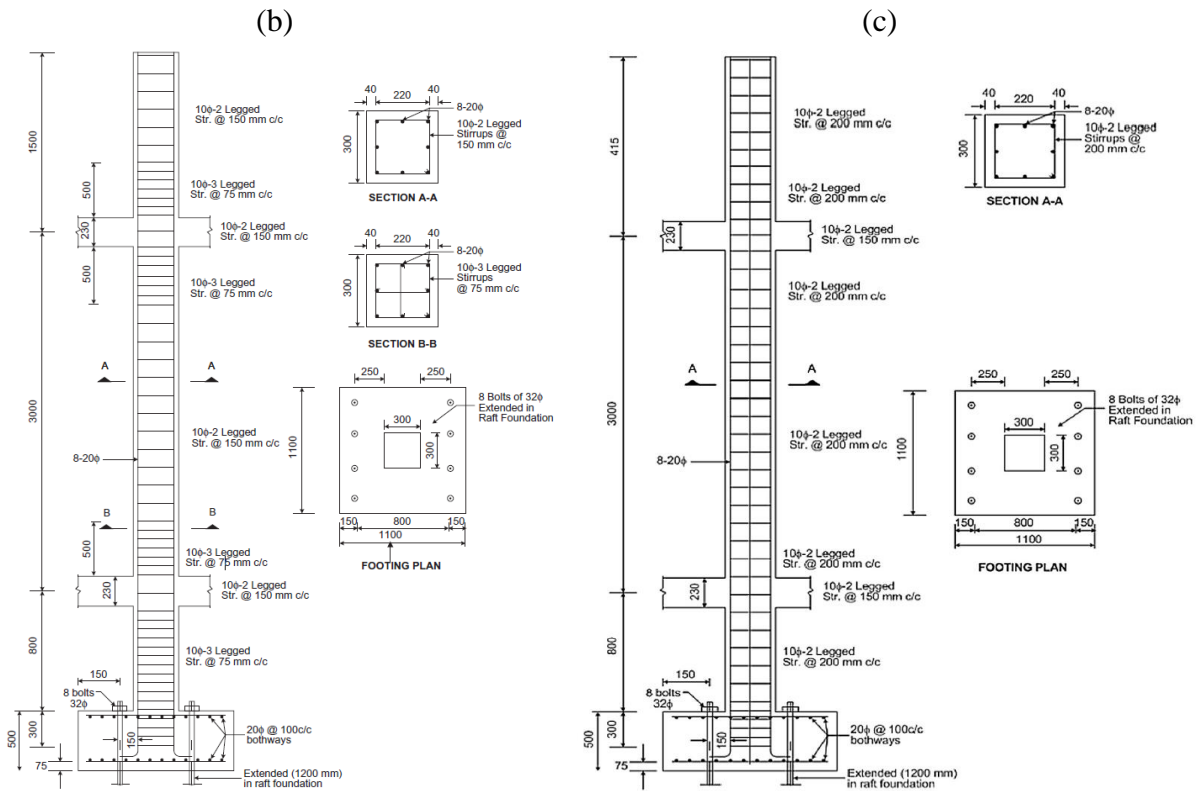


Figure 8-1. (Continued).

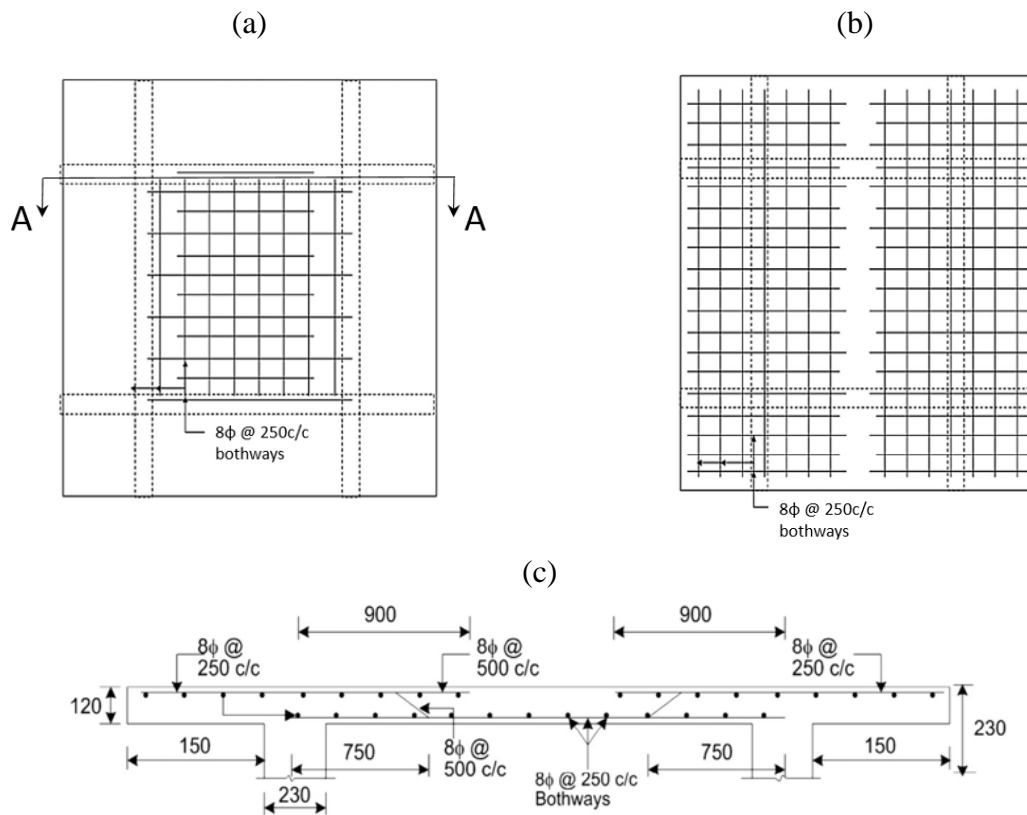


Figure 8-2. Reinforcement details in: (a) Top reinforcement of the slab, (b) bottom reinforcement of the slab and (c) transversal slab cross-section (Shah et al., 2017).

The test procedure utilized in the experimental tests followed three loading phases consisted of initially subjecting the test frame to a lateral cyclic load in a quasi-static fashion followed by one hour compartment fire and ultimately subjecting the frame to the residual monotonic pushover. The frames with its own specific designation used in the tests are listed in Table 8-2.

Table 8-2. RC Frame specifications in the experiment (Kamath et al., 2015; Shah et al., 2017).

Frame Specification	Ductile detailing	Masonry infill	Roof drift ratio as per FEMA 356:2000
“A”	+	-	2 %
“B”	+	-	4 %
“C”	-	-	4 %
“D”	-	+	4 %

8.2.1 Seismic load test

Ahead of the initialization of the first test phase, the gravity and the imposed loads were applied on the frames according to the guidelines of Indian standard IS 1893 (BIS IS 1893 Part I, 2002) and they amounted to 1 kN/m^2 and 2 kN/m^2 , respectively. The design loads were set to 25% of 2 kN (0.5 kN/m^2). The gravity loads were imposed on the structure in a self-calibrating loading manner, so that the loads of the upper floors of the G+3 structure could be realistically simulated. The vertical load was transferred through four hydraulic jacks positioned centrally on top of each column. Between the jacks and the column, a specially designed ball bearing assembly was installed to maintain the verticality of the jacks during the seismic load. The live load of the slab and the weight of the walls on the roof beams was simulated by placing the sandbags uniformly along the slab and roof beam surface (Figure 8-3). The simulated seismic lateral loading was applied using the prescribed displacement controlled by two double acting hydraulic actuators. The story drift was achieved by applying lateral cyclic displacement corresponding to the “Life Safety” structural performance level of FEMA 356:2000 (FEMA 356, 2000) for frame “A” and the “Collapse Prevention” performance level for the rest of the frames. The maximum achieved roof level displacement for Frame “A” was 75 mm corresponding to 2% of roof drift ratio and 150 mm for Frames “B”, “C” and “D” corresponding to 4% of roof drift ratio (FEMA 356, 2000). The frames were subjected to a number of push pull cycles with 10 mm successive increase with each cycle until the displacement reached the applied roof drift ratio (Figure 8-4).

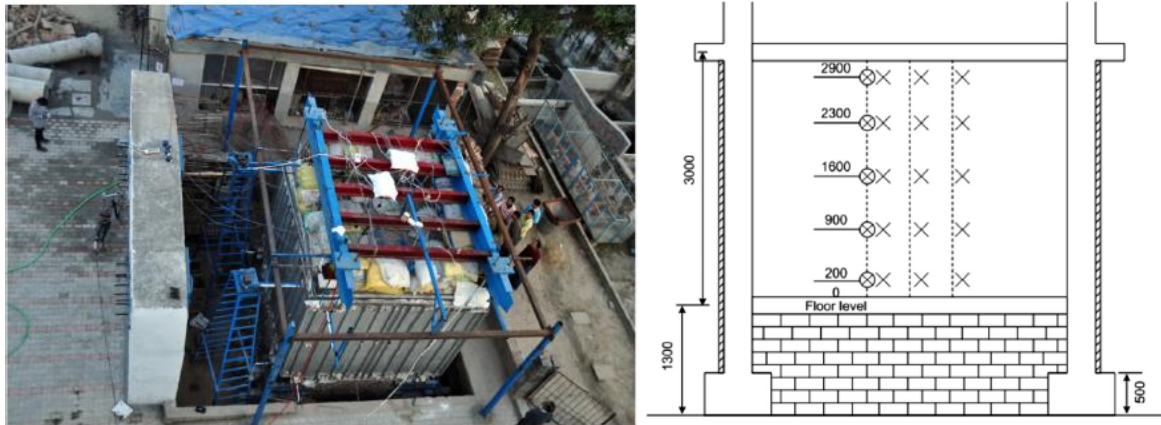


Figure 8-3. The RC frame before the fire test (with imposed, gravity and design loads) (a) and side view of the RC Frame with the vertically installed thermocouples (b) from Shah et al. (2017).

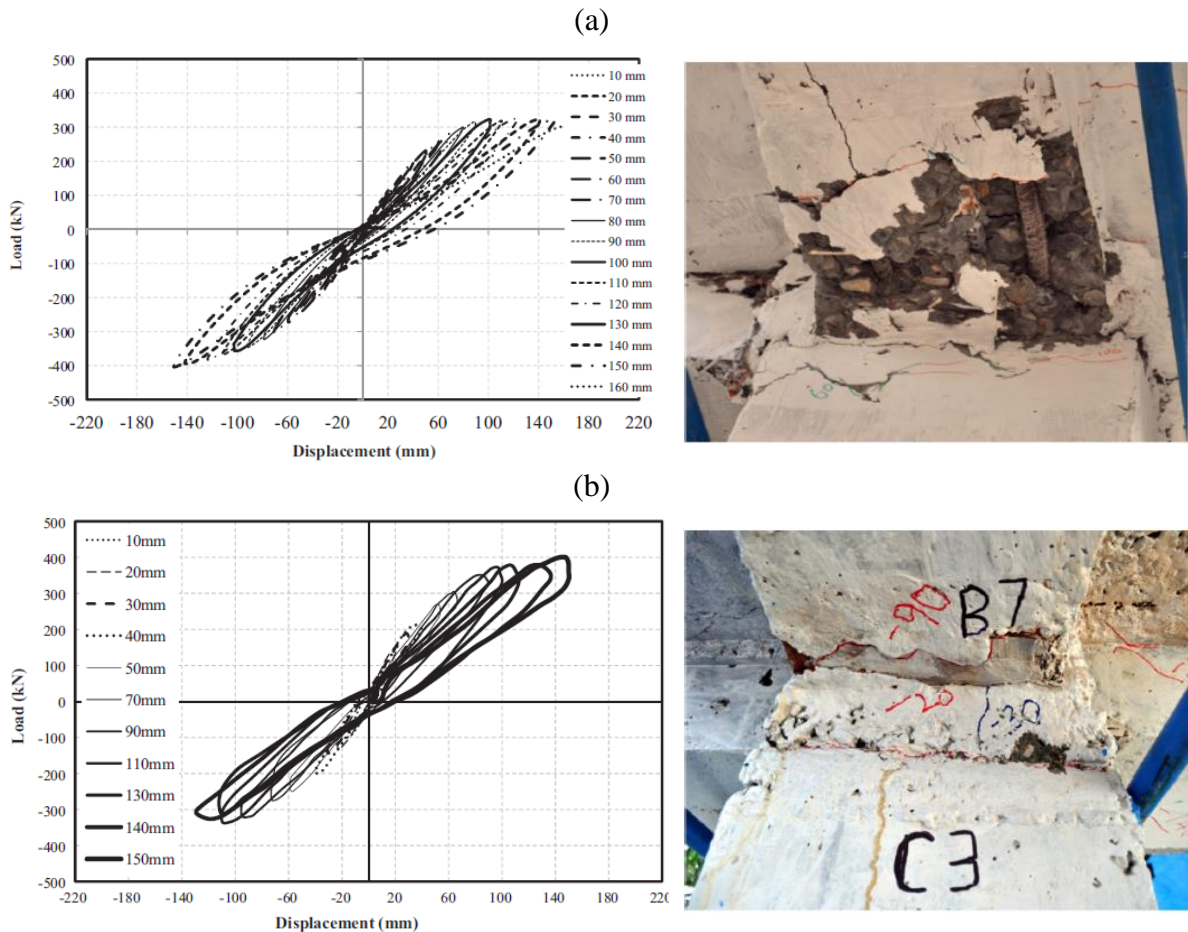


Figure 8-4. Measured hysteretic curves and the corresponding damage in the beam column joint section for frames: (a) "C" and (b) "B" (Shah et al., 2017).

8.2.2 Fire test

RC frame is a heterogeneous structure consisted of steel and concrete, which exhibit different thermal characteristics at elevated temperatures. Since concrete has a low thermal conductivity compared to steel, when an RC structure is exposed to elevated temperature without being subjected to cyclic load, the steel reinforcement bars are protected by the concrete cover. However, in a PEF event involving a high temperature fire exposure, major concrete spalling occurrences are observed. During spalling (explosive), large pieces of concrete are being detached from the structural members leaving the steel directly exposed to fire. Subsequent to the simulated seismic load, the test frame was subjected to a compartment fire test with the duration of one hour and subsequently left to cool down to the ambient temperature lasting in total 18h. The fire test duration and the target temperature were carried out following the procedure described by Thomas and Heselden (1972) to achieve the temperatures in the range of 900 to 1000°C using the kerosene oil as fuel. During the fire test, the test frame was encapsulated with four detachable fireproof panels, which were fastened to the metal frame. The fireproof panels had an opening of 1 m in height and 3 m in length on one side of the fire to ensure and enhance the accumulation of smoke for the rapid flashover and ventilation. The fire was facilitated by using a mild steel tray burner of size 1 m × 1 m × 0,05 m that was placed in the bottom center of the compartment. The achieved compartment temperature in certain thermocouples was however much higher than the targeted temperature due to the highly stochastic nature of fire (Figure 8-6). The temperature time history from thermocouples shown in Figure 8-5a. correspond to the illustrated scheme of vertically distributed “×” marks in Figure 8-3b with TMIC21 having the lowest vertical position and TMIC25 the greatest.

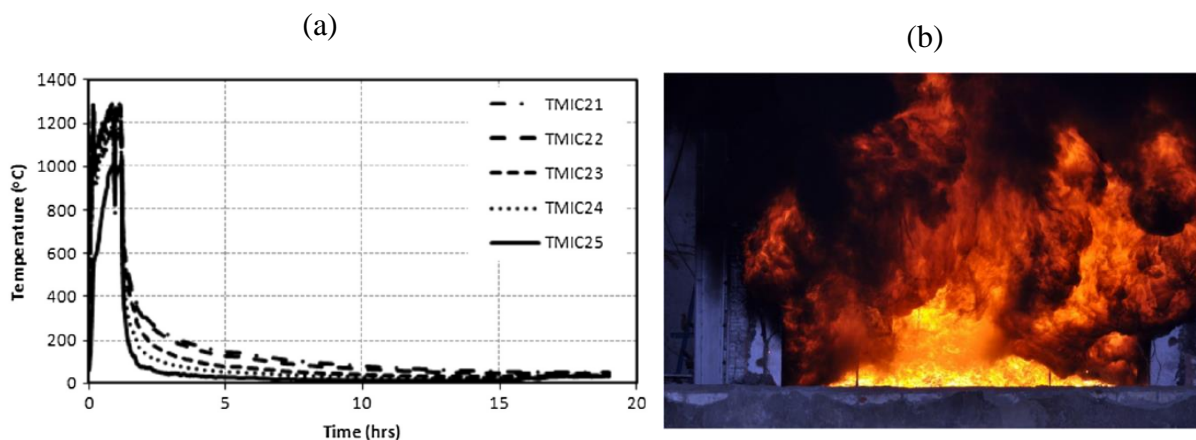


Figure 8-5. Measured temperature time curve inside the compartment at different heights (a); Compartment fire (b); spalling in the roof slab with non-ductile detailing (c) (Kamath et al., 2015).

(c)



Figure 5. (Continued).

The damage accumulated during the simulated seismic load was further aggravated with the thermally induced damage. All of the frames exhibited strong spalling effect, mostly emphasized on the inner slab surface. This led to the reinforcement exposure and a direct contact of fire with the steel reinforcement bars, which ultimately resulted in a more pronounced vertical deflection of the slab. The lack of collapse of the roof slab after severe spalling proves that the thermally assisted compressive membrane action can considerably enhance the load bearing capacity of the slab. Furthermore, considering the temperatures in certain structural members of different frame configurations, higher temperature can be observed in the same location in the frame “C” with non-ductile detailing compared to frame “B” with ductile detailing. This temperature buildup in the frame with non-ductile detailing can be attributed to more pronounced cracks developed during the simulated seismic load test and different compartment fire temperature in that point (Shah et al., 2017).

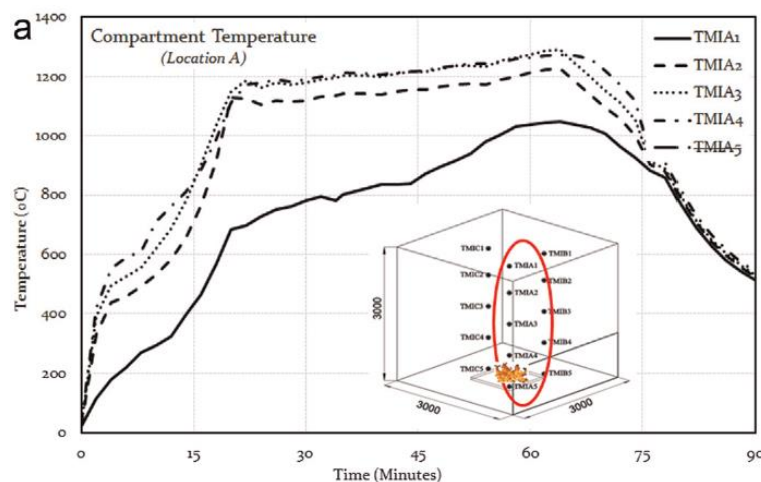


Figure 8-6. Measured compartment time-temperature curves at different heights in the first 90 minutes of the thermal phase (Kamath et al., 2015).

Figure 8-6 shows the temperature distribution along the vertical line inside the fire compartment. It is obvious, that the flashover has a significant influence on the temperature in the upper regions of the compartment, as there the temperature has its peak. It also displays just how the temperature is uneven in the compartment.

8.2.3 Residual test

The third test phase was initiated after the RC frames were exposed to the compartmentalized fire. The test frames were then again subjected to cyclic loading following the same time displacement history as in the initial phase of the test study. Figure 8-7a. and b show the load displacement curve of Frames “C” and the aftermath of the residual test, respectively. A substantial reduction of structural stiffness can be observed compared to the first seismic test. Furthermore, the reduction of the load bearing capacity of the frame “C” at the displacement of 150 mm was 35% while frame “B” with ductile reinforcement detailing exhibited only 5% reduction.

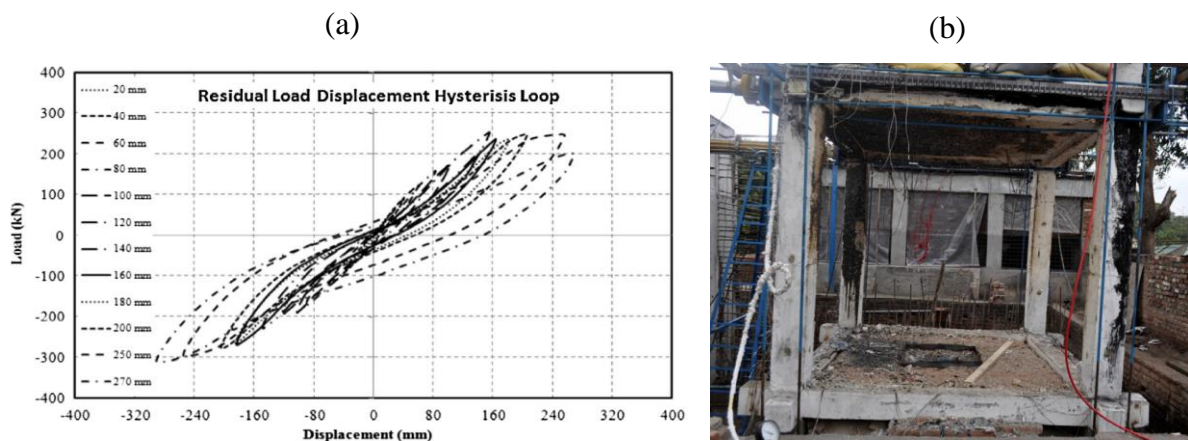


Figure 8-7. The residual load-displacement hysteresis loop of the frame without ductile detailing (a) and the RC frames after residual test (b) (Shah et al., 2017).

8.3 FE model, initial and boundary conditions

The finite element mesh of the RC frame was prepared in a pre- and post-processing program FEMAP according to the geometry specifications provided in the experimental data (Shah, 2017). The 3D view of the complete model with its corresponding structural denominations is shown in Figure 8-8a. The FE model of the ductile detailed frame consists of 580768 constant strain solid 3D finite elements with 4 nodes that represent concrete, brick and mortar; 3816 linear 8-node brick elements that constitute the reinforcement steel bars in the columns and beams and 4860 1D truss elements with two nodes. To reduce the computational cost, one

symmetry plane was utilized in the simulations (Figure 8-8b). All frame constituents are modeled as nonlinear except for the brick and mortar, which is out of the scope of this work. A row of tetrahedral elements on the location where the load was imposed were modelled as linear elastic to prevent local damage. Furthermore, both reinforcement configurations used in the numerical analysis are shown in detail in Figure 8-9. The effect of ductile detailing is visible at the beam column joints and in the stirrups line-up of the roof beams. The mechanical and thermal properties used in the simulations are summarized in Table 8-3.

Table 8-3. Material properties of steel and concrete used in the FE simulation.

Diameter of steel rebar [mm]	Steel reinforcement bars				Concrete
	8 Slab stirrups and beam reinf.	10 Column stirrups	16 Beam main reinforcement	20 Column main reinforcement	
Yield stress [MPa]	550.69	446.57	420.05	448.55	-
Ultimate (tensile) stress [MPa]	642.97	538.21	541.18	567.5	2.14
Compressive strength [MPa]	-	-	-	-	33.6
Yield strain [mm/mm]	0.0047	0.0042	0.0023	0.0021	-
Ultimate strain [mm/mm]	0.2070	0.1960	0.1689	0.1458	-
Elongation [%]	20.7	19.6	16.89	14.58	-
Young's Modulus [$\times 10^5$ MPa]	2.14	2.13	2.03	2.10	0.31
Poisson's ratio	0.18	0.18	0.18	0.18	-
Fracture energy [N/mm]	-	-	-	-	0.07
Heat conductivity λ [W/mK]	18	18	18	18	1.49
Heat capacity C_p [J/kgK]	490.0	490.0	490.0	490.0	900.0
Mass density ρ [kg/m ³]	7900.0	7900.0	7900.0	7900.0	2267.0

The imposed and gravity loads are set upon the slab and columns with the same magnitude as it was carried out in the experiment. The live load was imposed and simulated as a uniform load distribution on the top of the slab (Figure 8-8c). The bottom nodes of the frame columns and the brick wall were constrained in every direction and the push/pull cycles were imposed on the nodes at the end of the roof beams in x direction. At the end of the simulation, the load is evaluated in the same nodes where it was imposed. The inner surfaces of the structure were exposed to compartmentalized fire, as depicted with red color in Figure 8-8d.

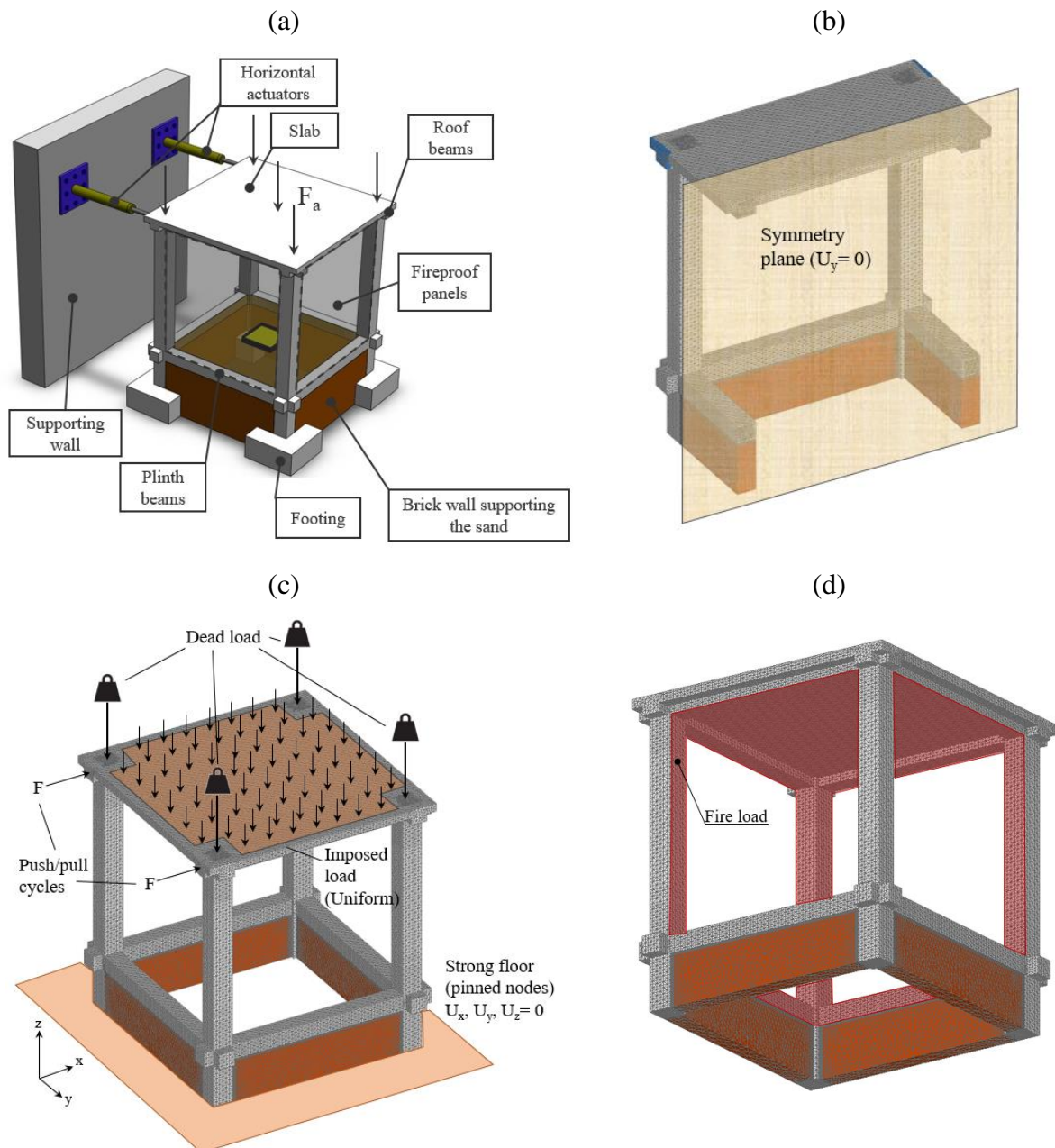


Figure 8-8. The discretized full model of the RC frame with masonry infill in the foundation (a); Symmetry plane (b); Active loads imposed on the RC structure (c) and the fire exposed surfaces (d).

The numerical study was divided in two parts. First, the thermo-mechanical model is validated against the experimental results obtained by Shah and Kamath (Shah, 2017; Kamath, 2015) and secondly, the results in terms of temperature distribution, deflections and load-carrying capacity is presented. The reinforcement detailing is illustrated in Figure 8-9. In the beam column region, it is clearly visible that the number of stirrups is larger in the case of ductile detailing as per guidelines IS13920:1993 (BIS 1993). The strong floor and accompanying reinforcement configuration are not shown, as they are not part of the numerical analysis. In the experiment, however, the RC frame was constrained on four footings having 500 mm in depth. Each footing was constructed in a way that eight 1200 mm long protruding bolts extended in the raft foundation, passed through it (Shah et al., 2017).

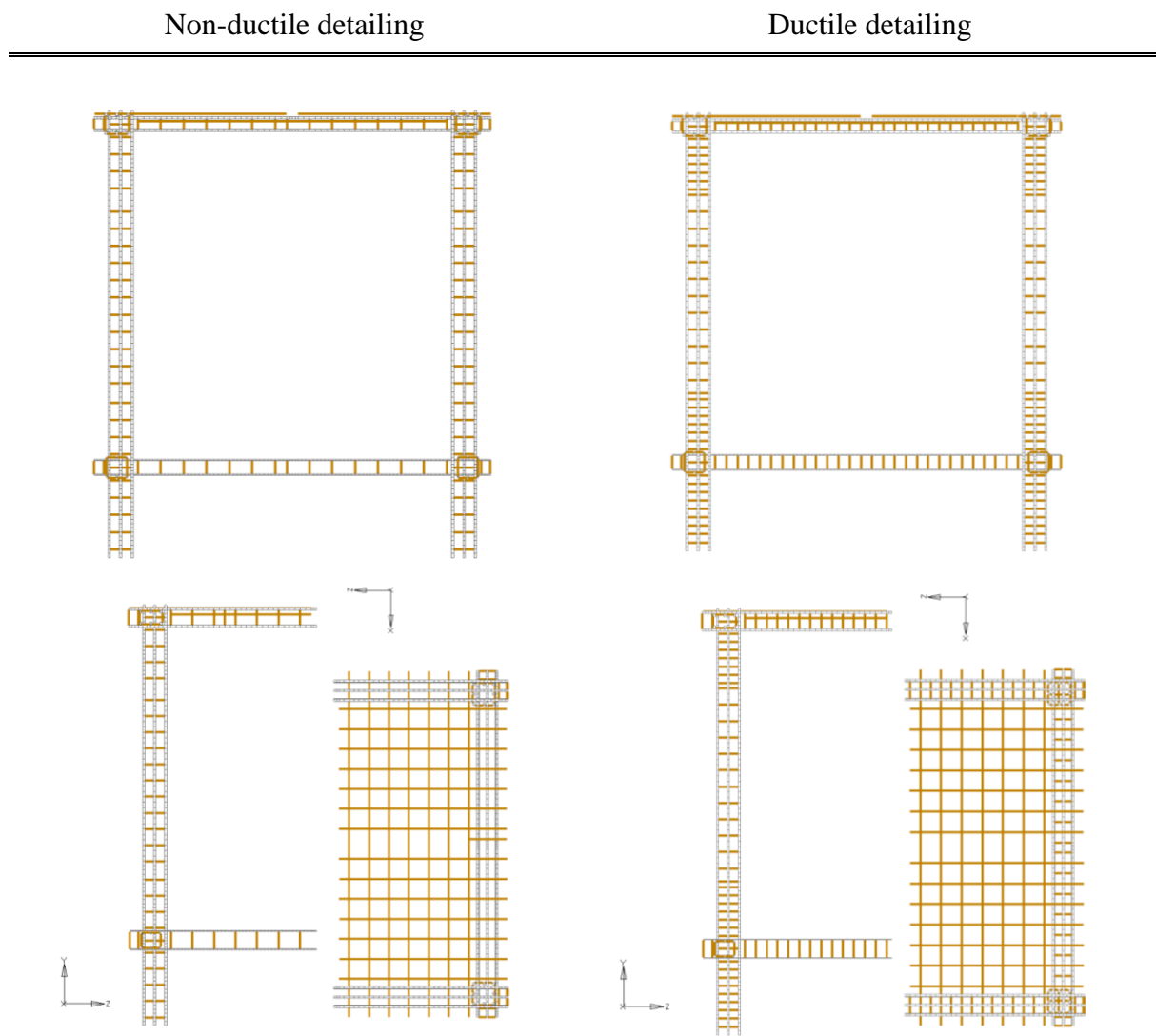


Figure 8-9. FE model of the reinforcement with and without ductile detailing as per IS13920:1993 (BIS, 1993).

Non-ductile detailing

Ductile detailing

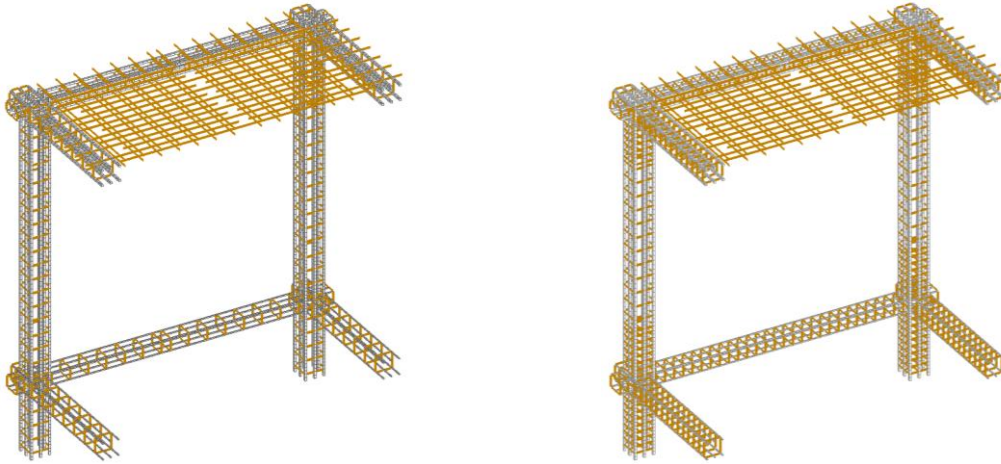


Figure 8-9. (Continued).

Same as conveyed in the previous chapter (Chapter 7), the 3D FE analysis was performed using the thermo-mechanical model for concrete and steel as the constitutive law. The 3D steel solid elements are represented by von-Mises plasticity and 1D truss elements are modelled by uniaxial stress-strain law for steel. Note that temperature dependent properties of concrete and steel were calculated using the local temperature.

8.4 Validation of the thermo-mechanical model

Following the test loading phases from the experiment, the numerical simulations consisted of three phases as well: (i) simulated seismic load, (ii) fire load and (iii) residual loading.

8.4.1 Simulated seismic load (cyclic analysis)

In the first phase, the imposed horizontal displacement of the upper frame story corresponded to the roof drift ratio of 4% according to FEMA 2000 having the magnitude of 150 mm. To reduce the computational time of numerical simulations, the successive increase of displacement in every cycle was increased to 50 mm from 10 mm utilized in the experiment. This manifested itself in only three complete cycles to reach the prescribed displacement magnitude instead of 15 in the experiment (Figure 8-10). The first phase of the simulation was stopped when there was no residual load left after the displacement has been reached.

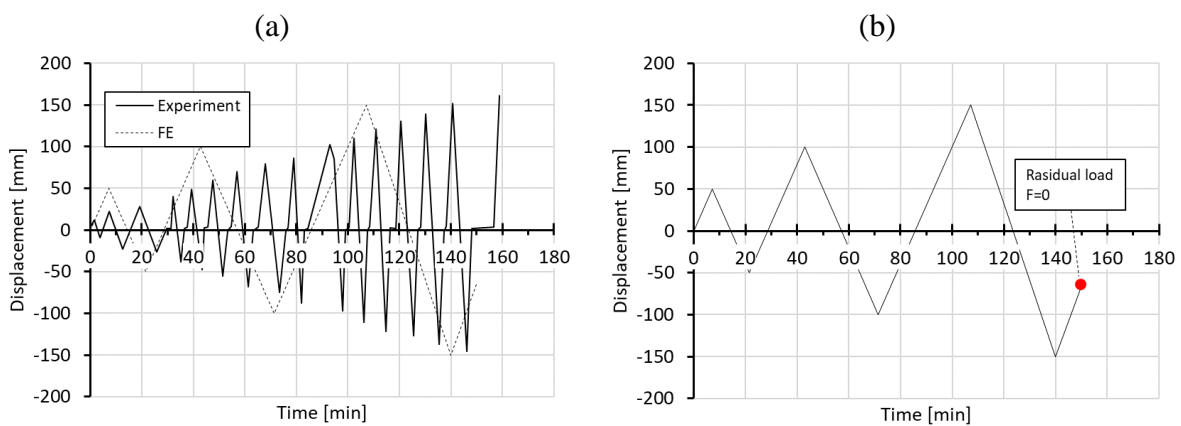


Figure 8-10. Time-displacement histories used in the FE analysis and the experiment (Shah et al., 2017).

Cyclic load in the form of push/pull cycles was applied in a quasi-static fashion and displacement-controlling mode on nodes as depicted in Figure 8-8c. The load displacement hysteresis of the initial seismic load from the FE analysis and the experiment are illustrated in Figure 8-11a and 8-11b. The observed initial structural stiffness is in a relatively good agreement with the data obtained in the experimental tests, as well as the peak loads. However, in the case of ductile detailing, the load at the displacement of 150 mm deviates from the loads obtained in the experiment. The load displacement cyclic hysteresis curve for the non-ductile detailed RC frame, in terms of peak loads and displacements, matches the experimentally obtained curves reasonably well. The initial stiffness from the numerical analysis is, however, slightly larger than in the experiment.

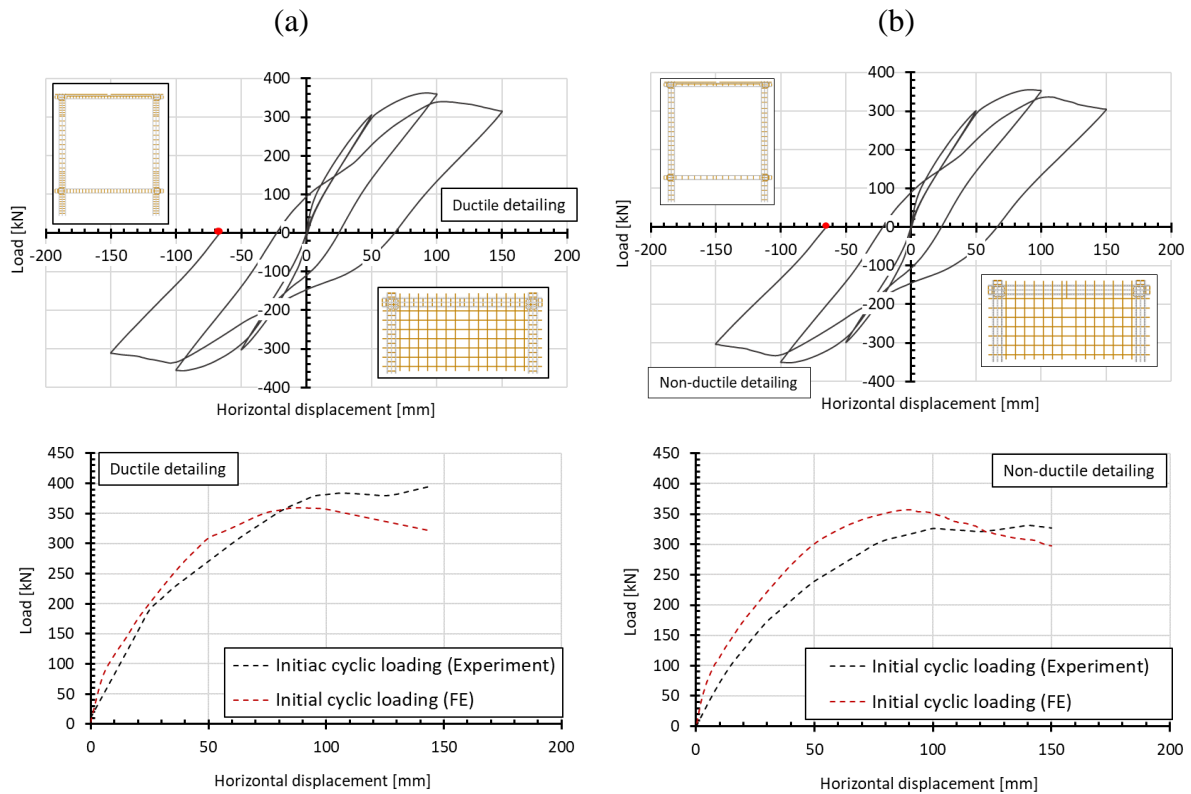


Figure 8-11. Load – displacement hysteretic behavior obtained from the simulated seismic load (first phase) for RC frame with ductile detailing (a) and without ductile detailing (b), with their corresponding experimental results shown below (Shah et al, 2017).

8.4.2 Fire simulation (thermal analysis)

After simulated seismic loading, the RC structure was exposed to fire as per Thomas and Heselden (1972) following the same fire curve from the experiment. Figure 8-12a shows the temperature time history at different locations in the compartment. Given that fire is a highly stochastic occurrence, the temperature during the experiment was not homogenous and equally distributed. In the experiment, the maximum air temperature in the compartment was observed in the location B and it amounted to 1432°C. The maximum temperature of other measured points varies depending on the location inside the compartment. However, in the FE simulation, the boundary conditions were considered as ideal and the temperature distribution along the concrete members was uniform. The fire curve used in the analysis was taken as an arithmetic mean of the points from the experiment and in Figure 8-12, it is illustrated together with an ISO 834 fire curve for comparison. In the FE simulation, the maximum air temperature was attained after 60 minutes of fire exposure and amounted to 1305°C. After the heating phase, the RC frame was cooled down to room temperature with a relatively fast cooling rate of 56°C/min. It should also be noted that although the temperatures in the compartment during the experiment

reached a uniform value, it should not be mistaken with the uniformity of the temperature of the structural members, as the fire dynamics depends on the number of factors such as the direction of wind blowing during the time of the test (Shah et al., 2017).

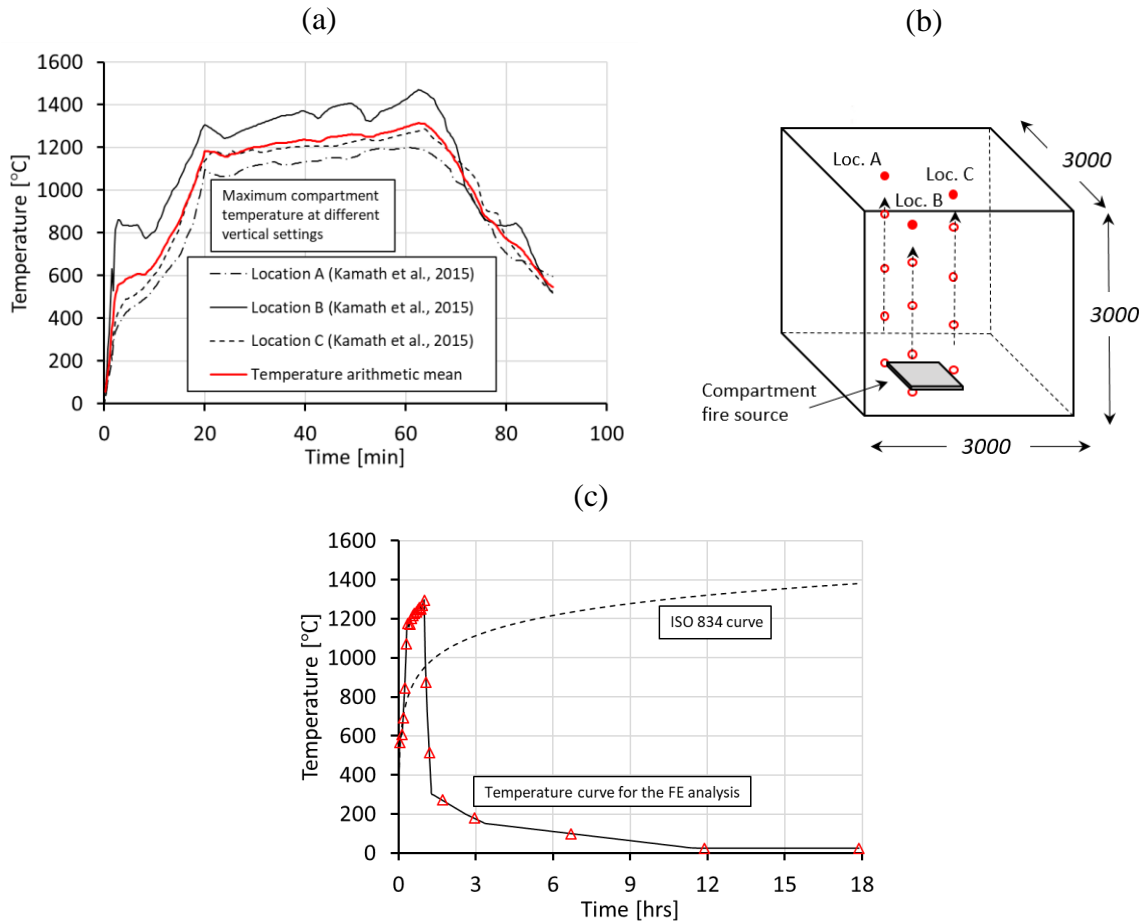


Figure 8-12. Compartment temperature as a function of time obtained in the first 90 min of the experiment (Kamath et al., 2015) (a); Locations of the thermocouples (b) and the time-temperature curve implemented in the FE analysis (c).

The locations of the temperature thermocouples whose values were used for the validation of numerical model are illustrated in Figure 8-13. From each structural member three thermocouple reference locations were used. The sensors in the slab were positioned on the right side in the line of symmetry at three different depths, while in the column and slab members, two out of three sensors were located in the proximity of the fire exposed side and one on the outside. The comparison of the temperature-time curves from the numerical analysis and the experiment for the case with the RC frame without ductile detailing is shown in Figure 8-14.

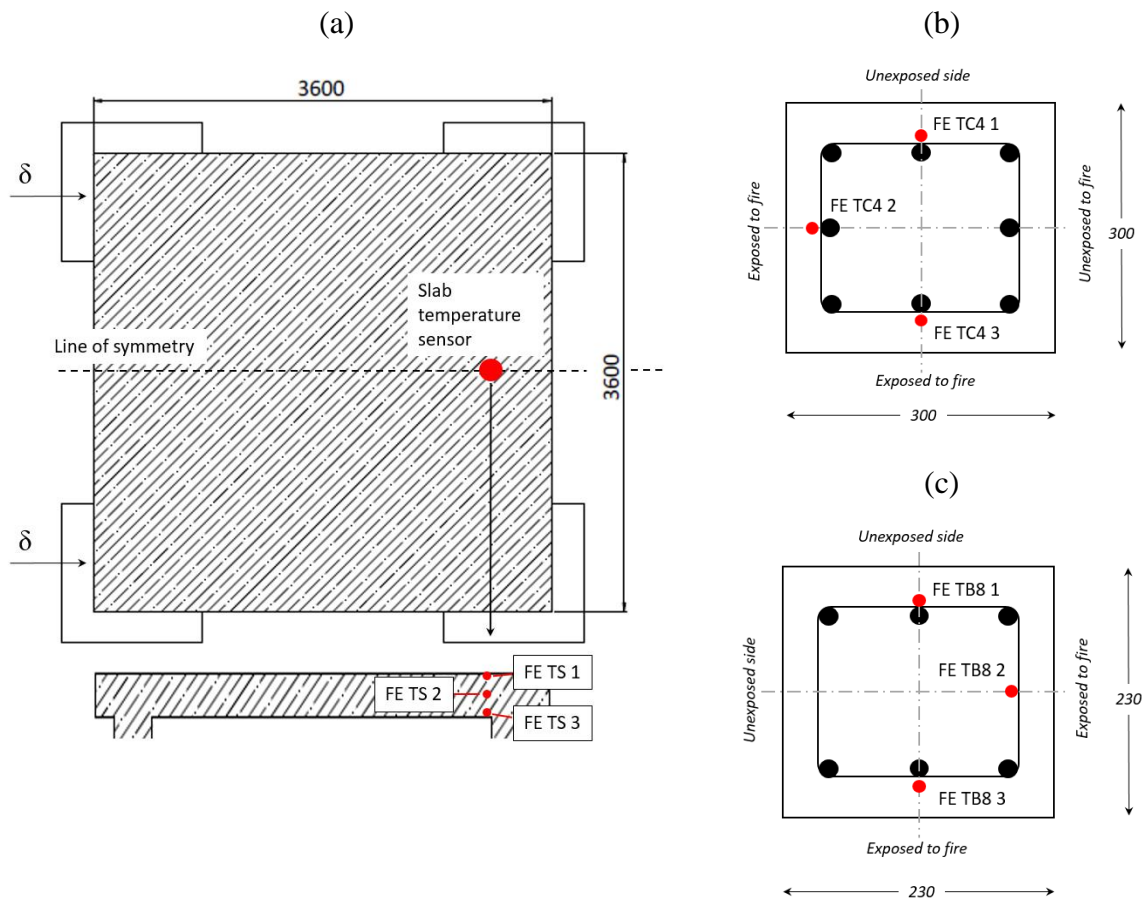


Figure 8-13. Location of the temperature sensors used in the validation of the numerical model in the RC frame without ductile detailing for: slab (a), Column (b) and beam (c).

From the measured locations illustrated in Figure 8-13, the numerically obtained temperature-time curves colored in black are compared with their corresponding experimental values shown in red. The FE analysis results for the slab and beam exhibit a very good agreement with the experimental data, not only in peak temperatures but in values throughout the complete temperature-time history as well. The numerically obtained column temperatures agree very well with the test data, particularly in the center of the member cross section. However, the thermocouple EXP TC4 2 located on the column side exposed to fire conveys much lower temperature than the sensor on the other fire exposed surface (EXP TC4 3). This indicates just how much the fire depends on the gas flow pattern inside the compartment and how greatly the temperature deviates from one surface to another, otherwise on the same height and the same structural member. Of course, the boundary conditions in the simulation are ideally distributed, thus having approximately the same temperature on the exposed surfaces at the same height. To obtain exactly the same temperatures, one would have to model the fire dynamics exactly as in the experiment, which is out of the scope of the present work. The temperature sensors close to the exposed surface of each structural member reach their peak values approx. after 65

min, while the sensors on the outer surfaces reached their maximum considerably later due to the thermal resistance (inertia) of concrete.

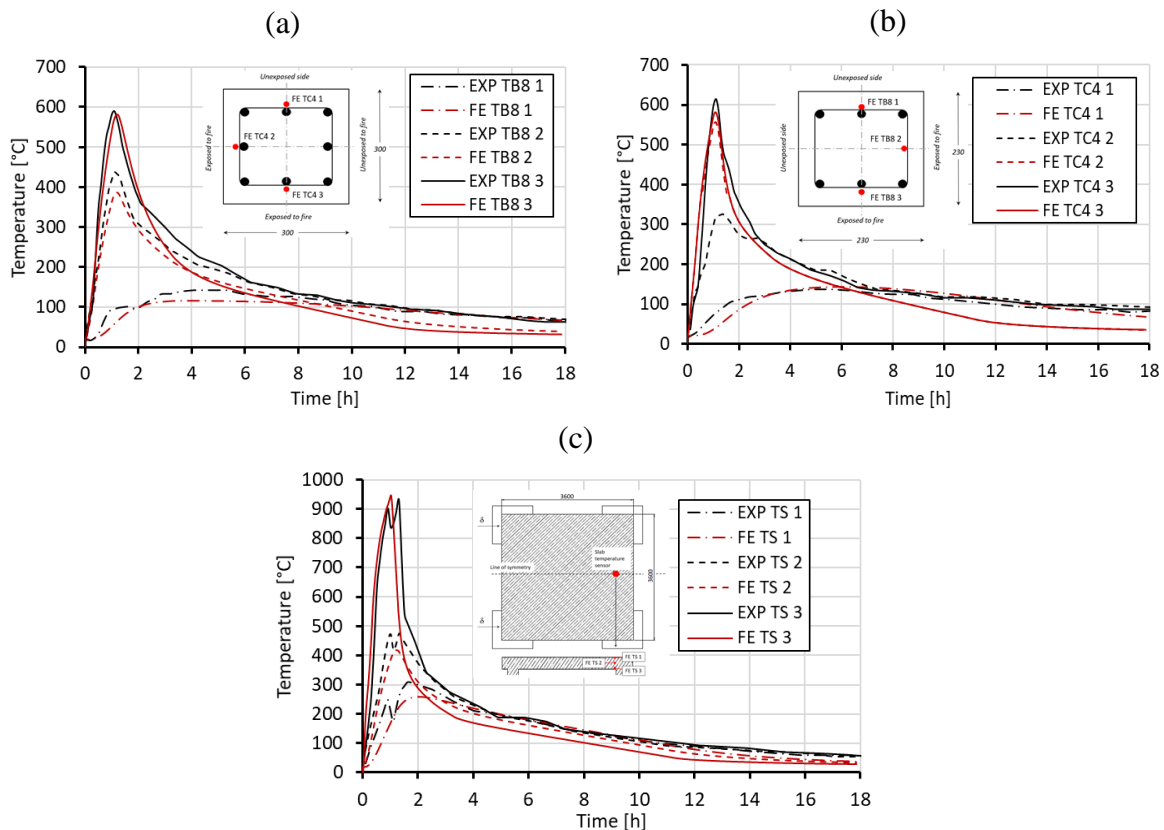


Figure 8-14. Comparison of the FE results with the experimental data for temperature time curves at different locations in: beam (a); column (b) and slab (c) – Frame with non-ductile detailing.

The temperature distribution in the RC frame with ductile detailing as a function of depth or height of the structural member from the numerical analysis is shown in Figure 8-15. The values from the thermocouples used in test (Kamath et al., 2015) are in a relatively good agreement with the numerical values. The temperature distributions are shown for the column C4, beam B5 and the slab. Their corresponding locations are illustrated on the 3D view of the RC frame inserted in the diagrams. The cross sectional temperature distribution is provided successively in 10 min intervals until the end of the heating phase. As expected, the maximum temperatures observed in the members have occurred after 60 min at the location closet to the exposed surface. Comparing the temperatures at the end of the heating phase on the unexposed surface, the highest temperature of 135°C was recorded in the slab member. The temperature comparison was made with B1 plinth beam because only B1 beam had appeared to present the expected temperature profile again indicating stochastic nature of the fire process and the gas fluxes. The highest temperature recorded in the plinth beams during the test was 1111°C on the surface of the B4 beam. The column C4 experienced a temperature drop along the lateral direction in the N-S direction (shown in Figure 8-15c) to approx. 150°C at the end of the heating

phase, which is in a good agreement with the test data. The comparison was made with column C4 since the highest maximum temperature during the test was recorded in the mid-section of that column. The maximum temperature gradient after 60 min of fire exposure in the column C4 during the test was 4.6 °C/mm, while in the simulation it amounted to 5.9 °C/mm.

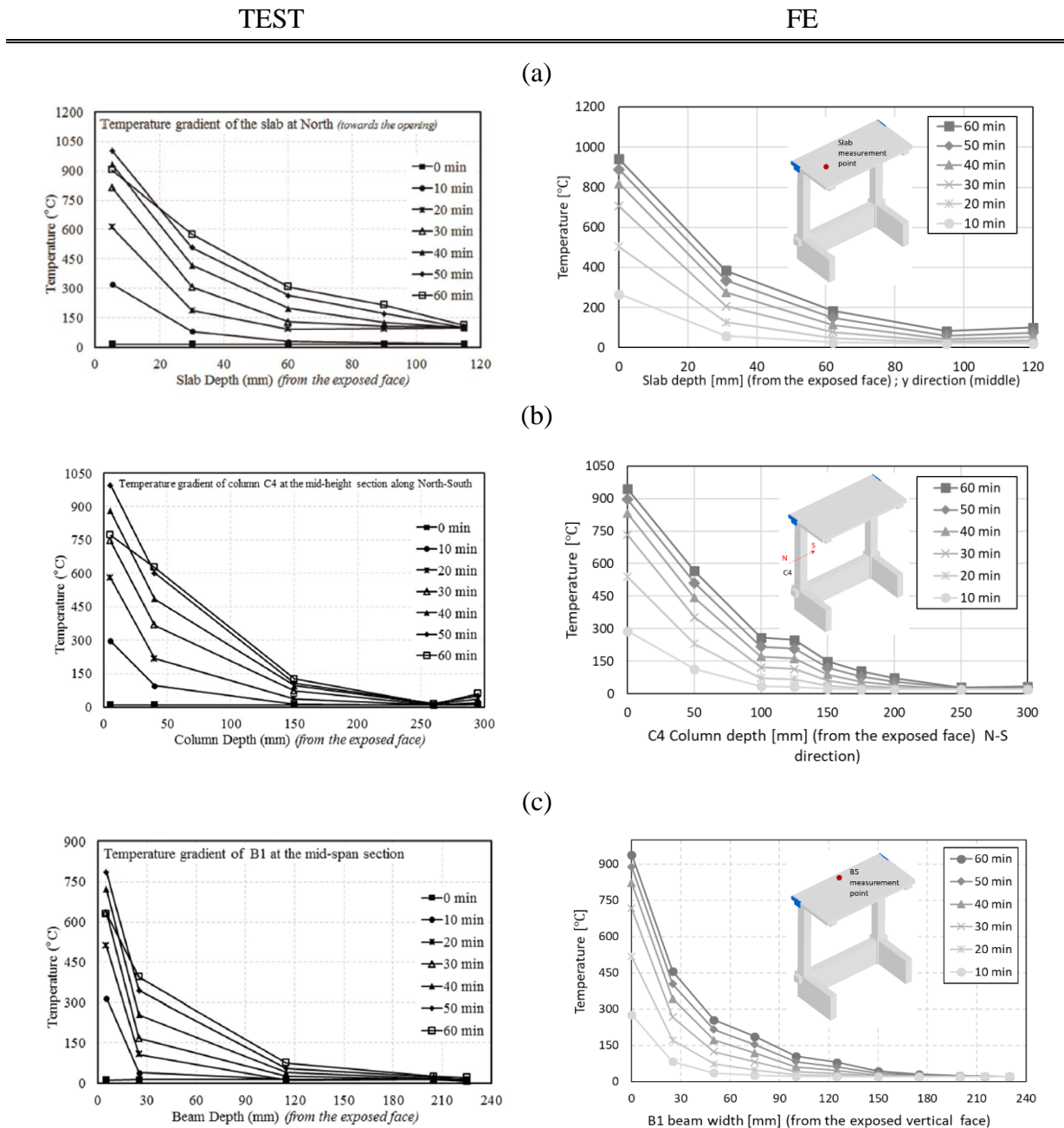


Figure 8-15. Comparison of the FE results and the experimentally obtained temperature data along the cross-section of different structural RC frame members: slab (a), column (b) and beam (c).

Figure 8-16 shows the thermal deflections of three main structural members (column, beam and slab) in the non-ductile detailed RC frame as functions of time. The location of the measured deflection points that correspond to the curves in the graphs are illustrated on a 3D model in

Figure 8-16c. The axial deflection of two pivotal midpoints of columns C1 and C2 show that both columns underwent initial axial thermal expansion as the temperature increased. The simulated data correspond well with the test values in terms of peak deflections with 7 mm and 2.11 mm for C1 and C2, respectively. Note however that the thermal expansion of the columns in the experiment is stiffer. Due to the imposed compressive loads on the columns and the deterioration of concrete mechanical properties, both columns recovered back to their initial positions. Furthermore, column C4 experienced shortening towards the end of the cooling phase having a net decrease of 1.7 mm in the test and 0.2 in the simulation.

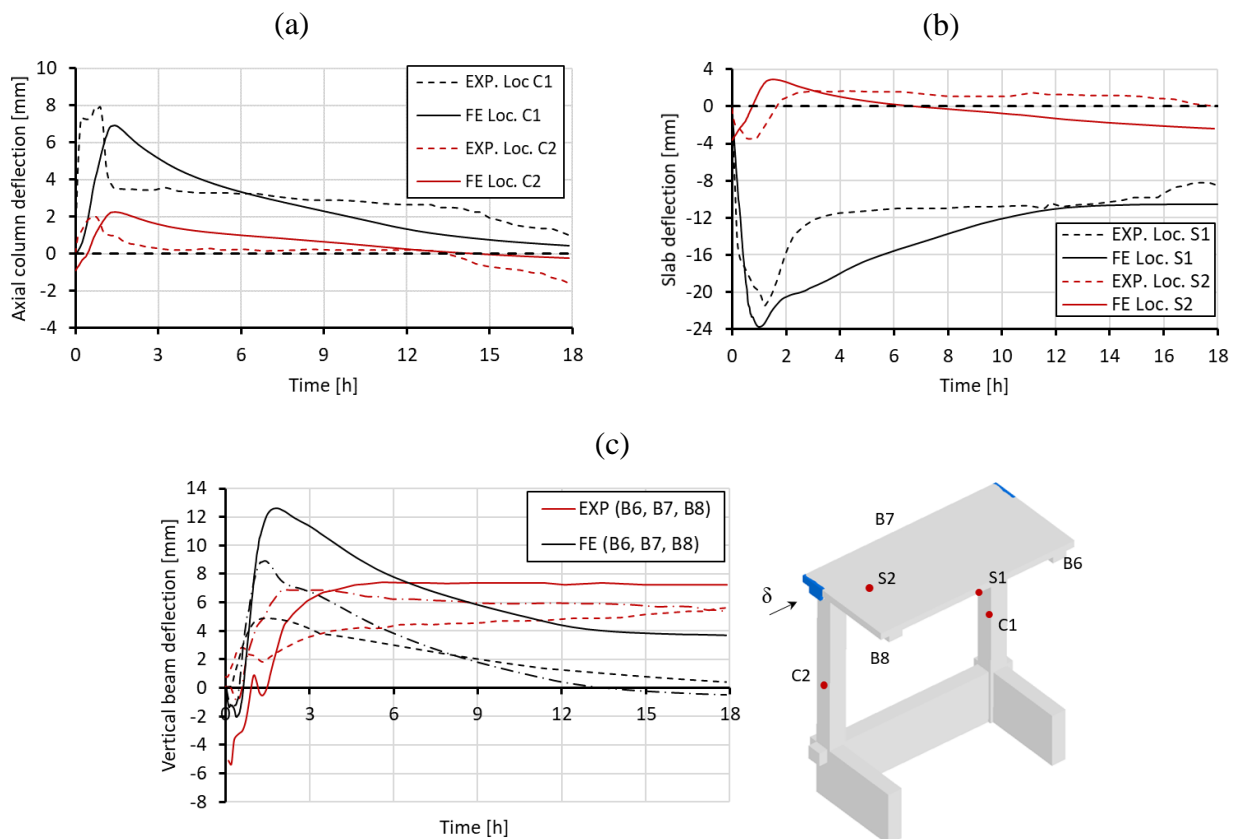


Figure 8-16. Comparison of the FE results with the experimental data for temperature time curves at different locations in: columns (a); slab (b) and beams (c) – Frame with non-ductile detailing.

The vertical deflection of the slab as a function of time is shown in Figure 8-16a. It was evaluated at two pivotal points located at the center of the slab and in the close proximity of the C2 column. Both points exhibited an almost instant negative deflection having a maximum value of 3.5 and 24 mm for locations S2 and S1, respectively. The magnitude of the deflection is dependent on the increasing thermal gradients inside the slab with time and the resulting differential thermal expansion through the thickness of the slab (Shah, 2016). The peak deflection occurs somewhat earlier in the FE analysis due to slightly different temperature levels and temperature gradients observed in the test. The center of the slab after experiencing

its initial negative deflection reversed to 12 mm on cooling after 18h. This is due to the deterioration of mechanical properties during cooling and the load induced thermal strains. Since the layers of the slab exposed to fire experience a negative temperature difference with the core of the slab, i.e. they become colder, the slab is forced to bend upwards. Having in mind that the heat induced thermal dilatation is partially unrecoverable; it causes a residual dilatation after cooling. The vertical deflection of beams diverge from the experimental data in terms of peak values and time when they occurred. Since beams and columns are framed together when the fire occurs, the deflection of each member largely depends on the complex interaction of the beams with columns and their thermal responses. It can be observed that both beams in the test and in the simulation experienced an initial downward deflection due to the thermal expansion of concrete and steel and then recovered as the cooling phase pitched in. The interaction of beams and columns can be best observed in the mutual deflection behavior of components B6-C1, B7-C1-C2 and B8-C2. The biggest deflections of 12.3 and 7 mm were observed in beam B6 and column C1, respectively. On the other hand, the lowest maximum deflections of 4.9 mm and 2.11 mm were recorded in beam B8 and column C2, respectively.

8.4.3 Residual analysis

The residual analysis (third phase) was performed using the monotonic pushover (uniaxial lateral loading) and cyclic loading in a quasi – static manner. Principally, the load displacement curves obtained from the monotonic pushover analysis should be similar to the hysteretic backbone of the cyclic analysis.

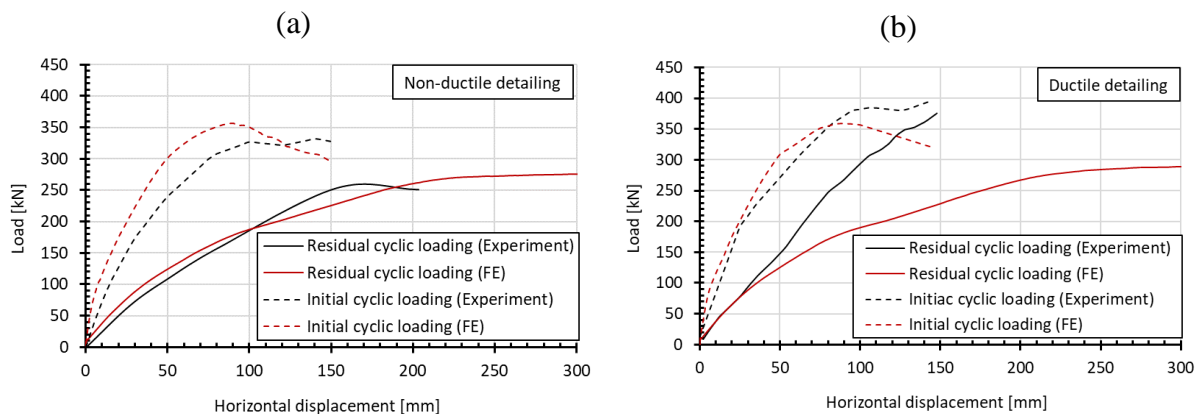


Figure 8-17. Load – displacement curves obtained from the residual analysis for the RC frame with: non-ductile detailing (a) and ductile detailing (b).

Cyclic load was applied in a quasi-static manner and displacement-controlling mode on the same nodes as in the initial seismic analysis. Comparing the load displacement curves from initial and residual cyclic analysis in Figure 8-17, a substantial amount of loss in material

resistance and initial stiffness can be observed in the residual phase in both, experiment and the FE simulation. The results show, in general, a good agreement of the simulated models with the experiment. However, the residual test analysis of the RC frame with ductile detailing deviate strongly from the numerically obtained values. As already emphasized both by designer of the experiments (Kamath et al., 2015; Shah et al., 2017) and the author of this work, the imposed compartmentalized fire from the experiment is of stochastic nature and depends on the smoke flux, attainment of a good flashover and the direction of wind resulting in different temperatures and gradients in different structural members. This in conjunction with possibly different outcome from the initial seismic analysis can lead to different load bearing capacities. Furthermore, the possible reason for the underestimated resistance and stiffness of the ductile frame can be attributed to the fact that stirrups were discretized with 1D truss elements, which have no bending stiffness, i.e. they cannot transfer shear forces.

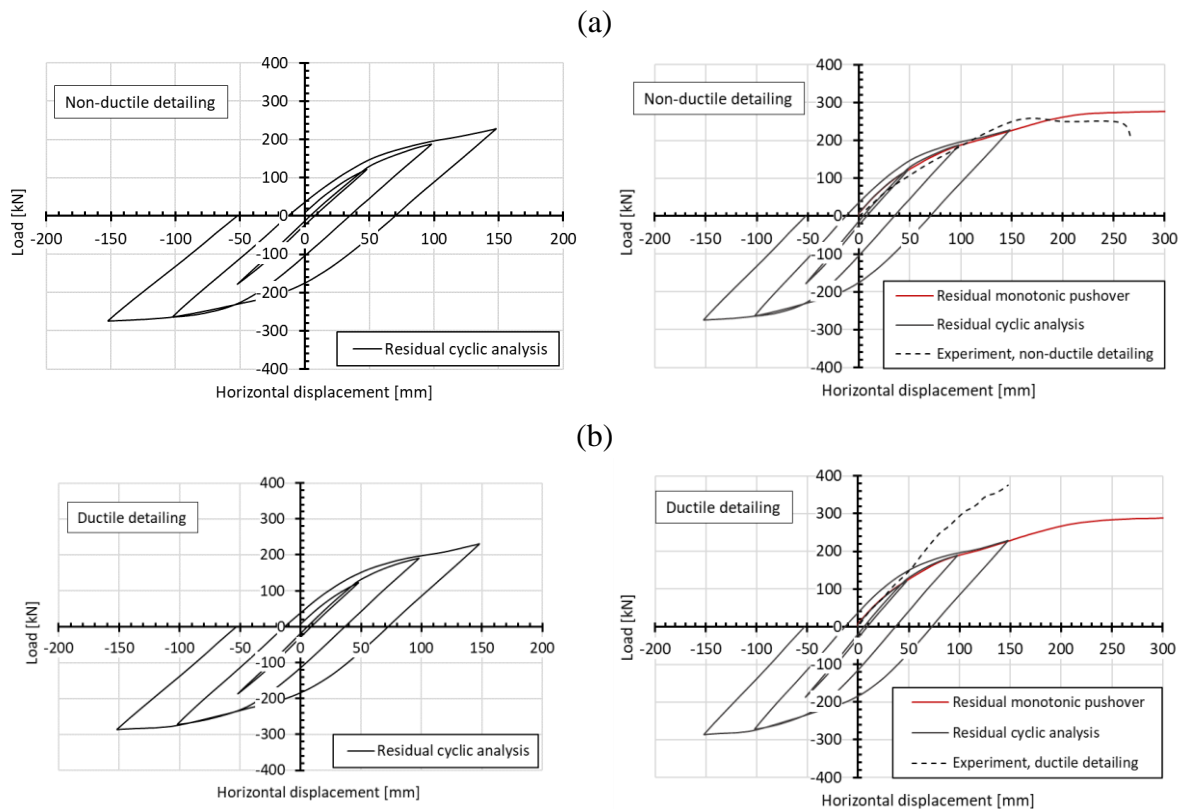


Figure 8-18. Load – displacement cyclic hysteresses with the LD curve from the monotonic residual pushover analysis for the RC frame with: non-ductile detailing (a) and ductile detailing (b).

The difference in the residual peak loads at the displacement of 150 mm between the FE simulation and the experiment of the non-ductile detailed frame amounts to 9%. Furthermore, the relatively small difference of 5 % in residual peak load at 300 mm displacement between the RC frames with and without ductile detailing points out that both reinforcement

configurations have similar response in the third loading phase. Figure 8-19 and Figure 8-20 illustrate the failure modes and crack patterns in the RC frame with and without ductile detailing at the end of each loading phase. The critical crack opening depicted with red color is equal or greater than 1 mm. After the initial cyclic loading, longitudinal cracks perpendicular to the direction of loading can be observed in the beam column joint at both, plinth and roof beams, on each side.

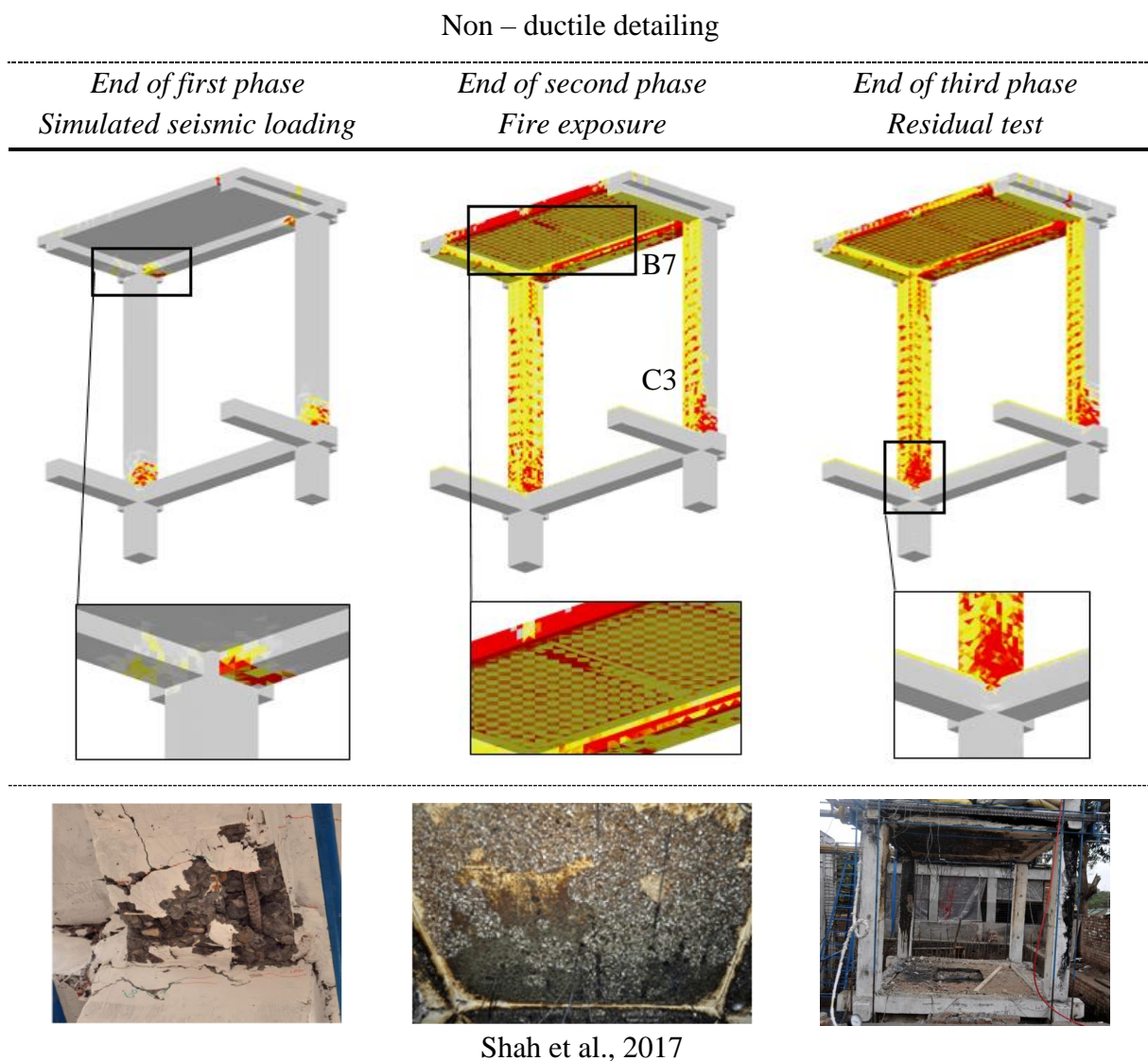


Figure 8-19. Crack patterns and failure modes from the numerical analysis of RC frame with non-ductile detailing.

In both reinforcement configuration, a long crack at the contact area between the slab and beam on the opposite side of the loading point can be observed. Comparing the visually observed damage between the RC frames, a more pronounced cracking pattern can be noted in the RC frame without ductile detailing. The state of both RC frames after the fire exposure indicate a strong thermally induced damage in each structural member, especially the slab and the roof

beam parallel to the direction of loading. The mechanical damage in the beam-column joints that occurred during the initial cyclic loading was further aggravated with the thermally induced damage, predominantly on the contact between slab B7 and column C3. As a consequence of the composite action between the slab and the roof beams, flexural cracking was observed in the N-S direction in both cases, as observed in the experiment.

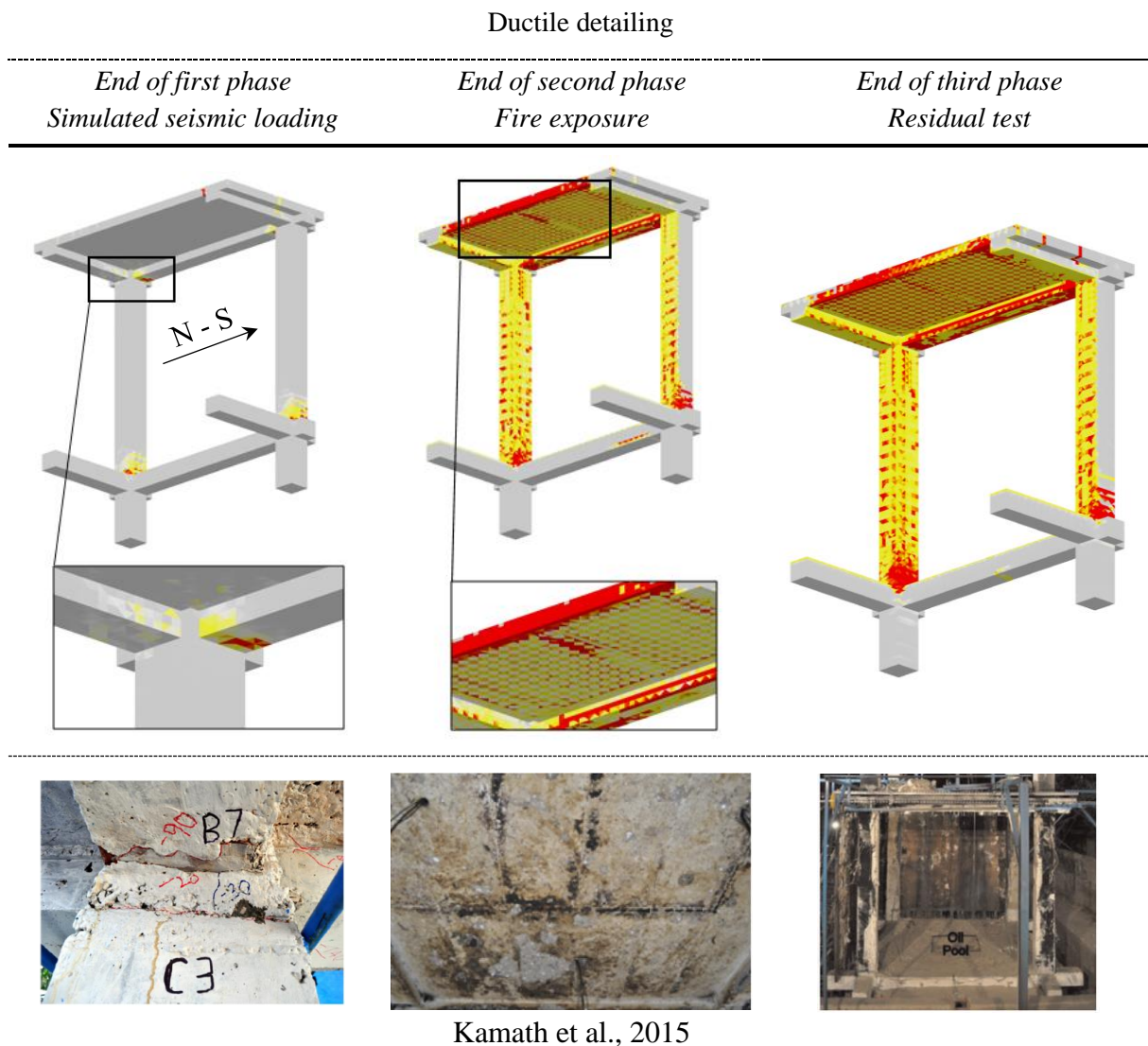


Figure 8-20. Crack patterns and failure modes from the numerical analysis of RC frame with ductile detailing.

The RC frame with ductile detailing did not undergo extensive spalling after fire exposure. At the end of the third phase, each of the structural elements was intensively damaged with cracks as wide as 5 mm. Overall, it can be pointed out that the numerical analysis agrees relatively well with the experiment in terms of load displacement and crack patterns considering different heat fluxes on different structural surfaces occurred in the test.

8.5 Parametric study

8.5.1 Thermal exposure according to ISO 834 fire curve

In the present parametric study, the identical loading sequence as in the experiment from Shah (Shah et al., 2017) was employed. The frames were initially subjected to quasi-static cyclic loading in a successive manner with 50 mm increasing displacement cycle as in the model validation study. The maximum displacement amounted to 150 mm, after which the frames were unloaded and exposed to fire. In the thermal analysis, both frames with ductile and non-ductile detailing were exposed to fire exposure durations of 15, 30, 60, 90 and 120 min as per ISO 834 fire curve (Eurocode 2, EN 1992-1-2, 2004) (Figure 8-21). Finally, the thermally pre-damaged frames were subjected to monotonic pushover load in both hot and cold (residual) state in order to determine the residual load capacity.

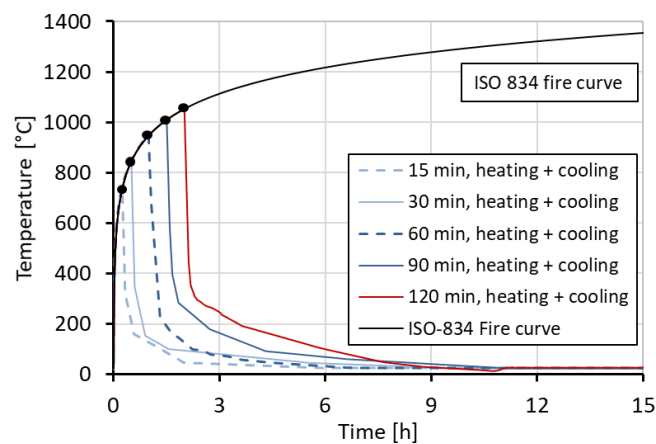


Figure 8-21. Heating and cooling regimes in the thermal parametric analysis as per ISO 834 fire curve (Eurocode 2 EN 1992-1-2, 2004).

The mechanical damage in the RC frames occurred during the initial seismic loading are not going to be discussed, as they are the same as in the model validation analysis. The temperature distribution was similar in both cases, with and without ductile detailing since they have suffered similar mechanical damage in the initial seismic loading phase. Therefore, only temperature distribution for the RC frame without ductile detailing is shown in Figure 8-22 and will not be discussed further in this section. After 90 min of heating, all of the exposed surfaces reached the temperature of 800°C. Figure 8-22 and Figure 8-23 show the temperature distributions along the slab, column and beam cross sections at the end of the fire exposure phase for 15, 30, 60, 90 and 120 min. It is obvious that the temperatures distribution across the cross section of the slab was more homogenous than in the columns and beams resulting in the most sustained thermally induced damage. The red line in the graphs represents the first layer

of the reinforcement bars (closest to the exposed surface). It can be observed that after 120 min of fire exposure the highest temperature manifested itself in the reinforcement section of beams and the slab with approx. 600°C, whereby the measured temperature of the reinforcement in the columns amounts to 373°C. The most critical points on the structure were the beam-column joints perpendicular to the direction of loading.

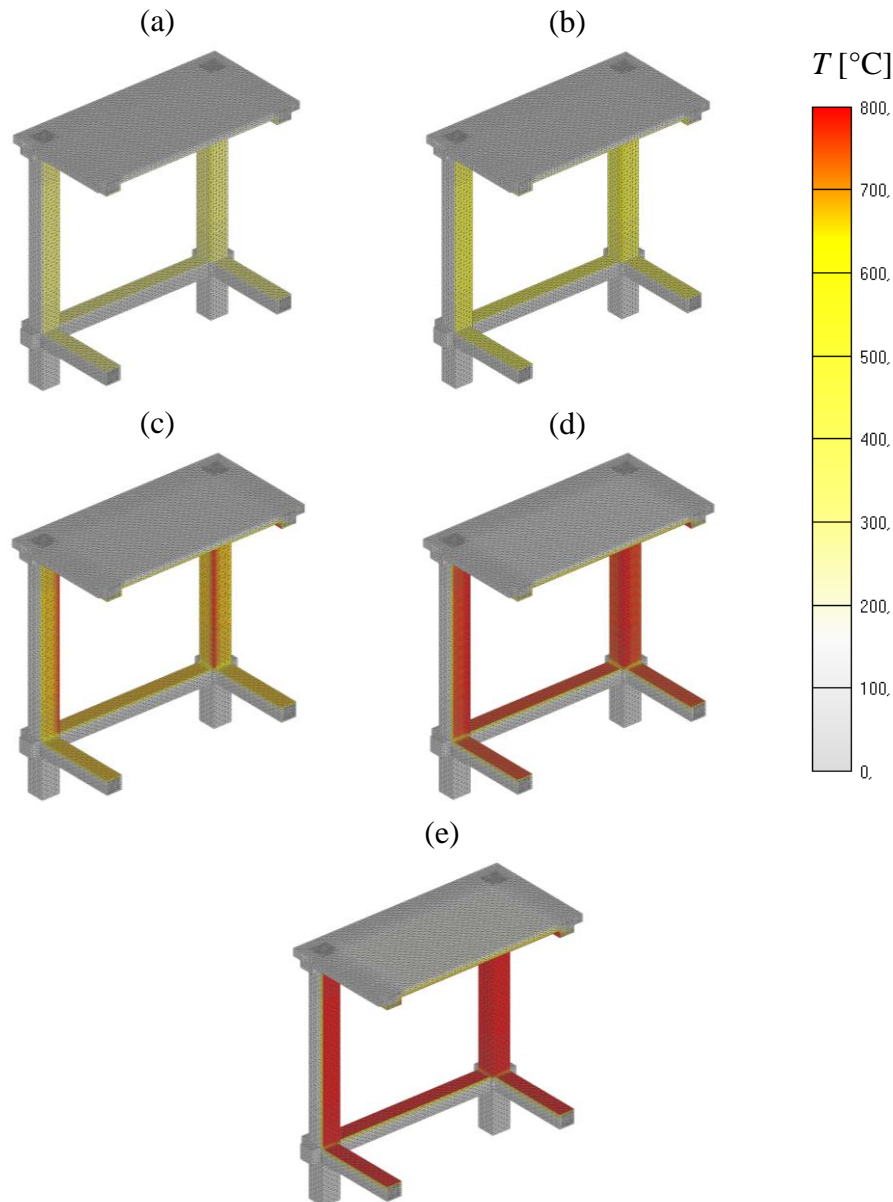


Figure 8-22. Temperature distribution on the exposed surfaces of the RC frame: 15 min (a), 30 min (b), 60 min (c), 90 min (d) and 120 min (e).

Due to the larger cross-sectional area of the column, the temperature gradient may seem larger than in the other structural elements, although it does not differ much. For example, the temperature at the distance of 25 mm from the exposed surface measures up to 505°C in the column, while it amounts to 547 and 573°C in the slab and the beam, respectively. However,

due to the larger distance of the reinforcement bars from the exposed surface, the temperature in that point is lower in columns than in the beams and the slab. The first reinforcement layer temperatures in the column after 15, 30, 60 and 90 min amount to 51.8, 110.1, 215.1 and 298.9°C, respectively. At the distance between 150 mm from the exposed surface and the outer surface, both beam and column exhibited a uniform temperature of approx. 90°C after 120 min of heating. Since the cross section of the slab is rather thin, the uniformity of the temperature for the fire durations above 30 min could not be achieved.

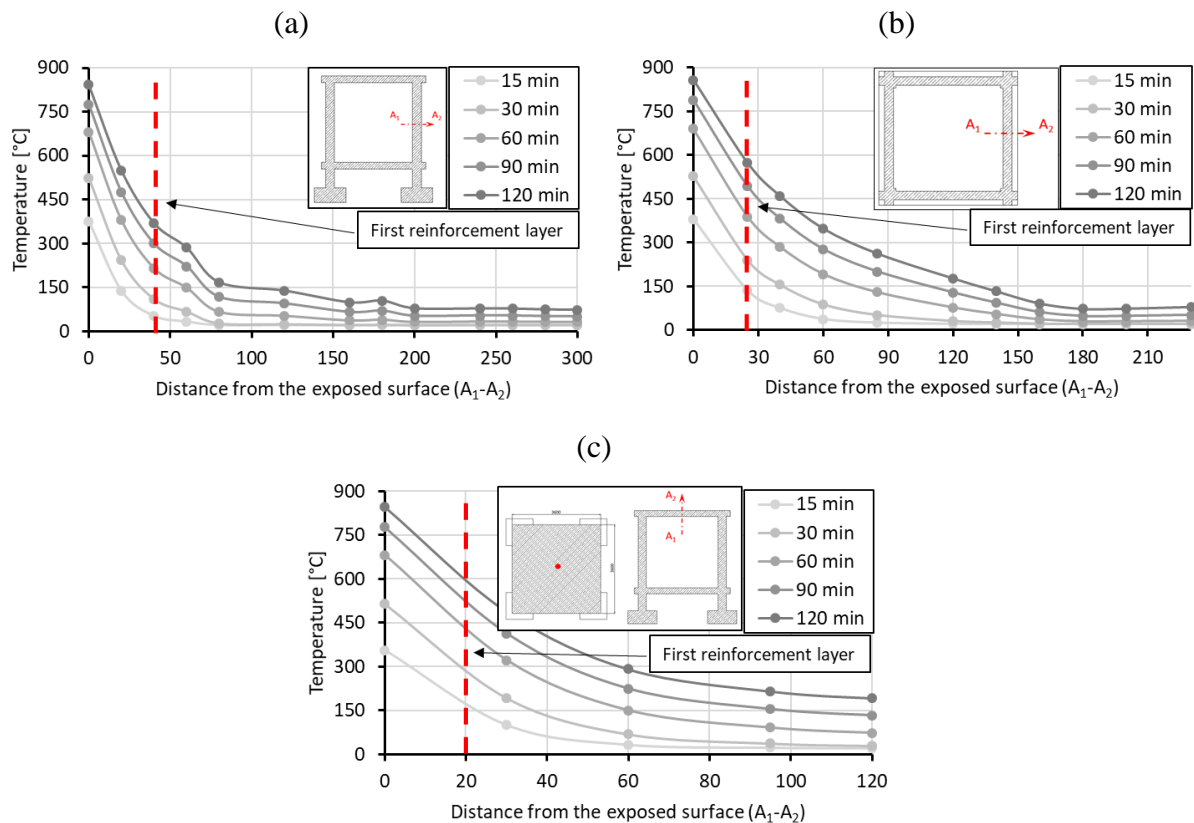


Figure 8-23. Temperature distribution along the cross section for: Column (a), beam (b) and slab (c) at the end of heating phase for different fire durations.

The mechanical damage from the first phase and the thermally induced damage after 15, 60 and 120 min of fire exposure for both hot and cold state is shown in Figure 8-24. It is obvious that the mechanical damage induced during the initial seismic phase was further aggravated by the thermally induced damage in the fire exposure. As opposed to the critical cold state in the case of preloaded anchors in Chapter 6, here the thermally induced damage is more expressed in the hot state. This can be attributed to the almost fully restored mechanical properties of the reinforcement steel bars in the cold state, as already discussed in the previous chapter. It is shown that with the increase of the fire duration, the accumulated damage in the structure expands.

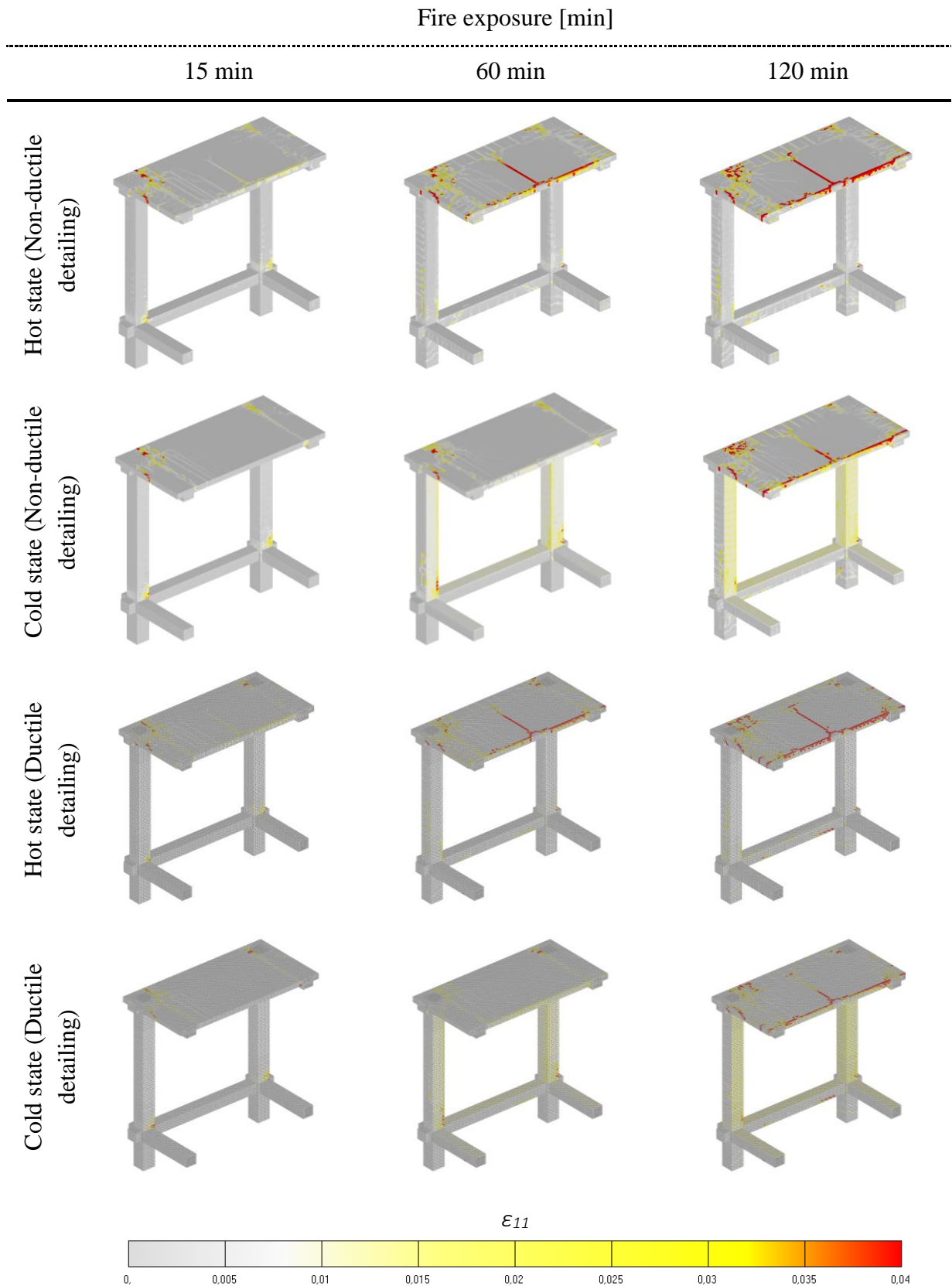


Figure 8-24. Crack patterns in the RC frame for both detailed and non-ductile detailed RC frame after 15, 60 and 120 min of fire duration (red criteria corresponds to minimum crack width of 1.0 mm).

The most severe damage is observed on the top of the slab close the weaker reinforced areas (gap in the top slab reinforcement) and the beam column sections perpendicular to the direction of loading. The results also suggest that the damage was pronounced along the beam in the direction of loading indicating that the weak points in the hot state are close to the position of stirrups.

The red zones in Figure 8-24 are the maximum principal strains, which correspond to the crack width equal or greater than 1.0 mm. The thermally induced damage of the frame for all fire durations localizes around the beam column section and in the midline part of the slab where the upper reinforcement gap is located. The thermally induced damage of the structural members of the RC frame increases with the fire duration increase. Numerically obtained fracture patterns suggest that the RC frame is damaged more profoundly in the hot than in the cold state. Again, this can be attributed to the thermally induced damage and softening of the steel reinforcement bars. This is valid for both reinforcement cases, with and without ductile detailing. However, the thermally induced damage is much less pronounced in the case with ductile detailing suggesting that the structure was less damaged in the initial seismic loading. The residual capacity of the RC frame depends however, on the stresses localized in the main longitudinal reinforcement bars after fire exposure. Figure 8-25 shows the maximum principal stresses in the main longitudinal bars having diameter of 20 and 16 mm. The red colors depict the areas where the maximum principal stress is equal or larger than 420 N/mm^2 , which represents the minimum yield criterion for used steel. Comparing the stress distribution, a more pronounced stress state is observable in the hot state, for both reinforcement configurations. It can be deduced that up to 60 min of heating, the reinforcement bars can still recover their mechanical properties during the cooling process. However, at 90 and 120 min, despite its recovery capabilities, even when cooled down, steel exhibits a high stress state, meaning that the material had underwent plastic deformation during the heating phase. The stress state of the steel bars turned out to be less prominent in the RC frame without ductile detailing in both hot and cold state, since the number of stirrups was less condensed around the main reinforcement. However, the thermally induced damage was less expressed in the case with ductile detailing due to the less extensive cracks developed during seismic loading in the first phase. The absence of robust cracks left the steel reinforcement bars still covered with the concrete layer and the heat was not able to penetrate deep in the concrete structural members.

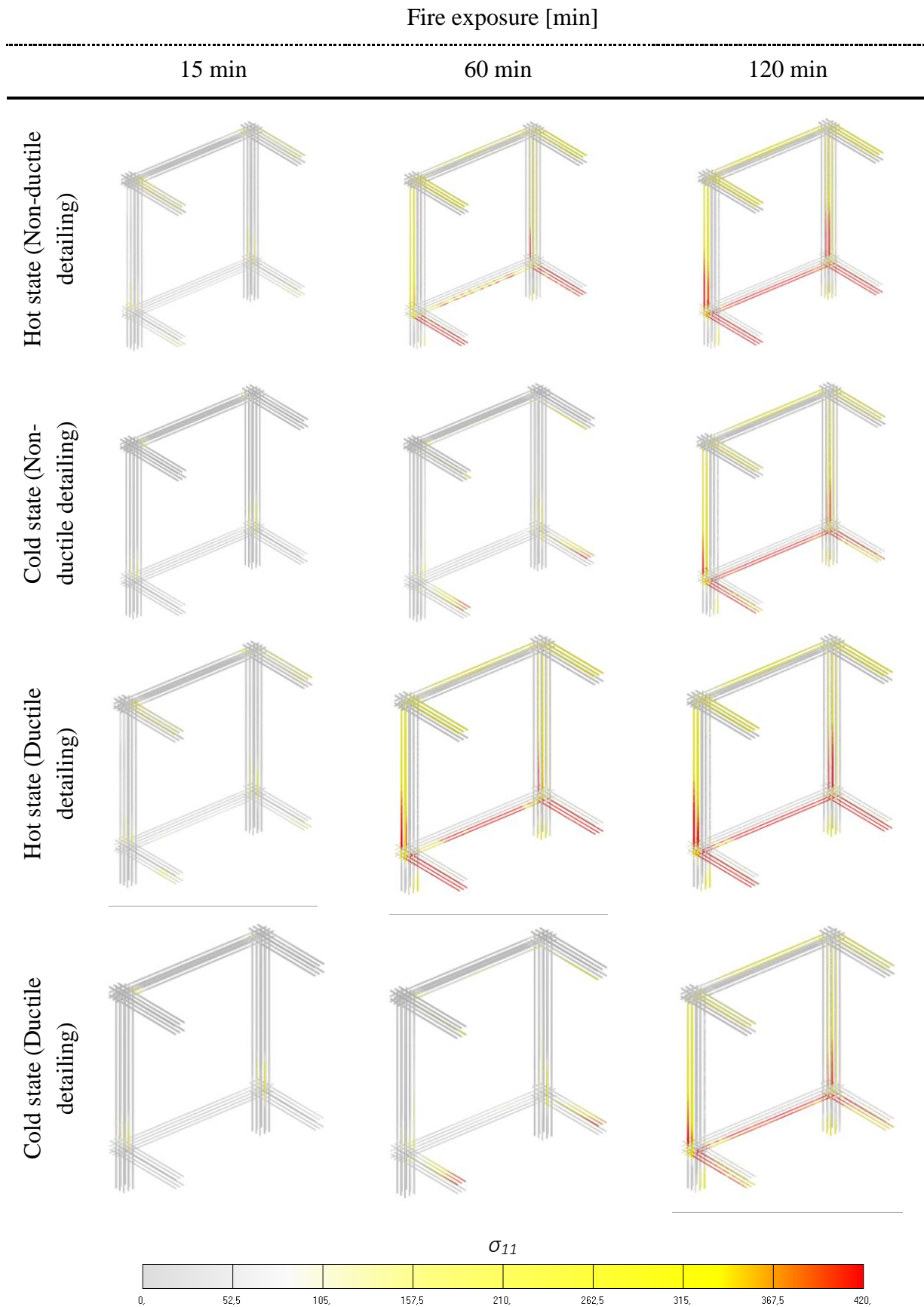


Figure 8-25. Maximum principal stresses in the main reinforcement bars for both detailed and non-ductile detailed RC frame after 15, 60 and 120 min of fire duration.

8.5.2 Residual capacity (parametric study)

The residual test was carried out in the form of a monotonic pushover to the prescribed displacement of 400 mm. The aim was to obtain the residual capacity of the RC frames with and without ductile detailing after initial seismic loading and the subsequent fire exposure according to ISO 834 fire curve. The residual curves are displayed in terms of load and horizontal displacements in Figure 8-26 and Figure 8-27.

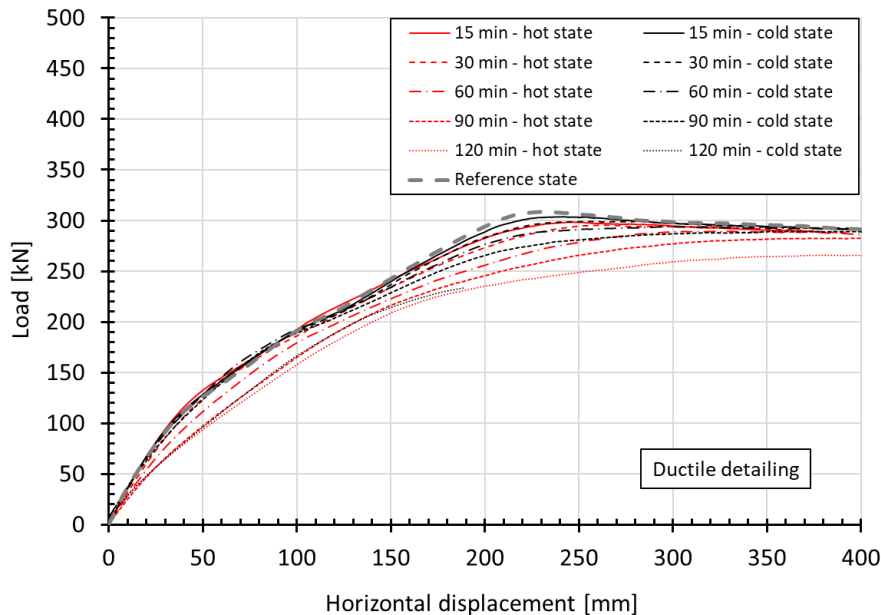


Figure 8-26. Load displacement curves obtained from the residual pushover analysis of the RC frame with ductile detailing for the complete fire exposure range.

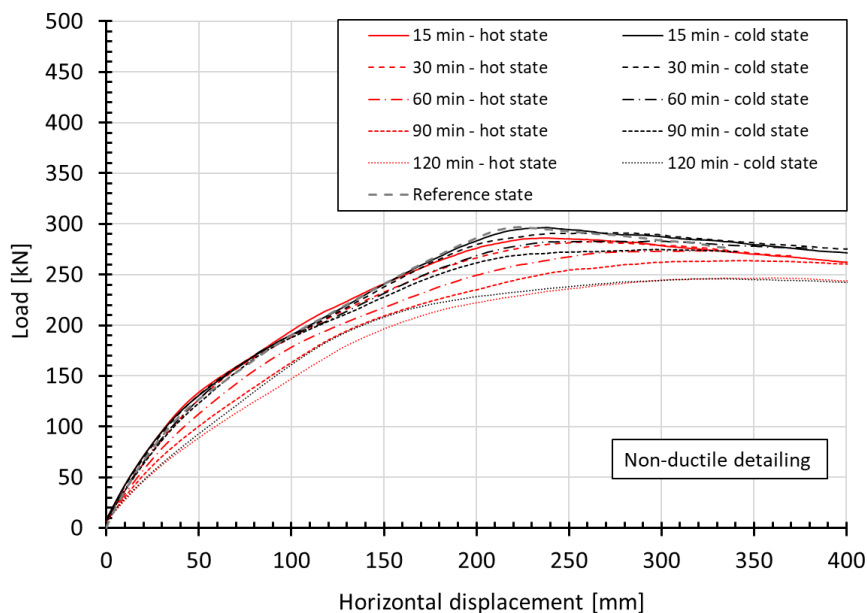


Figure 8-27. Load displacement curves obtained from the residual pushover analysis of the RC frame without ductile detailing for the complete fire exposure range.

The load displacement curves of both RC frames with and without ductile detailing exhibit a decreasing tendency with the prolonged fire duration. After 15 min of fire exposure in the hot state, the residual behavior of both frames have not underwent any significant change in comparison with their corresponding reference state. With the increase of fire exposure time, for both frames, the ductility increases and the initial stiffness decreases. The decrease in initial stiffness is however more pronounced in the RC frame without ductile detailing. The reason for this is the stronger thermally induced damage that the reinforcement steel has sustained. Furthermore, the initial stiffness is larger in cold state than in the hot state for both RC frames. The RC frames suffered greater reduction of load bearing capacity in the hot than in cold state and as the fire exposure increased the difference between hot and cold state became higher. Although the residual resistance after 120 min of fire exposure was approx. the same for both hot and cold state, the RC frame with ductile detailing exhibited almost 10% greater load bearing capacity. This difference can also be noted when comparing RC frames in hot state after 90 min of fire duration (Figure 8-28).

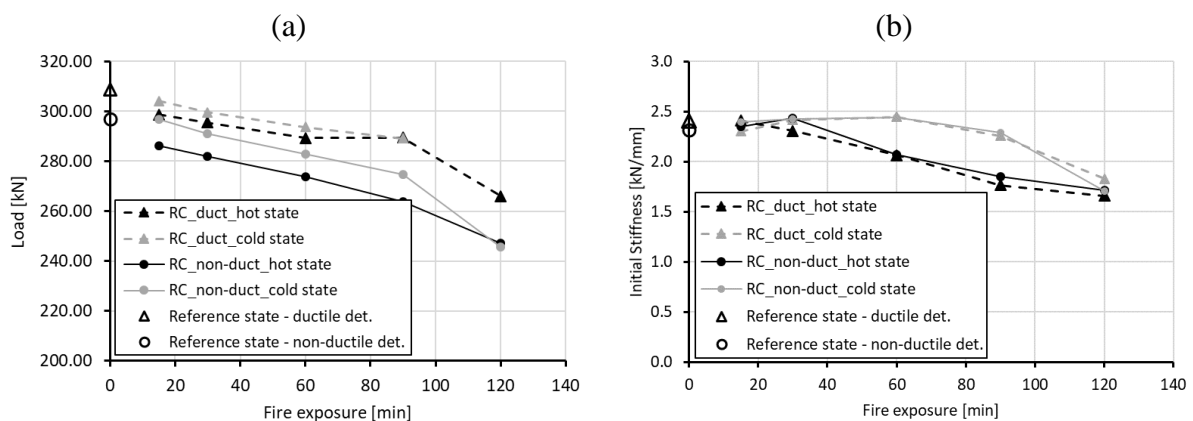


Figure 8-28. The load bearing capacity (maximum residual load) (a) and the initial stiffness of the RC frame (b) after fire exposure in both, hot and cold states.

The crack patterns after the residual monotonic pushover in Figure 8-29 also suggest more pronounced damage in the hot than in the cold state in both reinforcement-detailing cases. Further, damage is slightly more expressed in the RC frame without ductile detailing for longer fire exposure times in hot state, while crack patterns look very similar to that of the cold state.

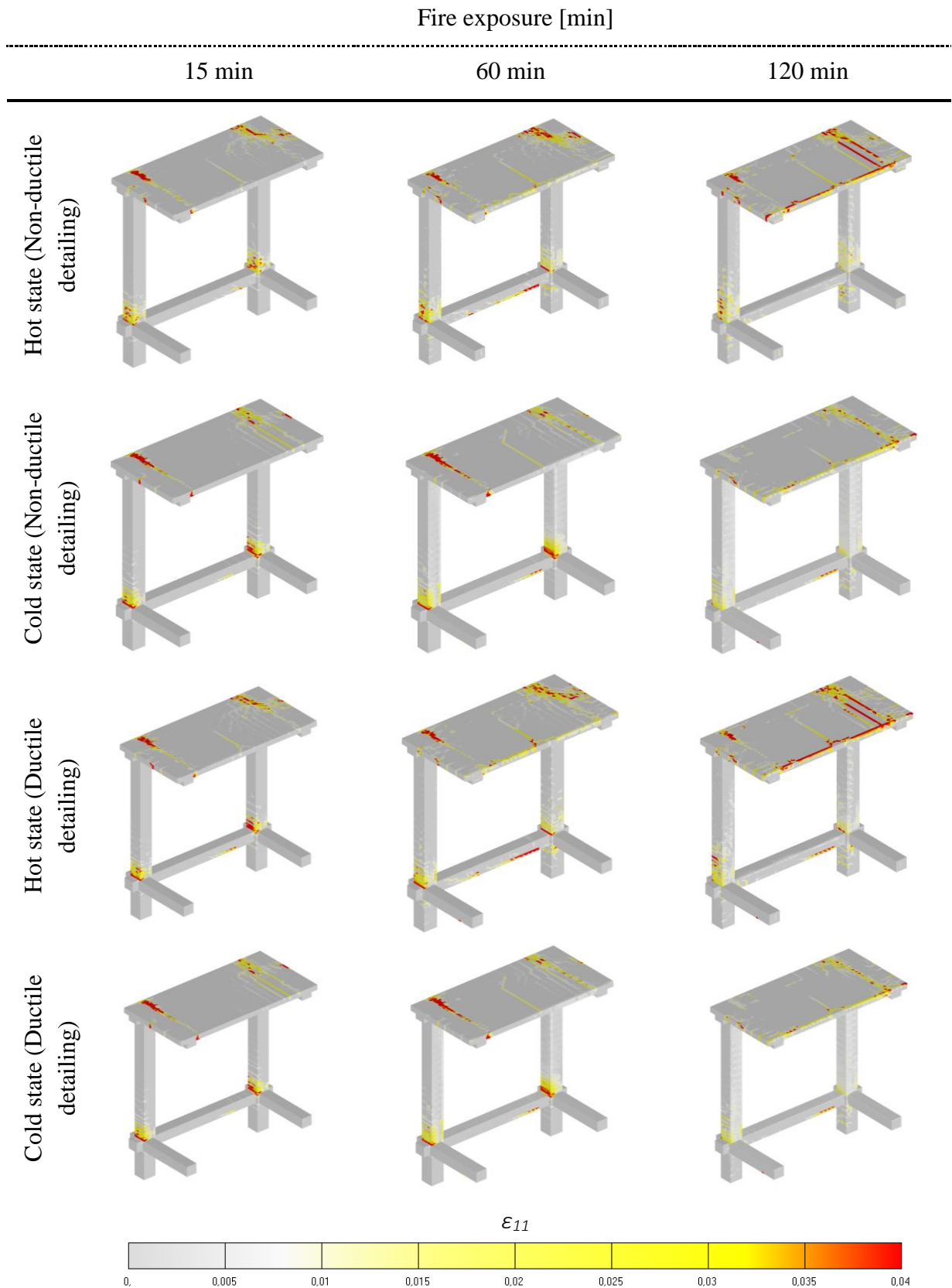


Figure 8-29. Crack patterns for both detailed and non-ductile detailed RC frame after 15, 60 and 120 min of fire duration (red criteria corresponds to minimum crack width of 1 mm).

8.6 Conclusions

In the present numerical study, RC frames with and without ductile detailing, as a part of a larger G+3 story structure were subjected to post-earthquake fire and subsequently the residual pushover and cyclic loading. The aim was first to validate the thermo-mechanical microplane model with the experiments carried out by Shah et al. (2017). Subsequently, the extensive parametric study was performed using the ISO 834 fire curve with fire durations of 15, 30, 60, 90 and 120 min. After the thermal exposure, each frame was tested for residual load bearing capacity. The following conclusions can be drawn: (i) the thermo-mechanical model was able to successfully validate the experimental results in terms of mechanical damage during the first (initial seismic loading) and the third (residual analysis) loading cycle as well as the thermally induced damage during the fire exposure. Furthermore, the complex interactions of the RC structural members in terms of thermal deflections were validated as well; (ii) in the experiment, the damage caused by fire greatly differs from one structural element to another suggesting that the indecent heat fluxes (at the same elevation) varied strongly inside the compartment and were highly dependent on the wind direction and the flux of gases. This is observable from the temperature distribution analysis in the tests as well indicating two adjacent surfaces of the same structural element and the same elevation having large temperature discord. In the numerical analysis, the boundary conditions were assumed to be ideal and the heat flux was uniform across the heated surfaces resulting in similar damage for all structural elements. This is the reason why both RC frames had similar residual load bearing capacity diverging only by a small margin of 3% at 150 mm of displacement, unlike in the tests where this difference was 35%; (iii) parametric analysis indicated a reduction in material strength and initial stiffness with the increase of fire duration. The RC frames suffered greater reduction of load bearing capacity in the hot than in cold state and as the fire exposure increased the difference between hot and cold state became more expressed. Furthermore, the difference in residual capacity between hot and cold state after 120 min of fire exposure became negligible. The residual peak loads after 120 min of fire duration at 150 mm displacement for RC frames with and without ductile detailing was 15% and 19% lower compared to its reference state, respectively.

9. CONCLUSIONS AND OUTLOOK

The primary aim of the present work was to investigate the influence of fire exposure on the static, cyclic (quasi-static) and dynamic response of plain and reinforced concrete structures. The framework of the study was divided into four parts: (i) Effect of preloading on anchors loaded in shear perpendicular and close to the concrete edge after fire exposure; (ii) Influence of fracture energy on the dynamic response of the CTS after fire exposure; (iii) RC Frame subjected to thermal and dynamic loading and (iv) RC frame subjected to cyclic loading and subsequent fire exposure (Post Earthquake Fire scenario).

In the first part of the study, the thermo-mechanical model was validated against test data with a single, two, and four-headed anchor group. Although the model could realistically replicate the test results in terms of shear resistance, the initial stiffness in certain cases was overestimated. The main reasons can be attributed to the local damage effects that cannot be properly accounted for in the macroscopic FE analysis. Furthermore, in the analysis, the ideal heating boundary conditions are not the same as in the experimental tests. Potentially, it would be more realistic to calculate the thermally dependent material properties with the nonlocal (average) temperature of the representative volume. In the second part of the numerical study, the parametric analysis was performed to analyze the influence of preloading on the load bearing capacity of anchors. The study shows that with the increase of fire exposure, the resistance of anchors decreases, for both hot and cold (residual) states. The load bearing capacity is reduced more in the cold state than in the hot state due to the larger thermally induced damage. The preloading has a negative influence on the load bearing capacity of the anchor since it further aggravates the thermally induced damage during the heating and cooling process. The residual resistance reduction trend with increasing fire duration is the same as in the case without preloading. However, the study indicates that for fire durations of 30 min and more, the residual capacity becomes smaller than the design load, i.e. the anchor fails during heating or cooling.

The experimental results presented in this work indicate a decreasing tendency of the fracture energy with temperature increase for concrete specimens of two different (small and medium) sizes. However, these results deviate from the available data in the literature (Zhang and Bićanić, 2002), which was used to simulate the dynamic response of the CT specimens in the preceding numerical study (Ruta, 2018) and most of the here presented thermo-mechanical studies as well. Although the previous study shows a relatively good agreement in terms of

failure modes and crack propagation velocities, the reaction histories and the increase of reaction as a function of displacement rate are more pronounced in the numerical tests than in the experiment. By implementing the descending temperature dependency in the thermo-mechanical model, a better agreement not only in the reaction histories but also in the failure modes of the CT specimen is obtained. Although the increase of reaction was dampened, there is still a notable difference in comparison to the experimental results.

The dynamic (impact) and static response of the RC structure previously exposed to fire were investigated. In the preceding study (Ruta, 2018), the thermo-mechanical model was successfully validated in terms of temperature distributions. However, the reactions of the RC frame as a function of horizontal displacement were underestimated. The solution was to extend the numerically prescribed displacement and thus increase the loading rate. Then again, this led to a much stronger impact, which in conjugacy with thermally pre-damaged concrete resulted in strong damage localization in the impact zone and ultimately premature RC frame failure. By calculating the thermally dependent material properties with a nonlocal (average) temperature, a mitigated reduction of properties due to elevated temperature was achieved in the impact zone. With the introduction of the nonlocal temperature field, only the temperature on the surface zones of nonlinear concrete material was affected while the reduction of steel properties was calculated with local temperatures. The application of the nonlocal temperature is mainly applicable in conjunction with dynamic (impact) analysis. This ultimately resulted in the RC frame achieving its prescribed horizontal displacement failure and exhibiting realistic dynamic impact factors. The parametric analysis showed that the fire exposure of RC frames and related thermally induced damage significantly influence their behavior and resistance. For quasi-static loading, the reduction of structural resistance is the highest for the hot state because the steel reinforcement after cooling almost fully recovers. In contrary to the peak resistance, the initial stiffness is controlled by concrete properties and it decreases with increasing fire exposure. The results from the dynamic analysis show that the reduction of resistance and the initial stiffness is significantly higher for the hot state and the overall response is more brittle due to the contribution of inertia. Comparing the reactions with the increase of the loading rate, it was shown that the influence of strain rate becomes more pronounced than the contribution of inertial effects. Thus, the contribution of the rate sensitive constitutive law for concrete to dynamic structural resistance and failure mode is notable.

The last numerical study was the most comprehensive one encompassing the validation of the thermo-mechanical model and subsequent parametric study of the RC frames with and without ductile detailing subjected to post-earthquake fire. Although the resistance of RC frames with

ductile detailing was somewhat underestimated, the model was successfully validated against experimental data showing good agreement in terms of temperature distribution, thermal dilatations of the structural members, failure modes, crack patterns and the loads from the initial seismic and the residual cyclic analysis. The parametric study was carried out for five different fire durations (15, 30, 60, 90 and 120 min in both hot and cold states) by employing the ISO 834 fire curve. Furthermore, the same loading sequence as in the validation analysis consisted of initial seismic loading, thermal exposure and the residual monotonic pushover, was employed. The results indicated, as expected, that the hot state at longer fire exposure times was more critical than the cold state. This is due to the reduction of steel mechanical properties beyond the yield limit. The initial stiffness and the peak loads were reduced with the increased fire duration. Moreover, the ductile detailed RC frame exhibited higher peak loads in the residual analysis for both, hot and cold states. The overall peak load reduction after 120 min of fire exposure for RC with and without ductile detailing amounted to 14% and 19%, respectively.

In view of the preceding discussions and conclusions in terms of nonlocal temperature field implementation and the influence of fracture energy on the dynamic response, it should be noted that further work on different geometries and loading rates is needed to verify the presented model. In the case of thermally pre-damaged anchors, it would be interesting to investigate the influence of the nonlocal temperature on the resistance response (static and dynamic case). Furthermore, the design formula for the shear resistance of fasteners should account for the influence of preloading. In the case of RC frames subjected to PEF, the deviation in temperature distribution in the cross-section of certain structural elements can be attributed to the stochastic nature of fire and gas flows that occurred during the experimental tests. Therefore, to obtain a better overlapping with test results, one should model each part of the RC frame member with different heat fluxes that correspond to the ones obtained in the experiment, especially in the beam-column joints area. Currently, in the literature, there is only a very limited number of experimental and numerical studies of RC structures exposed to extreme conditions, such as fire and impact. Thereby, more experimental and numerical investigations are needed to design efficient structures that will be capable to sustain such complex loading conditions.

BIBLIOGRAPHY

- Abrams, M.S. (1971). Compressive strength of concrete at temperatures to 1600°F, Temperature and concrete, ACI Special publication, No. **25**, Paper SP25, Detroit, 847-70.
- Abrams, M.S. (1979). Elastic and strength properties of Hanford concrete mixes at room and elevated temperatures, Final report to Battelle Pacific Northwest Laboratories, Richland, Portland cement association, Skokie, IL.
- American Concrete Institute Committee 318 (2014). Building code requirements for structural concrete (ACI 318-14) and commentary (ACI 318R-14) Farmington Hills, MI.
- American concrete institute Code-216.1-14(19). (2014). Code Requirements for Determining Fire Resistance of Concrete and Masonry Construction Assemblies.
- Anderberg, Y., Thelandersson, S. (1976). Stress and deformation characteristics of concrete at high temperature: 2. Experimental investigation and material behavior model, Bulletin of Division of Structural Mechanics and Concrete Construction, Bulletin **54**, 86.
- Anderson, N.S., Meinheit, D.F. (2005). Pryout capacity of cast-in headed stud anchors, PCI Journal, 90–112.
- Aoyagi, Y., Ohnulma, H. and Kawasaki, M. (1972). Behavior of flexurally restrained prestressed concrete beams under temperature gradient, Concrete for nuclear Reactors, ACI special publication, Detroit, **34** (2), 799-821.
- Arioz, O. (2007). Effect of elevated temperatures on properties of concrete, Fire Safety Journal. **42** (8), 516-522.
- ASCE (1992). Structural fire protection, ASCE committee on fire protection, Manual No. **78**, Reston, Va.
- ASTM International - E2748-12a (2012). Standard Guide for Fire-Resistance Experiments, West Conshohocken, PA, ASTM International.
- Baker, G. (1996). The effect of exposure to elevated temperatures on the fracture energy of plain concrete, Materials and Structures, **29**, 383.
- Bamonte, P., Gambarova, P.G. and Muciaccia, G. (2020). Ultimate Capacity of Undercut Fasteners Installed in Heat-Damaged Concrete, ASCE, p. 13.

- Banthia, N. P., Mindess, S. and Bentur, A. (1987). Impact behaviour of concrete beams, *Materials and Structures*, **20**, 293-302.
- Barragán, B.E., Giaccio, G.M. and Zerbinio, R.L. (2001). Fracture and failure of thermally damaged concrete under tensile loading, *Materials and Structures*, **34**, 312-319.
- Batista Abreu, J.C., Vieira Jr. L.C.M., Abu-Hamd, M., Schafer, B. (2014). Review: development of performance-based fire design for cold-formed steel, *Fire Science Reviews* **3** (1), 1.
- Bažant, Z.P. and Thonguthai, W. (1978). Pore pressure and drying of concrete at high temperature. *Journal of the Engineering Mechanics Division*, **104** (5), 1059–1079.
- Bažant, Z.P. and Oh, B.H. (1983). Crack band theory for fracture of concrete, *Materials and Structures*, **16** (3), 155–177.
- Bažant, Z.P., Gambarova, P.G. (1984). Crack shear in concrete: crack band microplane model, *Journal of Structural Engineering*, **110** (9), 2015–2035.
- Bažant, Z.P. (1984). Size effect in blunt fracture: concrete, rock, metal, *Journal of Engineering Mechanics*, **110** (4), 518–535.
- Bažant, Z.P. and Oh, B.-H. (1986). Efficient numerical integration on the surface of a sphere, *Zeitschrift für angewandte Mathematik und Mechanik, ZAMM*, **66** (1), 37–49.
- Bažant, Z.P. and Prat, P.C. (1988a). Effect of Temperature and Humidity on Fracture Energy of Concrete, *ACI Materials Journal*, **85**, 262-271.
- Bažant, Z. P., and Prat, P. C. (1988b). Microplane model for brittle plastic material: I. Theory, *Journal of Engineering Mechanics*, 1672–1688.
- Bažant, Z.P.; Ožbolt, J. (1990). Nonlocal microplane model for fracture, damage and size effect in structures, *Journal of Engineering Mechanics*, **116**, 2485–2505.
- Bažant, Z.P., Kazemi, M.T. (1991). Size dependence of concrete fracture energy determined by RILEM work-of-fracture method, *International Journal of Fracture*, **51** (2), 121–138.
- Bažant, Z. P. & Kaplan, M. F. (1996). *Concrete at high temperatures*, Longman Essex, UK.
- Bažant, Z. P. et al. (2000a). Large-strain generalization of microplane model for concrete and application, *Journal of Engineering Mechanics*, **126**, 971–980.

- Bažant, Z. P., Adley, M. D., Carol, I., Jirásek, M., Akers, S. A., Rohani, B., Cargile, J. D. & Caner, F. C. (2000b). Large-strain generalization of microplane model for concrete and application, *Journal of Engineering Mechanics*, **126** (9), 971–980.
- Bede, N., Ožbolt, J., Sharma, A. and Irhan, B. (2015). Dynamic fracture of notched plain concrete beams: 3D finite element analysis, *International Journal of Impact Engineering*, **77** (1), 176–188.
- Behnam, B., Ronagh, H. (2013). Post-earthquake fire resistance of CFRP strengthened reinforced concrete structures, *Structural Design of Tall and Special Buildings*, **23**, 814–832.
- Belytschko, T., Liu, W. K., and Moran, M. (2001). *Nonlinear finite elements for continua and structures*, John Wiley, Hoboken, NJ, USA.
- Bentur, A., Mindess, S. and Banthia, N. (1987). The behavior of concrete under impact loading experimental procedures and method of analysis, *Materials and Structures*, **19**, p. 113.
- BIS (Bureau of Indian Standards) (2000). Code of practice for plain and reinforced concrete, IS 456, New Delhi, India.
- BIS (Bureau of Indian Standards) (1993). Ductile detailing of reinforced concrete structures subjected to seismic forces-code of practice (reaffirmed 2008), IS 13920, New Delhi, India.
- BIS (Bureau of Indian Standards) (2002). General provisions and buildings: Criteria for earthquake resistant design of structures, IS 1893 (Part 1), New Delhi, India.
- Bischoff, P. and Perry, S. (1991). Compressive behavior of concrete at high strain rates, *Materials and Structures*, **24**, 425-450.
- Borodin, E.N., Mayer, A.E. (2015). Structural model of mechanical twinning and its application for modeling of the severe plastic deformation of copper rods in Taylor impact tests, *International Journal of Plasticity*, **74**, 141-157.
- BS EN 14651 (2007). Test method for metallic fibre concrete. Measuring the flexural tensile strength (limit of proportionality (LOP), residual). 1-20.
- de Borst, R. and Paul P.J.M. Peeters. (1989). Analysis of concrete structures under thermal loading, *Computer methods in applied mechanics and engineering*, **77** (3), 293-310.

- Bošnjak, J. (2014). Explosive spalling and permeability of high performance concrete under fire – numerical and experimental investigations. Dissertation, Institut für Werkstoffe im Bauwesen, Universität Stuttgart.
- Bousquet, A., Marie, S., and Bompard, P. (2011). Cleavage crack propagation characterization in a nuclear pressure vessel steel, *Technische Mechanik*, **32**, 118–129.
- Boyce, B. L., Crenshaw, T. B., and Dilmore, M. F. (2007). The strain rate sensitivity of high—Strength high—Toughness steels, SANDIA Rep., Sandia National Laboratories, Albuquerque, NM.
- Carol, I., Prat, P. and Bažant, Z. P. (1992). New explicit microplane model for concrete: theoretical aspects and numerical implementation, *International Journal of Solids and Structures*, **29** (9), 1173–1191.
- Caverzan, A., Ezio, C. and Marco di Prisco. (2013). Dynamic tensile behaviour of high performance fibre reinforced cementitious composites after high temperature exposure, *Mechanics of Materials* **59**, 87-109.
- Chen, B., Liu, J. (2004). Effect of aggregate on the fracture behavior of high strength concrete, *Construction and Building Materials*, **18** (8), 585–590.
- Clark, CL (1953). High-temperature alloys. Pitman Metallurgy Series, Pitman Publishing Corporation, Toronto.
- Colombo, M., Martinelli P. and Marco di Prisco. (2015). A design approach for tunnels exposed to blast and fire, *Structural Concrete* **16** (2), 262-272.
- Costes, F. (2004). Modélisation thermomécanique tridimensionnelle par éléments finis de la coulée continue d’aciers, Ecole Nationale Supérieure des Mines de Paris, Paris, France.
- Cottrell, A. H. (1964). The mechanical properties of Matter, John Wiley & Sons, New York.
- Cruz, C.R. (1966). Elastic Properties of Concrete at High Temperature, *Journal of the Portland Cement Association Research and Development Laboratory (PCA Bulletin 191)*, January, 37-45.
- Curbach, M. (1987). Festigkeitssteigerung von Beton bei hohen Belastungs-geschwindigkeiten, PhD. Thesis, Karlsruhe University, Germany.
- Cusatis, G. (2011). Strain-rate effects on concrete behavior, *International Journal of Impact Engineering*, **38** (4), 162–170.

- Demir, U., Goksu, C., Unal, G., Green, M., and Ilki, A. (2020). Effect of Fire Damage on Seismic Behavior of Cast-in-Place Reinforced Concrete Columns, *ASCE*. **146** (11).
- Dilger, W. H., Koch, R. and Kowalczyk, R. (1978). Ductility of plain and confined concrete under different strain rates, American Concrete Institute, Special publication, Detroit, Michigan, USA.
- Dougill, J. W. (1972). Modes of failure of concrete panels exposed to high temperatures, *Magazine of Concrete Research*, **24** (79).
- Eakins, D.E., Thadhani, N.N., (2006). Instrumented Taylor anvil-on-rod impact tests for validating applicability of standard strength models to transient deformation states, *Journal of Applied Physics*, **100**.
- Eligehausen, R. and Reick, M. (1996). Behaviour of anchors in fire – Report of fire tests 1995. Report Nr. 21/4-96/1 (unveröffentlicht), Institut für Werkstoffe im Bauwesen, Universität Stuttgart, Stuttgart.
- Eligehausen, R., Mallée, R., Silva, J.F. (2006). Anchorage in concrete construction, Berlin: Ernst & Sohn.
- Ervine, A., Gillie, M., Stratford, T.J. and Pankaj, P. (2012). Thermal Propagation through Tensile Cracks in Reinforced Concrete, *Journal of Materials in Civil Engineering*, ASCE, **24** (5), 516-522.
- European Committee for Standardization (2003). Eurocode 1 1991-1-2: Actions on structures - Part 1-2: General actions - Actions on structures exposed to fire. Brussels, Belgium
- European Committee for Standardization (2004a). Eurocode 2 1992-1-2: design of concrete structures. Part 1-2: general rules-structural fire design. Brussels, Belgium.
- European Committee for Standardization (2004b). Eurocode 4 EN 1994-1-1 Design of composite steel and concrete structures - Part 1-1: General rules and rules for buildings. Brussels, Belgium.
- European Committee for Standardization (2005a). Eurocode 3 EN 1993-1-2 Design of steel structures - Part 1-2: General rules - Structural fire design. Brussels, Belgium.
- European Committee for Standardization (2005b). Eurocode 4 EN 1994-1-2 Design of composite steel and concrete structures - Part 1-2: General rules - Structural fire design. Brussels, Belgium.

- European Committee for Standardization (2016). EN 13501-2: Fire classification of construction products and building elements - Part 2: Classification using data from fire resistance tests, excluding ventilation services. Brussels, Belgium.
- fédération internationale du béton (fib) (2007). CEB-FIP bulletin 38: Fire design of concrete structures - materials, structures and modelling, Lausanne, Switzerland.
- Bulletin No. 66. Chapter 5, Code-type models for concrete behavior, In Model Code 2010—Final Draft, Ernst & Sohn, Berlin, Germany, 2012, Volume 2.
- FEMA (Federal Emergency Management Agency) (2000). Prestandard and commentary for the seismic rehabilitation of buildings, FEMA 356, Building Seismic Safety Council, Washington, DC.
- Felicetti, R., Gambarova, P.G., Sora, M.P.N., Khoury, G.A. (2000) Mechanical behavior of HPC and UHPC in direct tension at high temperature and after cooling, Fifth International RILEM Symposium on Fibre-Reinforced Concrete (FRC), 749–758.
- Freund, L. B. (1972a). Crack propagation in an elastic solid subjected to general loading-I, constant rate of extension, Journal of the Mechanics and Physics of Solids, **20** (3), 129–140.
- Freund, L. B. (1972b). Crack propagation in an elastic solid subjected to general loading-II, non-uniform rate of extension, Journal of the Mechanics and Physics of Solids, **20** (3), 141–152.
- Fuchs, W., Eligehausen, R., Breen, J.E. (1995). Concrete capacity design (CCD) approach for fastening to concrete, Structural Journal. **92** (1).
- Garboczi, E., Bentz, D. (1996). The effect of the interfacial transition zone on concrete properties: the dilute limit, Material for the new millennium, **2**, 1228–1237.
- Gary, M. (1916). Brandproben an Eisenbetonbauten, Ernst & Sohn.
- Gawin D., C. E. Majorana and B. A. Schrefler. (1999). Numerical analysis of hygro-thermal behavior and damage of concrete at high temperature, Mechanics of Cohesive-frictional Materials **4** (1), 37-74.
- Giaccio, G., Rocco, C., Zerbino, R. (1993). The fracture energy (G_F) of high-strength concretes, Materials and Structures, **26** (7), 381–386.

- Gopalaratnam, V.S., Shah, S.P., Batson, G.B., Criswell, M.E., Ramakrishnan, V., Wecharatana, M. (1991). Fracture toughness of fiber reinforced concrete, *ACI Materials Journal*, **88** (4), 339–353.
- Grosser, P.R. (2012). Load-bearing behavior and design of anchorages subjected to shear and torsion loading in uncracked concrete, PhD thesis. University of Stuttgart, Germany
- Hager I. (2013). Behavior of cement concrete at high temperature. *Bulletin of the Polish Academy of Sciences. Technical Sciences* **61** (1).
- Hager I, Pimienta P. (2005). Déformation thermique transitoire des bétons à haute performance, *Revue Européenne de Génie Civil*, **9**, 373–383.
- Hahn, G.T., Hoagland, R.G., Kanninen, M.F., Rosenfeld, A.R. (1973). A preliminary study of fast fracture and arrest in the DCB test specimen.
- Hansen, C.T., Eriksson L. (1966). Temperature change effect on behavior of cement paste, mortar, and concrete under load, *ACI Journal Proceedings*, **63**.
- Hansen, K.K., 1986. Sorption isotherms: a catalogue, Technical University of Denmark, Department of Structural Engineering and Materials.
- Harmathy, T.Z. (1970). Thermal properties of concrete at elevated temperatures, *Journal of Materials*. **5** (1), 47–74.
- Harmathy, T. & Allen, L., (1973). Thermal properties of selected masonry unit concretes, *ACI Journal Proceedings*, **70**, 132-142.
- He, Y., Huo, J., Xiao, Y. (2011). Experimental study on dynamic behavior of concrete at elevated temperatures, *Advanced Science Letters*, **4**(3), 1128–1131.
- Hildenbrand, G., Peeks, M., Skokan, A., Reimann, M. (1978). Untersuchung der Wechselwirkung von Kernschmelze und Reaktorbeton, Kraftwerk Union Erlangen / Reaktortechnik.
- Hillerborg, A. (1985). Results of three comparative test series for determining the fracture energy G_F of concrete, *Materials and Structures*, **18** (5), 407–413.
- Hopkinson, B. (1914). A method of measuring the pressure produced in the detonation of high explosives or by the impact of bullets, *Phil. Trans. Roy. Soc. London, Series A*, **213** (10), 437–456.

- Huo, J., He, Y., Xiao, L., Chen, B. (2013). Experimental study on dynamic behaviors of concrete after exposure to high temperatures up to 700 °C, *Materials and Structures*, **46** (1–2), 255–265
- Hwang, Y.K., Bolander, J.E. & Lim, Y.M. (2020). Evaluation of dynamic tensile strength of concrete using lattice-based simulations of spalling tests, *International Journal of Fracture* **221**, 191–209.
- International Organization for Standardization (1999). ISO 834-1 Fire resistance tests - Elements of building construction - Part 1: General requirements, Geneva, Switzerland.
- Issa, M.A., Islam, M.S., Chudnovsky, A. (2000). Size effects in concrete fracture—part II: analysis of test results, *International Journal of Fracture*, **102** (1), 25–42.
- Jebara, K., Ožbolt, J., Hofmann, J. (2016). Pryout failure capacity of single headed stud anchors, *Materials and Structures*, **49**, 1775–1792.
- Jirásek, M., and Bažant, Z. P. (2002). *Inelastic analysis of structures*, Wiley, New York.
- Jirásek, M.; Marfia, S. (2005). Nonlocal damage model based on displacement averaging, *International Journal for Numerical Methods in Engineering*, **63**, 77–102.
- Kamath, P., Sharma, U.K., Kumar, V., Bhargava, P., Usmani, A., Singh, B., Singh, Y., Torero, J., Gillie, M. and Pankaj, P. (2015). Full-scale fire test on an earthquake-damaged reinforced concrete frame, *Fire Safety Journal*, **73**, 1-19.
- Kanazawa, T., Machida, S., Teramoto, T., and Yoshinari, H. (1981). Study on fast fracture and crack arrest, *Experimental Mechanics*, **21** (2), 78–88.
- Khalilpour, S., BaniAsad, E., Dehestani, M. (2019). A review on concrete fracture energy and effective parameters, *Cement and Concrete Research*, **120**, 294-321.
- Khoury G. A., Brian N. Grainger and Patrick JE Sullivan. (1985a). Transient thermal strain of concrete: literature review, conditions within specimen and behavior of individual constituents, *Magazine of concrete research*, **37** (132), 131-144.
- Khoury, G. A., Grainger, B. N. and Sullivan P. J. E. (1985b). Strain of concrete during first heating to 600 °C under load. *Magazine of concrete research*, **37** (133).
- Khoury, G. A. (1996). Performance of heated concrete: mechanical properties. Report submitted to the Nuclear Inst. Inspectorate of the Health and safety executive, 232.

- Khoury G.A. (2000). Effect of fire on concrete and concrete structures, *Progress in Structural Engineering and Materials*, **2** (4), 429-447.
- Khoury G. A. (2006). Strain of heated concrete during two thermal cycles. Part 1: strain over two cycles, during first heating and at subsequent constant temperature, *Magazine of Concrete Research*, **58** (6), 367-385.
- Kim, J.S., Jung, W.Y., Kwon, M.H., Ju, B.S. (2013). Performance evaluation of the post-installed anchor for sign structure in South Korea, *Construction and Building Materials*, **44**, 496–506.
- Kodur V, Dwaikat, M., Fike, R. (2010). High-Temperature Properties of Steel for Fire Resistance Modeling of Structures. *ASCE, Journal of Materials in Civil Engineering*, **22** (5).
- Kodur, V., Kand, S., Khaliq, W. (2011). Effect of Temperature on Thermal and Mechanical Properties of Steel Bolts. *ASCE. Journal of Materials in Civil Engineering*, **24** (6).
- Kodur, V. (2014). Properties of Concrete at Elevated Temperatures, *International Scholarly Research Notices*, **20** (14), Article ID 468510.
- Kolsky, H. (1953). *Stress waves in solids* Clarendon Press, Oxford.
- Kordina Karl and Claus Meyer-Ottens (1981). *Beton-Brandschutz-Handbuch*, Beton-Verlag,
- Krausz, A.S. and Krausz K. (1988). *Fracture Kinetics of Crack Growth*, **1**, Springer Netherlands.
- Lakhani, H., Singh, T., Sharma, A., Reddy, GR, Singh, RK. (2014). Prediction of Post Fire Load Deflection Response of RC Flexural members using Simplistic Numerical Approach, *Structural Engineering and Mechanics*, **50** (6).
- Larcher, M. (2009). Development of discrete cracks in concrete loaded by shock waves, *International Journal of Impact Engineering*, **36** (5), 700-710.
- Li, Q. M., and Meng, H. (2003). About the dynamic strength enhancement of concrete-like materials in a split Hopkinson pressure bar test, *International Journal of solids and structures*, **40** (2), 343-360.
- Li, Z., Xu, J., Bai, E. (2012). Static and dynamic mechanical properties of concrete after high temperature exposure, *Materials Science and Engineering: A*, **544**, 27–32.

- Luccioni, B. M., Figueroa, M. I. and Danesi, R. F. (2003). Thermo-mechanic model for concrete exposed to elevated temperatures, *Engineering Structures*, **25** (6), 729-742.
- Malhotra, V., Carette, G., Bilodeau, A. (1994). Mechanical properties and durability of polypropylene fiber reinforced high-volume fly ash concrete for shotcrete applications, *Materials Journal*, **91** (5), 478–486.
- Malvar L.J. and Ross C.A. (1998). Review of strain rate effects for concrete in tension *ACI Materials Journal*, **95** (6), 735-739.
- Mashiri, F.R., Mirza, O., Canuto, C., Lam, D. (2017). Post-fire behavior of innovative shear connection for steel-concrete composite structures, *Structures*, **9**, 147–156.
- Mehta, P. K. and Monteiro, P. J. M. (2006). *Concrete: Microstructure, Properties, and Materials*, McGraw-Hill, New York, NY, USA.
- Meyer-Ottens, C. (1972). The question of spalling of concrete structural elements of standard concrete under fire loading, Technical University of Braunschweig.
- Mirza, O., Uy, B. (2009). Behavior of headed stud shear connectors for composite steel–concrete beams at elevated temperatures, *Journal of Constructional Steel Research*, **65** (3), 662–674.
- Mo, K.H., Yap, K.K.Q., Alengaram, U.J., Jumaat, M.Z. (2014). The effect of steel fibers on the enhancement of flexural and compressive toughness and fracture characteristics of oil palm shell concrete, *Construction and Building Materials*, **55**, 20–28.
- Nallathambi, P., Karihaloo, B., Heaton, B. (1984). Effect of specimen and crack sizes, water/cement ratio and coarse aggregate texture upon fracture toughness of concrete, *Magazine of Concrete Research*, **36** (129), 227–236.
- Nanni, A. (1988). Splitting-tension test for fiber reinforced concrete, *ACI Materials Journal*, **85** (4), 229–233.
- Naus, D. J., Batson, G. B., and Lott, J. L. (1974). *Fracture mechanics of concrete, Fracture Mechanics of Ceramics*, Springer, Boston, MA, 469-482.
- Nielsen, C.V., Bićanić, N. (2003). Residual fracture energy of high-performance and normal concrete subject to high temperatures, *RILEM Materials and Structures*, **36** (8), 515–521.
- Ožbolt, J. and Bažant, Z. P. (1992). Microplane model for cyclic triaxial behavior of concrete, *Journal of Engineering Mechanics*, ASCE, **118** (7), 1365-1386.

- Ožbolt, J. (1998). MASA-macroscopic space analysis, Internal Report. Institute of Construction Materials, University of Stuttgart, Germany.
- Ožbolt, J., Li, Y., and Kožar, I. (2001). Microplane model for concrete with relaxed kinematic constraint, *International Journal of Solids and Structures*, **38** (16), 2683–2711.
- Ožbolt, J., and Reinhardt, H. W. (2002). Numerical study of mixed mode fracture in concrete, *International Journal of Fracture*, **118** (2), 145–162.
- Ožbolt J., and H.W. Reinhardt. (2005a). Rate dependent fracture of notched plain concrete beams, CONCREEP-7.
- Ožbolt J., Kožar, I., Eligehausen, R. and Periškić, G. (2005b). Instationäres 3D Thermo-mechanisches Modell für Beton, *Beton-und Stahlbetonbau*, **100.1**, 39-51.
- Ožbolt, J.; Periškić, G.; Reinhardt, H.W.; Eligehausen, R. (2008). Numerical analysis of spalling of concrete cover at high temperature, *Computers and Concrete*, **5**, 279–294.
- Ožbolt, J.; Balabanić, G.; Periškić, G.; Kušter, M. (2010). Modeling the effect of damage on transport processes in concrete, *Construction and Building Materials*, **24**, 1638–1648.
- Ožbolt, J., Sharma, A., and Reinhardt, H.-W. (2011). Dynamic fracture of concrete-compact tension specimen, *International Journal of Solids and Structures*, **48** (10), 1534–1543.
- Ožbolt, J., and Sharma, A. (2012). Numerical simulation of dynamic fracture of concrete through uniaxial tension and L-specimen, *Engineering Fracture Mechanics*, **85** (1), 88–102.
- Ožbolt, J., Bošnjak, J., and Sola, E. (2013). Dynamic fracture of concrete compact tension specimen: Experimental and numerical study, *International Journal of Solids and Structures*, **50** (25–26), 4270–4278.
- Ožbolt, J., Sharma, A., Írhan, B., and Sola, E. (2014). Tensile behavior of concrete under high loading rates, *International Journal of Impact Engineering*, **69** (1), 55–68.
- Ožbolt, J.; Bede, N.; Sharma, A.; Mayer, U. (2015). Dynamic fracture of concrete L-specimen: Experimental and numerical study, *Engineering Fracture Mechanics*, **148**, 27–41.
- Ožbolt, J., Tonković, Z., Lacković, L. (2016). Microplane Model for Steel and Application on Static and Dynamic Fracture. *ASCE Journal of Engineering Mechanics*, **142**.
- Ožbolt, J., Lacković, L., Ruta, D. (2020). Impact Analysis of Thermally Pre-Damaged Reinforced Concrete Frames, *Materials* 2020, **13** (23), 5349.

- Ožbolt, J., Lacković, L., Tian, K. (2021). Post-fire concrete edge failure in single and multiple anchors pre-loaded in shear, *Fire Safety Journal*, **122**.
- Pampanin, S., Christopoulos, C., and Chen, T.H., (2006). Development and validation of a metallic haunch seismic retrofit system for existing under-designed RC frame buildings, *Earthquake Engineering and Structural Dynamics*, **35**, 1739-1766.
- Pan J., Zou R. and Jin, F. (2016). Experimental Study on Specific Heat of Concrete at High Temperatures and Its Influence on Thermal Energy Storage, *Energies* **10** (1), 33.
- Parmar, R.M.; Singh, T.; Sharma, S.; Reddy, G.R.; Singh, R.K. (2014). Experimental Investigation on Behavior of Reinforced Concrete Structures under Fire and Impact Loads, Report, Bhabha Atomic Research Centre, Mumbai, India.
- Periškić G. (2009). Entwicklung eines 3D thermos-hygro-mechanischen Modells für Beton unter Brandbeanspruchung und Anwendung auf Befestigungen unter Zuglasten, PhD Thesis, Institut für Werkstoffe im Bauwesen, University of Stuttgart.
- Peterson, P.E. (1980). Fracture energy of concrete: method of determination, *Cement and Concrete Research*, **10** (1), 79–89.
- Poh, K. W. (2001). Stress-strain-temperature relationship for structural steel, *Journal of Materials in Civil Engineering*, **135**, 371–379.
- Prabel, B., Marie, S., Combescure, A. (2008). Using the X-FEM method to model the dynamic propagation and arrest of cleavage cracks in ferritic steel, *Engineering Fracture Mechanics*, **75**, 2984-3009.
- Rakvåg, K.G., Børvik, T., Hopperstad, O.S. (2014). A numerical study on the deformation and fracture modes of steel projectiles during Taylor bar impact tests, *International Journal of Solids and Structures*, **51**, 808–821.
- Reick, M. (1998). Brandverhalten von Befestigungen in Beton bei zentrischer Zugbeanspruchung - Auswertung der Versuche mit Stahlversagen, Bericht Nr. 21/8-98/1 (unveröffentlicht), Institut für Werkstoffe im Bauwesen, Universität Stuttgart, Stuttgart.
- Reick, M. (2001). Brandverhalten von Befestigungen mit großem Randabstand in Beton bei zentrischer Zugbeanspruchung (Fire resistance of anchors far from an edge in concrete with axial loading). (in German), PhD thesis, University of Stuttgart.

- Reinhardt, H. W. (1982). Concrete under impact loading, tensile strength and bond, *Heron*, **27** (3).
- Reinhardt, H.W., Weerheijm, J. (1991). Tensile fracture of concrete at high loading rates taking account of inertia and crack velocity effects, *International Journal of Fracture*, **51**, 31.
- RILEM Committee - R.D. Recommendation (1985). Determination of the fracture energy of mortar and concrete by means of three-point bend tests on notched beams, *Materials and Structures*, **18** (106), 285–290.
- RILEM Committee 129-MHT (1998). Part 7: Transient creep for service and accident conditions, *Material and Structures*, **31**, 290-295.
- Ronagh, H. and Behnam, B. (2012). Investigating the Effect of Prior Damage on the Post-earthquake Fire Resistance of Reinforced Concrete Portal Frames, *International Journal of Concrete Structures and Materials*, **6** (4), 209–220.
- Rossi P, Toutlemonde F (1996). Effect of loading rate on the tensile behaviour of concrete: description of the physical mechanisms, *Materials and Structures*, **29** (2), 116–118.
- Rossoll, A. (1993). Local approach of ductile cast iron fracture toughness measured by Charpy test, PhD, Ecole Centrale Paris.
- Ruta, D. (2018). Numerical and experimental study of concrete structures under extreme conditions: impact and fire, PhD, Institut für Werkstoffe im Bauwesen, Universität Stuttgart, Stuttgart.
- Saito, H., (1965). Explosive spalling of prestressed concrete in fire, Building Research Institute, Japan, Occasional report No. **22**.
- Schneider, U. (1982). Verhalten von Beton bei hohen Temperaturen Deutscher Ausschuss für Stahlbeton, ed. Ernst & Sohn.
- Schneider, U. (1986). Properties of Materials at High Temperatures, Concrete, RILEM Technical Committee 44- PHT, 2nd. Edition, Technical University of Kassel, Kassel, Germany.
- Schneider, U. (1988). Concrete at High Temperatures – A General Review, *Fire Safety Journal*, **13**.

- Schuler, H.C., Mayrhofer, K. (2006). Spall experiments for the measurement of the tensile strength and fracture energy of concrete at high strain rates, *International Journal of Impact Engineering*, **32**, 1635-1650.
- Shah, S.P., Rangan, B.V. (1971). Fiber Reinforced Concrete Properties, *ACI Journal*, **68** (2), 126-135.
- Shah, A.H., Sharma, U.K., Kamath, P., Bhargava, P., Reddy, G.R., Singh T. (2016). Fire performance of earthquake-damaged reinforced concrete structures, *Materials and Structures*, **49**, 2971–2989.
- Shah, A.H., Sharma, U.K. and Bhargava, P. (2017). Outcomes of a major research on full scale testing of RC frames in post earthquake fire, *Construction and Building Materials*, **155**, 1224-1241.
- Sharma, U. K., et al. (2012). Full-scale testing of a damaged reinforced concrete frame in fire, *Proceedings of the Institution of Civil Engineers - Structures and Buildings*, **165** (SB7), 335–346.
- Sharma, A.; Bošnjak, J.; Ožbolt, J.; Hofmann, J. (2016). Numerical modelling of reinforcement pull-out and cover splitting in fire-exposed beam-end specimens. *Engineering Structures*, **111**, 217–232.
- Sierakowski, R.L. (1985). Dynamic Effect in Concrete Materials. In: Shah S.P. (eds). *Application of Fracture Mechanics to Cementitious Composites*, NATO ASI Series (Series E: Applied Sciences), Springer, Dordrecht, **94**.
- Siregar, A., Rafiq, M.I., M. Mulheron, M. (2017). Experimental investigation of the effects of aggregate size distribution on the fracture behaviour of high strength concrete, *Construction and Building Materials*, **150**, 252–259.
- Shorter, G. and Harmathy, T. (1965). Moisture clog spalling, *Proceedings of the Institution of Civil Engineers*, **20**, 75–90.
- Simcenter FEMAP. v11.3 (2016). Siemens AG, Munich.
- Song, L., Izzuddin, B.A., Elnashai, A.S. (2000). An integrated adaptive environment for fire and explosion analysis of steel frames – part I: analytical models, *Journal of Constructional Steel Research*, **53** (1), 63-85.

- Tanguy, B. (2001). Modélisation de l'essai Charpy par l'approche locale de la rupture: application au cas de l'acier 16MND5 dans le domaine de transition, PhD, Ecole des Mines de Paris.
- Taylor, G. I. (1938). Plastic strain in metals, *Journal of the Institute of Metals*, **62** (1), 307–324.
- Taylor, G.I. (1948). The use of flat ended projectiles for determining yield stress 1: Theoretical considerations, *Proceedings of the Royal Society London: A*, **194**, 289-299.
- Tanchev, R. & Purnell, P. (2005). An application of a damage constitutive model to concrete at high temperature and prediction of spalling. *International Journal of solids and structures*, **42** (26), 6550–6565.
- Thelandersson, S. (1987). Modelling of combined thermal and mechanical action in concrete, *Journal of Engineered Mechanics*, **113** (6).
- Tian, K., Ožbolt, J., Periškić, G., Hofmann, J. (2018a). Concrete edge failure of single headed stud anchors exposed to fire and loaded in shear: Experimental and numerical study, *Fire Safety Journal*, **100**, 32–44.
- Tian, K., Ožbolt, J., Sharma, A., Hofmann, J. (2018b). Experimental study on concrete edge failure of single headed stud anchors after fire exposure, *Fire Safety Journal*, **96**, 176–188.
- Tian, K. (2019). Concrete failure of headed stud fasteners exposed to fire and loaded in shear: experimental and numerical study, Dissertation, University of Stuttgart, Germany.
- Torelli, G., Mandal, P., Gillie, M., Tran V.-X. (2016). Concrete strains under transient thermal conditions: A state-of-the-art review, *Engineering Structures*, **127**, 172–188.
- Vecchio, F. J., and Sato, J. A. (1990). Thermal gradient effects in reinforced concrete frame structures, *ACI Structural Journal*, **87** (3), 262–275.
- Volkov, G., Borodin, E., Bratov, V. (2017). Numerical simulations of Taylor anvil-on-rod impact tests using classical and new approaches. *Procedia Structural Integrity*, **6**, 330–335.
- Wang, A.J. (2012). Numerical Investigation into Headed Shear Connectors under Fire, *Journal of Structural Engineering*. **138** (1), 118–122.
- Weerheijm, J. (1992). Concrete under impact tensile loading and lateral compression, Dissertation, Technische Universiteit Delft, Delft, Netherlands.

- Weerheijm, J. and van Doormaal, J.C.A.M. (2007). Tensile failure of concrete at high loading rates: New test data on strength and fracture energy from instrumented spalling tests, *International Journal of Impact Engineering* **34** (3), 609–626.
- Weidner, A. M. et al. (2015). Dynamic Properties of Concrete at Moderately Elevated Temperatures, *ACI Materials Journal*, **112** (5).
- Wen, B., Zhang, L., Wu, B. and Niu, D. (2018). Structural Performance of Earthquake-damaged Beams in Fire, *KSCCE Journal of Civil Engineering*, **22** (12), 5009–5025.
- Whiffin, A.C. (1948). The use of flat-ended projectiles for determining yield stress II: Tests on various metallic materials, *Proceedings of the Royal Society London: A*, **194**, 300–322.
- Wilkins, M.L., Guinan, M.W., (1973). Impact of cylinders on a rigid boundary, *Journal of Applied Physics*, **44**, 1200 – 1206.
- Wu, H., Zhang, Q., Huang, F. and Jin, Q. (2005). Experimental and numerical investigation on the dynamic tensile strength of concrete, *International Journal of Impact Engineering*, **32**, 605–617.
- Xu, S., Zhao, Y. & Wu, Z., (2006). Study on the average fracture energy for crack propagation in concrete, *Journal of Materials in Civil Engineering*, **18** (6), 817–824.
- Yafei, S., Yongjun, T., Jing, S., and Dongjie, N. (2009). Effect of temperature and composition on thermal properties of carbon steel, *Proc., CCDC '09: Control and Decision Conference*, 17-19 June 2009, IEEE, Piscataway, NJ, 3756–3760.
- Yan, A., Wu, K.-R., Zhang, D. and Yao, W. (2001). Effect of fracture path on the fracture energy of high-strength concrete, *Cement and Concrete Research*, **31** (11), 1601–1606.
- Yu J., Yu K., and Lu Z. (2012). Residual fracture properties of concrete subjected to elevated temperatures, *Materials and Structures*, **45**, 1155–1165.
- Yu K., Yu J., and Lu Z. (2016). Fracture properties of high-strength/high-performance concrete (HSC/HPC) exposed to high temperature, *Materials and Structures*, **49**, 4517–4532.
- Zhai C., Chen, L., Xiang, H. and Fang, Q. (2016). Experimental and numerical investigation into RC beams subjected to blast after exposure to fire, *International Journal of Impact Engineering*, **97**, 29-45.

Zhang, B., Bićanić, N., Pearce, C.J. and Balabanić, G. (2000). Residual fracture properties of normal- and high-strength concrete subject to elevated temperatures, Magazine of Concrete Research, **52** (2), 123–136.

Zhang, B. and Bićanić N. (2002). Residual Fracture Toughness of Normal-and High- Strength Gravel Concrete after Heating to 600°C, ACI Materials Journal, **99** (3).

Zhukov, V. (1970). Explosive failure of concrete during a fire. Translation No. DT, 2124.

Zielinski, A.J. (1982). Fracture of concrete and mortar under uniaxial impact tensile loading, PhD, Delft University Press.

Figures from the Web:

Figure 1-1a: <https://www.stratford-herald.com/>

Figure 1-1b: <https://theage.com.au>

Figure 1-1c: <https://www.constructionweekonline.com/>

Figure 2-15: <https://www.alphastructural.com/>

CURRICULUM VITAE

Personal data

Luka Lacković

Born on the 19th April 1991

in Zagreb, Croatia

Education

2006 – 2009	Classical Gymnasium, Zagreb, Croatia
09/2009 – 03/2013	Faculty of Mechanical Engineering and Naval Architecture, Zagreb; Degree: Bachelor of Science (B.Sc.)
03/2013 – 12/2014	Faculty of Mechanical Engineering and Naval Architecture, Zagreb; Degree: Master of Science (M.Sc.)

Experience

09/2014 – 12/2014	Visiting Researcher, University of Stuttgart
02/2015 – 05/2015	Apprenticeship, AVL Zagreb
10/2015 - Present	Research Assistant, Institute of Construction Materials, University of Stuttgart